REVIEW ARTICLE

Check for updates

Emerging processing guidelines for solid electrolytes in the era of oxide-based solid-state batteries†

Moran Balaish,‡*[ab] Kun Joong Kim, [ID] ‡[b] Hyunwon Chu, [ID][c] Yuntong Zhu, [ID][c] Juan Carlos Gonzalez-Rosillo, [ID][d] Lingping Kong, [ID][ce] Haemin Paik, [ID][c] Steffen Weinmann,[b] Zachary D. Hood, [ID][f] Jesse Hinricher,[c] Lincoln J. Miara [ID][g] and Jennifer L. M. Rupp [ID] *[abc]

The current most mature, competitive, and dominant battery technology for electric vehicles (EVs) is the Li-ion battery (LIB). As future EVs will rely on battery technology, further innovation is essential for the success of mobility electrification towards improving the driving range and reducing the charging time and price competitiveness. The commonly cited next generation technologies are hybrid and solid-state batteries (SSBs) enabling high energy densities using lithium. Through a critical approach, we dismantle the oxide-based solid-state battery electrolytes, their chemistries and ceramic manufacture. We evaluate the relevance of solid-state electrolytes and their integration into battery types compared to Li-ion batteries considering a holistic life cycle thinking of sustainable battery production. We evaluate the relevant oxide-based materials and requirements, the material supply chain, and diverse recycling concepts. We raise critical questions about the development of oxide-based SSBs mainly for large-scale production and EV applications, which demand attention to fill current scientific and technological gaps. Next, we critically discuss three major ceramic synthesis routes toward oxide-based solid electrolytes: solid-state processing, wet-chemical solution processing, and vapor deposition. In-depth processing guidelines, hindrances, and opportunities are highlighted. Through a high-level approach, the advantages and disadvantages of each processing method are introduced, while accounting for four major processing metrics applicable for obtaining high Li-ion conducting solid-state Li oxide electrolytes: chemistry of the precursors, dopants and stoichiometry, synthesis temperature, and atmosphere and pressure. We broaden the processing discussion from a single electrolyte component to electrode/electrolyte tandems examining interfaces during cell fabrication, possible cell architectures, design-specific processing methods, challenges, and mitigating solutions for both bulk-type batteries and thin film batteries. Finally, future perspectives and key guidelines for the realization of all SSBs are analyzed and discussed.

[a] *TUMint. Energy Research GmbH, Lichtenbergstr. 4, Garching 85747, Germany. E-mail: moran.balaish@tum.de, jrupp@tum.de*

[b] *Department of Chemistry, Technical University of Munich, 85748 Garching, Germany*

[c] *Department of Materials Science and Engineering, Massachusetts Institute of Technology, Cambridge, MA 02139, USA*

[d] *Catalonia Institute for Energy Research (IREC), Jardins de les Dones de Negre 1, Planta 2, 08930, Sant Adrià del Besòs, Barcelona, Spain*

[e] *Department of Mechanical Engineering, San Diego State University, San Diego, CA 92182, USA*

[f] *Applied Materials Division, Argonne National Laboratory, Lemont, IL 60439, USA*

[g] *Advanced Materials Lab, Samsung Semiconductor, Inc, Cambridge, MA, USA*

† Electronic supplementary information (ESI) available. See DOI: https://doi.org/10.1039/d5cs00358j

‡ Equal contributions

1. Oxide electrolytes for solid-state batteries

1.1. Solid-state batteries for electric vehicles: a day late, a dollar short or will the effort pay off?

With energy demands and oil prices spiking, accelerating the transition from fossil fuels and internal combustion engine vehicles to battery production for electric vehicles (EVs) and renewable energy is a matter of growing urgency. This transition relies on further improvements in the cost, energy density, cycle life, safety, and, ideally, recyclability of current batteries. Rechargeable batteries, which offer safety, long cycle life, and high energy and power density, have been a long-term goal of the energy storage community, with cost-effective mass-

This journal is © The Royal Society of Chemistry 2025

Chem. Soc. Rev., 2025, **54**, 8925–9007 | 8925

produced Li-ion batteries (LIBs) leading technological innovations and constantly improving on performance. Since the invention of LIBs in the 1980s and their subsequent commercialization by SONY in 1991, they have been used in a wide range of applications in our daily lives to power consumer electronics. However, since 2019, the biggest demand sector for LIBs has changed mainly to EVs, and today LIBs are powering millions of vehicles. According to the World Economic Forum, in 2022, 1 in every 7 passenger cars bought globally was an EV, ramping up to a total of 10.6 million EV sales globally.[1] In fact, today's successfully commercialized EVs can power a $\sim$600-km-long driving range with $\sim$100-kWh-scale LIB stacks (Tesla model S Plaid).[2] The current dominant technology for EVs,

namely LIBs, is the most competitive and mature battery technology to date and is considered a continuously improving benchmark. Commercial LIB cells can deliver long cycle life (up to several thousands of cycles), high charge/discharge rates ($>$1C), high energy content (average specific energy/energy density of $\sim$250 Wh kg^{-1}/$\sim$600 Wh L^{-1} and $\sim$140 Wh kg^{-1}/ $\sim$170 Wh L^{-1} at the cell and pack level, respectively),[3] and low capital costs (120 and 151 US\$ per kWh in 2022 at the cell and pack level, respectively).[3–7] In the EV market, the dominant technology uses lithium nickel cobalt manganese cathodes (Li(Ni, Co, Mn)O$_2$, NCM) and, to a lesser extent, lithium nickel cobalt aluminum cathodes (Li(Ni, Co, Al)O$_2$, NCA); however, due to its avoidance of critical elements and low cost at

Moran Balaish

Moran Balaish is a battery specialist at BMW's Battery Competence Center (Munich, Germany). She holds a PhD in Energy Engineering from the Technion and was a Fulbright postdoctoral fellow at MIT. Her research focuses on solid-state lithium conductors for energy storage, neuromorphic computing, and sensing. Her broader interests include electrochemical analysis, oxide and polymer surface chemistry, and materials for green energy. Dr Balaish has received several honors, including the MIT-Technion Postdoctoral Fellowship, Zuckerman Scholarship, and Fulbright Fellowship. She brings interdisciplinary expertise in electrochemistry and materials science to advance next-generation battery technologies.

Kun Joong Kim

Kun Joong Kim is a group leader in the Chair of the Electrochemical Materials Laboratory at the TUM. He received his PhD in Materials Science and Engineering from POSTECH and conducted postdoctoral research at MIT. His research focuses on inorganic materials science and engineering for electrochemical devices based on electroceramics that exhibit ionic, electronic, or mixed conductivity. Kim enjoys designing and prototyping advanced ceramic architectures and their interfaces for novel solid-state fuel cells, batteries, and beyond. Kim and his team's work spans from conceptualization to performance validation through scalable and sustainable fabrication, aiming to demonstrate proof-of-concept devices with practical potential.

Hyunwon Chu

Hyunwon Chu is a PhD candidate in Materials Science and Engineering at MIT, a visiting researcher at TUM, and a prospective postdoctoral scholar at LBNL. Prior to his PhD studies, he earned his bachelor's and master's degrees from KAIST. His research explores solid-state ionics and interface engineering, focusing on how defect chemistry in bulk and interfaces affects device performance. He uses processing to tune defect interactions and charge transport, combining synthesis and advanced characterization. His recent work expands into amorphous materials to better understand disordered ionic systems and guide the design of stable, high-performance electrochemical devices.

Yuntong Zhu

Yuntong Zhu is an Engineering Program Manager at Tesla. She received her PhD in Materials Science and Engineering from MIT in 2023, with research focused on amorphous Li-garnet films for solid-state batteries and lithionic applications. She holds dual BS degrees in Materials Science and Engineering, and Industrial and Systems Engineering from Georgia Institute of Technology. Her current interest centers on the design and scalable development of advanced lithium-ion battery materials to enhance cell performance and cost-efficiency in electric vehicle and energy storage applications.

8926 | *Chem. Soc. Rev.*, 2025, **54**, 8925–9007

This journal is © The Royal Society of Chemistry 2025

reasonable performance (especially good cycle life), lithium iron phosphate (LiFePO$_4$, LFP) has proven to be a viable option for low-cost entry-level EVs and is projected to have a market share of 60% from 2030 to 2050, with the rest of the market dominated by NCM and NCA cathodes (Fig. 1a).[8] The choice of a graphite anode and a metal-oxide cathode in the present LIB design shows the physicochemical limitation to reach the US Department of Energy's (DOE) EV *pack* goals of useable specific energy (C/3) of 235 Wh kg^{-1} and 500 Wh L^{-1}; 15-year calendar life; and a cycle life of 1000 deep discharges, among other requirements, at a cost of 100–125 US$ per kWh (or 75 US$ per kWh at the cell level).[9] Nonetheless, extrapolating the current improvement rate in NCM-based LIBs shows that an average price of ∼$100 per kWh at the pack level (and 300 Wh kg^{-1}) is expected by 2026,[6,7,10–13] even in the case of raw material price rises due to constraints within global supply chains and considering the recent 7% rise in LIB packs from 2021 to 2022, averaging $151 per kWh and slight forecasted rise to $152 per kWh in 2023.[7,14] It is important to note that a recent report has forecasted reaching the DOE pack cost target in 2032.[5] But will EVs become cheaper than their combustion-engine counterparts? In 2015, the battery made up more than 57% of the total cost of a midsize U.S. car. By 2024, this value dropped to ∼25% and by 2025, it is expected to be only 20%.[15] According to BloombergNEF's annual battery price survey, LIB pack prices have fallen 80% from $732 per kWh in 2013 to $151 per kWh in 2022.[7] As EV demand rises with a 20% compound annual growth rate for the next decade, it becomes crucial for carmakers to be able to procure and produce battery packs for EVs at a larger scale. According to the 2021 electric vehicle battery supply chain analysis report, the global capacity for LIBs will increase from 450 GWh in 2020 (and 492 GWh in 2021)[4] to >2850 GWh by 2030 (Fig. 1b) and potentially ∼6 TWh by 2050.[8] According to the International Energy Agency, EV sales are expected to set off in the next decade, reaching a tantalizing number of 30 million cars by 2030.[16] To produce a mass market of affordable electric cars, Gigafactories (a term coined by Tesla to refer to factories producing batteries for EVs at a large scale) as well as large-scale manufacturing approaches are needed. In 2020, more than 75% of the LIB cell production capacity was attributed to only 7 large companies, with South Korea's LG Chem (5 plants, 80 GWh), China's BYD (6 plants, 60 GWh), and Japan's Panasonic (10 plants, 54 GWh) in the lead, but many more will be needed over the next decade. Currently, battery manufacturers around the globe have announced the construction of >80 new gigafactories to produce LIBs, potentially reaching a production capacity of ∼3–4 TWh by 2030.[17]

In conventional LIBs, organic solvents with Li salts have been used as the electrolyte. This organic electrolyte exhibits high Li-ion conductivity and has contributed much towards the cutting-edge performance of LIBs. Nonetheless, the complexity of the electrolyte constituents, including salts, multiple solvents, and additives, inevitably leads to many safety challenges, including solid-electrolyte interphase (SEI) formation, electrode dissolution and corrosion, and electrolyte flammability, especially when considering the storage of large amounts of energy in a small volume. Thermal runaway is one such event that occurs when the battery electrode's reaction with the electrolyte becomes self-sustaining, and the reactions enter an autocatalytic mode. This situation is responsible for many safety incidents and fires associated with battery operations[18,19] and has necessitated the use of complex control strategies to maintain battery health. As the future EV will rely on battery technology, further innovation in LIBs (at the material level, new and optimized battery design and production) is essential for the success of mobility electrification towards improving the driving range and reducing the charging time and price competitiveness, especially in times of rising commodity and electrolyte prices. Moreover, the next technological breakthrough, from energy-dense anodes like silicon (Si) and Li-metal anodes to

Juan Carlos Gonzalez-Rosillo is a Ramón y Cajal researcher at the Catalonia Institute for Energy Research (IREC). He earned his PhD in Materials Science and Nanotechnology from the Universitat Autònoma de Barcelona/ICMAB-CSIC in 2017. Following his PhD, he completed a three-year postdoctoral stay at the Massachusetts Institute of Technology (MIT). His research centers on developing solid-state devices for energy storage, with a particular emphasis on thin film integration and operando characterization. He explores novel processing concepts for ultrathin solid electrolytes and investigates the fundamental principles of ionic migration at the nanoscale.

Juan Carlos Gonzalez-Rosillo

Professor Jennifer Rupp is Professor of Electrochemical Materials at the Technical University of Munich and CTO of TUM International Energy Research. Formerly at MIT and ETH Zurich, her research focuses on solid-state ionic materials for batteries, fuel cells, and hybrid energy devices. She received the 2024 Richard Fulrath Award from the American Ceramic Society and was named a Max Planck Fellow the same year. Rupp is Vice President of the International Solid State Ionics Society and co-founder and CSO of Qkera, a battery material manufacturing company. Her work bridges fundamental materials science with real-world energy technologies.

Jennifer L. M. Rupp
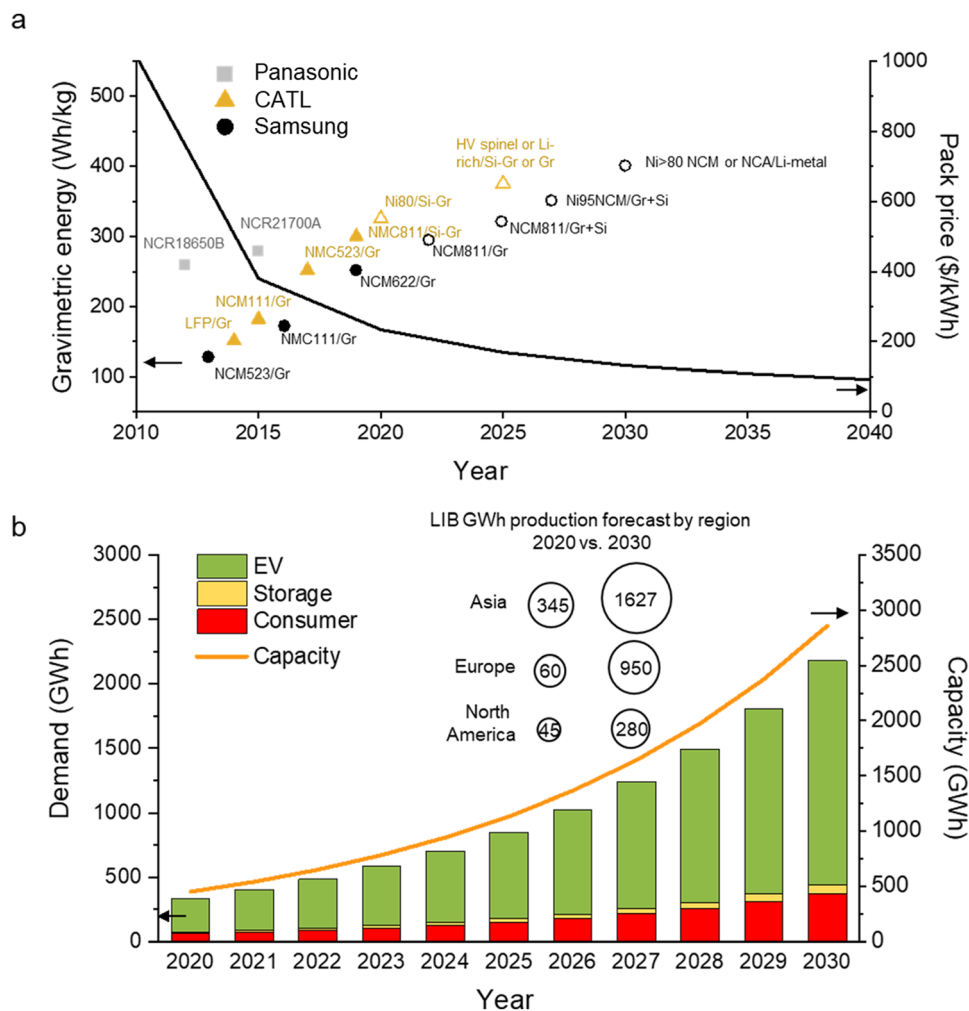
Fig. 1 Gravimetric energy density, cost, demand and capacity of Li-ion and Li metal chemistry in 2010–2040. (a) Gravimetric performance of different batteries for automotive applications. The predicted LIB pack-cost estimates and aggregation of individual expectations throughout 2040. Reproduced with permission ref. 8. (b) Global lithium battery demand and capacity forecast by sector in 2020–2030. Reproduced with permission ref. 16 and 17.

solid-state electrolytes, in addition to new processing techniques and manufacturing processes for electrodes, electrolytes, and full battery cells could be a game changer. Thus, although the cost and performance of LIBs continue to improve, next generation technology (and beyond) is continuously sought and developed. In addition to the conventional "lower costs and improved safety" considerations to secure widespread adoption, several other factors should be kept in mind when considering the adoption of new technologies in the automotive sector:

(i) The validation cycles for the incorporation of new technology for battery manufacturers and automakers can be lengthy. Historically, it has taken ∼4–6 years for a new technology to be fully commercialized in the automotive sector if the battery has already been examined on a rigorous test cycle.[12] This realization is important when considering realistic timelines of new technologies contributing to the global EV market based on the following maturity stages: advanced research (∼4–5 years), prototyping (∼3–4 years), solution

engineering (∼1–2 years), solution testing (∼2–3 years) and preparation (∼1 year).[20]

(ii) A holistic life-cycle perspective from mining to raw-material processing, cell-component production, and battery-pack production all the way to the EV and recycling and re-use at the end of life. Waste management and battery recycling/repurposing approaches at the battery's end-of-life (EOL) ('spent batteries', i.e., batteries with a 20% loss of reversible capacity) to recover as much material as possible or for second-life applications are currently lacking for both LIBs and next-generation technologies such as solid-state batteries and sodium-ion batteries. These are crucial for ensuring a stable supply chain of valuable secondary resources for critical materials (e.g., reusable cathode mixtures)/metals (from the cathodes, anodes, or electrolytes) and essential for the sustainability of automotive electrification.[21] Alternatives should be found for high-priced elements that may drive the cost ($ per kg, kgCO$_{2eq}$ per kg) and set a lower bound on battery price.

8928 | Chem. Soc. Rev., 2025, 54, 8925–9007

This journal is © The Royal Society of Chemistry 2025

(iii) The cell performance must be crucially improved without increasing the material and manufacturing costs for next-generation battery technologies to be scalable.[22] The performance of any new technology should exceed that of current state-of-the-art Li-ion cells and meet the goal of ~ 400 Wh kg^{-1} (and ~ 1000 Wh L^{-1}), including a wide operational range, to justify the transition.

(iv) Providing scalable synthesis protocols for Li-solid state electrolyte materials at scale and ideal drop-in solutions is of essence, especially for the oxide-based ones. Conventional LIB electrodes are typically processed *via* scalable solution-based approaches using a slot die or doctor blade as coating techniques. In another reference technology, namely solid oxide fuel cells, a combination of tape casting, lamination, (co-)sintering and screen printing is largely used.[23] Next-generation ceramic synthesis technologies for components like solid electrolytes should be as compatible as possible with the current electrode production and cell assembly routes for LIBs currently used in Gigafactories to allow for a smooth technology transition. Lowering the manufacturing costs by incorporating dry-processing approaches should be promoted as much as possible if new technologies allow.[24] If 'drop-in' technologies are not possible, the synthesis of electrode and electrolyte materials should at least be done *via* scalable and cost-effective technologies to enable manufacturing at scale (*e.g.*, atmospheric control should be considered for air-sensitive materials such as Li metal).

(v) Providing workflows that enable active learning between cell performance and strategic modulation of material chemistry, microstructure, interfaces, and transport/storage properties helps accelerate battery development. Most of the battery-related research and development is in one way or the other an optimization problem. Computational modeling and active learning like machine-learning are significant to optimize from chemistry to manufacture and direct how to tailor the relationship between a material's chemistry, structure, microstructure and performance, since this is vital to accelerate the discovery and optimization of future materials and processes.

One of the commonly cited next generation technologies is solid-state batteries (SSBs). SSBs, which are resistant to self-ignition, offer several benefits for next-generation energy storage, including favorable volume energy densities, improved safety, and decreased charging/discharging duration even at increased temperature.[25] In addition, several solid electrolytes have been shown to exhibit excellent thermo-chemical stability and may result in a $\sim 35\%$ increase in specific energy and a $\sim 50\%$ increase in energy density at the cell level[26] if the graphite anode is replaced with a Li-metal anode (if compatible). This improved stability can also improve the volume efficiency of SSB packs in a module without the need for a bulky cooling system, simplifying protection and connection; thus, another increase in the energy density at the battery-module level is foreseen. Therefore, SSB designs could provide favorable options for both safety and high energy density for energy-storage applications. The cell design of a SSB replaces the polymer separator and liquid electrolyte of a classic LIB with a solid-state electrolyte ceramic component, with a mass fraction potentially as large as ~ 50 wt% in different cell designs. It is important to note at this point that there are various options to bridge the gap between the LIB and SSB concept, such as operating in hybrid battery concepts, enabled by solid electrolytes and Li anodes, but maintaining high diffusion and fast cycling through the use of a liquid electrolyte/catholyte on the cathode side. Hence, there are various design options not solely being restricted to a full SSB for which a solid electrolyte can be employed addressing also different technology readiness levels (TRLs) for market introduction. Concerning the solid electrolyte the focus is on three major solid-electrolyte material classes, namely, oxides, sulfides, and polymers. These differ in terms of ionic conductivity; chemical, electrochemical, thermal, and mechanical stability; and processability. The first SSB was based on a 1-μm-thick amorphous lithium phosphorus oxynitride (LiPON) solid electrolyte starting in the late 1990s and a definitive example of successful demonstration with stable cycling over 10 000 cycles with metallic Li metal under ambient conditions.[27] Nonetheless, several unavoidable yet important questions remain:

Can SSBs outperform state-of-the-art LIBs in terms of major key performance parameters (namely, energy density, charging rate, cycle life, safety, cost, lifetime, ease of recyclability)? How can one economically manufacture bulk-type SSBs to store >1 GWh of energy in such a way that is cost competitive with state-of-the-art LIBs?

It is expected that when considering an oxide-based solid electrolyte and cathode composite processing and associated cell assembly, the technology transferability is at the lower end.[24] Oxide-based Li-ion conductors can be synthesized using a variety of ceramic processing methods. The size, microstructure, and phase of the solid electrolytes can significantly differ depending upon the processing method selected, which together affects the thickness, stability, and conductivity of the solid electrolyte. Manufacturing costs deviate depending upon the processing metrics required for each method. Therefore, rational selection and thorough optimization of the fabrication process are crucial for optimizing the performance and efficiency of solid electrolytes.

The objective of this review is to facilitate material and process selection toward oxide-based SSB design, highlighting attractive manufacturing strategies suitable for large-scale production. Other works summarizing recent progress in inorganic solid electrolytes and their properties toward SSB application can be found in ref. 28–35. A previous extended review article provides strategies for optimizing solid-state electrolytes as well as emerging strategies for employing high-safety Li-metal anodes.[36] Their roadmap includes descriptions of typical material uses and configurations, the advantages and disadvantages of each route, and potential application issues. A general overview of the interfacial challenges and mitigating strategies in SSBs can be found in recent review articles,[37–40] with some focusing on sulfide-[34,41] or garnet-based SSBs[42–44] or a comparative analysis of both sulfide and oxide electrolytes.[45] A more comprehensive discussion on materials, interfaces, and

This journal is © The Royal Society of Chemistry 2025

Chem. Soc. Rev., 2025, **54**, 8925–9007 | **8929**

performance, including advanced characterization techniques for SSBs, can be found in ref. 46 and 47. In the current review, we provide a literature analysis on the processing of bulk, thick-, and thin-film oxide-based electrolytes for SSBs and explore the processing steps and critical processing parameters towards achieving low-resistance oxide solid electrolytes. Understanding the changes upon the bulk to thin-film transition of solid-state electrode and electrolyte materials is of great importance to both bulk- and thin-film SSB application. Additionally, we review rational battery architectures of cathode/electrolyte and Li metal/electrolyte tandems and provide the relevant processing considerations. In a recent Nature Energy[48] review paper, we presented cost guidelines for SSB production-chain costs (processing and material costs) based on a reference solid oxide fuel cell (SOFC) technology. We showed that to meet the desired costs of US$100 per kW per h at the cell level for advanced high-performance (350 Wh Kg^{-1}) batteries for EVs, inexpensive large-scale fabrication techniques with reduced processing temperature, duration, and scrap are required to reach the target of < US$4 per m^2 for both the material and processing costs. Here, we target a perspective of reduction of the oxide electrolyte thickness, and a cost-effective thin-film fabrication strategy is discussed with emphasis on the wet-chemical film deposition technique. We provide an intensive processing assessment of conventional solid-state processing, wet-chemical solution processing, and vapor deposition technologies of oxide SSB electrolytes. Based on that, possible oxide-cell design options for bulk- and thin-film SSBs are discussed and evaluated. In the following, Section 1 discusses the choice of the oxide electrolyte, introduction of the practical ionic-conductivity limit defined as a function of thickness, area specific resistance (ASR), and selected oxide materials based on their ionic conductivity reported as bulk, thick-film, or thin-film form. We also examine important supply chain, material supply, recyclability, and re-use of battery-related materials and components of LIBs and offer recent insights into how the transition from LIBs to SSBs might affect such issues.

1.2. Material selection and requirements of oxide-based Li-solid electrolytes

SSBs have three major components: the anode, cathode, and solid electrolyte. Among the different potential anode materials (i.e., silicon, graphite, lithium titanate), Li metal is considered the most promising anode active material owing to its high theoretical specific capacity (3860 mAh g^{-1}) and low standard electrochemical redox potential of −3.04 V vs. the standard hydrogen electrode (or 0 V vs. Li$^+$/Li), enabling the highest energy density at the anode side. Another promising option, which has been explored mostly for sulfide-based SSBs, is a Si-based anode with a theoretical capacity of 3590 mAh g^{-1} (for Li$_{3.75}$Si) and a lithiation potential of 0.4 V vs. Li$^+$/Li. Si anodes can be processed as thin films (e.g., with LiPON[49] and LLZO[50] solid electrolytes), as powder-pressed anodes (with 77.5Li$_2$S–22.5P$_2$S$_5$ as the solid electrolyte),[51] and more recently, as sheet-type Si electrodes (with 75Li$_2$S–25P$_2$S$_5$/Li$_3$PS$_4$[52] and Li$_6$PS$_5$Cl[53] solid electrolytes) to serve as anode materials in SSBs. Both Li[54]

and Si[55] are emerging anode materials for SSBs that are expected to undergo substantial volume changes upon metal stripping/plating and alloying/dealloying, respectively, and will likely require operation under stack pressure to minimize void formation and morphological irregularities at the anode/solid-electrolyte interface. Alternatively, a host scaffold can be used to accommodate the volume changes and dendrite formation attributed to effectively lowering the current densities during plating; however, this will come at the expense of the gravimetric energy.[56]

The composite cathode is usually comprised of the cathode active material, transition-metal-based oxides (LiCoO$_2$; LCO, NCM, NCA, and LFP), ionic and/or electronic conductor additives (e.g., solid electrolyte, carbon, etc.), and potentially a polymer binder. As for liquid LIBs, the search for high-energy-density cathode materials has focused on high-nickel, low-cobalt layered oxides (NCM, NCA), such as the benchmarked NMC622 (LiNi$_{0.6}$Mn$_{0.2}$Co$_{0.2}$O$_2$) and NMC811 (LiNi$_{0.8}$Mn$_{0.1}$Co$_{0.1}$O$_2$) with a capacity of ∼180 and 200 mAh g^{-1}, respectively. An alternative cathode material is LFP with a practical capacity of 160 mAh g^{-1} and an average voltage of 3.3 V vs. Li$^+$/Li. Although LFP exhibits poorer performance compared with NMC-type cathodes, its greater service life, safety, and lower material and synthesis costs have made it a viable option for low-cost entry-level EVs. Moreover, it has been reported that by adopting new battery design, LFP-based LIBs can have 64% volume packing efficiency, leading to pack-level energies of 135 Wh kg^{-1} (and 210 Wh L^{-1}) when in a cell-to-pack configuration ("blade battery", namely wide and short cells assembled directly into a pack).[3,4]

As the manufacturing of SSBs will rely greatly on the material properties of the solid-electrolyte material class (namely oxides, sulfides, halides, and/or polymers), it is essential to briefly clarify some of the major design requirements:[57,58]

(a) High Li-ion conductivity (>1–10 mS cm^{-1}) with negligible electronic conductivity and grain-boundary resistance over the entire employed range of Li activity (elemental Li, a_{Li} = 1, to at least that of LiCoO$_2$, a_{Li} = 10^{-70}) and temperature (preferably room temperature) to allow use as a solid-electrolyte membrane and/or catholyte in thick cathodes.

(b) A wide electrochemical stability window, including a low reduction potential and high stability against Li metal, is preferred (e.g., for Li$_7$La$_3$Zr$_2$O$_{12}$ (LLZO), the theoretical and experimental electrochemical stability windows are 0.05–2.9 V[59] and ∼0–6 V[60,61] vs. Li, respectively).

(c) Stability against chemical reaction with both electrodes, especially with elemental Li or Li-alloy during the processing of battery components (i.e., electrolyte and electrode/electrolyte tandem), preparation, and operation of the battery cell.

(d) Mechanical stability for both battery cell fabrication (single layer and multilayer processing) and operation (stack pressure, temperature), especially considering (i) rigid electrode/electrolyte interface with evolving mechanical stresses; (ii) contraction and expansion of the electrode's active material, which result in volume changes (during lithiation/delithiation of the cathode, Li plating/stripping), morphological evolution,

8930 | Chem. Soc. Rev., 2025, 54, 8925–9007

This journal is © The Royal Society of Chemistry 2025

and poor interfacial contact through cycling; and (iii) interphase formation and growth.[62]

(e) Matching coefficient of thermal expansion (CTE) of the oxide-based electrolyte and electrode materials in the case of high-temperature processing to lower potential residual stress.

(f) Ease of processing and cell manufacturing *via* sheet-to-sheet manufacturing. Both cost-effective and scalable manufacturing routes are desired.

(g) In terms of safety, the thermal stability of the solid electrolyte against metallic Li should be high to prevent potential thermal runaway brought by the reactive Li metal and oxygen from the oxide solid electrolyte at elevated temperatures[63] or evolution of SO_2 and H_2S in the case of sulfide-based solid electrolytes reacting with moisture or oxidized in air.[64]

(h) Environmental benignity, non-hygroscopicity, low cost, and ease of preparation, processing, handling, and potentially recycling.

Based on the considerations mentioned above, a wide range of inorganic electrolyte chemistries and structure types have been considered that satisfy several, but typically not all, of the criteria mentioned above, including:

(i) Oxides such as NASICON-type $Li_{1+x}Al_xTi_{2-x}(PO_4)_3$ (LATP) and $Li_{1+x}Al_xGe_{2-x}(PO_4)_3$ (LAGP), lithium superionic conductor (LISICON) $Li_{4\pm x}Si_{1-x}X_xO_4$ (X = P, Al, or Ge),[65,66] perovskite $Li_{3x}La_{2/3-x}TiO_3$ (LLTO), and garnet-type $Li_7La_3Zr_2O_{12}$ (LLZO).

(ii) Sulfides such as Li_2S–GeS_2–P_2S_5, $Li_{10}GeP_2S_{12}$ (LGPS), argyrodite-type $Li_6(P, Sb)S_5X$ (X = Cl, Br, I), $Li_7P_{2.9}Mn_{0.1}S_{10.7}I_{0.3}$.

(iii) Polymers (mainly dominated by polyethylene oxide (PEO)), phosphates (*e.g.*, $LiTi_2(PO_4)_3$, $LiGe_2(PO_4)_3$, *y*-Li_3PO_4).

(iv) Halides (*e.g.*, $LiBH_4$, $LiBH_4$–LiX (X = Cl, Br, or I), $LiBH_4$–$LiNH_2$, Li_3AlH_6).

These material classes serve as solid electrolytes in SSBs, either alone or combined, and we thus briefly discuss major characteristics for each material class below. For comprehensive review, analysis, and outlook on the chemical, electrochemical, and mechanical properties of oxide/sulfide (or polymer) solid (or quasi-solid) electrolytes for diverse battery applications, please refer to our previous papers.[45,67]

1.2.1. Polymers. Solid electrolytes including only polymers as an elastic matrix with Li salt have also been considered but are beyond the scope of this review paper and are discussed elsewhere.[68–73] In general, although polymers may exhibit limited ionic conductivity with low Li-ion transference number,[74] they offer favorable and fast processing speeds with relatively easy adaptability to current battery manufacturing platforms, including slurry casting and roll-to-roll technologies, and as a soft medium that can accommodate volume changes during battery operation. To mitigate some of the challenges with polymers, composite polymer-ceramic electrolytes have been proposed and show in some material combination cases improved transport at high flexibility. However, the overall lack of electrochemical stability especially towards low voltage anodes cannot be resolved by composite strategies and manufacture remains critical; refer ref. 75 for further discussions.

In practice, polymers are the only solid-state electrolytes that have seen limited commercial applications thus far such as in Bolloré Bluecar® and Bluebus electric vehicles as public car-sharing services in cities such as Paris, Indianapolis, and Singapore.[76] In addition, the potential combination of oxides and sulfides in different cell designs may be the compromise needed to allow all-solid-state batteries to be feasible both on the large manufacturing scale and in terms of performance targets.

1.2.2. Sulfides. The highest room-temperature ionic conductivity on the order of 10^{-2} S cm^{-1} with a Li$^+$ transference number of basically 1 was reported in sulfide-based materials. As a group, sulfides are divided into amorphous glasses and glass-ceramics as a part of the binary system $(100 - x)Li_2S$–xP_2S_5 (LPS), and crystalline sulfides, which contain the largest number of lithium superionic conductors mostly belonging to the extensively researched argyrodites Li_6PS_5X (X = Cl, Br, I; 2 mS cm^{-1} for Li_6PS_5Cl and 12 mS cm^{-1} for $Li_{5.5}PS_{4.5}Cl_{1.5}$),[77] thio-lithium superionic conductor (LISICON)-type materials such as β-Li_3PS_4 (<1 mS cm^{-1}),[78] and the $Li_{10}GeP_2S_{12}$ (LGPS, 12 mS cm^{-1} at 27 °C)[79] material class. The superior conductivity of sulfides has been explained by several mechanisms; however, importantly, the large, highly polarizable sulfur anion acts as a large bottleneck for diffusion and screens lithium from the effects of neighboring cations, leading to weaker interactions between the sulfur species and Li ions, making the conduction species (Li$^+$) more mobile.[80,81] Their combined properties allow extremely fast Li-ion diffusion as seen in materials such as $Li_{6.6}Si_{0.6}Sb_{0.4}S_5I$ (24 mS cm^{-1} at room temperature) and $Li_{9.54}Si_{1.74}P_{1.44}S_{11.7}Cl_{0.3}$ (25 mS cm^{-1} at room temperature), both with low activation energies.[25,82] Sulfides are soft and ductile and thus offer good interfacial contact with electrode materials at low processing temperatures and ease of processability and can accommodate, to some extent, volume changes of the active material during cycling. Nonetheless, the greatest Achilles heel of sulfides is their poor chemical and electrochemical stability against both electrodes (Li-metal anode and cathode active material), leading to limited interface stability and high interfacial resistance.[83,84] Additionally, sulfides suffer from extreme sensitivity to moisture with toxic H_2S gas evolution,[64] which obligates handling in either an inert environment and/or dry rooms depending on the production step (*i.e.*, if handled as a powder or as a compact layer). Out of all the material classes in the sulfide family, argyrodites are considered the most promising materials for commercial applications suitable for use as the solid electrolyte and/or catholyte or anolyte, considering no precious elements are required and the lower interfacial resistance compared to LGPS; however, the narrow electrochemical stability window, and thus high interfacial resistance at both the anode and cathode sides, requires further engineering solutions, such as coating layers, oxygen doping, tailored particle size of the solid electrolyte, or defect-free processing.[85,86]

1.2.3. Oxides. (i) Several Li-oxide based materials possess acceptable room-temperature ionic conductivity on the order of 1 mS cm^{-1} (as solid electrolytes but not so much when used as the catholyte in thick cathode composites). For example, NASICON-type $Li_{1.3}Al_{0.3}Ti_{1.7}(PO_4)_3$ (LATP; 0.7 mS cm^{-1} for

This journal is © The Royal Society of Chemistry 2025

Chem. Soc. Rev., 2025, **54**, 8925–9007 | 8931

$Li_{1.3}Al_{0.3}Ti_{1.7}(PO_4)_3$,[87] perovskite $Li_xLa_{(2-x)/3}TiO_3$ (LLTO; 0.5 mS cm^{-1} for $La_{0.60}Li_{0.22}TiO_3$),[88] recently discovered Li_2TaPO_8,[89] and garnet-type $Li_7La_3Zr_2O_{12}$ (LLZO; 2 mS cm^{-1} for $Li_{6.55}Ga_{0.15}La_3Zr_2O_{12}$).[90,91] (ii) In most oxides, the electrochemical stability window is superior with an oxidation potential higher than ~ 3 V, which allows their coupling with high-voltage cathode materials; these oxides also exhibit a low reduction potential ranging from ~ 0.05 (LLZO) to 0.69 V (LiPON) vs. Li^+/Li, respectively. (iii) They exhibit relatively high chemical stability, which negates the need for an inert gas atmosphere during processing (and, in some cases, allows the coupling with Li metal). (iv) They exhibit good mechanical stability with high fracture toughness. Nonetheless, oxides are also stiff and brittle and suffer from defect-driven mechanical failures and high elastic modulus (~ 100–200 GPa) that translates into poor electrode/electrolyte interfacial contact and charge transport; in addition, high temperatures are required for densification and improved contact area between electrodes. Overall, these factors translate at present into energy-, time-, and cost-intensive processing with low throughput related to the high-temperature and long sintering steps (Table S1, ESI†) compared to state-of-the-art LIBs and roll-to-roll processing requirements. For NASICON-type LATP and LAGP as well as perovskite-type LLTO, although sufficient room-temperature ionic conductivity on the order of mS cm^{-1} was reported as well as low sintering temperatures of only 600–700 °C in the case of LATP and good stability in an ambient atmosphere, their applicability as solid electrolytes in Li-metal-based SSBs is limited due to the poor chemical and thermal stability against Li metal.[63,92] Indeed, among Li-oxide solid electrolytes, only LLZO has demonstrated good stability against Li metal, with the others exhibiting high grain-boundary resistance and instability against Li-metal anodes. With respect to intrinsic stability and reactivity, oxide electrolytes represent a considerable improvement over sulfide electrolytes. At 0 K, the thermodynamic stability window relative to decomposition into competing phases can be determined from calculated thermochemical data, as has been demonstrated previously.[93,94] For comparison, sulfides have a narrow intrinsic electrochemical stability window, typically between 1.5 and 2.7 V; however if they do not contain transition metals (e.g. Li_6PS_5Cl), they may form passivating interphases against the anode, extending the useable cathodic range.[94] Oxides and polyanionic oxides offer a broader electrochemical stability window than sulfides, for example LLZO (0.05–2.9 V), LLTO (1.75–3.7 V), and LATP (2.16–4.31 V),[95] providing great promise of improved oxidation stability.[96] In fact, some polyanionic oxides such as phosphates and borates are stable above 6.0 V; however, the conductivity is so poor that their use is restricted to cathode coatings or extremely thin separators.[97] The chemical reactivity between the electrolyte and cathode (active materials) or moisture sensitivity is similarly suppressed in oxides. Importantly, chemical reactions occur during cell fabrication as well as operation. Even with the lower thermodynamic driving force of the chemical reaction with commonly used cathode materials, oxide electrolytes such as LLZO still face challenges to assure stability during cell fabrication.[98] This instability stems from the elevated temperature required for making good solid–solid contact between the oxide-based solid electrolyte and the oxide cathode, attributable to the unique and intrinsic nature of oxides.[67]

Bulk-type SSB research has largely progressed, yet continuous research is required to continue to meet performance targets.[99] Several key challenges[67] include the Li dendrite penetration through the solid electrolyte at high current density (>1 mA cm^{-2}), limiting the fast-charging capability, and the need for material and cell-manufacturing strategies incorporating mechanically stable 10–20 μm solid-electrolyte membranes with high room-temperature ionic conductivity (over 10^{-4} S cm^{-1}) and chemo-mechanically stabilized interfaces with ultrathin Li-metal films and cathode. The high room-temperature Li-ion conductivity ($>10^{-4}$ S cm^{-1}) and low electronic conductivity, but importantly good electrochemical stability and compatibility with Li metal, make the oxide Li garnet an advantageous electrolyte material. While sulfide sheets exhibit mechanical softness (ductility) and low elastic modulus, which enable low-temperature densification via high-pressure calendaring, oxide sheets require high-temperature densification and adhesion via sintering, a critical processing step that can lead to Li loss, chemical interdiffusion at the cathode–electrolyte interface, and formation of insulating impurity phases and consequently high interfacial resistance and poor battery performance. Nonetheless, the art of manufacturing thin (<20 μm) 30×10 cm^2 or even 60×25 cm^2 oxide-based solid-electrolyte sheets that are homogeneous and defect-free, with no cracking, shrinking, delamination, or warping, requires herculean efforts and processing science innovation. The latter implies the need for practical processing options based on cost-effective and/or low-temperature processing for a robust unit-cell architecture for large-scale fabrication at cost. Within the next 10 years, there are hopes for the introduction of SSBs into the EV market to a wider extent. For all SSBs, materials (including for interfacial mitigation strategies) and processing, key factors in manufacturing scalability, cell configuration/design, and device performance, are all affecting the battery-cell costs,[22] with the material cost setting a lower bound on the battery price, dictating the manufacturing process. Recently, it was assessed that the performance gain outweighs both the overall material and manufacturing costs for SSBs.[22] In other words, emphasis on increasing the cell performance without increasing the material and manufacturing costs should be a major focus in the next years, and these factors are thus considered throughout the paper through evaluation and analysis of materials, cell designs, and processing routes towards high-performing oxide-based SSBs.

1.3. How to design for global distribution: practical conductivity and thickness of oxide electrolytes

To design for global distribution, batteries are expected to meet their targeted energy density (as well as maximum charging/discharging rates) over a wide range of operating temperatures

8932 | Chem. Soc. Rev., 2025, 54, 8925–9007

This journal is © The Royal Society of Chemistry 2025

(approximately −10 to 50 °C). The gravimetric and volumetric energy densities of Li-metal SSBs are largely determined by the cathode active material mass loading, electrolyte thickness, amount of excess Li, and components' density or areal loading. While the gravimetric energy is more sensitive to the high density of oxide solid electrolytes and thus dependent on the particular solid-electrolyte chemistry used (and its density), the volumetric energy (highly relevant for EV applications) is more sensitive to areal loading of the active material and is not affected by the different solid electrolyte chemistries at a fixed solid-electrolyte thickness.[62] The thickness of the solid electrolyte is related to the area-specific resistance (ASR) and inversely related to the solid electrolyte and energy densities. In general, a thinner electrolyte is ideal for high energy density, power performance (reduced internal resistance), and rate performance with shorter times for ion transport across the solid electrolyte (according to $t = L^2/D$, where t is the Li$^+$ diffusion time, L is the solid electrolyte thickness, and D is the Li$^+$ diffusion constant). More explicitly, given that the electrolyte contributes to the overall cell resistance according to the relation $R\ [\Omega] = L\ [\text{cm}]/(\sigma\ [\text{S cm}^{-1}] \times \text{area}\ [\text{cm}^2])$ (where R and L are the electrolyte resistance and thickness, respectively, and σ is the ionic conductivity), a significant decrease in ionic conductivity can lead to impracticality in using Li oxides as solid electrolytes. Similarly, instead of electrolyte thickness, a universal metric is typically used, namely the ASR $[\Omega\ \text{cm}^2]$, which conveniently gives an upper limit to the thickness (L) of solid oxide electrolytes (ASR $[\Omega\ \text{cm}^2] = L\ [\text{cm}]/\sigma\ [\text{S cm}^{-1}]$).[100–102] For context, the gold standard, a typical liquid-electrolyte-type LIB (LiPF$_6$ in EC:DMC) has a 15–40-μm-thick separator with a cell resistance in the range of 0.15–0.4 Ω, which may increase the resistance by one order of magnitude due to the porosity of the separator, considering a typical ionic conductivity of 10^{-2} S cm^{-1} (although the transference number of 0.3–0.5 may lower the effective ionic conductivity to 3–5 mS cm^{-1}, respectively).[103,104] An Arrhenius plot of several Li$^+$ conducting oxide solid electrolytes, comparing LiPON, NASICON, perovskites, and garnet-type LLZO, is presented in Fig. 2a. The three
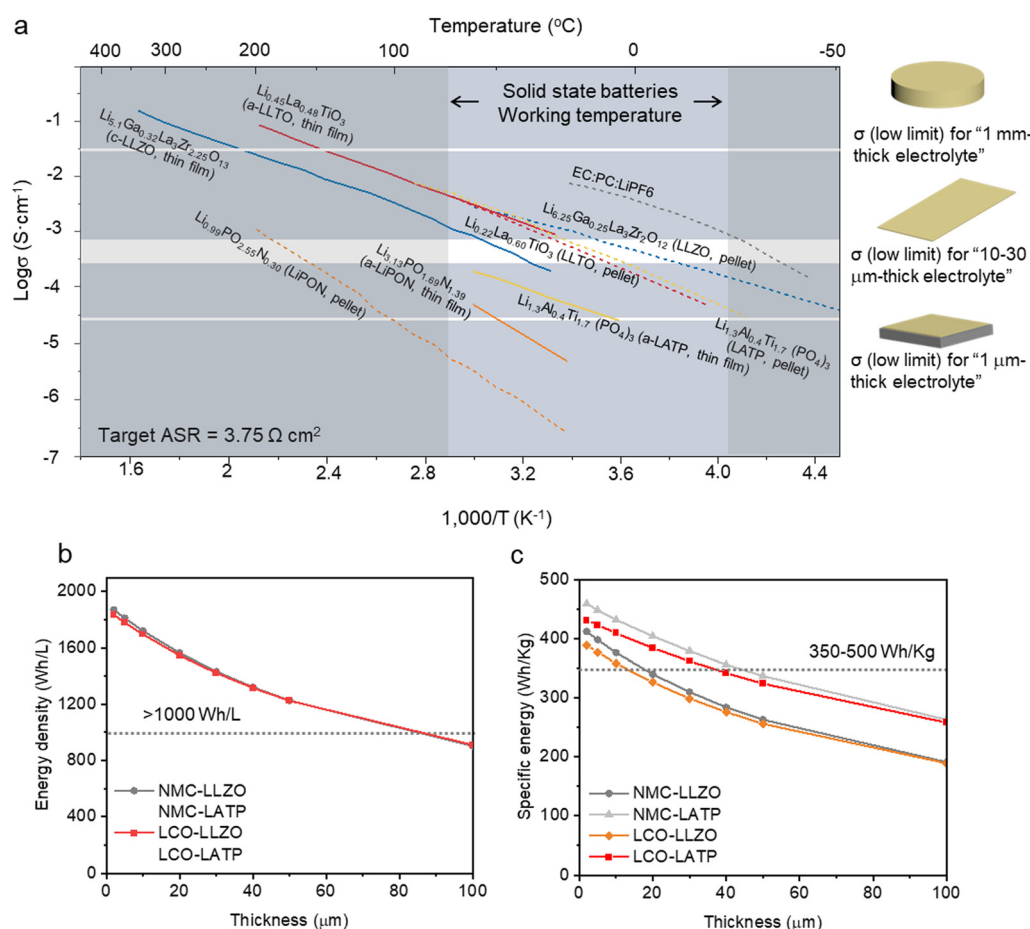
Fig. 2 (a) Arrhenius plot of several oxide electrolytes, including LiPON, NASICON, perovskites, and garnet-type LLZO. The minimum conductivities required for 1 mm-thick, 10–30 μm-thick and 1 μm-thick solid electrolytes assuming a target area specific resistance (ASR) of 3.75 Ω cm^2 are shown. (b) and (c) Calculated gravimetric energy density (Wh kg^{-1}) and volumetric energy density (Wh L^{-1}) as a function of electrolyte thickness for the following systems: Li/LLZO or LLTO/NMC811, Li/LATP/NMC811, Li/LLZO or LLTO/LCO, and Li/LATP/LCO. Due to the density similarity, the energy densities of the LLZO/LCO and LLZO/NMC systems are same as those of the LLTO/LCO and LLTO/NMC systems.

This journal is © The Royal Society of Chemistry 2025

Chem. Soc. Rev., 2025, **54**, 8925–9007 | **8933**

light grey shaded areas represent the calculated ionic conductivities for electrolyte thicknesses of 1 mm (pellet), 10–20 μm (e.g., free-standing film), and 1 μm (film deposited on the substrate) required to reach a targeted ASR of 3.75 Ω cm² (value taken from a LIB system with a 25-μm-thick porous separator soaked in a liquid electrolyte (LiPF$_6$ in EC/DMC)). It is evident that using pellet-type electrolytes for SSBs, as opposed to 1- and 20-μm-thick electrolytes, is simply not a volume-efficient design, as it leads to high specific resistance, energy loss, and poor energy density.[99] If we assume that the electrolyte components should not contribute more than 3.75 Ω cm² to the total cell ASR,[100] then for a 30-μm-thick solid electrolyte, the ionic conductivity of the LLZO film electrolyte attains the target value of 8×10^{-4} S cm^{-1} ($\sigma = L/$ASR = 0.003/3.75) only over 60 °C, and for bulk NASICON, bulk LLZO, and bulk and thin-film LLTO, the operation temperature must be over 25 °C. For an electrolyte thickness in the range of 20–10 μm, as a result of this calculation the associated ionic conductivity ($\sigma_{L=10-20\,\mu m}$) of the electrolyte should exceed 5.3×10^{-4} S cm^{-1} ($\sigma = L/$ASR = 0.002/3.75) and 2.7×10^{-4} S cm^{-1}, respectively, over the whole operation temperature (approximately −10 to 50 °C at minimal stack pressure).[105] Nonetheless, none of the here presented electrolytes, including conventional liquid electrolytes, cover the entire temperature range, which can have a noticeable effect on the cold-weather performance in EVs.[106] At least, solid electrolytes possess the advantage of improved ionic conductivity at moderately high temperatures compared with liquid electrolytes, which undergo severe chemical degradation and drying.[107] Either way, due to processing challenges, reported conductivities of 10–20-μm-thick oxide solid electrolytes are scarce and, when presented, are typically below the targeted conductivities even at room temperature, thereby requiring improvement. Decreasing the oxide solid-electrolyte thickness (e.g., LLZO, LLTO, LATP) toward 1 μm may offer reliable performance over a wide range of temperatures yet introduce additional mechanical, handling, and cell-design considerations. In this case, the ionic conductivity ($\sigma_{L=1\,\mu m}$) of the electrolyte should exceed 2.6×10^{-5} S cm^{-1} ($\sigma = L/$ASR = 0.0001/3.75). In this range, the bulk conductivities of several oxides (LLZO, LLTO, LATP) meet the threshold over the whole temperature range. Likewise, the calculated threshold conductivities based on electrolyte thickness and target ASR can be used as a specific goal for any solid-electrolyte research for practical SSB manufacturing and performance validation. Nevertheless, some reported conductivities from thin-film electrolytes (e.g. amorphous LiPON film) fail to meet the threshold, resulting in limited rate-performance due to the high ohmic ASR caused by low conductivity.[27]

To make informed decisions about potential oxide-based SSB designs, we also estimated the gravimetric and volumetric energy densities as a function of the solid-electrolyte thickness based on different oxide-based solid electrolyte and cathode combinations (e.g., LLZO, LLTO, LATP and LCO, NCM, NCA, respectively). Fig. 2b and c depicts the calculated gravimetric energy density (Wh kg^{-1}) and calculated volumetric energy density (Wh L^{-1}) as a function of electrolyte thickness for the following systems: Li/LLZO/NMC811, Li/LATP/NMC811, Li/LLZO/LCO, and Li/LATP/LCO. Theoretical densities of LLZO, LLTO, LATP, LCO and NMC are 5.07, 5.01, 2.93, 5.05 and 4.77 g cm^{-3}.[108–110] Due to the density similarity, the energy densities of the LLZO/LCO and LLZO/NMC systems are same as those of the LLTO/LCO and LLTO/NMC systems. The calculations assume an all SSB cell with a solid-electrolyte material (e.g., LLZO or LATP with 95% relative density) combined with a composite cathode (either NMC811 or LCO active material with a reasonable stable specific capacity of 180 or 160 mAh g^{-1}, respectively) at 75 : 25 vol% of cathode : solid electrolyte (100% dense; solid electrolyte in the composite cathode is the same as the solid-electrolyte separator). The mass loading or thickness of the cathode is limited by the sluggish kinetics of ions in the solid medium. In the following calculation, the areal loading of the cathode active material was fixed at 4.5 mAh cm^{-2}. The Li-metal anode excess, namely in the form of Li metal, was set to 25% excess (which in principle necessitates a high Coulombic efficiency considering the limited Li reservoir), and the calculated energies were determined for the "as-processed" battery cell in its fully charged state (see ESI† for all assumptions). Typically, minimal Li is desired to achieve higher energy densities. Yet, due to the large volume variation of lithium metal during plating/stripping, mechanical pulverization of the lithium metal and associated loss of electrical contact can occur, leading to poor cycle life and capacity fading; therefore, sufficiently excess Li is typically introduced.[111]

As expected, in all cases, the gravimetric and volumetric energy density increases upon reducing the electrolyte thickness. In the Li/LLZO/NMC811, Li/LATP/NMC811, Li/LLZO/LCO, and Li/LATP/LCO systems, the gravimetric energy density and volumetric energy density for a 20-μm-thick solid electrolyte are 340, 404, 326, and 384 Wh kg^{-1} and 1564, 1564, 1547, and 1547 Wh L^{-1}, respectively. Achieving the target gravimetric and volumetric energy densities of 350–500 Wh kg^{-1} and 1000 Wh L^{-1}, respectively, will require reducing the solid-electrolyte thickness even further (Fig. 2c). For instance, reducing the LLZO solid-electrolyte thickness from 20 to 10 μm in the Li/LLZO/LCO cell will increase the gravimetric energy density to the target value of 358 Wh kg^{-1}, and reducing the solid-electrolyte thickness to 15 μm in Li/LLZO/NMC811, Li/LATP/NMC811, and Li/LATP/LCO will further increase the gravimetric energy density to 357, 418, and 396 Wh kg^{-1}, respectively. It must be considered that our calculation provides an estimation of the upper limit of the solid-electrolyte thickness required to deliver a certain energy density, yet some of the assumptions are still difficult to realistically meet. In realistic scenarios, the chemical, electrochemical, and chemo-electro-mechanical stability of the battery components and interfaces, which are a direct result of the chemistries selected, are also of utmost importance to ensure high coulombic efficiency and satisfactory cycling performance and stability. This is especially true considering the rigid and heterogeneous nature of the solid–solid interfaces, which could result in challenges including interfacial degradation due to chemical reactions, electrochemical decomposition and volume

8934 | Chem. Soc. Rev., 2025, 54, 8925–9007

This journal is © The Royal Society of Chemistry 2025

change.[112–114] In practice, the limited Li excess, which informs the potential cycle life of the cell (at a certain anodic coulombic efficiency) before capacity fading, and other considerations such as electrode/electrolyte degradation (including interfacial degradation), packing and additional components required at the cell level (*e.g.*, tapes, laminate films, *etc.*) and at the pack and module level will lead to more stringent requirements on the solid-electrolyte thickness and/or necessitate other design or cycling protocols (current density, capacity, cutoff voltages, rest times, *etc.*).[115] The former, namely a thinning of the solid electrolyte below $\sim$20 μm, and *de facto* to $\sim$10 μm, encapsulates dendrite penetration concerns as well as mechanical, processing, and cell integration challenges and constraints on battery design. Moreover, although different solid electrolyte chemistries are considered in the calculation (*i.e.*, LLZO, LLTO, LATP), the difference in interfacial stability between Li metal and the solid electrolytes is not considered and can decrease the cycle life significantly and hamper the development of high-energy-density SSBs.

As the solid electrolyte would also serve as the separator between the anode and cathode components, a thin electrolyte may lead to other challenges, including Li dendrite propagation, poor mechanical stability, and difficulties in processing, handling, and manufacturing. Notably, for defect-free, reliable large-scale manufacturing, handling and physical abuse tolerance, free-standing oxide solid electrolytes at thicknesses lower than $\sim$20 μm might not be realistic, and new battery designs and architectures will need to be considered. For example, for a solid electrolyte directly deposited on a cathode electrode, thinner solid electrolytes on the order of $\sim$5–10 μm are, in principle, a feasible design. The incorporation of the solid electrolyte in the composite cathode may lead to tortuous and longer pathways for the Li$^+$-ion transport and thus require a faster ionically conducting solid electrolyte ($\sim$10^{-2} S cm^{-1}) to compensate for the lower effective ionic conductivity due to the high tortuosity associated with solid-state cathode composites.[116–119] Overall, despite the much wider electrochemical window being a huge advantage, there is still room for improvement in the conductivities of oxide-based solid electrolytes, especially at room-to-lower operational temperatures in order to find the sweet spot of thickness. This entails a low enough ASR and high energy density and power performance, while mitigating potential dendrite formation, propagation, and associated manufacturing challenges when dealing with a too thin brittle component (unless the cell design accounts for that; see Section 6).

1.4. Can the material supply chain keep up with the increasingly growing battery demand for EVs?

According to Elon Musk, in order to maintain and preserve the electrical power for one day for the entire human population, there is a need for 100 factories like Gigafactory 1.[120] Its final capacity upon completion was, as of May 2016, planned to be 150 GWh per year of battery packs. In 2024, Tesla delivered about 1.77 million EVs, and at scale, these factories would enable companies like Tesla to produce at least 1.5 million EVs

per year.[121] Considering an average EV with 60 kWh of battery storage, this works out to $\sim$400 discharges per person per year. To transition the roughly 80 million passenger vehicles sold per year to an all-electric fleet, roughly 4800 GWh of battery capacity would have to be produced per year (including recycling of old batteries). How would those numbers play out when considering the large-scale production of SSBs? SSBs, similar to LIBs, are "material-dependent" technologies, namely designed around certain materials that typically account for $\sim$70% of the total cell costs (half of the cost is attributed to the active cathode and anode materials).[122] The expeditious growth of the EV market, estimated to make up 8–14% of the total light-duty vehicle fleet by 2030 and 25–50% by 2050,[8] and the consequent increase in battery demand for EVs have brought to the surface the potential risks associated with the EV battery supply chain, in particular with the extraction of battery-related raw materials and the processing and refining of raw materials into battery-grade precursors. From a material's perspective, transitioning to an all-electric fleet running on either hybrid or all solid state batteries would require the world production of millions of tons of Li, La, Zr, Ta and/or Ti, P for the solid electrolyte (*e.g.*, LLZO or LATP) in addition to millions of tons of Ni, Co, and Mn for the cathode material (*e.g.*, LCO or NMC) per year, estimated to be hundreds of percentages beyond the current world production in 2030, necessitating the construction of new mines and sustainable recycling approaches.[123] Clearly, the EV battery supply chain is intricate and includes the following steps: mining and extraction of minerals and raw materials, processing and refining of raw materials into battery-grade precursors, manufacturing of battery components (anode and cathode materials, electrolytes, casting, *etc.*), production of battery cells and packs (including electronics, sensors, management systems), manufacturing of EVs and integration of battery and hardware, and recovery of critical materials and/or re-use of spent batteries.[16] The increasing demand for materials might not only affect the required mining quantities as well as environmental, geopolitical, and social issues but also prices, as the global supply (mining and/or refining) of most critical raw materials (CRMs) for battery-related production is geographically concentrated, which may limit their availability.[124] Li and Co (and to a lesser extent Ni) are considered critical elements considering the predicted drastic increase in the demand for Li batteries for EVs, the current production capabilities, worldwide reserves, and other supply risks.[122,124–126] The global production of Li and Co is dominated by Australia and Chile ($\sim$80%), and Congo (59%) (where mining often involves modern-day slavery, child labor, hazardous and toxic work conditions, and deaths),[127,128] respectively.[129] Most of the battery manufacturing occurs in Asia, where in 2016–2017, $\sim$50% and $\sim$80% of the global share of Li and Co, respectively, were consumed by the rechargeable battery industry.[17,122] In 2021, about 11% of global nickel production came from Russia, which is one of the world's suppliers of high-grade nickel ($>$=99.98% purity), which is the specific type needed for producing nickel sulfates required for battery grade cathode materials. The Ukraine–Russia war

This journal is © The Royal Society of Chemistry 2025

Chem. Soc. Rev., 2025, **54**, 8925–9007 | **8935**

led to a temporary dramatic price jump, and although nickel prices are expected to further go down in the future due to new developments in nickel mining technology, potential nickel shortage is still considered high risk for LIB production.[130] The poor geographic diversification and the short list of major global suppliers (for the extraction stage/ mining and/or processing stage/refining) are at risk of introducing supply disruptions caused by government policy or social– political instability, vulnerability to supply reliability, and price uncertainty.[122]

For LIB technology and contingent on the chemistry, LIB prices are sensitive to lithium, nickel, and cobalt prices. Indeed, LIB costs have decreased by almost one order of magnitude over the past 10 years due to manufacturing scaling, pack engineering, and performance improvements.[6] Yet, the prices of lithium, cobalt, and nickel have fluctuated dramatically from $20 per kg (in 01/2017) to ~$82 per kg (in 12/2022), from ~$30 per kg (2014) to ~$80 per kg (2022) and ~$37 per kg (02/2023), and from ~$10 per kg (in 2000) to ~$50 per kg (2007) and ~$30 per kg (in 01/2023), according to the daily metal prices.[131,132] It was recently suggested that the element price sensitivity is relatively low as a 50% increase in the commodity price ($ per metric ton) of Li, Co, and Ni, respectively, will lead to a 5.6%, 2.4%, and <4.7% increase in the price of the NMC 811 battery pack.[12] Xu et al. estimated that from 2020 to 2050 in a more conservative scenario (of LIBs with NCX cathodes), the global demand for Li, Co, and Ni would increase by a factor of 17 (to 0.62 Mt), 17 (to 0.62 Mt), and 28 (to 3.7 Mt), respectively, potentially outgrowing global production capabilities and depleting the known reserves of Li, Ni, and Co by 2050 or earlier (depending on the chemistries explored), necessitating an increase in current supplies to meet demands.[8] Habib et al.[133] concluded that the demand for Co, Li, and Ni will surpass their existing reserves by as early as ~2030, which is predicted to translate into a price increase and/or a sharp shift towards alternative chemistries such as LFP. Benchmark Mineral Intelligence estimated the 2022 supply of Li, Co, and Ni versus the 2035 demand and concluded that 74, 62, and 72 new mines, respectively, are needed to be built with an average mine site capacities of 45, 5, and 42 kilo tons to keep up with the exceptional volumes of demand of key raw materials for EVs and LIBs.[134] In such cases, not only supply–demand considerations need to be evaluated but also the ramp up of production, namely, potential consumption– production imbalance. New recycling technologies could reduce the new mining requirement needs, for example to ~59 and ~38 new mines based on the forecasted volumes of recycled lithium and cobalt, respectively, according to Benchmark.[122]

But how is material demand expected to change in the case of large-scale SSB production? From the material availability and sustainability point of view, Li-based SSBs rely on similar components as liquid-based LIBs, namely transition-metal-based cathode materials, carbon (optional) and polymer additives (optional), and metal current-collector foils (e.g., aluminum, copper, but potentially also nickel or stainless steel in the case of SSBs). The difference may arise from the material and processing costs of the solid electrolyte (as the separator or as a part of the cathode composite) and anode materials. Based on material data from Kravchyk et al.,[135] Schneider et al.[126] estimated the mass fraction of different oxide-based SSB designs (cathode-supported and scaffold-type tri-layer Li/LLZO/LCO cell designs) and determined that the LLZO as a 10–20 μm-thick separator has the largest weight share with more than 50 wt%, followed by the cathode active material with ~30 wt%, and Li metal with 2 wt% (the remainder is attributed to the Al and Cu current collectors). At the elemental composition level, La and Co accounted for ~67 wt%, Zr ~12 wt%, and Li slightly below 3 wt% of the total composition. The introduction of new elements to produce SSBs (and potentially to the recycling process) requires the assessment of their criticality, which can be done via their supply risk (SR) and economic importance (EI, cost and performance) indicators. The supply risk not only considers the material's scarcity in the Earth's crust but also the global supply (supply concentration, country governance, import reliance, trade restrictions, and supply-chain bottlenecks), production criticality, and EOL recycling capabilities.[124] The criticality assessment of materials is especially important when recycling methods and protocols towards the recovery of specific elements are developed. Nonetheless, a high supply risk score may originate from the lack of EOL recycling and poor sustainability but also from high future technology demand, regulation risks, political instability, by-product dependence, etc.[125] Blengini et al. identified 30 CRMs (namely SR ≥ 1 and EI ≥ 2.8) as a part of the 2020 European Union's list, which included Li, Co, La, natural graphite, Ge, Ga, Si, Ta, Ti, V, and Mg among others.[124] The different materials are typically produced from primary resources by mining, processing, and refining, component manufacturing all the way to commercial use and finally recycling, where batteries are dismantled, and their components are recycled, leading to secondary raw material sources to produce new battery active materials. Here again, China is the major global supplier (either for extraction and mining or for production and refining) of 66% of the individual critical raw materials, including Li (44%), La (86%), Ga/Ge (80%), Mg (89%), natural graphite (69%), Si (66%), Ti (45%), and V (39%) followed by South Africa (9%); Congo (5%), which is the main global supplier of Co (59%) and Ta (33%); USA and Australia (3%); and Chile (2%), which is the main global supplier of Li (44%).[124] Transitioning to hybrid or all SSBs will not only increase the demand for new CRMs such as La and Ta among others but also for Li. The increase in the demand for Li is attributed to the fact that the concentration of Li in inorganic solid electrolytes is up to 1 order of magnitude higher than in a conventional liquid electrolyte (1.4 wt% in LLTO, 2.5 wt% in LATP, and 5.8 wt% in LLZO compared to 0.6 wt% in 1 M $LiPF_6$ in EC/DMC/DEC). This higher concentration of lithium in the solids will result in an expected additional lithium demand of about 10–20 g kWh^{-1} due to the transition from liquid to solid electrolytes. A similar contribution due to the addition of an ~5-μm lithium–metal anode instead of a graphite anode at the

8936 | Chem. Soc. Rev., 2025, 54, 8925–9007

This journal is © The Royal Society of Chemistry 2025

cell level is expected. Both contributions together are expected to add up to ~30% of the standard lithium demand for NMC811 cathode materials (100 g kWh^{-1}).[24] In a recent analysis,[22] Huang and colleagues estimated that for large-scale production of solid-state lithium batteries, the cost of many of the solid electrolytes will have to be reduced by 100 times from the current lab-scale pricing of these precursors, which still remains at thousands or tens of thousands of $ per kg. As materials may set a lower bound on the SSB costs, their availability, the scaling of the precursor material supply chain, price uncertainty, and volatility may play critical roles in the scale-up of SSBs, especially when CRMs such as in the case of Ta-doped LLZO (namely, Li, La, and Ta) are used. The high-priced Ta element, having a price volatility of 40% in the last 5 years,[22] is commonly used as a dopant in LLZO to reduce the processing temperature while maintaining high ionic conductivity. Material selection will also play a crucial role in dictating the manufacturing processing route for the solid electrolyte as well as in the entire cell design.

The material demand and cost may be difficult to predict and uncertainties are large, mainly due to difficulties in estimating the future required battery capacity, and thus may vary significantly depending on the scenario used. For instance, the expected Li, Co, and Ni demand for EV batteries in 2050 has been reported to vary between 0.6 and 1.7 Mt, 0.25 and 1.25 Mt, and 0.6 and 7.6 Mt, respectively.[8] Nonetheless, material and precursor selection guidelines should aim to exclude high-priced elements, such as Ta and Ge, and favor more abundant alternatives (e.g., argyrodite material class Li_6PS_5X in sulfides, Al-doped LLZO) when possible. Challenges associated with bringing new technologies include scaling material production, which can take several years, as well as supply chain issues when production capacities are not ramped up to meet demands. This is the case not only for battery-grade high-nickel and/or manganese cathodes but also for inorganic solid electrolytes (e.g., Li_3PS_4, Li_6PS_5Cl, LLZO), where no material supply chain currently exists.

1.5. How to promote holistic life cycle thinking of sustainable battery production: from liquid to solid?

It is certain that enabling the widespread adoption of SSBs for EV applications will require performance improvement alongside cost-effective materials and scalable processing options of the battery cell components and manufacturing. It will also require a responsible and holistic life cycle thinking perspective for the SSB industry from raw material mining to the synthesis of active materials, electrode production, cell and system assembly, end-use and EOL recycling, striving towards a circular economy.[136] According to Arthur D. Little (ADL) analysis,[137] the total annual European LIB recycling market will require >700 kilo tons of recycling capacity by 2030, which will increase three-fold by 2040. EOL EV batteries will require adequate dismantling, handling, storage, transportation, and recovery policies and protocols that are both economically and environmentally friendly. Promoting responsible and economic life-cycle policies of EOL EV batteries (and manufacturing scrap) is considered challenging because of uncertainties in the future EV's dominant battery chemistry and components, including unstandardized sizes and form factors, in addition to a lack of collection, storage, and transport infrastructures. Here, EU- and US-wide regulations can better account for the projected LIB EV growth by enforcing battery tracking and visibility of the supply chain across all battery manufacturers.[137]

For the last few decades, the recycling and handling of EOL LIBs, mainly driven by industry, has not been considered economically profitable given the relatively low material cost, and no special efforts have been placed on the collection, storage, and transport of EOL battery waste. Most recently, the rapidly increasing worldwide demand for LIBs projected at $135.1 billion by 2031,[138] alongside (i) the fluctuating material cost due to the global demand and supply chain and (ii) the uneven distribution and production of the main materials (e.g., Li, Co, Mn) in politically sensitive countries, has attracted tremendous attention towards re-manufacturing, re-purposing, recycling, and waste management of batteries or a combination thereof depending on the battery degradation status.[123,129,139–145] Re-manufacturing or re-purposing of batteries refers to refurbishing batteries for their original automotive use or their reconfiguration for less-demanding applications (e.g., stationary storage), respectively. Although such paths are more economically and environmentally desirable and should be exhausted before batteries are subjected to any form of recycling, battery secondary use can only extend their market lifespan by an additional 8–15 years and ultimately will require either recycling of EOL EV LIBs and extraction of critical materials in order to synthesize new battery materials or disposal and waste management.[129,146] By 2025, the worldwide recycling capacity of LIBs is expected to be approximately half of the 700 000 tons of batteries reaching EOL, not necessarily due to lack of recycling capacity but rather due to lower volumes of production scrap and low collection rates of EOL batteries, which does not make it profitable to extract all the substances, leading to current US recycling capacities for LIBs of only ~5%, compared to the 99% recycling rate of lead-acid batteries.[139,142,147] LIBs are not designed for easy and efficient recycling with only ~25–40% of LIBs able to be recycled in an effective way.[139,142,147] Nonetheless, similar to lead-acid batteries, policies (e.g., requirement of identifiers, standardization of cell modules, and incentivizing production-to-recycling manufacturing processes)[139,141,142,147] and regulations for the recycling of LIBs can ensure sufficient collection and recycling rates.

1.5.1. From liquid. Two established LIB recycling technologies are the pyrometallurgical and hydrometallurgical methods, which have been explored at the industrial level; however, energy, environmental (high greenhouse gas emissions), and profitability considerations have limited their widespread adoption in the context of LIB recycling. A third method, direct recycling, has received considerable attention recently as it can potentially offer ~80% lower energy consumption with 1/5 less greenhouse gas emissions compared to the conventional

This journal is © The Royal Society of Chemistry 2025

Chem. Soc. Rev., 2025, 54, 8925–9007 | 8937

methods.[147] The pyrometallurgical, hydrometallurgical, and direct recycling methods are briefly discussed below in the context of LIB recycling.

The elemental recycling of LIBs typically consists of a combination of pretreatments and metal-extraction processes. The pretreatments include (i) dismantling and discharging of the battery to secure personnel safety by eliminating the risk of electric shocks and fire and explosion hazards due to the flammability and ignition of the organic compound, (ii) mechanical pretreatment (e.g., pack/module disassembly if applicable, shredding/crushing, and sieving) of battery components such as steel casting, metal foils, plastic, and black mass based on their physical properties (e.g., size, density, conductivity, magnetic properties, etc.). The mechanical-separation process aims to maximize the extraction of the "black mass", which is the valuable mixture of the cathode and anode active materials. Subsequently, (iii) a mild thermal treatment and/or washing steps are performed to dissolve, decompose, and evaporate the organic binders and/or liquid electrolytes and potentially carbon species.[139,141] Next, a metal-extraction process, such as pyrometallurgical or hydrometallurgical, or a combination thereof, is undertaken. The pyrometallurgical method, which requires fewer mechanical-separation steps, is a simpler and mature commercial technique that uses high-temperature furnaces to decompose the battery materials, reducing the metal oxides and forming a mixture of molten slag (typically containing metals such as Li, Al, Mn) and metal alloys (typically containing Cu, Ni, Co, Fe, etc.).[8] The 'smelting' process of entire battery cells and modules, which evaporates the electrolyte and burns off the remaining organic components, is used as an additional energy source during the thermal process. The hydrometallurgical method uses different acid-based leaching procedures followed by a metal-separation step such as precipitation of impurities (to recover Al, Fe, Cu), solvent extraction (for the recovery of Mn, Co, Ni), ion exchange, and precipitation (e.g., to recover Li with Na_2CO_3 or Na_3PO_4) to potentially recover critical elements (99% for Ni, Co, and Mn) and synthesize new battery precursors from waste.[8] Typically, the pyrometallurgical process is followed by a refining step such as hydrometallurgy to separate and recover metal salts from alloys.[8,21,123] An alternative recycling path, currently at the lab-scale level, with economic and environmental advantages is the direct recycling process,[146] where the cathode materials are recovered and regenerated to the pristine stage while maintaining their structural integrity (no chemical breakdown) by means of re-lithiation and hydrothermal treatments.[8,129] It has been suggested that hydrothermal regeneration may also be used to recover solid electrolytes, negating the need to pre-separate co-sintered cathode–solid electrolyte composites.[139] Direct recycling has an even higher energetic and economic value considering that EOL EV LIBs typically still retain 80% of their original capacity. In fact, it has been estimated that in the case of LIBs, the direct-recycling approach has prevailed in terms of all major metrics, including energy efficiency, recycling ease, low emissions, and low cost, when compared to the pyro- and hydro-metallurgical processes, but

fell short in the demanding requirements of a streamlined recycling infrastructure, considering the lack of prior labelling, collection regulations, transport, storage, and international sorting and separation procedures.[146] Overall, the approach remains unclear towards its economic and technical feasibility.

1.5.2. To solid. To incentivize the recycling of Li-metal SSBs, the elements selected and their respective concentration, recycling rate, recycling efficiency, and carbon footprint should result in a feasible economic workflow. The workflow should include flexible, robust, and high-efficiency recycling technologies in addition to technical considerations such as production, collection, transportation all the way to secondary use and, ultimately, recycling. The recycling of SSBs will require adjustments and re-evaluation of current recycling procedures and business models associated with the recycling of conventional LIBs, especially considering that cell chemistry and design may vary significantly from the liquid electrolyte and from one solid-electrolyte material class to another and within each material class itself. For instance, the liquid electrolyte in a conventional LIB is typically not recovered and is washed away by solvents (e.g., N-methyl-2-pyrrolidone) due to cost considerations (estimated at $12–20 per kg material costs of $LiPF_6$ in organic solvents, making up to 10–15% weight fraction of the LIB cell).[48] In contrast, the material costs of oxide-based solid electrolytes (estimated to be $2000 per kg to $50 per kg depending on the production scale)[48] will likely necessitate their recovery.[139] In addition, compared to traditional LIBs, SSBs will potentially introduce new designs, components, and elements, which are in part considered CRMs (e.g., Ta, La, Ge, etc.) and Li, which is found in all three major components of the SSB, namely the anode, electrolyte, and cathode, either in its metallic or ionic form as a part of a ceramic component. Moreover, SSBs do not only introduce a new component, namely the solid electrolyte, but may also introduce a cathode composite, where both the cathode active material and solid electrolyte are intimately mixed, which complicates the mechanical-separation process.

Oxide solid electrolytes can potentially pose less safety risks (less harmful fumes, no hydrofluoric acid formation, no fluorine, or phosphorus compounds) compared to liquid electrolytes. They can also be handled under ambient conditions and potentially have a positive economic effect on transport issues to recycling facilities, which otherwise (i.e., in the case of liquid electrolytes) require stringent testing and regulations associated with road, air, and sea shipments considering the risk of thermal runaway. However, the recycling of oxide-based SSBs using either the pyrometallurgical or hydrometallurgical method and the recovery of valuable metals such as La, Ta, Ge, Ti, Zr, Sn, or rare-earth metals can present challenges due to the difficulty in separating these metals from the smelted alloy and/or slag and their potential for interference with the solvent-extraction process, respectively, and require adjustments of current recycling technologies.[139,141] For instance, for the hydrometallurgy method, the traditional pretreatment including mechanical handling and separation is the main practical method currently used to separate and recover the

8938 | Chem. Soc. Rev., 2025, 54, 8925–9007

This journal is © The Royal Society of Chemistry 2025
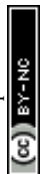
black mass but may become challenging when introducing oxide solid electrolytes to the system, considering both their intimate contact with other components of the cell (cathode/anode) and their brittleness and potential damage expected during the shredding and crushing treatments. In that respect, the pyrometallurgical method, which does not require a mechanical-separation pretreatment, shows a substantial gain towards recycling SSBs, which can be fed directly at the battery packs and modules, but is also considered a high-energy demanding technology with low recovery rates that produces significant amounts of CO_2.[139] Moreover, as SSBs are not flammable and thus do not contribute to exothermic reactions and cannot supply a significant portion of the process energy, it is less likely that such an approach will be cost effective.

The cathode in conventional LIBs makes up $\sim$30–50% of the total battery mass and $\sim$50% of the total EV battery costs and contains most of the critical metals of importance. Thus, it comes as no surprise that the current recycling focus is on recovering valuable metals from the cathode material, in particular Co, with significant irrecoverable losses of the anode, electrolyte, copper, aluminum, and plastics. In principle, as in the recycling of LIBs, the recovery of metallic components in their different chemical forms from the cathode materials in SSBs can be achieved *via* pyrometallurgical recycling (*e.g.*, to recover Co, Ni, Cu) and/or hydrometallurgical recycling (*e.g.*, to recover Co, Ni, Mn, Cu). Some elements such as Al and graphite cannot be recovered *via* pyrometallurgical recycling or their recycling may become potentially economical in the future (*e.g.*, Li, Mn, Si, graphite).[8] Even in the case of the hydrometallurgical recycling process, which has relatively low recovery rates, it is still economically viable when focused on the recovery of cathode materials containing Co (and to some extent Al) but not so much for cathode materials containing Fe and Mn, such as LFP and LMO, or any other elements, which are typically cheaper to mine rather than recycle.[129,146] The transition to cobalt-free SSBs may offer economic and social advantages but will require creating new business models and corresponding recycling procedures that can demonstrate economically and environmentally efficient recycling protocols of other materials as much as possible and at a certain scale. For instance, the disposal fee of low-value cathode chemistries (*e.g.*, LFP) is higher than that for NMC, which balances the overall expected revenue from the disposal fee and from the recovered recycled materials.[137] Compared to pyrometallurgical recycling, hydrometallurgical recycling is a more expensive, less mature technology; however, it is associated with higher recovery rates (>90%) of high-purity materials with lower energy costs and CO_2 emissions and shows more flexibility in terms of recycling different cathode chemistries.[139,141] Moreover, the hydrometallurgical methods may enable oxide-based SSB recycling by carefully controlling the leaching (*e.g.*, counter anions, chelation agents, extractants) and precipitation processes to recover both cathode and solid-electrolyte precursor compounds.[139] According to Schwich *et al.*, through a multistep hydrometallurgical process of LLZO and cathode composite black mass, elements such as La, Zr, and Ta can be potentially recovered by

using an aggressive leaching solution (*e.g.*, strong acid) followed by specific element precipitation steps at varied pH values to allow for the extraction of the following metals (in the order given): Ta, Cu, Zr, Al and Fe, La, Co–Ni–Mn, and ultimately Li.[123] Nonetheless, the introduction of new oxide–cathode composites, with intimate contact between the solid electrolyte and cathode components, will impose new hurdles, complicating the recycling process and requiring the development of new recycling processes to selectively separate and precipitate the solid electrolyte from the cathode components. Moreover, the proposed approach requires experimental validation, and its economic viability has not been analyzed. It should also be noted that strong acid-based leaching may have high extraction efficiencies for diverse transition-metal oxides; however, it also generates large amounts of waste solutions that will require special handling, treatments, and disposal. In the common hydrometallurgical process, organic acids have been used to address toxic fumes and generate biodegradable waste; however, their efficiency in extracting metals from LLZO and composite cathodes is expected to be limited.[146]

An alternative recycling path, currently at the lab-scale level, with economic and environmental advantages is the direct recycling process,[146] where the cathode materials are recovered and regenerated to the pristine stage while maintaining their structural integrity (no chemical breakdown) by means of re-lithiation and hydrothermal treatments; however, this approach is in its infancy and requires further development, especially to achieve economically viable recycling of oxide-based SSBs.[8,129] Once different SSB cell concepts and designs (including hybrid designs) are considered with different oxide components in the solid electrolyte and cathode composite (*e.g.*, LLZO as the solid electrolyte and LATP as the ionic conductor in the cathode composite layer), new recycling strategies must be developed. In a conventional LIB direct recycling process, after the dismantling of the batteries, the electrode active material (mainly the cathode powder) can be extracted *via* simple solvent dissolution or thermal decomposition methods to remove the binder, carbon, salts, and other additives. While for sulfide-based solid electrolytes, such dissolution approaches are feasible even with low-cost solvents such as alcohols, this step can be challenging in an oxide-based all SSB considering the co-sintering of the composite cathode and the solid electrolyte, which is performed to ensure chemical bonding but is expected to be a major hurdle towards the mechanical-separation process, which will be difficult to achieve. The follow-up step will involve the regeneration of active battery materials and structural reordering *via* re-lithiation. In addition, oxide-based solid electrolytes handled under ambient conditions may suffer from degradation due to Li^+/H^+ exchange in the presence of H_2O and CO_2, requiring subsequent thermal treatment for structure and conductivity recovery.[148]

1.6. Solid-state batteries: mass market or niche applications?

The global battery market size was estimated to be $104.31 billion in 2022 and is projected to reach $329.84 billion by

This journal is © The Royal Society of Chemistry 2025

Chem. Soc. Rev., 2025, **54**, 8925–9007 | **8939**

2030.[149] Although SSB market predictions should be considered with a degree of skepticism, according to the Grand View Research Report, the global solid-state battery market is expected to reach \$87.5 billion by 2027[150] with the global thin-film battery market, projected to grow tremendously in the future (with a compound annual growth rate (CAGR) of 35.52% between 2020 and 2027), estimated to reach \$5.2 billion by 2027.[151] The latter is attributed to the growing need for miniaturization of electronic devices and wearable devices, wireless internet of things (IoT) sensors, and implantables.

SSBs can be classified into two main categories based on the scale of the electrolyte and electrode dimensions, namely the footprint area and volume: (i) bulk-type full-battery cells with tens of micrometers in thickness and a footprint of 20–9000 mm^3 and (ii) thin-film battery unit cells with a total thickness of hundreds of nanometers and a footprint of 1–10 mm^3 (a few to tens of mm^2 footprint area of substrate) (Fig. 3).[152] The architecture and processing of a SSB are thereby determined by the tradeoffs between the desired energy density, power density, dimensions, and price, all tailored to the given application. For instance, for EV applications ($\sim$350–500 Wh kg^{-1} and 600–1150 Wh L^{-1}) and battery-pack costs of $<$100 US\$ per kWh, bulk-type SSB cell components roughly require a composite cathode with a thickness of $<$200 μm, a $<$20-μm-thick electrolyte, and an anode with a thickness of tens of micrometers (Fig. 3) to offer a competitive alternative to LIBs with improved energy densities and safety and faster charging. In fact, SSBs based on Li metal and polymer electrolytes have already seen commercial use in electric buses and stationary applications developed by BlueSolutions[153] and are being developed at the material, component, and cell/pack-manufacturing levels in large public companies, startups, and

private companies. Private companies include but are not limited to companies such as IONIC Materials (Li/graphite, polymer SE), ProLogium (Li/graphite/Si, oxide ceramic SE), SolidPower (Li/Si, sulfide ceramic SE), ilika (Si, oxide ceramic SE), and QuantumScape (anode-free, ceramic SE, gel catholyte), with partnerships and investments from Hyundai, Mitsubishi, Renault, A123, Mercedes-Benz, BMW, Ford, Samsung, Honda, Jaguar, Land Rover, and Volkswagen.[154] In contrast, for various compact low-power applications that require small, lightweight, and autonomous energy sources (e.g., medical implants, wearable and hearable smart electronics, and wireless IoT devices), rechargeable thin-film batteries with improved safety and shape flexibility, high ionic conductivities ($>$10^{-7} S m^{-1}), mechanical integrity, and extended battery life are needed. Thin-film batteries based on traditional liquid-based LIB technologies typically have a limiting coin-cell shape and are not suitable for on-chip applications due to size and leakage constraints. Thin-film batteries based on lithium–polymer chemistries offer more shape flexibility but suffer from poor volumetric energy density. Finally, solid-state thin-film batteries offer scope for miniaturization and flexibility towards diverse on-chip integration via layer-on-layer stacked or inter-digitated architectures on a substrate (Fig. 3). One of the most extensively studied thin-film Li-based solid electrolytes is lithium phosphorus oxynitride glass, LiPON, discovered 30 years ago by Bates and co-workers at Oak Ridge National Laboratory.[155–157] Since that time, LiPON, deposited mainly through sputtering, has gained tremendous success as the first and only commercialized thin-film solid-state electrolyte for thin-film battery applications.[158,159] The widespread use of LiPON in thin-film solid-state batteries has been enabled by the demonstration of its outstanding long-term cyclability
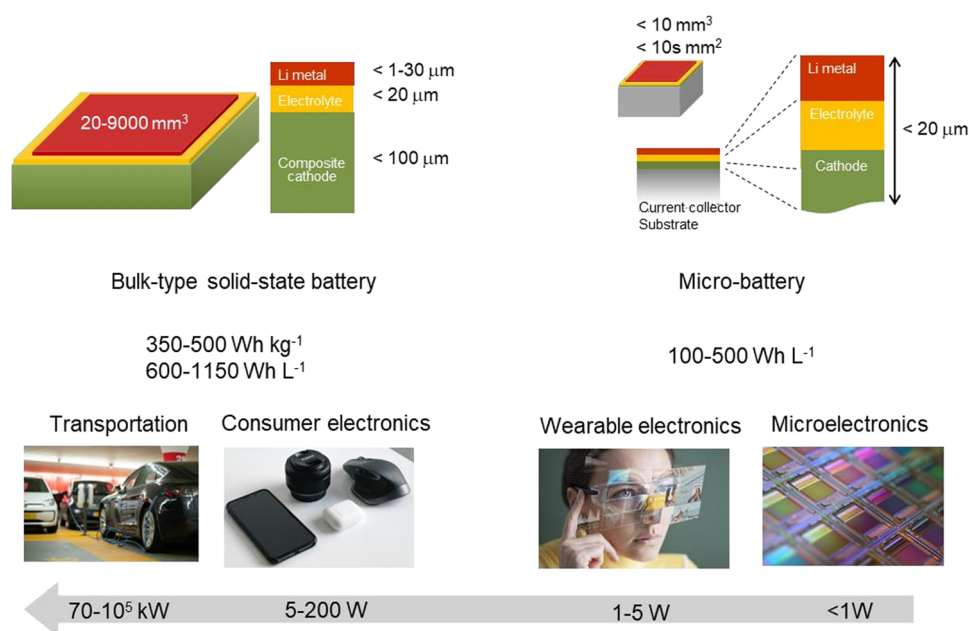

Fig. 3 Major requirement differences between bulk and micro solid-state batteries, in terms of thickness [μm], footprint area [mm^3], energy density [Wh kg^{-1} and Wh L^{-1}] and power consumption [W] in major applications.

($>10^4$ cycles) and stability towards a metallic lithium anode when paired with the high-voltage $LiNi_{0.5}Mn_{1.5}O_4$ cathode, despite the low volumetric energy density, a common challenge for all thin-film solid-state batteries.[27] Extensive efforts are being placed on the practical processing of (favorably) an anode-free thin-film battery configuration, where the lithium–metal anode is formed upon the first charge of the thin-film battery. Solid-state thin-film batteries based on LiPON as the solid electrolyte can potentially be incorporated in the billions of miniaturized electronic devices and sensors manufactured every year. For solid-state thin-film batteries (as well as bulk-type SSBs), the most important energy-density metric is the volumetric energy density (Wh L^{-1}), followed by fast charging and long cycle life. Thus, the search for a solid-state thin-film battery chemistry and design with outstanding energy storage per unit volume remains ongoing.

Throughout Section 1, critical questions were raised to help form guidelines towards the development of oxide-based SSBs, mainly for large-scale production and EV applications. Motivated by the realization and importance of the cost-effective processability and subsequent cell design and overall performance of Li oxides, we shift gears and take a deep dive into discussing the different processing approaches and their associated solid-electrolyte thickness ranges. Approaches to processing solid-state electrolytes using three major ceramic fabrication methods are discussed in Sections 2, 3, and 4 (Fig. 4): solid-state processing, wet-chemical solution processing, and vapor deposition technologies, respectively. These sections are not intended to present an exhaustive review of the processing conditions of each material, but to put into perspective the effects of the different deposition parameters in Li-ion thin- and thick-film conductors using examples from the literature. For example, we include quantitative comparisons of processing methods, achievable conductivities, film thicknesses, processing temperatures, and interfacial resistances for key oxide electrolytes (LLZO, LLTO, LATP, LAGP, and LiPON) in Tables S1–S4 (ESI†). Additionally, we provide general processing guidelines (Sections 2–4) and metrics (Section 5) that can serve as a starting processing guide of solid-state electrolyte films and conclude this section by highlighting the most needed and promising research directions. The rational solid-state battery architecture and design as well as scalable fabrication and processing are critical for the future implementation of SSBs, either bulk-type or thin-film batteries, and differ considerably depending on the electrochemical requirements. Also, many of the processing ceramic guidelines of the Li-oxide based components can directly be implemented for hybrid battery designs as well. In Section 6, we discuss different possible architectures of Li-metal-oxide-based SSBs that stem from all the considerations raised in the previous sections. Future perspectives and guidelines are offered towards the most promising oxide materials, cell designs, processing routes, and holistic sustainable approaches.
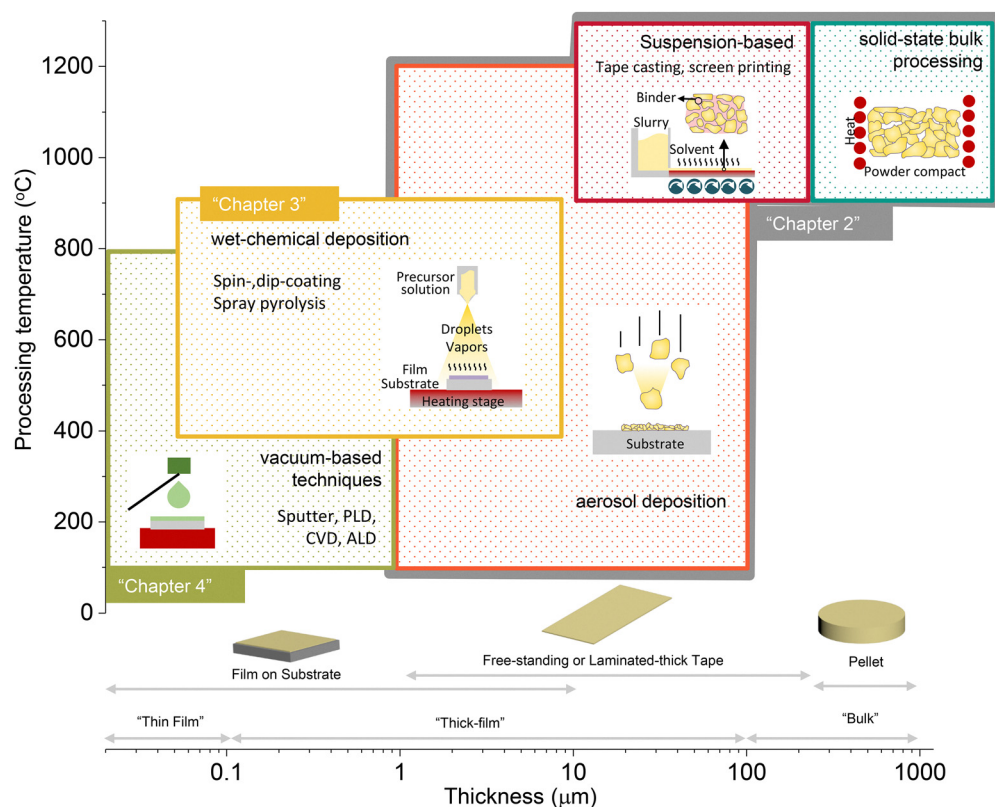

Fig. 4 A pedagogical approach to processing solid-state electrolytes using three major ceramic fabrication methods: solid-state processing, wet-chemical solution processing, and vapor deposition technologies.

This journal is © The Royal Society of Chemistry 2025

Chem. Soc. Rev., 2025, 54, 8925–9007 | 8941

2. Conventional solid-state processing of oxide-based electrolytes

The most widely used method to prepare polycrystalline solid-oxide electrolytes is solid-state processing, where a mixture of solid starting materials react to produce a new Li-metal oxide phase. This process involves the decomposition of the solid precursors and chemical reactions between intermediate solids *via* diffusion as well as possible species reactions with the atmosphere. This simple and direct method, to transform solid reactants into a final product, produces a large volume of powder electrolytes and can be used to prepare a wide variety of ceramic compounds.[160,161] Solid-state processing is especially advantageous for complex ceramic production, as it allows for precise control over both stoichiometry and phase composition. There are also fewer restrictions on precursor selection for the solid-state method compared to the sol–gel route, where the solubility and precipitation rates must be controlled (refer to Section 3).[162,163] Carbonates, hydroxides, nitrates, sulfates, acetates, oxalates, alkoxides, and other metal salts can all be used to produce simple or complex oxide electrolyte powders.[164] The high processing temperatures during the solid-state synthesis decompose most anionic groups, causing the byproducts to evolve into the gas phase. The process minimizes residual organics, resulting in high-purity powder products. In addition, solid-state processing does not require a high-vacuum atmosphere to achieve a uniform microstructure, which is beneficial for practical applications. The oxidation states of the metal ions can also be controlled based on the atmosphere and reactant selection, which aids in fine-tuning of complex transition-metal oxides.[165] Because of these advantages, solid-state reactions have been widely applied in developing multi-element Li-oxide electrolyte materials, including perovskite LLTO,[166] garnet LLZO[167] and NASICON-type LATP,[168] and crystalline LiPON[169] powders and pellets. However, solid-state processing also has several limitations, including the sluggish reaction and diffusion rates, loss of reactants at high temperature, and difficulty of particle-size control. The reaction may proceed very slowly; therefore, controlling the reaction temperature and/or mixing quality can affect the processing duration and final-product quality.[170] Because solid-state reactions occur by nature in the solid phase, high temperatures are generally required to initiate solid state diffusion and overcome the activation energy for decomposition.[164] Based on the Vogel–Tammann–Fulcher (VTF) equation, which provides the Arrhenius relaxation process of material-transport properties (*i.e.*, viscosity),[171] the relation between the melting point (T_m) and the glass-transition temperature (T_g) is represented by the "$T_g/T_m = 2/3$ rule".[172] As a consequence, the reaction temperature is typically maintained at 1/2 to 2/3 of the lowest melting point of the reactants to obtain the desired electrolyte phase and density.[173] The high temperatures required for the solid-state processing routes make them less cost-effective[174] unless producing materials on a large, industrial scale. In addition, the starting materials should have large surface areas (small particles) to maximize contact of reactants

and achieve a homogeneous product. Therefore, additional processing steps including thorough grinding and mixing are always necessary to reduce the particle size and realize a well-dispersed mixture of reactants,[160] which also increase the processing complexity and costs. Specific to Li-oxide based ceramics is the fact that increasing the temperature would induce the formidable disadvantage of Li evaporation (boiling point of Li: 1330 °C, refer to Section 2.3), resulting in the production of a non-uniform or undesired phase or microstructure.
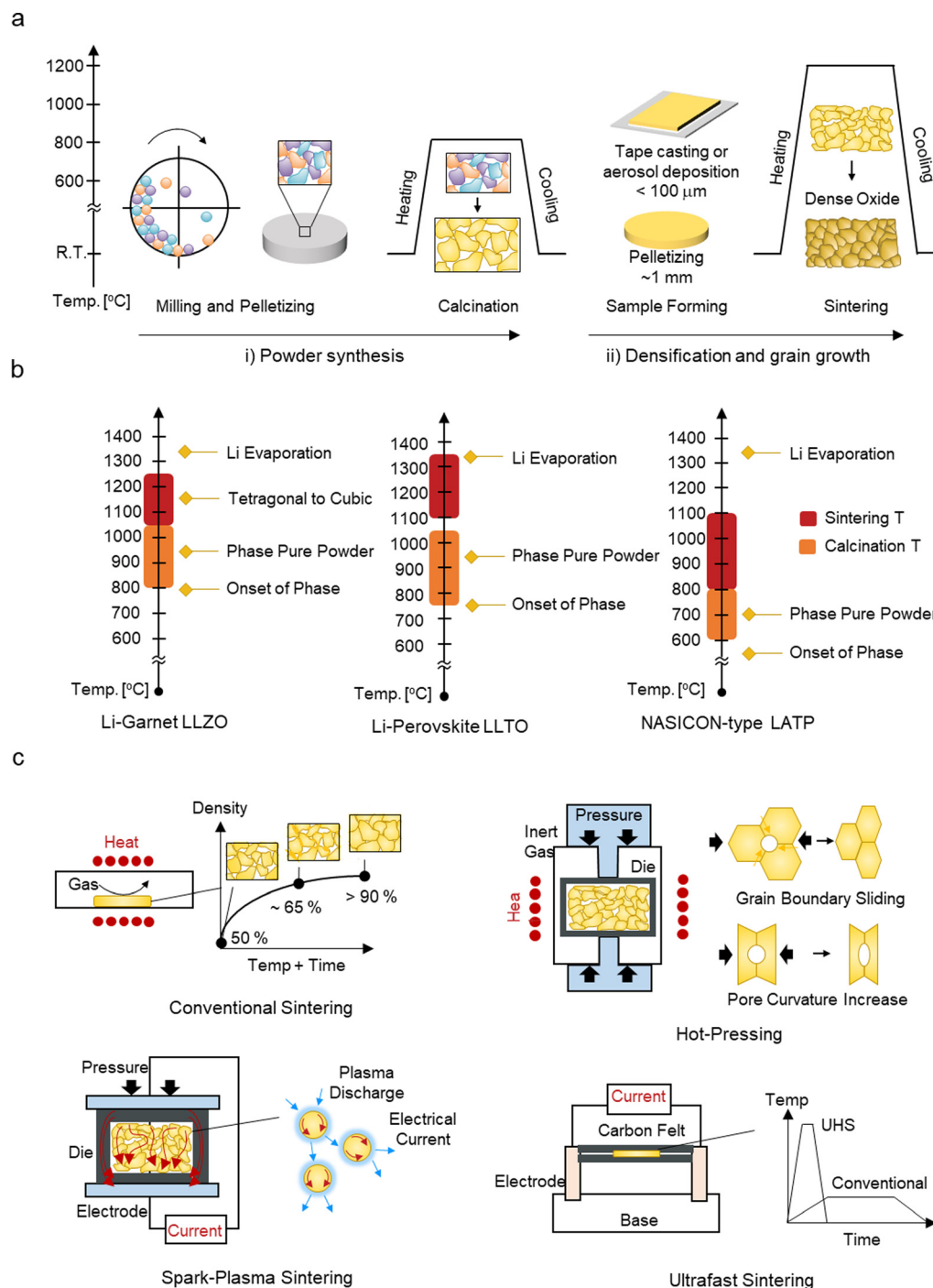
In the following, this section will review the details of the conventional solid-state processing steps specific for Li-oxide solid electrolytes. The two major sample forms such as pellet-type and tape electrolytes are discussed, as well as the processing characteristics and respective processing steps. Advanced processing techniques that aim to overcome the aforementioned limitations of conventional solid-state processing are also introduced.

2.1. Processing guidelines of solid-electrolyte pellets

Solid-state processing generally produces dense and thick pellet-type electrolytes (300 μm–1 mm in thickness) from the solid-state diffusion reactions of powders. For the practical application of solid-state electrolytes, with the aim of replacing liquid electrolyte–polymer separator systems (∼20 μm), bulk pellets, given their dimensions, are less advantageous because of the reduction in volumetric and gravimetric energy density. However, pellet electrolytes can serve as a good model system to develop and optimize electrolyte materials in terms of their chemistry, targeted phases and processing protocols. In general, pellet preparation consists of two distinct processing steps (Fig. 5a): (i) powder synthesis (calcination) and (ii) pellet densification (sintering). The former includes the removal of unnecessary compounds and the desired phase formation as a Li oxide in powder form, and the latter involves densification and grain growth of the green body to achieve high relative density.

(i) Powder synthesis: the solid-state reaction route for powder synthesis includes one or multiple mechanical mixing/grinding/packing and high-temperature calcination steps.[175] Grinding and packing before calcination can maximize the contact area between the precursor particles to achieve rapid reaction rates. High-temperature calcination helps solid–solid reactions proceed at an appreciable rate.[175] Optimum calcination temperatures are often determined using a combination of thermogravimetric and calorimetric techniques to determine when precursors have reacted off. For undoped LLZO, the initial phase of the Li-garnet structure forms at 800 °C once the Li precursor decomposes and impurity phases such as La_2O_3 or $La_2Zr_2O_7$ are detected (Fig. 5b). At higher temperature, cubic LLZO becomes the dominant phase from 950 °C to 1150 °C, as the thermal energy accelerates the conversion reaction and phase transition.[176] During the passive cooling process, the cubic-to-tetragonal transition (tetragonal distortion) often occurs near 650 °C.[176] The ionic conductivity of tetragonal LLZO is 4–5 orders lower than that of cubic LLZO;

8942 | *Chem. Soc. Rev.*, 2025, **54**, 8925–9007

This journal is © The Royal Society of Chemistry 2025

Fig. 5 Solid state processing: principle, temperature, and advanced techniques. (a) Typical steps for fabrication of dense oxide from precursor milling to sintering. (b) Typical events during calcination and sintering steps for LLZO, LLTO and LATP. (c) Advanced sintering tools: hot pressing, field-assisted sintering technique (FAST), spark plasma sintering (SPS), ultrafast high temperature sintering (UHS), and plasma activated sintering (PAS) techniques for fast and effective pellet densification.

the unfavorable phase change is often prevented by aliovalent dopants such as Ta, Al, and Ga.[177] Similarly, the LLTO electrolyte starts to form above the precursor decomposition temperature of 750 °C[178] and crystallizes in its perovskite structure at approximately 950 °C, forming the tetragonal phase (Fig. 5b).[179] Cubic perovskite LLTO can only be obtained under limited conditions with controlled Li stoichiometry[180] or through rapid quenching;[181] however, both tetragonal and cubic phase LLTO showed comparable ionic conductivity, in contrast to LLZO.[182] LATP synthesis generally requires lower calcination temperature (~700 °C) than the synthesis of Li-garnet or Li-perovskite oxides (Fig. 5b). The Li-precursor decomposition occurs near

This journal is © The Royal Society of Chemistry 2025

Chem. Soc. Rev., 2025, **54**, 8925–9007 | **8943**

500 °C; however, to avoid impurity phases such as titanates (TiO_2) of anatase or rutile phase, or titanium phosphate (TiP_2O_7), a heating temperature above 700 °C is required for LATP.[183] As such, the powder calcination process requires a high enough temperature above the decomposition/reaction temperature of the precursors to attain the desired electrolyte composition. Physical grinding should be repeated in between powder calcination not only to regularly mix the raw materials but also to obtain a smaller particle size and favorable phase of electrolyte powders. Conventional solid-state reaction produces powder particle sizes in the sub-micron to tens of micrometer range after the calcination as the high-temperature process promotes the particle size growth of Li ceramic oxides.[184,185] Barai et al. observed that the LLZO particle size can increase by 10 fold during the powder calcination process at 900 °C.[186] As the precursor decomposition and solid–solid reactions are kinetically limited, decreasing the particle size is essential to enable fast and homogeneous powder calcination.[164] In addition, the size distribution of the oxide ceramic particles later affects the sintering ability and the final microstructure.[187,188] For these reasons, particles with average sizes in the nanoscale range are targeted using planetary ball-milling (500–900 nm example of LLZO) or high-energy ball-milling (200–400 nm example of LLZO).[189] For example, Lee et al. demonstrated that increasing the rotation speed of ball-milling can decrease the LLZO particle size to 668 nm on average,[190] and Wood et al. showed that the combination of an aprotic solvent and surfactants can further reduce the particle size to 220 nm.[191]

(ii) Pellet densification: after calcination of the powder, a green body is prepared by cold-pressing the powder to a compact, and densification is achieved by firing the sample at higher temperature. The optimum sintering temperature is generally around 2/3 of the materials' melting temperature,[164] frequently extended to Li ceramic oxides. By slowly increasing the temperature, the densification, which is the increase in the density of a material, can proceed along the following stages of the sintering process: neck growth (relative density ∼65%), pore redistribution (∼90%), and pore shrinkage (∼98%) steps (Fig. 5c).[192] For solid-state battery (SSB) applications, the ceramic electrolyte should ideally achieve around 95% of its theoretical density.[193] During the heating stage, densification and grain growth processes occur simultaneously and compete with each other. Excessively high temperatures often lead to the formation of large grains.[194,195] As the densification rate generally decreases with increasing grain size (i.e., the scaling laws),[196] it leads to a reduction in relative density and mechanical strength. Conversely, at too low sintering temperatures, limited neck growth results in insufficient contact at grain boundaries,[197] lowering the final pellet density as well. Therefore, the sintering process should be carefully tuned to selectively enhance the densifying mechanisms. The thermodynamic driving force for sintering is the reduction of excessive surface energy, which occurs as interfaces decrease, which coincides with the straightening of the grain boundaries over sintering time. Overall, the kinetics of the process is often governed by material transport through the grain boundary

and volume diffusion. Therefore, processing parameters such as temperature, particle size, composition, and atmosphere can directly affect the thermodynamics and kinetics of the densification process.[164] The sintering of LLZO typically requires a sintering temperature of 1050–1230 °C and a duration of 5–36 h to achieve a high relative density (>95%) (Table S1, ESI†).[198–200] A smaller particle size helps to promote the close contact of powders and the material transport from inner grains to pores.[201] However, at the same time, too small a particle size may reduce the green-body density and cause poor neck growth during the initial stage of densification.[202] Cheng and co-workers compared the particle size effect on pellet densification, suggesting that reducing the average particle size from 10 to 1 μm can result in high relative densities of up to 94% at lowered sintering temperature (1100 °C for LLZO).[202] Instead of using a standard sintering strategy at a single temperature, a two-step sintering process can be beneficial for producing highly dense electrolytes with small grain sizes.[203] This approach involves a short high-temperature sintering phase followed by an extended low-temperature phase, which promotes initial neck growth while suppressing excessive grain growth to maximize densification. The refined grain structure resulting from this method can minimize lithium-ion blocking at grain boundaries, thus enhancing the total ionic conductivity. By utilizing the two-step process—sintering at 1250 °C for 10 min, followed by 1150 °C for 5 h— Huang and colleagues achieved a high relative density of 98% in Ta-doped LLZO.[204] This high density, coupled with fine grains, reduced intergranular voids and improved the percolation pathways for lithium transport, leading to improved electrochemical performance.

The selection of dopant species is also important to achieve higher density and better microstructure of the ceramic Li-oxide based pellet. In ceramic science, it is generally accepted that extrinsic doping with solid solutes reduces the average grain size, as solute drag effects counteract the active grain growth during densification.[164,205] Guo and co-workers found that the grain size of Y-doped LLZO decreases with increasing Y doping ratios, while pore removal occurs more rapidly.[206] This observation supports the competing effects of densification and coarsening during the later stages of sintering, highlighting the role of dopants in regulating excessive grain growth. Smaller and more uniform grains, facilitated by dopants, are beneficial for suppressing interfacial resistance at grain boundaries, thus improving the overall ionic conductivity. However, dopants do not always influence the sintering process uniformly. For instance, gallium (Ga)-doped LLZO severely suffers from abnormal grain growth (AGG) and low resulting density, whereas Ta doping enables uniform distribution of the grain size and high relative density.[207] This disparity arises because excess Ga ions segregate at the grain boundaries and form a $LiGaO_2$ secondary phase.[208] While this particular phase acts as a sintering aid, its localized presence enhances the abnormal growth of specific grains rather than promoting uniformity in pellets.[194] Such nonuniform microstructures can introduce local transport bottlenecks, impeding ion mobility and reducing reproducibility in electrochemical performance. Another simple approach to affect the density is through the use of pure

8944 | Chem. Soc. Rev., 2025, 54, 8925–9007

This journal is © The Royal Society of Chemistry 2025

O_2 as the processing atmosphere.[209] Li and coworkers prepared Ta-doped LLZO in an O_2 atmosphere, obtaining a 96% packing density of the LLZO pellets.[210] Flowing O_2 contributed to the grain boundary-to-pore mass transport and enhanced the densification mechanisms.[195] Increased densification under controlled atmospheres minimizes intergranular porosity, which in turn reduces the tortuosity of Li-ion pathways. Compared with LLZO, there have been limited systematic studies on the sintering behavior of Li-perovskite LLTO or NASICON-type LATP; however, similar trends were observed based on the common material characteristics. The sintering of LLTO is generally performed at 1100–1350 °C for 2–24 h (Table S1, ESI†).[211,212] Above 1200 °C, the relative density generally exceeds 95% and further sintering is dominated by grain growth.[212] Some studies have reported the maximum relative density at the intermediate temperature of 1200 °C;[213] the bell-shape dependence might originate from the faster coarsening step at higher temperatures. Similarly, LATP requires conventional sintering in the temperature range of 800–1100 °C (Table S1, ESI†). The relative density of 80% at 760 °C can increase up to 92–95% at higher temperatures of 780–840 °C; however, the sample contains few secondary phases as reaction intermediates.[214] In comparison, the use of a higher temperature of 1080 °C can produce a phase-pure electrolyte pellet but with slightly lower relative density (89.9%), possibly due to the rapid grain growth.[215] These examples highlight the importance of balancing densification and grain growth to optimize both structural integrity and electrochemical functionality in solid electrolyte systems.

Overall, a highly dense pellet achieved from the sintering step enhances various electrical, chemical, and mechanical properties of the electrolyte. Multidimensional defects, such as pores and grain boundaries, are often considered as the major bottleneck for Li^+ ion transport[216,217] and electrochemical stability,[209,218] due to the low ionic conductivity and high electronic conductivity at such interfaces.[219,220] Therefore, the pellet density directly affects the charge transport properties of the final electrolyte products.[221] For instance, increasing the relative density from 85% to 98% leads to a two order of magnitude increase in the total ionic conductivity of the cubic LLZO electrolyte from 9.4×10^{-6} to 3.4×10^{-4} S cm^{-1}.[222] Similarly, the grain-boundary ionic conductivity of LLTO improves by over 3 times upon increasing the sintering temperature (1.5×10^{-5} S cm^{-1} at 1200 °C to 5×10^{-5} S cm^{-1} at 1350 °C) based on the close contact of the boundaries.[212] Increased density not only facilitates ion transport but also strengthens the interfacial connectivity between grains, minimizing resistive bottlenecks across the bulk electrolyte. Increasing the pellet density is beneficial for improving the chemical stability of electrolyte pellets. The reactions between a Li-oxide electrolyte and H_2O/CO_2 preferentially occur at grain boundaries and pore surfaces;[223] therefore, highly dense pellets ($\sim$96% density) showed better air stability with the high conductivity (3.06×10^{-4} S cm^{-1}) maintained even after 3 months of air exposure (initially 4.48×10^{-4} S cm^{-1}).[224] Microstructural compactness also plays a crucial role in

suppressing the reactions at surfaces and interfaces, which are otherwise vulnerable to degradation during storage and cycling. Microstructural features and interfaces, including grain boundaries and pore characteristics, also influence the short-circuiting of Li oxide electrolytes, as such interfaces can act as nucleation sites[218] and percolation pathways[225] for Li metal penetration. To address this issue, Wang and colleagues demonstrated that increasing the sintering temperature of LLZO from 1120 °C to 1180 °C improved the relative density of the pellet from 87.5% to 93.9%, subsequently enhancing the critical current density from below 0.1 mA cm^{-2} to 0.5 mA cm^{-2}.[226] These results underscore the relationship between mechanical integrity and electrochemical robustness, as higher density reduces the possibility of filament growth and cell failure. Finally, high-density samples often ensure improved mechanical properties, including the elastic modulus, hardness, and fracture toughness. For example, the elastic modulus of LATP-pellet electrolytes exhibited well-matched proportionality to the sintering temperature (118 GPa at 950 °C and 127 GPa at 1100 °C sintering), as the pore reduction has a beneficial role on the physical contact of grains.[227] The Vickers hardness or fracture toughness can also be improved by optimizing the sintering process of LATP or LLZO,[227,228] both empowered by the facile densification.

While the engineering of pellet-type Li-oxide electrolytes has relied on solid-state processing techniques, the conventional approaches still have limitations in terms of achieving a small sample thickness of the electrolyte ceramic that can be realistically polished down to, at the thinnest, hundreds of micrometers.[229] Therefore, pellet-type samples are primarily suitable for model studies to test various characteristics of Li-oxide electrolytes,[230] but not ideal for practical applications in current battery systems. To bridge this gap, the following strategies for tape fabrication are designed to employ the merits of solid-state processing for powder preparation, while optimizing further parameters to produce electrolytes with a reduced thickness range. To bridge this gap between model systems and realistic battery form factors, the following strategies for thick-film fabrication are designed to retain the compositional and microstructural advantages of solid-state synthesis while enabling scalable electrolyte architectures with reduced thickness.

2.2. Thick-film fabrication: tape casting and aerosol deposition techniques towards low-resistance solid electrolytes

In the previous section, pellet-type Li-oxide electrolytes were mentioned as showing promising ionic conductivity ($\sim10^{-3}$ S cm^{-1}) at room temperature. However, the thickness ($\sim$1 mm) of the electrolyte pellets exceeds the market requirement for high-energy applications. Electrolyte sheet thicknesses of <28 μm for LLZO and LLTO, and <65 μm for LATP are necessary to achieve an energy density of 300 Wh kg^{-1} for Li/LCO cells. Likewise, thicknesses of <4 μm for LLZO and LLTO, and <21 μm for LATP are needed to realize an energy density of 400 Wh kg^{-1} for Li/NCM811 batteries (Fig. 2b). Because pellet-type electrolytes have definite

This journal is © The Royal Society of Chemistry 2025

Chem. Soc. Rev., 2025, 54, 8925–9007 | 8945

limitations in terms of thickness reduction, different processing routes must be considered to design thinner electrolyte sheets either by tape casting or by aerosol deposition technologies (Fig. 4).

Tape casting has been widely used in the manufacturing of electrolyte sheets and has a long history in ceramic processing science for a variety of functional ceramic products. In solid-oxide fuel cells, anode-supported electrolyte multilayer cells have been successfully prepared using the tape-casting and sintering process.[231,232] The process involves the following steps: (i) slurry preparation, (ii) slurry coating, and (iii) drying and sintering. In the slurry-preparation step, as-synthesized electrolyte powders are dispersed with solvents and binder materials to form electrolyte slurry. The electrolyte slurry contains various ingredients, including solvents, binders, surfactants and additives. In slurry coating, the slurry mixture is coated on a carrier substrate or film (*e.g.*, Mylar (polyethylene terephthalate (PET)) film) using casting tools such as a doctor blade or rod coater. The tape thickness can be controlled by adjusting the blade casting thickness and/or slurry viscosity.[233] In drying and sintering, the coated tape (also called "green tape") is dried and sintered at high temperature to obtain a free-standing electrolyte ceramic separator.[234] The tape quality is affected by the materials (solvent, dispersant, binder, plasticizer, and substrate) and engineering parameters for electrolyte materials during tape casting (namely, particle size, electrolyte composition, slurry solid content, slurry viscosity, substrate wetting, and tape pressing).[235] Laine and coworkers used 90-nm-grain sized LLZO nanoparticles and prepared slurry, which was tape-cast on a Mylar (PET) substrate and peeled off to produce a free-standing membrane tape.[213] Nonetheless, a green tape with low thickness presents challenges for obtaining a favorable microstructure and high ionic conductivity, given that the tape has a much higher surface to volume ratio, leading to faster Li evaporation.[236] This elevated Li volatility can disrupt local stoichiometry during sintering, promoting the formation of secondary phases or excessive grain boundary defects that hinder Li-ion percolation pathways and ultimately reduce conductivity. To mitigate the problems caused by Li loss, excess Li (7.5–10 wt%) should be added to the initial slurry powder. The sintering temperature and duration should be also reduced compared with those used in the pellet preparation process. Based on this knowledge, LLZO sheets with a thickness of <30 μm and a theoretical density of 94% were successfully fabricated using tape-casting and sintering at 1090 °C for 1 h, achieving a high ionic conductivity of 2.0×10^{-4} S cm^{-1} (Table S1, ESI†).[236] In later studies, smaller initial particle sizes and higher sintering temperature enabled the processing duration to be further decreased below 1 h (1130 °C, 0.3 h) to obtain a LLZO sheet with low thickness (25 μm) and high bulk ionic conductivity (1.3×10^{-3} S cm^{-1}).[201] A similar route has been demonstrated for LLTO tape preparation. The thickness of the LLTO sheet electrolyte was successfully reduced to 25 μm with slurry casting of 3100 mPa s viscous slurry, followed by pressing at 100 °C and sintering at 1260 °C. The high density of the sheet enabled clear transparency, high ionic conductivity

(2.0×10^{-5} S cm^{-1}), and superior mechanical property (208 MPa) (Table S1, ESI†).[108] Recently, a few noticeable advances have been made to produce the 3D-structured multilayer tape of LLZO. The Wachsman and Hu team successfully prepared a tri-layer (porous-dense-porous) structure of LLZO electrolytes by employing a sacrificial pore former (poly(methyl methacrylate (PMMA) beads).[101] The slurry containing the porogen particles was coated on both sides of the dense LLZO electrolyte tape, generating a porosity of 70% to build the 3D scaffold for electrode materials.[237] The structure allowed the electrolyte thickness to be reduced to less than 20 μm with a reasonable conductivity (2.2×10^{-4} S cm^{-1})[237] and helped to form close physical contact between the electrode materials, decreasing the interface resistance to ~7 Ω cm^2.[101] This suggests that the extended surface area of porous LLZO can facilitate both ionic transport within the electrolyte and charge transfer at the electrolyte/Li interfaces, thus optimizing anode symmetrical cell performance.

Another unique approach for prepare thin oxide electrolyte is the powder aerosol deposition. The powder aerosol deposition is a powder-based processing method to prepare ceramic films using fine particles at relatively low deposition rates (~10 mm^3 min^{-1}).[238–240] In this process, micron-sized ceramic particles are mixed with a carrier gas, accelerated to a speed of several hundred meters per second by gas flow, and sprayed into the deposition chamber. The technique enables a wide range of thicknesses between 1 and 100 μm for substrate-supported ceramic films (Fig. 4). In addition, the particles in an aerosol flow deposit with high kinetic energy, forming a dense film even without post-heat treatment.[241] Based on the motivation, Ahn and coworkers successfully fabricated a 20 μm thick LLZO film by aerosol deposition.[239] However, without an annealing process, the achievable ionic conductivity was too low, 1.0×10^{-8} S cm^{-1} (at 140 °C), because of the small grain size of the electrolyte particles and their high reactivity with moisture.[239] A similar trend was observed in Ta-doped LLZO films, which exhibited a conductivity of 2.0×10^{-7} S cm^{-1} at room temperature. Thus, the deposited film prepared using the aerosol technique was treated at 600 °C, and the annealing led to a strong recovery of the conductivity up to 7.0×10^{-5} S cm^{-1} as thermal treatment promoted crystallization and reduced boundary resistance by grain growth.[238] Using the same technique, a LLTO film electrolyte with a thickness of 10–20 μm was fabricated as well by sintering at 1200 °C; however, a total ionic conductivity of only 6.38×10^{-7} S cm^{-1} was achieved.[242]

Despite engineering advancements, the understanding of the optimum tape production process remains limited, with no standardized procedures established. In addition, due to a high surface-to-volume ratio, the surface chemistry changes or surface impurities such as Li_2CO_3 would later affect negatively the electrical, chemical, and mechanical properties of the final electrolytes. Given that tape fabrication techniques for Li-oxide electrolytes are at a relatively early stage of development compared to pellet processing, further detailed characterization and testing of the tapes are recommended. As there is a clear limitation of pellet-type samples for market applications,

8946 | *Chem. Soc. Rev.*, 2025, **54**, 8925–9007

This journal is © The Royal Society of Chemistry 2025

more research attention should be focused on developing the tape fabrication process. However, considering the low deposition rate and high price tag of current tape production techniques, they are less likely to be used for mass production of solid electrolytes, but perhaps in the short-run more suited for thin cathode coating layers.

2.3. Towards phase-pure Li-oxide electrolytes: controlling Li stoichiometry in sintering

To obtain electrolytes with higher Li^+ conductivity and the desired phase and microstructure, many studies have been conducted to adjust the precursors, dopants,[243] Li content,[244–247] and other processing metrics (such as the sintering temperature, pressure, or atmosphere)[224]—each of which directly influences grain growth, phase stability, and defect concentrations that govern Li-ion transport. Despite the trials, the mass loss due to Li evaporation during pellet sintering is still inevitable due to the high temperature ($\sim$1050–1250 °C) and long duration ($\sim$8–36 h) of the sintering process required to promote the transition to favorable phases and a dense microstructure.[248,249] For example, a sintering temperature above 1100 °C is typically adopted to prepare the LLZO electrolyte because the transition to the high Li^+ conducting cubic phase (compared to the low Li^+ conducting tetragonal phase) completes at 1130–1150 °C without doping (Fig. 5b).[195] Similarly, LLTO perovskites reach the complete conversion above a final sintering temperature of 1350 °C to remove the intermediate reaction species (*i.e.*, $LiTiO_4$),[213] enabling a grain bulk Li^+ conductivity of $\sim$$10^{-3}$ S cm^{-1}.[166,250] However, increasing the sintering temperature and duration will generally trigger Li evaporation while processing the solid electrolytes; also it leads to grain growth affecting the microstructure and electrochemistry severely.[251] In LLTO electrolytes, the relative sintered density increased from $\sim$75% to 99% upon increasing the sintering temperature from 1100 °C to 1250 °C and above. Grain growth becomes prominent at higher temperatures, where the average grain size remained at 1 μm at 1200 °C and below and sharply increased to 5 μm at 1350 °C. In contrast, the amount of Li loss followed the opposite trend of negligible Li loss (1100 °C) to 23% loss (1350 °C). This highlights a critical processing trade-off, where moderate sintering at 1200 °C balances densification and phase formation while limiting Li loss and excessive grain growth, enabling optimal percolation paths for Li-ion transport. As a result, the sintered LLTO pellet at an intermediate temperature of 1200 °C exhibited the highest grain conductivity of 1.2×10^{-3} S cm^{-1}.[212] A similar trend was also observed for LLZO electrolytes; at temperatures above 1250 °C, the formation of the Li-deficient $La_2Zr_2O_7$ phase becomes significant due to severe Li evaporation, which destabilizes the cubic garnet framework and leads to a parasitic pyrochlore-type phase that exhibits negligible Li-ion conductivity.[252]

Two engineering approaches have been adopted to mitigate the problem of Li loss during the synthesis. One typical solution is to cover the green pellet with its mother powder, which has the same composition as the green body. The mother powder acts as a sacrificial component to protect the green pellet to form the desired phase, readily supply Li around the grains, and sometimes protect the cation redox states during sintering. The mass amount of the mother powder usually reaches a 1:1 ratio with the sample, and the powder cannot be reused.[253] Therefore, the extra use of electrolyte powders containing rare-earth elements (La in LLZO and LLTO) results in high processing costs.[254,255] Recently, low-cost Li-containing compounds have been selected to replace the expensive electrolyte mother powder. For example, Li_2CO_3 separated from the sample can provide a Li_2O atmosphere above 730 °C, compensating for Li loss during the sintering step.[253] In addition, the $(Li_2O)_{0.733}$–$(ZrO_2)_{0.267}$ mother bed powder, when used instead of the mother LLZO bed powder, supported the pellet densification process, achieving a relative density of 95% with a conductivity of 5.7×10^{-4} S cm^{-1}.[256] However, this method does not allow for precise control of Li evaporation, and hence the sample quality may vary significantly across different batches. The second engineering approach to mitigate the Li loss is to sinter solid electrolytes using fast sintering techniques (detailed in Section 2.4), where the loss of Li can be effectively suppressed due to the extremely short thermal exposure times (seconds to minutes), which reduce both evaporation and grain growth.

2.4. Improving ionic conductivity through advanced densification strategies

Recent reports suggest that intrinsic/extrinsic defect features (including pores, cracks, dislocations, and grain/phase boundaries) can contribute to undesirable resistance in polycrystalline solid-oxide electrolytes. Increasing the relative density of the solid electrolytes and minimizing microstructural defects have been pursued to minimize the interfacial and grain-boundary resistances of solid electrolytes.[257] For instance, the grain conductivity of LLTO is $\sim$$10^{-3}$ S cm^{-1} at room temperature; however, its grain-boundary conductivity is less than 10^{-7} S cm^{-1}, reducing the total conductivity of LLTO electrolytes by 2–3 orders of magnitude.[217] To overcome the limitation of conventional solid-state synthesis and cold-press-based conventional sintering, two additional key approaches to further enhance the solid-electrolyte pellet density have been introduced: (i) advanced sintering tools and (ii) sintering additives.

(i) Advanced sintering tools: hot pressing,[258,259] field-assisted sintering technique (FAST),[260,261] spark plasma sintering (SPS),[262,263] ultrafast high temperature sintering (UHS),[264] and plasma activated sintering (PAS)[265] techniques enable fast and effective pellet densification through sealing of the electrolyte powder in a closed chamber, compression by a high pressure, and heating simultaneously to repress the mass loss (Fig. 5c). Hot pressing is conducted by loading the electrolyte powder into a graphite die and then heating and pressing at the same time. The resulting product is removed from the press and heated again to eliminate residual graphite on the surface and thus unwanted electronic conductivity.[246] Hot pressing with a uniaxial pressure (62 MPa, 1100 °C) enabled Al-doped LLZO to achieve an extremely high theoretical packing density

This journal is © The Royal Society of Chemistry 2025

Chem. Soc. Rev., 2025, **54**, 8925–9007 | **8947**

of 99%, with only a few impurities (less than 1 wt% $La_2Zr_2O_7$). The low impurity ratio also substantiates that the hot-pressing process is effective not only for pellet densification but also to prevent Li loss during sintering. The high pellet density lowered the contribution of the grain-boundary resistance to below 8% of the total resistance, consequently realizing a total ionic conductivity of 3.7×10^{-4} S cm^{-1} at room temperature.[266] SPS employs a pulsed DC current directly passing through the graphite dies to generate spark and plasma between electrolyte particles under loading uniaxial pressure.[267] This technique allows rapid densification of ceramic pellets as Joule heating results in a fast heating rate (up to 600 °C min^{-1}), which is an order-of-magnitude faster than that of conventional sintering. For LATP electrolytes, SPS can be applied to densify the pellet using a pulsed current of 700–800 A under a pressure of $\sim$30 MPa, which corresponds to a high heating rate of 100 °C min^{-1}. The temperature was maintained at 1100 °C for 10 min. Compared with the conventional sintering process (1000 °C, 2 h), SPS enhanced the relative density of the LATP pellet up to 97% (conventional sintering: $\sim$85%).[268] Similarly, a high density of 99.4% can be obtained in LATP electrolytes by employing SPS sintering, resulting in a conductivity of up to 1 $\times$ 10^{-3} S cm^{-1}.[269] Most recently, Wang *et al.* published pioneering work on ultrafast high temperature sintering (UHS), which features a high heating/cooling rate ($\sim$10^3 to 10^4 °C min^{-1}) and a high sintering temperature (up to 3000 °C). By supplying high thermal energy using resistive Joule heating carbon strips, rapid reactive sintering of the pellet can be performed within $\sim$10 s. Thereby, the technique effectively decreased the Li loss by <4 mol% for LLZO pellet samples while maintaining a high ionic conductivity (1 $\times$ 10^{-3} S cm^{-1}).[264] This work illustrates the generality to other Li-oxide electrolytes; LATP and LLTO electrolytes can be produced directly from green pellets within 1 min of sintering. The same research group also demonstrated that the ultrafast sintering technique could improve the electrolyte processing, making highly conducting and dense tapes in as little as 3s.[270] As such, the fast sintering process helps to prevent significant Li evaporation at high temperatures and significantly shortens the processing time; however, the cost effectiveness and scalability of these solid-state processing methods are yet to be determined.

Another interesting technique is cold sintering. Cold pressing techniques aim to achieve an $\sim$10-times-lower temperature than conventional sintering methods, by leveraging liquid phase dissolution/reprecipitation in conjunction with applied pressure. The process involves four key steps: liquid phase formation, phase redistribution, material precipitation, and final densification.[271] Ceramic powders are initially wetted to establish a liquid phase at the particle interfaces. This liquid phase dissolves the sharp edges of particles and promotes their rearrangement under mild pressure and temperature. Once the liquid phase fully diffuses into pores due to enhanced mass transport, the rearranged microstructure with reduced porosity can then be stabilized through a subsequent solution-precipitation reaction to form a dense solid.[271,272] Cold sintering has been adopted in a variety of simple and complex oxide

materials. For instance, the proton conductor $BaTiO_3$ generally requires high-temperature sintering above 1200 °C to reach >90% relative density. In contrast, the cold sintering process only requires a reaction temperature of 180 °C to achieve >95% density of the sample.[272] In Li-oxide materials, the Randall team demonstrated that a density of 85–90% in LLZO composite samples could be achieved through sintering at 120 °C for 1.5 h in a DMF-based mixture.[273] The team applied a similar approach in LATP-composite-electrolyte pellets and showed that 90% densification was possible at 130 °C in a water-based mixture pellet, which realized a conductivity of 10^{-4} S cm^{-1} in cell-level applications.[274] Cold sintering has the potential to reduce costs in solid-state processing by enabling extremely low sintering temperatures, benefiting not only pellet production but also ceramic tape fabrication. The reduced temperature can also enhance compatibility in co-sintering with a wide range of cathode materials, where flexibility has been limited by parasitic cation interdiffusion and secondary phase formation due to elevated sintering temperatures. Based on these merits, further investigations would be valuable to further elucidate the cold-sintering mechanisms and evaluate the impact of cold sintering on electrochemical properties, for instance, how solvent selection affects liquid phase composition and modifies grain boundary type and chemistry in Li oxide electrolytes.

(ii) Sintering additives: sintering additives, chemical species that remain at the grain–grain interface and promote densification, can be introduced either during the precursor stages or just before the sintering process.[275] Sintering additives for Li oxide electrolytes should generally possess sufficient ionic conductivity to avoid significantly hindering total conductivity, while also exhibiting low electronic conductivity to preserve single-ion conducting behavior. A typical sintering additive for LLZO is alumina (γ-Al_2O_3). Upon adding Al_2O_3, it forms a liquid phase during the sintering process by reacting with the precursors. The liquid-phase-assisted sintering can increase the packing density (up to 98%), as the liquids fill in the regions between the grains, which locally changes the effective grain-boundary/grain sintering pressure and expels the residual pores in solid-electrolyte pellets.[246] Likewise, other sintering agents are observed to have effects, changing the grain boundary types and the relative density of oxide electrolytes. Li_2O additives lead to the development of glassy phases at the LLZO grain boundaries and facilitate liquid-phase sintering, increasing the relative density to 97.3%. The maximum Li$^+$ conductivity with the optimum concentration of Li_2O (6 wt%) reached 6.4×10^{-4} S cm^{-1} at room temperature.[276] In addition, the inclusion of SiO_2 in LLTO promoted new intergranular phase formation and enhanced grain boundary conductivity. The lithium silicate phases created at the boundaries acted as sintering aids, improving grain contacts during sintering, but without significantly reducing Li$^+$ ion conductivity. The total conductivity increased to nearly 10^{-4} S cm^{-1} at 30 °C with the addition of 5 vol% SiO_2; however, further SiO_2 addition led to a decline in conductivity as the amorphous phase was less conductive than LLTO.[277] It is noteworthy that sintering agents

8948 | *Chem. Soc. Rev.*, 2025, **54**, 8925–9007

This journal is © The Royal Society of Chemistry 2025

are effective not only for increasing the pellet density but also for decreasing the sintering temperature and speed. Because the high porosity in ceramic electrolytes is driven by the severe volatilization of Li components, decreasing the sintering temperature is an alternative route to obtain higher pellet density and ionic conductivity of electrolytes, thus making sintering additives and dopants an important strategic factor. Li_3BO_3 is a sintering additive that forms a liquid phase at 750 °C, resulting in sintering temperatures with densification as low as 800–900 °C. During the sintering process, Li_3BO_3 does not react with the electrolyte and forms a separate liquid phase. The rearrangement and grain growth of LLZO particles can be promoted through the intergranular liquid phase. In addition, after sintering, Li_3BO_3 remains as an amorphous phase at the grain boundary, forming a Li-conducting thin layer and increasing the pellet density. As a result, a LLZO–Li_3BO_3 electrolyte realized a reasonable ionic conductivity of 1×10^{-4} S cm^{-1} even with a much lower sintering temperature of 900 °C.[278] The same strategy can also be applied in densification for the tape. Jonson and colleagues adopted 0.5 wt % Li_3BO_3 additive in their 150-μm LLZO tape and achieved high density ($\sim$90%) and conductivity (2.83×10^{-4} S cm^{-1}) at lower-temperature sintering (1000 °C).[279] In addition, sintering agents with higher melting point have been proven to reduce the sintering temperature by creating a eutectic composite with solid-electrolyte precursors.[280] For example, the incorporation of Al helps to form a Li$^+$-conducting thin layer (Li_2O–ZrO_2–Al_2O_3 eutectic) in the grain-boundary regions, promoting the liquid-phase densification. The phase assists in increasing the density of LLZO pellets from 2.6 (without Al) to 4.4 g cm^{-3} (with Al) and also shortening the sintering time from 36 to 6 h at 1200 °C. In addition, the formation of the eutectic phase leads to the simultaneous replacement of Al^{3+} with Li$^+$ and increases the empty structural sites in the lattice. This increases the ionic conductivity of both the grain and grain-boundary regions, resulting in a total conductivity of 2.0×10^{-4} S cm^{-1} at room temperature.[280] Similarly, additives with higher melting points such as Li_4SiO_4 (1255 °C) and Li_3PO_4 (873 °C) are also effective for producing highly dense (>96%) and ionically conducting ($\sim$6.1 $\times$ 10^{-4} S cm^{-1}) LLZO electrolytes.[281]

In brief, solid-state processing methods have been widely applied to obtain Li solid-oxide electrolytes with high-throughput or at large scale at lower cost. Solid-state Li electrolytes can be easily synthesized via a simple mixing and baking process with solid metal salts. In addition, advanced processing techniques have been adopted to achieve thinner, phase-pure, and highly dense electrolyte ceramic products. Despite the great advantages of conventional or advanced solid-state processing techniques, these methods still face difficulties in terms of achieving good control over the electrolyte particle size (i.e., nanocrystalline powders) or morphology compared to solution-based techniques. This issue stems from the limitation of the sub-solidus process itself and is not easily solvable simply by advancing the engineering parameters. The weakness of the processing methods mentioned above has motivated the development of alternative fabrication approaches such as wet-chemical solution-based synthesis (Section 3) or vapor deposition technology (Section 4).

3. Wet-chemical solution processing of solid electrolytes

Wet-chemical solution-based methods, used for either powder synthesis or film deposition, are appealing because of their reduced processing costs and high scalability, avoiding the need for an expensive vacuum chamber or high-energy source such as those needed in vacuum-based deposition methods. These features are a tremendous advantage for solid-electrolyte manufacturing, where high production capacity is required. Moreover, Li-oxide solid-electrolyte films processed via wet-chemical techniques may easily achieve a thickness range of the solid electrolyte that is comparable to or thinner than the polymer separator ($\sim$20 μm) in traditional Li-ion batteries, ranging from sub-micron to several micrometers, overlapping with the typical thickness achieved by both vacuum-based deposition techniques ($< \sim$1 μm) and solid-state synthesis (1 μm–1 mm) (Fig. 4). Wet-chemical synthesis, benefiting from the high adaptability of the chemical composition and processing conditions (e.g., deposition temperature and time), can be defined majorly as consisting of three steps (Fig. 6a): (i) solution-phase mixing, (ii) deposition, and (iii) post-processing. In (i) solution-phase mixing, the precursor solution is prepared by dissolving salts, carboxylates, and metallo-organic compounds in organic (or less commonly inorganic) solvents. In (ii) deposition, spin/dip coating, spray pyrolysis, chemical bath deposition, or more sophisticated direct writing methods are used to obtain the desired coverage of films. Finally, in (iii) post-processing, heat treatment is performed under a specific atmosphere to reach the desired phase. Post-processing can be of particular interest for automated high-throughput material synthesis and can reduce the material discovery and optimization time. For instance, the optimal ionic conductivities of many current state-of-the-art solid electrolytes, such as LLZO and LLTO, have been achieved by adding one or more external cation dopants. In principle, the process of surveying available dopants is possible with both traditional solid-state synthesis and wet-chemical methods; however, solid-state synthesis generally requires a longer time with multi-step mechanical milling and higher temperatures for the calcination and sintering steps than those required for annealing solution-processed films. With automatic controlled wet-chemical solution-based deposition, many parameters and film properties such as the chemical composition, density, crystallinity, near-order chemistry and structure, and inter-atomic bonding can be readily tailored, thereby accelerating the material optimization process, which is not easily achievable with vacuum-based processing that requires target synthesis. To date, most of the oxide-based solid electrolytes, including perovskite-type LLTO,[282–289] garnet-type LLZO,[290–294] NASICON-type LATP,[295–298] LAGP,[299] and LiPON,[300] have been synthesized via wet-chemical solution-based processing routes

This journal is © The Royal Society of Chemistry 2025

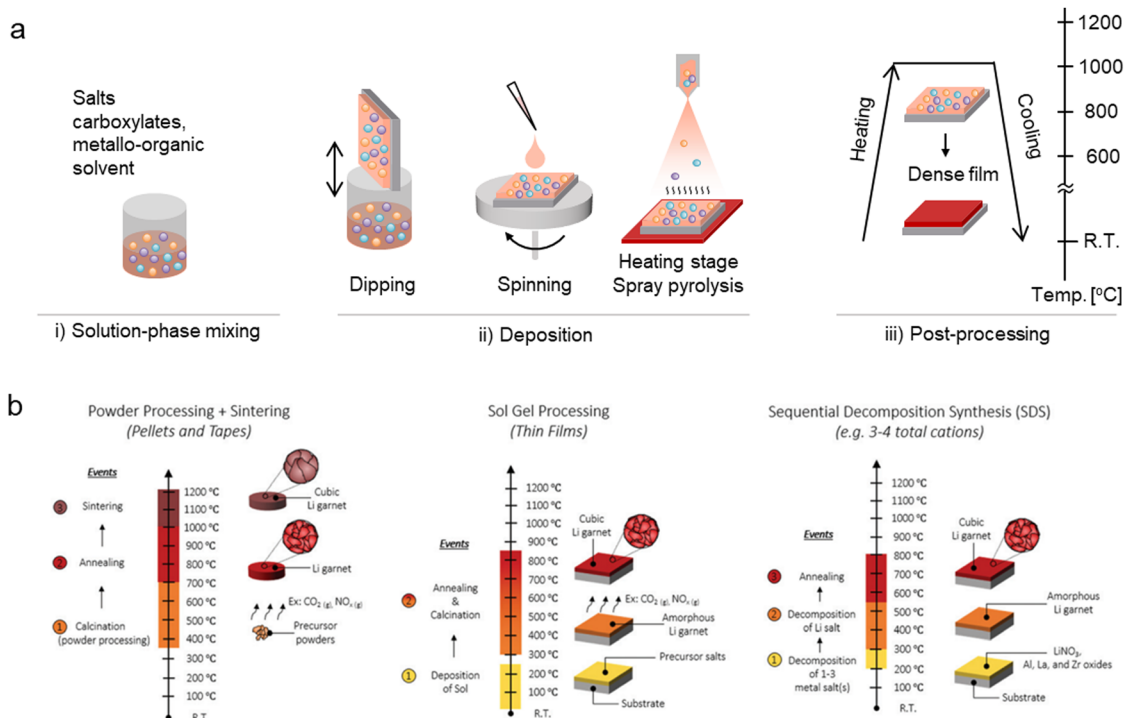Chem. Soc. Rev., 2025, **54**, 8925–9007 | 8949

Fig. 6 (a) Typical steps in wet-chemical synthesis. (b) Processing temperature, events, and ionic conductivity of Li garnets synthesized *via* powder, sol–gel, and sequential decomposition synthesis (SDS). Reproduced with permission ref. 318.

as powders (and further processed as ceramic pellets). Among them, LLTO,[301–303] LLZO,[162,248,304–309] LATP,[310–314] and LAGP[315] have also been deposited as films *via* solution-based methods (Table S2, ESI†). Among these electrolytes, the processing of pure oxide-based LLTO and LLZO has advanced faster than that of polyanionic oxides, LiPON, and LATP, mostly due to the limited selection availability of phosphate-based precursors. So far, the ionic conductivities achieved for solution-processed films are generally lower ($\sim 10^{-5}$ to 10^{-8} S cm^{-1}) than those achieved by solid-state processing ($\sim 10^{-4}$ to 10^{-5} S cm^{-1}), which can be mainly explained by the larger grain-boundary-to-grain volume ratios and often an insufficient lithiation in the films after post-processing, which is still to be worked on.[316,317] Interestingly, for LLTO films, the highest ionic conductivity achieved is 1.78×10^{-5} S cm^{-1} when processed at low temperature (500 °C) in the amorphous state,[285] indicating the possibility of enhancing film conduction by eliminating the grain-boundary area with reduced processing temperature.

3.1. Wet-chemical processing steps for solid-electrolyte film deposition

Solution processing can be generally classified into two types based on the final forms of the materials obtained: (i) techniques to synthesize powders/particles and (ii) techniques to deposit films. For the first type, sol–gel, Pechini, or co-precipitation methods are the most prominent examples that have been used to synthesize a variety of ceramic oxide powders.[319–321] These techniques generally involve the use of inorganic or metallo-organic precursors and solvents with

desired solubility and evaporation points to prepare at least two precursor solutions.[322,323] Then, the precursor solutions are mixed in single- or sequential multi-steps and undergo hydrolysis and condensation to form an inorganic complex composed of oxo (M–O–M) bonds. Usually, for inorganic salt precursors, hydrolysis proceeds *via* the removal of a proton from an aqua ion $[M(OH_2)_n]z^+$ to form hydroxo (–OH) or oxo (=O) ligands; condensation reactions involving hydroxo ligands result in the formation of bridging hydroxyl (M–μ(OH)–M) or oxo (M–O–M) bonds.[322,323] The next step involves heat treatment at an elevated temperature where the solvents evaporate, and the resultant inorganic complex undergoes further decomposition to form the desired oxides in powder form.[322] These synthesized powders can be further pressed into pellets or mixed with tape-casting solvents for solid-state synthesis in pellet/tape-casting forms followed by the sintering step (Fig. 6b,[318] as detailed in Section 3). In contrast, wet-chemical solution processing can be applied for thin- or thick-film deposition within the thickness range of 100 nm to 10 μm (Fig. 4).[323,324] Similar to aforementioned powder synthesis, the precursor solution is prepared with inorganic or metallo-organic precursor salts and solvents with desired solubility and evaporation points. In some cases, the pH of the solvents is also a consideration as it can play a significant role in the phase-formation process and activation of condensation reactions or affect the final film morphology.[325–327] However, unlike the wet-chemical solution-processed powders, which require an additional heat-treatment step at a higher temperature to form sintered tapes or pellets,

wet-chemical solution-deposited films only require single-step annealing and no sintering to complete phase formation with a dense nanocrystalline microstructure at reduced temperature (generally 1/2 to 2/3 of the sintering temperature required by solid-state synthesis).[323,328]

In general, there are three major steps for all the solution-based film-deposition methods:[323] (i) precursor-solution preparation, (ii) solution transfer and deposition, and (iii) post-processing and crystallization. The precursor-solution preparation involves mixing and dissolving the precursor salts in the solvents and constantly stirring for hours or days to ensure complete mixing. The precursors can be dissolved in the solvents at once or, if the objective is to obtain a gel, two or more separate solutions need to be prepared first (form the "sol") followed by a second mixing step to form a gel. Additional dilution may be required to reach the desired concentration and pH prior to deposition.[285,287] Since solution-processed films skip pressing and sintering after phase formation, their residual strain, microstructure, and short-range chemical order are highly influenced by the choice of precursors and solvents—factors that can significantly impact Li-ion conductivity or transference number, as shown in studies on solution-derived LLZO films and their TTT diagrams and phase evolution.[307–309] For LLTO films processed by spin coating, it has been reported that the ionic conductivity can be varied by two orders of magnitude if different precursor salts are selected, despite the amorphous nature of all the films.[285] This study indicates that precursors may alter the near-order structure and chemistry and that various amorphous phases can exist with the same film chemistry.[285] This is also in line with classic processing knowledge on other wet-chemically derived binary oxide ceramics.[205,309,329,330] The solution-transfer and deposition step can be classified into five main categories depending on the deposition technique: dip coating, spin coating, spray pyrolysis, chemical bath deposition, and direct writing (e.g., inkjet printing). Even with the same solution chemistry, the variation of the deposition route may affect the deposited droplet size and shape and therefore the microstructure and grain size/shape, which can later lead to differences in film's transport properties and affect the performance of solid-state batteries.[331] For example, Bitzer et al. reported that the precursor solution concentration can affect the film density and surface morphology of LLZO thin films deposited by spin coating. A solution with too low a concentration (<0.02 mol L^{-1}) can lead to inhomogeneous coverage of the substrate surface, whereas a solution with too high a concentration (<0.08 mol L^{-1}) can lead to undesirable cracks, which can potentially be detrimental to ion conduction.[291] Finally, in post-processing and crystallization, the deposited film is generally subjected to a post-annealing treatment to reach the desired phases and microstructure via nucleation and grain growth. For Li-oxide solid-electrolyte films, the annealing temperature is generally set between 500 °C and 1000 °C to form amorphous, biphasic, or crystalline films.[282,285,291,292,307–309,323,332] Because ceramic films by their nature do not require sintering to complete the densification step, the post-annealing temperature is notably lower than that for pellets or tapes processed by solid-state synthesis routes.[333] The benefits of this lower temperature are two-fold. First, from a mass manufacturing viewpoint, the required thermal budget for processing is lowered. Second, from a film chemistry perspective, the risk of reaction or dopant interdiffusion is reduced at the solid electrolyte and electrode interfaces, which generally occurs at elevated temperature, and undesired lithium evaporation at high temperature is prevented.

3.2. Further room for improvement: hindrances and opportunities for wet-chemical processing

Despite the abovementioned characteristics and strengths of wet-chemical solution-processed electrolyte films, the limited control over the surface morphology as well as the roughness and crack formation during drying and post-annealing have long posed challenges.[323] A promising strategy to address these challenges is to employ single- or multi-step temperature- or pH-controlled chemical reactions, either to deposit all precursor salts simultaneously or to guide drying and densification through sequential sub-reactions.[334] This approach can be particularly attractive for deposition involving Li, as Li salts possess a wide and relatively low decomposition temperature range (i.e., 100 °C to 550 °C)[335] compared to other metal salts that are often used in solid-electrolyte synthesis (e.g., Zr, Ti, La),[336,337] which have typical decomposition temperatures higher than 250 °C. For instance, recent work on sequential deposition synthesis (SDS) has demonstrated that the reaction of the Li salt can be separated from the non-lithiated ceramic formation, which would result in lithiation of the material at a higher temperature via a two-step pyrolysis reaction.[334] In the first pyrolysis reaction, the undecomposed Li salt melted and acted as a grain-boundary agent to mitigate cracks, promote densification, and improve the overall film density.[307] Here, the role of lithium is similar to that previously observed in bulk-type LLZO pellets, where Li_2O is added to form glassy-like phases at the grain boundary and promote densification owing to the effect coined "liquid-phase sintering".[276] Similarly, Li has been incorporated as a dopant in gadolinium-doped ceria ($Ce_{0.9}Gd_{0.1}O_{1.95}$) to improve the film density and reduce the sintering temperature.[338] This technique also helps bring the wet-chemical solution-processed solid electrolyte to the ~ 1–10-µm thickness range with high density and film quality,[335] which can be favorable for future solid-state battery architecture to optimize the energy density and ensure safety but is generally less reachable with most vacuum-based methods.[321,339] In addition, wet-chemical solution-based processing often results in lower chemical and phase purity compared with most vacuum-processing techniques. For example, garnet-type LLZO, a material that is extremely moisture sensitive, requires high-purity non-aqueous solvents to avoid proton exchange with Li ions, which can significantly reduce the Li-ion conductivity, especially along grain boundaries.[340,341] Solution-based processing also shares issues that are generally observed in vacuum-based processing, such as Li loss during deposition and high-temperature post-annealing, and it often

results in local de-lithiated phases with a significant reduction in Li conduction.[342] Two possible methods can potentially help overcome this challenge: (i) the use of an over-lithiated precursor solution before deposition and (ii) reduction of the post-annealing or post-processing temperature to avoid Li evaporation at high temperature. Regarding the first approach, wet-chemical solution processing offers an advantage of easy adjustment of the lithiation degree in precursor solutions, similar to how an excess Li precursor (10–20 wt%) is adopted to compensate for Li loss during calcination and sintering processes in conventional solid-state synthesis and pellet densification. However, special attention is required to optimize the synthesis protocol and the lithiation degree. Otherwise, too much over-lithiation in the precursor solution may lead to considerable pore formation during decomposition of the salts stemming from the generation of gaseous phase decomposition byproducts and lead to decreased film density and poor film quality.[334] Regarding the second option, grain-boundary-free amorphous solid-electrolyte films may possess the advantage of lower processing temperature requirements and the avoidance of defective grain boundaries. In particular, wet-chemical methods can be especially suitable for amorphous film processing as they are more scalable and cost-efficient than vacuum-based deposition techniques. LLZO has been successfully deposited also in an amorphous phase.[307–309,343] In addition, the low deposition temperature (mostly room temperature or <300 °C) of wet-chemical methods offers a natural benefit compared with solid-state methods that require high-temperature sintering (commonly >1000 °C), which is not suitable for amorphous structure synthesis (Table S2, ESI†). From a practical perspective, the nature of the grain-boundary-free structure may further improve the mechanical toughness and resistance toward dendrite propagation of the film as compared to its crystalline forms.[344] For instance, a nanoindentation study on RF-sputtered LiPON films indicates the high ductility of LiPON films and the ability to recover deformation over time compared to crystalline solid-state electrolyte conductors, such as crystalline LLZO and crystalline LLTO.[345] Further investigations are needed to understand whether the observed mechanical behavior holds for wet-chemical processed amorphous electrolyte films.

3.3. General processing steps for diverse solid-electrolyte deposition techniques

Here, we briefly discuss the general processing steps and major considerations for the five aforementioned deposition techniques, namely, dip coating, spin coating, spray pyrolysis (*e.g.*, SDS), chemical bath deposition, and direct writing. These techniques do not support the deposition of free-standing electrolyte films, and direct deposition on cathodes or catholytes is required to integrate these solid-electrolyte films into all-solid-state batteries.

Spin coating represents the most frequently applied technique by far in the solution processing of solid-state electrolytes.[282,285,291–293,327,332] This method takes advantage of centrifugal force through rotation of the substrates (usually on a spin coater) to uniformly spread the deposited solution to the designated coverage area and form the initial film. Generally, the spin-coating process can be divided into three major stages:[323] (1) dispensing of the coating solution, (2) fluid-flow-dominated thinning, and (3) solvent evaporation and coating "setting" (*i.e.*, decomposition of the precursors to form solvent-free amorphous films). During the first stage, a quantity of the desired coating solution is dispensed onto a smooth substrate with a pipette or syringe. At this stage, the spin coater can be set at low spin speed to facilitate the outflow of the solution to fully wet the substrate surface. In the second stage, the spinning speed of the spin coater is accelerated (*e.g.*, to thousands of rotations per minute) and held for a set time (often 30 s to 2 min) to allow the combined effect of fluid flow and solvent evaporation to leave a very thin and uniform layer (usually a few tens of nanometers) of coated material on the substrate. The as-deposited film then enters the third stage of processing, which generally includes drying (typically at 80–400 °C) and calcination (typically 150–500 °C) at elevated temperatures that enable solvent evaporation and decomposition of precursors but that are not high enough to crystallize the film or form any undesired phases.[346] Therefore, the film is usually in a solvent-free amorphous state.[285,291] The amorphous nature can suppress grain boundary resistance, yet may limit long-range Li-ion conduction due to structural disorder. Generally, the drying and calcination step of a single deposited layer can take 2 min to 2 h.[282,283,293] As the single deposition from spin coating results in a layer that is too thin (<100 nm) to be used as a solid electrolyte for battery applications, deposition of multiple layers is generally required, which is achieved by repeating the aforementioned three stages.[285,291,293,296] Importantly, complete drying and precursor decomposition during the third stage are required before starting the next round of deposition; this step will not only improve the film density but also reduce the number of chemical impurities remaining in each layer, which can be difficult to remove in the later phase—formation stage. Incomplete removal of residual organics or nitrates can result in microstructural inhomogeneities such as porosity or secondary phases, which degrade ionic conductivity. By repeating the coating steps, film thicknesses between 50 nm and 1 μm can be achieved for several solid-electrolyte materials, including LLZO,[291–293,347] LLTO,[282,283,285,287,303,348,349] and LATP.[296,327,332] To date, the ionic conductivity achieved by spin-coated LLZO is on the order of 10^{-6} S cm^{-1} for various amorphous and nanocrystalline phases, comparable to the value achieved by other wet-chemical techniques.[291–293,347] For LLTO films, spin coating has led to greater variation in the room-temperature Li-ion conductivity, which ranges from 10^{-9} to 10^{-5} S cm^{-1}.[282,283,285,287,303,348,349] This range is possible because of the large difference in grain-boundary areas in nanocrystalline and amorphous LLTO films. Notably, the grain-boundary resistance of LLTO is significant and often places a limit on the total ionic conductivity that LLTO can achieve.[217,350,351] For this reason, grain-boundary-free amorphous LLTO films exhibit better transport properties than their crystalline counterparts.[282,285] Other factors, such as the
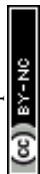
8952 | *Chem. Soc. Rev.*, 2025, **54**, 8925–9007

This journal is © The Royal Society of Chemistry 2025

precursor salt selection[285] and deposited film thickness,[283] can also affect the conductivity of the films. For spin coating, the surface morphology of each previous layer (or of the substrate for the first layer) can greatly affect the film coverage and morphology of the later layers.[323] Therefore, ensuring the wettability of the substrate is vital for enabling a good start of film deposition. Several modifications can be made to improve the solution wetting, including pre-surface treatment of the substrate to change its nature from hydrophobic to hydrophilic or *vice versa*,[323] and adding a surfactant to the solution formulation to facilitate fluid-thinning processing without interfering with the phase formation.[292,303,323] For instance, Triton X-100 has been added to precursor solutions during LLZO deposition[292] and the triblock copolymer $[H(CH_2CH_2O)_n(CH_2CH(CH_3)O)_m(CH_2CH_2O)_nH]$ with $n/m = 20/70$ has been used in LLTO deposition,[303] resulting in better film morphology with a smoother surface and fewer pores in each layer. These morphological improvements reduce defect density and promote more homogeneous ionic pathways, thereby improving film-level conductivity and interfacial contact with electrodes. Compared with other wet-chemical solution-processing and vapor-deposition techniques, spin coating can be advantageous as it can provide high film quality for thicknesses even up to 1 μm; however, the increased thickness requires multi-layer deposition, which can extend the processing time to days.[349] One major disadvantage of spin coating is that it poses a limitation on the size of the substrate. As the substrate size increases, the high-speed spinning and film thinning become more difficult. A more pronounced thickness gradient from the substrate center to the rims can also be observed with increasing substrate size. In addition, the material efficiency of spin coating is considerably lower than that of other solution-processing methods, such as dip coating or spray pyrolysis, as more than 95% of the precursor materials can be flung off and disposed of during the spin process.[352] In addition, spin coating has limited applicability for non-flat surfaces[323] and, thus, may not be the best choice for 3D battery designs. Nonetheless, its ability to form controlled microstructures with tunable porosity and thickness profiles makes it a powerful platform for systematic investigation of structure–property relationships in thin-film electrolytes.

Dip coating is another common wet-chemical solution-based deposition method that requires less complex and less expensive experimental settings and usually requires less time to complete deposition than other wet-chemical solution-based deposition techniques, such as spin coating. Dip coating generally involves dipping the substrate in and out of the pre-mixed precursor solution vertically at a designated moving speed. The microstructure of films processed by dip coating generally depends on several factors,[323,353] including (1) the chemical structure (molecule size, organic chain length) and concentration of the precursors in the solution; (2) the reactivity of the precursors, including the condensation or aggregation rates; (3) the time scale of the deposition process; and (4) the magnitude of the shear forces and capillary forces that accompany film deposition, which are related to the surface tension

of the solvent and can result in different thickness gradients and surface microstructures. All these factors are interdependent and can also affect the local packing density and film thicknesses. The film thickness is also determined by the competition between the surface tension, gravity, and viscosity of the solution.[323,333] Usually, faster withdrawing of the substrate leads to thicker films; however, a very slow withdrawing speed can also result in thick films if the "capillarity regime" is applied, where the solvent evaporation is faster than the movement of the drying line, leading to continuous feeding of the solution to films.[354] To date, dip coating has been successfully applied in the deposition of solid electrolytes such as LLZO[290,291] and LLTO,[355] with film thicknesses up to 1 μm achieved. Specifically, dip-coated crystalline cubic LLZO films with lithium dodecylsulfate added as an ionic surfactant during synthesis and Li_2CO_3 powders presented in annealing crucibles exhibit a dense microstructure with an ionic conductivity of 2.4×10^{-6} S cm^{-1} at room temperature,[290] comparable to the conductivity achieved by other wet-chemical processing methods. Another example of dip-coated crystalline LLTO films show a limited conductivity of 10^{-8}–10^{-7} S cm^{-1} at 120 °C.[355] These conductivities are considerably lower than those reported for LLTO pellets and even LLTO films deposited by spin coating, mainly due to the porosity in the film and small crystallite sizes that lead to a large grain-boundary area, and undesirably increase the contribution of the grain-boundary resistance. Overall, modifications (*e.g.*, adding a surfactant, reducing the deposition thickness) are needed to obtain dense films with spin coating. There are also a few variations of traditional dip-coating techniques including (1) drain coating,[356] which involves removing the solution at a constant draining rate instead of lifting the substrate; (2) angle-dependent dip coating,[357,358] which involves dipping the substrate in and out of the solution at a non-vertical angle; and (3) non-planar substrate dip coating,[359] which uses a non-planar substrate (*e.g.*, rods) and could potentially be of interest for certain battery designs, such as cylinder batteries.

Another important solution-processing technique is spray pyrolysis (*i.e.*, SDS, if multi-step decomposition and phase synthesis is involved). The spray pyrolysis process can be broken down into several sub-processes that consist of[323,360] (1) generation of solution from a bulk liquid to form an ensemble of small spherical liquid droplets, (2) transport of the droplets to the substrate surface, and (3) nucleation and aggregation of the droplets to reach the desired film thickness (Fig. 6b). During the first step, the precursor solution is generally fed by a syringe into an atomizer (spray nozzle) with pre-set pressure and forms a uniform dispersion of liquid droplets. Here, the inlet/outlet design and internal gas flow of the atomizer can change the droplet size and later affect the decomposition dynamics and density of the deposited film.[360,361] For the second step, the generated liquid droplets are deposited onto substrate surfaces with externally applied gas pressures. By changing the gas pressure, the deposition rate and coverage area can be adjusted. In some cases, additional external forces such as electromagnetic forces can be applied to

This journal is © The Royal Society of Chemistry 2025

Chem. Soc. Rev., 2025, **54**, 8925–9007 | **8953**

facilitate the deposition process and adjust the direction of the droplets. Typically, the deposition proceeds with the substrate placed on a hot plate and the temperature set around solvent-evaporation and precursor-salt-decomposition points.[360] This enables the third step of film growth and phase formation with continuous removal of gaseous byproducts during deposition,[323] which, compared with other wet-chemical solution-processing techniques such as spin coating and dip coating, reduces the porosity of the film while enabling the deposition of larger thickness ranges (*i.e.*, up to tens of microns) in comparatively shorter deposition times. For instance, a recent study demonstrated that 1–10-um-thick cubic phase LLZO electrolyte films can be synthesized *via* SDS within 1 h.[334] This thickness range has never been accessed using other thin-film processing methods (*e.g.*, spin coating, pulsed laser deposition, *etc.*) or solid-state synthesis methods (*e.g.*, tape casting).[362] These characteristics of spray pyrolysis can be particularly advantageous for solid-electrolyte manufacturing, which requires a dense layer of micrometer thickness to be processed in a reasonable time frame.[321,339] In addition, sprayed films can, in principle, be easily transferred to industrial standard roll-to-roll battery manufacturing, reducing the setup and process changing costs. In addition, spray pyrolysis can be used for substrates that do not lend themselves to spin coating, including substrates with uneven or 3D surfaces or those with larger coverage of pores and area requirements.[323] From the film-quality perspective, the sprayed films typically result in lower defect densities than spin-coated films,[363] as spin coating allows for air to become entrapped in the features under the advancing liquid wavefront.[323] However, spray pyrolysis requires more sophisticated equipment than spin coating or dip coating and has more parameters to optimize in order to obtain a dense film with the desired microstructure, local chemistry, and phases. For these reasons, only recently, a few studies on the aerosol deposition of LATP[364] and LAGP[365] or spray pyrolysis of LLZO[307–309] have been reported. The Li-ion conductivities achieved were all on the order of 10^{-6} S cm^{-1},[361,364,365] comparable to those of films deposited by other wet-chemical methods; nevertheless, the conductivities are still one-two-orders-of-magnitude below those achieved for solid-state-synthesized pellets/tapes. Given the early-stage development and limited reports of spray techniques applied to Li-solid electrolyte processing, we anticipate that there is substantial room to improve the transport properties of spray films in the next decade. Another drawback of spray pyrolysis is its poor control of the film surface roughness as compared to spin coating or dip coating. For instance, recent work on SDS-processed LLZO films indicated a roughness (R_a) of 0.4 μm. Depending on the design and size scale of the battery, the high roughness of the electrolyte film may be beneficial for lowering the interfacial resistance between the electrode and the solid electrolyte. However, it may also induce unnecessary processing errors when applied to batteries with smaller size scales (*i.e.*, thin-film and on-chip batteries).

Chemical bath deposition and direct writing techniques are two types of techniques first developed for deposition of inorganic films but less frequently visited in the field of solid-state electrolytes. Chemical bath deposition usually proceeds by immersing the substrate in a precursor solution (one time or multiple times), and by controlling the temperature, solution concentration, and pH, solid phases can be exsolved and grown on the substrate without any subsequent heat treatment.[323,366] This technique has been mostly used to synthesize sulfide, selenide, and other non-oxide films for many years;[367,368] only in the past 30 years has it begun to be applied to single and binary oxide films[323,369] with no reported use in more complex oxide-based solid electrolytes to date. In contrast, direct writing such as inkjet printing is a fairly new technique that was only recently developed.[370,371] The major challenge in applying printing techniques to deposit a patterned thin-film electrolyte layer is the formulation of suitable inks.[372] The ink chemistry determines not only the phases and microstructure characteristics of the films but also the stability and precision of the printed patterns.[323] Thus, careful selection of compatible substrates is also required for different ink formulation. With further research, these techniques can be coupled with automated manufacturing routes and are of great interest for 3D thin-film batteries.[373,374]

3.4. Tuning the processing parameters of wet-chemical-processed solid-electrolyte films

All the different processing techniques share a few parameters that can critically affect the film quality, phase formation, and transport properties of the film. Most of these parameters can be easily tuned but are dependent on each other; therefore, holistic experimental design is always required to optimize film deposition. Specifically, these parameters can be classified into three categories based on the processing stages (*i.e.*, precursor solution preparation, solution transfer and deposition, and post-processing and crystallization into the desired phase) with which they are associated. In the precursor solution preparation stage, we identify three major parameters:

(i) Precursor salt chemistry: precursor salt chemistry plays a foundational role in determining the quality and performance of solid electrolyte films prepared *via* solution-based deposition methods. The choice of the precursor strongly influences the phase purity, microstructure, and resulting ionic conductivity of the final film.[285] To enable effective film formation, precursor salts must generally meet three criteria:

(1) they should contain the target cations in the correct stoichiometry;

(2) their decomposition byproducts should evaporate cleanly during annealing without leaving carbonaceous or reactive residues; and

(3) they should be sufficiently soluble and chemically stable in solvents for extended periods (ideally several weeks), without reacting prematurely with other precursors in the solution.

These requirements constrain the number of viable chemistries, particularly for complex multi-cation systems. Developing stable and compatible precursors for compositions like LLZO and LLTO—each involving at least three distinct cations—is especially challenging and often requires extensive screening

8954 | *Chem. Soc. Rev.*, 2025, **54**, 8925–9007

This journal is © The Royal Society of Chemistry 2025

and optimization. For phosphate-based electrolytes such as LIPON and NASICON-type materials (*e.g.*, LATP and LAGP), the scarcity of soluble and reactive phosphate precursors has limited their development using solution-based methods. Lithium-containing films often require compensation for Li volatility during the post-annealing step. For example, in LLZO systems, up to 10–30 wt% excess lithium is commonly added to the precursor solution—and in some SDS-based processes, this excess can reach 250 wt%—to achieve desired stoichiometry and avoid lithium deficiency in the final phase.[282,285,291,293] Despite the high Li excess, the overall Li consumption remains relatively low due to the thin nature of the resulting films (~ 10 μm), especially when compared to conventional bulk processing methods involving millimeter-scale electrolytes. The selection of precursor salts can also have a substantial effect on the phase formation and crystallization of films. For example, Zhang *et al.* reported that the conductivity of spin-coated amorphous LLTO films can vary by up to two orders of magnitude (from 10^{-7} S cm^{-1} to 10^{-5} S cm^{-1}) with changes in the precursor and solvent selection.[285] Another example of a spin-coated perovskite-type $BaSrTiO_3$ film demonstrated that selecting different precursors and synthesis routes can lead to notable variation in the crystallinity and film density.[375] These are attributed to differences in the decomposition pathways and volatility of precursors, which determine the phase stabilization and homogeneity of the film. In general, organic precursors with longer chain length and higher boiling point typically require higher temperature to complete the decomposition step. These features can also lead to an increase in local structural entropy and affect the onset crystallization and phase evolution kinetics when transitioning from amorphous to crystalline states.[330] The retained organic content can also delay crystallization to a higher temperature and result in an increased nucleation energy barrier, which can affect the nucleation behavior (homogeneous *versus* heterogeneous).[376] In some cases for multi-cation films, the decomposition temperature of precursor salts may be different and can result in the formation of intermediate phases. The intermediate phase may lower the driving force for final phase formation, and the transport properties may degrade if a residual intermediate phase is present in the final film.[323] These residual phases may act as blocking domains at the grain boundaries, impeding long-range lithium transport and thus reducing effective ionic conductivity.

(ii) Solvent: in general, the solvent should be non-reactive to precursor salts over the range of temperature between deposition and solvent evaporation. To date, the most commonly used solvents include 1-propanol,[290,303] 2-methoxyethanol,[282,285,292,293,296,355] ethanol,[291,303] ethylene glycol,[291] and citric/nitric/acetic acid.[248,283,285,287,296,327,332,348,345,377–381] Several additional factors need to be considered when selecting solvents, such as the functional groups of the organic solvents, which can affect the solubility of the precursor salt; the chain length of the organics, which can lead to variation in the evaporation temperature and alter the film-densification process; and the chemical safety in terms of human health and the

environment. In particular, for multi-layer spin coating, the solvent-evaporation temperature is linked to the temperature of the intermediate heating step between the deposition of each layer. For spray pyrolysis, the hot-plate temperature is generally set to enable complete evaporation of the solvents (close to the solvent-evaporation point).[360] Variation in the solvent chemistry may result in changes in the initial amorphous near-order structures and subsequently the crystalline characteristics such as the microstructure/grain boundary chemistry, which can lead to a significant difference in structural properties and electrochemical performance. For instance, a study on a sol–gel-synthesized $LiNi_{0.8}Co_{0.2}O_2$ lithium-ion battery cathode examined the effect of the solvent (ethanol, 1-propanol, 1-butanol, and water) on the structure and electrochemical properties.[382] The structural homogeneity (in the form of hexagonal ordering) was shown to be affected by the solvent selection, resulting in a notable difference in the electrode cycling performance with a discharge capacity ranging from 190 mAh g^{-1} (ethanol as solvent) to 154 mAh g^{-1} (water as solvent). This observation indicates that solvent chemistry can strongly influence the initial formation of a chelation complex, which decides the homogeneity of the materials during crystallization, thereby linking solvent choice directly to battery performance.[385]

(iii) Solution pH and concentration: the pH of the precursor solution is critical as some salts or gels require particular pH ranges to dissolve or remain stably suspended in solvents. Normally, monomeric aqueous ions are the only stable species at low pH, and various monomeric or oligomeric anions are the only species observed at high pH. At intermediate pH, well-defined polynuclear ions are often the stable solution species; however, the metal solubility is normally limited in this range and, when exceeded, results in the precipitation of oxyhydroxides or oxides.[383] The concentration of the precursor solution can affect the film density as residual solvents are evaporating out from films during intermediate or post-heat-treatment steps. A higher solution concentration can result in less organic evaporation per film volume and reduce the porosity; however, in cases with gradual solvent removal, such as multi-layer spin coating or spray pyrolysis, a reduced solution concentration can be preferred to enable reduced nuclei sizes and deposition of thin and dense layers with a reduced rate of deposition (but too low of a concentration can lead to inhomogeneous coverage on the substrate).[291] It is also important to mention that many wet-chemical processes require the preparation of more than one precursor solution before mixing them for final deposition, which allows the creation of transfer reactions from liquid precursors with more unstable salt dissolutions over time. In this sense, the concentration or relative concentration of different solutions can be interdependent and affect the chemistry and film properties in a more complicated manner. In addition, the solution concentration can also affect the phases and crystallization temperature of the as-deposited films. For instance, Joshi and Mecartney reported that in the case of $LiNbO_3$ films, a diluted precursor solution with a larger amount of water promoted homogeneous nucleation and allowed for

This journal is © The Royal Society of Chemistry 2025

Chem. Soc. Rev., 2025, **54**, 8925–9007 | **8955**

substantial grain growth.[368,383] It was postulated that the high amount of water increased the concentration of the amorphous building blocks in the sol through hydrolysis, which subsequently promoted early crystallization and allowed for more extended grain growth. In contrast, with lower water content in the precursor solution, the crystallization shifted to a higher temperature, resulting in heterogeneous nucleation and grain growth to a smaller extent. As discussed above, the film microstructure and grain sizes can greatly affect the ionic transport properties of the films. For example, the reduced ionic conductivity observed in LLTO thin films (as compared to LLTO pellets) has been attributed to their large grain boundary area and small grain sizes. Altering the nucleation and growth kinetics may be a possible way to help optimize the grain microstructure and improve the ionic conductivity. The pH and concentration of the solution can generally be adjusted during the precursor dissolution step by adding one more nonreactive solvent.[285,287,381]

In the solution deposition stage, there are two major parameters:

(i) Substrate selection: in principle, substrates for solution deposition are required to be chemically non-reactive against the deposited solution and the formed film up to the highest heat-treatment temperature. Substrates for wet-chemical film deposition can be classified into two categories: (1) battery components adjacent to the solid-electrolyte layer in a working battery and (2) supporting substrates that do not participate in electrochemical reactions during battery cycling. In the first category, candidate substrates include oxide-based or alloy-based battery cathode (e.g., LiCoO$_2$, NMC, etc.) and anode (e.g., Si, SiO$_x$, Si/C, etc.) materials printed on current collectors or in free-standing thick film, tape, or pellet forms, which can all be used directly as substrates for wet-chemical film deposition. When using electrode materials as the substrate, it is critical to ensure the chemical compatibility and thermodynamic stability between the electrode materials and the deposited solution, especially at the elevated calcination or post-annealing temperature. In the second category, supporting films that are porous and non-reactive (with Li, the solid electrolyte, and the cathode or anode) such as porous oxides (e.g., CeO$_2$) or porous carbon paper could be considered as potential supporting substrates for wet-chemical deposition. The porous supporting substrate should ideally function as a mechanical supporting layer for wet-chemical electrolyte film deposition while not interfering with the ionic conduction between the electrode and the electrolyte after battery integration. Practically, the substrate selection for Li-oxide solid electrolytes is limited, as Li can easily alloy with most of the metal substrates and can diffuse into many oxide substrates, resulting in off-stoichiometry in films at elevated temperature. Additionally, for certain materials, such as LLZO, many metal cations can diffuse into the solid-electrolyte film layer as dopants during the annealing step, further limiting the substrate selection. For instance, reports have shown significant Co diffusion into the cubic LLZO layer upon annealing above 700 °C (generally required to achieve a highly conductive cubic

phase), limiting the use of Co-containing cathodes, such as LiCoO$_2$ and NMC, as substrates for the solution deposition of crystalline cubic LLZO. Such interfacial reactions result in the formation of resistive phases that hinder ionic and electronic transport across the film–substrate interfaces. For epitaxial film deposition (this method is less commonly visited for solution-processing routes but can theoretically be achieved if the parameters are finely tuned), a single-crystal substrate with certain crystal orientation is required to enable orientated growth.[283] Additional surface properties of the substrates, such as wettability, surface roughness, and lattice mismatch microstrains between the substrate and the film, can be critical in determining the microstructure of the films.[384,385] If necessary, surfactants (e.g., lithium dodecylsulfate,[290] Triton X-100,[292] and triblock copolymer (H(CH$_2$CH$_2$O)$_n$(CH$_2$CH(CH$_3$)O)$_m$-(CH$_2$CH$_2$O)$_n$H) with n/m = 20/70)[303] can be added to improve the wettability of the precursor solution and reduce the formation of pores, thus enhancing the ionic conductivity.[290,292,303] An additional buffer layer may also be applied to the substrate before film deposition to reduce lattice mismatch strain and facilitate epitaxial growth if desired.[386,387]

(ii) Rate of deposition: it is generally observed that reducing the rate of deposition results in higher film density (low porosity) in solution-processed films, as it allows extensive control over the film drying process with a longer time to fully evaporate organic solvents and decompose precursor salts. More specifically, for spin coating and dip coating, reducing the film thickness per deposited layer provides more room for complete solvent evaporation within each layer before the final annealing step at a higher temperature and this reduces the drying stress, which can cause crack formation if exceeding a critical stress value.[388,389] Similarly, for spray pyrolysis, a slower solution/droplet deposition rate enables more complete solvent evaporation and precursor decomposition per precipitate and per thickness grown and therefore improves the density of the deposited film.[359] The improved film density can undoubtedly improve the overall ionic conductivity,[292,390] which is crucial for reducing the risk of dendrite formation and propagation.

In the post-processing stage, four parameters can critically affect the final film properties:

(i) Temperature: the final annealing temperature not only determines the phase and crystallinity of the film but can be critical in determining the rate of Li evaporation and interdiffusion or alloying between the as-deposited electrolyte film and the substrate (or electrodes). Generally, a lower annealing temperature is always preferred for economical scalability reasons. As a result, amorphous films with a much lower processing temperature can be advantageous over their crystalline counterparts when the ionic conductivities of both phases are comparable. For instance, for wet-chemically solution-processed LLTO films, the annealing temperatures required to obtain conductive crystalline phases range between 700 and 900 °C;[287,303,348,355] in contrast, amorphous phases can be synthesized at a much lower temperature of ~500 °C (contingent upon the precursors decomposed).[282,285,348] Interestingly, both wet-chemical-processed crystalline and amorphous

8956 | Chem. Soc. Rev., 2025, 54, 8925–9007

This journal is © The Royal Society of Chemistry 2025

LLTO films can achieve conductivity on the order of 10^{-5} S cm^{-1}.[285,287] This implies that sufficient short-range ordering of the conduction pathways in amorphous phases may be retained to support effective Li$^+$ migration, despite the absence of long-range crystallinity. Thus, for scalable manufacturing, it may be preferred to process LLTO films in amorphous states using wet-chemical methods because of the higher conductivity and reduced processing temperature.

(ii) Time: the annealing time and annealing temperature are interdependent. As traditional time–temperature–transformation (TTT) diagrams illustrate, to reach the same phases, a higher annealing temperature requires a shorter annealing time and *vice versa*.[309,329] However, even when characterized as the same phase, different annealing time–temperature combinations may, for example, lead to small variations in the Li or O non-stoichiometry and result in micro-strain and micro-stress,[391] which can affect the transport properties. The interdependent effect of the annealing time and temperature has not yet been quantitatively studied for Li electrolyte films and requires additional attention.

(iii) Heating/cooling rate: if the rate of heating or cooling is too high, macro-cracks can be formed on the films either due to fast residual organic/gas evaporation or due to uneven thermal expansion and contraction. Micro-cracks can result in a reduction in the ionic conductivities and lower the dendrite suppression resistance. In general, to minimize the formation of micro-cracks, heating rates below 5 °C min^{-1} are often applied for Li-oxide films during the solvent removal and precursor decomposition process. However, it should also be noted that if the ramp rate in the high-temperature region is too low, the Li stoichiometry in the film can be adversely affected as it leaves larger time windows for Li evaporation. Considering this effect, multi-heating-rate annealing programs may further improve the film density while preserving the desired film chemistry. The different heating rates can also result in different film microstructures and affect the ionic conductivities. For example, Wu *et al.* reported that applying rapid thermal annealing in the post-annealing process (after solvent drying and precursor decomposition of each spin-coated layer) can result in a smaller-grain, denser film and an overall higher ionic conductivity (2.7×10^{-6} S cm^{-1}) compared with films processed by conventional furnace annealing (1.4×10^{-6} S cm^{-1}) for spin-coated LLTO.[296]

(iv) Atmosphere: the most commonly used calcination or annealing atmospheres for Li-oxide electrolyte films include pure oxygen, (dry) air,[293,296] and argon.[282,285,291] Among these atmospheres, moisture and carbon dioxide are avoided to prevent surface degradation and Li-carbonate formation, especially for LLZO films. In some cases where metal (*e.g.*, steel) substrates are used, an argon atmosphere can be preferred to avoid undesired substrate oxidation, which can "absorb" a significant amount of Li and result in a Li deficit in electrolyte films.[291] The gas atmosphere can affect the film chemistry, especially the oxygen stoichiometry, and may require adjustment of the annealing temperature to achieve the same phase and material properties.[392] The variation in oxygen stoichiometry can affect the Li stoichiometry and generate additional electrons and may affect the electronic conductivity, and thus the transference number, of the film.[217,393] As reported in a recent study, high electronic conductivities may be the origin for Li-dendrite growth.[220] Further studies are needed to clarify the effect of the annealing atmosphere and oxygen partial pressure on the transport and electrochemical properties of solid-electrolyte films.

In short, recent advances in wet-chemically solution-processed solid-electrolyte films show great promise towards industrial upscaling with reduced processing cost and lowered thermal budget. In particular, chemical-solution-based processing could be integrated with automated high-throughput material synthesis to further accelerate material discovery and property optimization. However, inherent issues such as drying cracks and poor film density require more research efforts; innovative processing protocols, such as multi-step reactions, can be encouraging in improving electrolyte quality. Among the five techniques surveyed in this section, spin coating and dip coating are the most developed for solid-electrolyte processing reported for LLZO, LLTO, LATP, and LAGP films over the past two decades and can result in films with thicknesses of 50 nm to 2 μm. These techniques require less complicated setups and are appropriate for lab-scale testing demonstrations; however, the small coverage area per deposition and comparably low deposition rate limit their application for large-scale production. In contrast, spray pyrolysis (or SDS), although applied in ceramic oxide film deposition for many decades, is fairly new for Li-electrolyte deposition with only a recent demonstration of LLZO films that can reach a thickness of 1–10 μm.[318,362] Admittedly, this technique requires a more complicated experimental setup and has more deposition parameters that need to be optimized than dip or spin coating. Nevertheless, spray pyrolysis (or SDS) may be promising for efficient and scalable industrial processing as it offers a high coverage area per deposition with a high deposition speed (less time required to reach the same thickness).

In addition, the newly developed inkjet-printing technique, together with 3D printing, may be of particular interest for 3D thin-film battery design. Given the early stage of its development, attention should be paid to developing stable ink chemistries with high precision of the printed patterns. To date, the conductivities achieved by wet-chemical-processed electrolyte films are still lower than those of solid-state-synthesized ceramic pellets/tapes, mostly due to the insufficient film lithiation and large grain boundary areas within the film. Grain boundaries often serve as barriers to Li-ion transport, especially when dopant segregation occurs, emphasizing the need for grain-boundary-targeted engineering or post-treatments such as controlled atmosphere annealing or chemical doping.

In conclusion, to further improve the structure and transport properties of solution-processed electrolyte films and accelerate the academia-to-industry knowledge transfer for crystalline electrolytes, additional attention should also be paid to tailoring the grain-boundary chemistry and optimizing its electronic structure and ionic transport properties, as it may

This journal is © The Royal Society of Chemistry 2025

Chem. Soc. Rev., 2025, **54**, 8925–9007 | **8957**

result in significant variation of the dendrite resistance and conduction. Both precursor chemistries and formation of the oxides, as well as evolution of the local near-order structure from an amorphous to a crystalline nanostructure of wet-chemically processed films and electrochemical stability, require additional clarification. For example, partial crystallinity or retained amorphous regions can either aid or hinder Li-ion transport depending on their connectivity and Li solubility, calling for *in situ* structural probes to resolve the active transport pathways. Low-temperature wet-chemically solution-processed grain-boundary-free amorphous electrolytes could also be a potential option to improve battery safety with enhanced resistance toward dendrite propagation while maintaining high power density. To further proceed, we suggest developing more time–temperature–transformation (TTT) diagrams to systematically understand the phase formation and evolution from the solution phases to synthesized solid films and comparing these diagrams with ion-transport properties and transference measurements per phase equivalents, to aid in reducing the cost and time associated with phase and conduction optimization. Overall, wet-chemically derived Li-oxide electrolyte films show strong market potential due to their low cost, fast processability, and compatibility with roll-to-roll manufacturing. One may also mention that there are decades of ceramic wet chemically derived products that made it as films to the market as functional ceramics, and industry has the knowledge for processing. However, it needs a targeted approach to transfer more Li-oxide based chemistries from the lab to role-to-role processed products in plants.

# 4. Vapor deposition technologies for thin-film solid electrolytes

4.1. Physical vapor deposition of thin-film solid electrolytes

The most common physical vapor deposition (PVD) techniques to process solid-state electrolytes in a thin-film form (<1 μm) are radio-frequency (RF) magnetron sputtering (Fig. 7a), pulsed laser deposition (PLD) (Fig. 7b),[394] and, to a lesser extent, electron-beam evaporation.[395,396] The literature contains comprehensive reviews on the basics and fundamentals of PLD and sputtering and the readers are advised to refer to these.[394,397–400] RF sputtering and PLD techniques provide a stoichiometric transfer of a high-melting-point material from a single or several ceramic targets to dense, multi-cation films with low surface roughness (~ 0.4–10 nm). Typically, PVD methodologies can produce films ranging from a few tens of nanometers to several micrometers in thickness (Table S3, ESI†), and have thus far been successfully integrated mainly in the fabrication chain of LiPON-based solid-state thin-film batteries owing to the ease of amorphous film fabrication.[155–157] LiPON offers a wide electrochemical stability window (0–5 V *vs.* Li⁺/Li),[401] reasonable room-temperature single-ion conductivity (10^{-6} S cm⁻¹),[156,159] high electronic resistivity ($\sim 10^{14}$ Ω cm),[402] and ease of dense thin-film processability *via* sputtering. Despite its success, extensive efforts are

being placed on the practical processing of (favorably) lithium-stable, high-total-ionic-conductivity ($>10^{-3}$ S cm⁻¹) Li oxides with enhanced electrochemical stability (ideally from approximately -0.5 to 5 V) from millimeter-sized pellets to thin-film forms.[403] Thin films of NASICON-,[404,405] perovskite-,[406] and garnet[44]-type structures have been slowly garnering more scientific attention and are being processed using a variety of thin-film deposition methods, either in amorphous or in crystalline state (Table S3, ESI†).[407] To date, the limited applicability of PVD-deposited solid electrolytes in microfabricated batteries is related to the restricted PVD-deposited cathode thickness determined by the lithium diffusion coefficient resulting in a 2D geometry, providing lower gravimetric and volumetric energy densities. However, there is no fundamental reason to neglect the possibility of scaling-up PVD techniques to integrate solid electrolytes with thicknesses in the range of 0.5–5 μm with state-of-the-art cathodes and anodes deposited using non-PVD type techniques, contingent upon efficient cell design and electrode/electrolyte processing adjustments.[408]

RF sputtering and PLD techniques rely on vapor formation from a ceramic target, induced by ion- and photon-bombardment, respectively, at very low pressures (typically $\sim 10^{-4}$–10^{-1} mbar, respectively) producing particle ejection, which later condensates onto a substrate. PLD usually offers a better stoichiometric transfer from the ceramic target than RF sputtering, which requires careful calibration for each cation. One of the main advantages of these techniques lies in the potential of lowering the processing temperature attributed to the high energy distribution of the ejected particles (*i.e.*, "the plume"). At an atomic level, this lowered temperature even enables the stabilization of out-of-equilibrium phases, allowing the formation of desired phases that would otherwise be thermodynamically unfavorable. This feature allows film crystallization to be stabilized at lower temperature for some ceramic materials when compared to classic ceramic processing *via* solid-state reactions (see Section 2) and has the advantage of potentially avoiding post-annealing steps. For instance, PLD-grown epitaxial LLTO films were synthesized at temperatures as low as 750 °C, compared with classical pellet sintering above 1200 °C.[409] Although both PLD and sputtering typically yield deposition rates on the order of ~ 1–10 nm min⁻¹, sputtering can induce a higher gas ionization degree and broader spatial extent of the ablation source (larger uniform sputtering area up to 8″, depending on the chamber and target size *vs.* the few mm² per pulse in PLD) and is therefore more suitable in terms of scalability. The importance of the higher ionization degree induced on the surrounding gas has been well established in sputtered LiPON films, where higher incorporation of N during film growth[410,411] led to higher ionic conductivities compared with those of PLD-grown films.[412,413] It remains to be seen whether recent advances in industrial PLD systems working at rates of hundreds of Hz at the large wafer scale with growth rates in the nm s⁻¹ range can compete with well-established RF. As in conventional solid-state processing, the deposition conditions must be optimized for every material and technique, especially considering that the chamber shape

8958 | *Chem. Soc. Rev.*, 2025, **54**, 8925–9007

This journal is © The Royal Society of Chemistry 2025
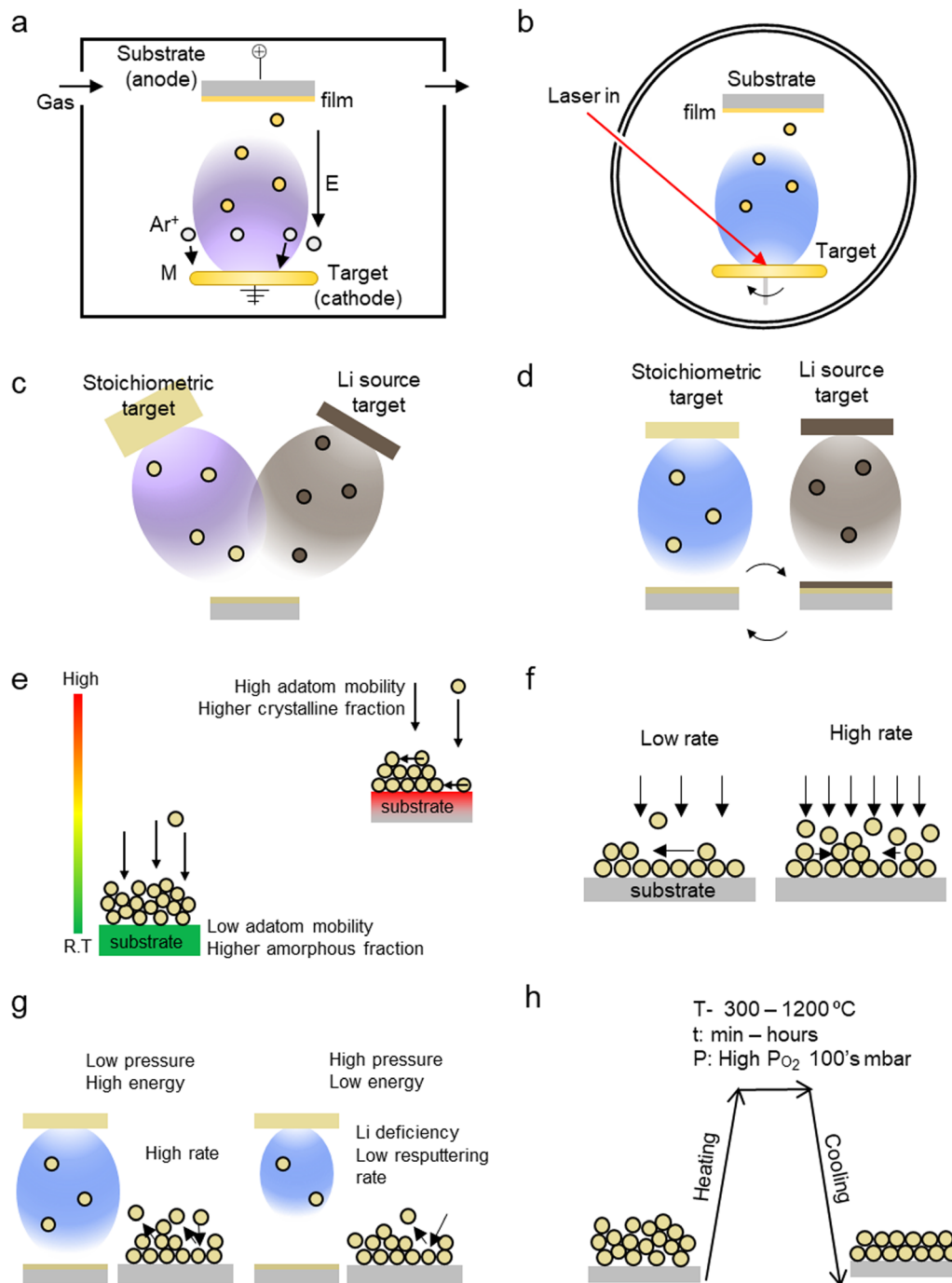
Fig. 7 Physical vapor deposition (PVD) techniques for solid-state electrolyte processing: (a) radio-frequency (RF) magnetron sputtering and (b) pulsed laser deposition (PLD). (c)−(h) Critical processing parameters of solid electrolytes prepared *via* the PVD technique: ceramic target composition, substrate temperature, deposition rate, ambient pressure in the chamber, energy of the deposited particles, and post-annealing steps.

can have an effect, for instance, on the sputtering processes.[394] Even for a mature technology like LiPON, any processing that does not produce an amorphous dense film with precise Li/P and O/N ratios results in significantly lower ionic conduction.[158,159] Nonetheless, the major issue remains the several-orders-of-magnitude decrease in the ionic conductivity attributed to the transition from bulky pellets to thin films of the solid electrolyte.[414] This difference can be explained by the

previously mentioned great technical challenges in the processing of Li-oxide thin-film ceramics due to the high volatility of Li and complex interconnected reactions between the different deposition parameters, often leading to off-stoichiometric films.[415] As a result, a practical configuration of LiPON necessitates an electrolyte that is not thicker than $\sim 1~\mu m$ (with an area of 1 cm^2), leading to a cell resistance in the range of tens to hundreds of Ω. Consequentially, a thin-film solid electrolyte

This journal is © The Royal Society of Chemistry 2025

Chem. Soc. Rev., 2025, **54**, 8925–9007 | **8959**

with a thickness of 0.5–1 µm and an ionic conductivity on the order of $\sim 10^{-4}$–10^{-5} S cm^{-1} should potentially enable wider adoption and integration of thin-film solid electrolytes in micro-battery applications. Lowering the electrolyte resistance by improving the ionic conductivity and optimizing the thickness and contact area using 3D architectures may lead to a reduction of the overall cell resistance.[416] Moreover, by shortening the ion-migration path and undamming the bottleneck of charge transfer at the electrolyte–electrode interfaces, faster charge and discharge rates may be achieved (currently limited to 2C in commercial LiPON-based thin-film batteries,[417] although rates up to 5C have been reported).[27,418] Practically speaking, the use of thin-film processing techniques opens the door for further reduction of the electrolyte thickness, which in turn can be translated into further increases in the gravimetric and volumetric energy densities and power densities of the batteries.

4.1.1. Critical processing parameters of solid electrolytes prepared *via* physical vapor deposition. Several critical issues can deteriorate the material properties, and consequently the electrochemical performance, of Li-based thin-film ceramics, including poor microstructure control, mainly determined by the deposition method and processing steps;[414,419,420] possible interfacial reactions with the substrate or adjacent layers;[419] the film density and crystallinity, including parameters such as the amorphous-to-crystalline fraction;[342,421] the grain size and orientation;[422] and secondary phases or local structural deformation and Li depletion at grain boundaries.[423,424] Although some of these pressing factors are intrinsic to the material selected, in most cases, by controlling standard parameters, such as the temperature, gas type and pressure, and energy of the ejected particles, some of the aforementioned issues can be alleviated. Therefore, an in-depth understanding of solid-state electrolyte thin-film processing is required to improve the electrochemical properties towards phase-stability engineering.

The steps to achieve solid-electrolyte thin films synthesized using PVD methodologies start with the preparation of the ceramic targets, followed by a deposition step under the desired conditions, usually without the need for a post-annealing step. Overall, for both PLD and sputtering, the following main set of fundamental parameters can be controlled (Fig. 7c–h):[394] (i) ceramic target composition, (ii) substrate temperature, (iii) deposition rate, (iv) ambient pressure in the chamber, (v) energy of the deposited particles, and (vi) post-annealing steps (if required). Another important parameter is the substrate supporting the thin-film electrolyte, which can be either a functional layer (*i.e.*, cathode layer) or other type of substrate (Si, stainless steel). Given that the most important concern in the processing of Li-based thin-film electrolytes is the fine control of the lithium concentration for both techniques, the optimization steps should target mitigation of Li loss during deposition and film crystallization. Li loss occurs mainly for two reasons: non-stoichiometric transfer from the ceramic target to the substrate or re-sputtering from the film once deposited, especially at high temperatures. However, it is important to note that the processing parameters cannot be

optimized independently of one another. We aim to illustrate here the complex interdependency of the aforementioned parameters and the consequences on the film crystallinity and morphology and the effects on the electrochemical performance.

(i) Ceramic target(s) composition: PVD techniques transfer a material from a ceramic pellet to a thin-film form through the rapid ejection of particulates *via* the production of a plume or plasma with a specific stoichiometry similar to that of the ceramic pellet. One common strategy in large-scale ceramic processing to tackle Li loss is to add 5–15 mol% of extra lithium during the processing of the ceramic chemistry (Fig. 7c). Often these amounts are sufficient to accommodate for the Li loss during sintering and enable the synthesis of dense pellets and stabilized phases (see discussion in Section 2.3). Notably, further overlithiation beyond >15 mol% leads pellet microstructures to crumble and fall apart in most Li solid-state conductor oxide electrolytes. An illustrative case of the direct overlithiation of the pellet and subsequent deposition can be found for LLTO. A 10–20 mol% Li excess in the target (that was not incorporated into the perovskite structure but rather enriched the grain boundaries, leading to a relative density over 90%) enhanced the conductivity of the films by a factor of 10,[415] and adequate parameter optimization led to an improvement of the ionic conductivity of epitaxial films up to 6.7×10^{-4} S cm^{-1}.[425] This improvement in conductivity is closely linked to the increased local Li content at grain boundaries, which lowers the activation energy for Li-ion hopping across the grain boundaries and enhances total ionic conductivity. However, other reports systematically show that increasing the Li concentration in the target led to a mixed phase of LLTO and Li$_2$TiO$_3$ in the target (no density reported) and, despite this extra Li, resulted in decreased secondary TiO$_2$ phases in the films (their porous morphology upon processing with the target with the highest Li concentrations precluded any electrical characterization).[426] Despite this, an optimal Li concentration in the target followed by an adequate optimization protocol can lead to dense epitaxial films with higher ionic conductivity in LLTO.[425] In other materials, such as LLZO, this particular strategy by itself does not seem to be effective enough to stabilize the cubic phase.[162] A viable strategy to compensate Li loss during deposition is to introduce a Li-rich secondary target, either *via* co-deposition (*e.g.*, RF sputtering, Fig. 7c) or by sequential multilayer deposition (*e.g.*, PLD, Fig. 7d). For instance, adding extra secondary targets such as Li$_2$O for sputtering[420,427] or Li$_3$N for PLD[414] has been successfully employed to control the Li content in LLZO films and ensure the formation of the target fast-conducting cubic LLZO phase. The latter resulted in the highest ionic conductivities obtained thus far for LLZO films of $\sim 10^{-5}$ S cm^{-1} after a post-annealing step at high O$_2$ partial pressures.[414,420] Similar to bulk-type synthesis, these studies also employed the addition of dopants as a strategy to reduce the crystallization temperature and increase the film density. This strategy has been demonstrated through the use of aluminum (Al), either by doping the PLD target[414] or by co-sputtering from an Al target,[420] and Ga, by

8960 | *Chem. Soc. Rev.*, 2025, **54**, 8925–9007

This journal is © The Royal Society of Chemistry 2025

sputtering an extra layer of Ga_2O_3.[427] Dopants such as Al^{3+} or Ga^{3+} typically occupy Li^+ sites and reduce the temperature required for cubic phase formation while improving microstructural uniformity, which in turn enhances ionic conductivity. However, it is important to precisely control the amount of extra Li and dopants present, as a high Li concentration or inhomogeneous Li distribution can lead to high porosity and secondary phases at grain boundaries[420] or cubic polymorphism[428] or modify the near-order local environments in amorphous films,[429,430] which are overall detrimental to the ionic conductivity.
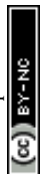
(ii) Substrate temperature: the substrate temperature, which affects the mobility of atoms deposited on the substrate and the probability for nucleation and growth, can largely determine the phase (amorphous or crystalline) of the deposited film and its chemical and electrochemical properties (Fig. 7e).[394] LiPON, mainly deposited through sputtering, provides an excellent example, where the amorphous nature of the thin film keeps the processing temperature (typically, room temperature) and manufacturing costs relatively low. Moreover, dense and grain-boundary-free films have been shown to be advantageous for Li-oxide films by introducing isotropic properties and obviating grain-boundary resistance, alleviating Li-dendrite propagation upon cycling,[431] and improving the electrochemical stability window and stability against Li metal,[432] ionic conductivity, and critical current density.[220] PVD-deposited LATP films, which have not been as thoroughly investigated as perovskite- and garnet-based electrolytes, exhibit an ionic conductivity of 2.46×10^{-5} S cm^{-1} and a low activation energy of 0.25 eV for pure amorphous films deposited by sputtering at 300 °C in a combined atmosphere of 1 Pa Ar and O_2.[433] Polycrystalline LATP fabricated by PLD at 700 °C and 80 mTorr O_2 exhibited an ionic conductivity of 10^{-6} S cm^{-1} and a high activation energy of 0.53 eV, and annealing of these films at 800 °C for 5 h in air resulted in conductivities as high as 10^{-4} S cm^{-1} and a low activation energy of 0.37 eV due to the formation of an amorphous intergranular Li- and P-rich phase.[405] Nonetheless, for sputtered or PLD-deposited LLZO, amorphous films exhibited a wide range of relatively low ionic conductivities of $\sim 10^{-8}$–10^{-6} S cm^{-1}. However, it remains unclear whether the network former–to–building block structure in PLD films has been sufficiently defined, as follow-up studies on amorphous LLZO synthesized via wet-chemical routes suggest unresolved structural details.[307–309] Numerous attempts to increase the room-temperature ionic conductivity by film crystallization,[434,435] where the substrate temperature was increased above 500 °C,[342] often led to delithiated pyrochlore phases, hindering the potential higher conductivity of the LLZO crystalline phases. In some cases, as for LLTO, the phase formation depends not only on the substrate temperature but also on the gas pressure.[415] Interestingly, it has been shown that amorphous LLTO films can be deposited up to 700 °C by PLD but only up to ~ 400–500 °C by sputtering.[406] We speculate that the different kinetic energies of the species ablated from the target during PLD compared with those for sputtering translates into a different near-order structure, thereby affecting the amorphous-to-crystalline temperature window, although more studies are needed for confirmation.

(iii) Deposition rate: the deposition rate is largely determined by the amount of material ablated from the target, i.e., the kinetics of the plasma in sputtering and the laser energy in PLD (Fig. 7f), and is typically on the order of ~ 1–10 nm min^{-1}, far behind that of state-of-the-art coating technologies such as tape casting and slot-die coating (1–100 m^2 min^{-1}). Because the energy source in PLD is pulsed, there is an extra parameter to tune the relationship between the kinetics of the impinging particles and the thermodynamics of the adatoms deposited at the substrate. This effect is more relevant at high temperatures, where both energies are comparable. At low temperatures, however, the surface diffusion is hindered and therefore the kinetic energies of the particle play a major role. For instance, proper optimization of the frequency at high temperatures (> 1000 °C) leads to single-phase LLTO films that otherwise include secondary phases.[425]

(iv) Gas type and pressure: in general, the gas pressure in the chamber has a double purpose (Fig. 7g). The first purpose is to provide reactive species that can be incorporated into the film, such as an O_2 atmosphere for oxides to compensate for oxygen loss during film deposition and a N_2 atmosphere in nitrides (e.g., LiPON). In the latter, the incorporation of N_2 in the structure from 0 at% to 6 at% is crucial for improving the ionic conductivity of the film by a factor of up to 45.[156,159] Interestingly, amorphous LLTO films, mainly deposited at room temperature by PLD, exhibit conductivities as high as 8.8×10^{-4} S cm^{-1}.[429] However, these films suffer from high electronic conductivity and require higher O_2 pressures (0.1–0.2 Torr) and deposition temperatures of ~ 300–400 °C to reduce the presence of oxygen vacancies and, thus, the electronic conductivity of the films.[423,424,436] Further increasing the deposition temperature leads to the onset of crystallization and reduces the ionic conductivity.[437] While at room temperature, this lithiation degree has been shown to strongly depend on the O_2 pressure,[426] the effect is less pronounced at the higher temperatures needed to achieve epitaxial grain-boundary-free films, and therefore, the lithiation control is more challenging.[409,438] The second purpose of the gas is to reduce the kinetic energy of the evaporated species. At high deposition pressures, the ejected species suffer a decrease in their kinetic energy and are scattered towards larger angles. For Li ions, which are even lighter than oxygen and volatile, the high pressure reduces the probability of reaching the substrate, leading to an overall Li non-stoichiometry. This Li deficiency can induce the formation of secondary phases and lower the ionic conductivity. At the same time, higher pressures can also help prevent Li loss in the deposited substrate. This delicate balance can be overcome by splitting the deposition step, performed in the PLD chamber at low temperatures ($T <$ 300 °C), and the crystallization step (if required), performed ex situ in a furnace under higher O_2 partial pressure.[414,420]

(v) Energy of the incoming particle flux: another way of controlling the kinetic energy is through the applied power on the plasma (W cm^{-2}), in the sputtering case, or the laser

This journal is © The Royal Society of Chemistry 2025

Chem. Soc. Rev., 2025, 54, 8925–9007 | 8961

fluence (J cm^{-2}), for PLD (Fig. 7g). A perfect example of the intricate relationships among these parameters is found for LLTO, where lowering the background pressure and increasing the laser fluence led to a decrease in the temperature required to achieve epitaxial films.[409] However, too low a pressure (or too high) can lead to undesired ion-blocking secondary phases such as TiO$_2$ and Li$_2$Ti$_2$O$_7$ in the case of LLTO, lowering the grain boundary conductivity and thus the total ionic conductivity.[415] Another strategy to mitigate the effect of high-energy particles reaching the substrate and causing re-sputtering of species (Li loss, especially at high temperature, but also oxygen defects) is the use of off-axis geometries, limiting the number of precipitates that can cause short-circuiting or make further device integration difficult.[420,439]

(vi) Post-annealing step: usually, PVD techniques use the advantage of the high kinetic energy of the ejected particles to stabilize out-of-equilibrium phases, thereby avoiding extra processing stages. However, the use of a post-annealing step is recommended when a thermodynamic equilibrium driving force is desired to induce or stabilize a phase transition or if high O$_2$ partial pressure is needed to minimize Li loss at higher temperatures (Fig. 7h).[414,420] For example, LLZO films deposited under the same conditions at room temperature and *ex situ* crystallized at pressures as low as 1 mbar mainly consisted of a delithiated La$_2$Zr$_2$O$_7$ phase, whereas a higher pressure of 200 mbar led to the evolution of cubic LLZO.[420] The improved crystallization at elevated oxygen pressures is attributed to suppression of Li volatilization and the stabilization of the high-conductivity cubic phase. For LATP, a post-annealing step at 800 °C for 5 h led to the formation of an intergranular Li- and P-rich phase and conductivities as high as 10^{-4} S cm^{-1} with a low activation energy of 0.37 eV.[405] A post-annealing step is also useful to decompose, diffuse, and densify Li-rich layers (Li$_2$O, Li$_3$N) into the solid-electrolyte host at pressures high enough to avoid Li losses.[414,420] Similarly to UHS processes in bulk systems, there are fast crystallization techniques, such as rapid thermal processing (RTP)[440,441] and flash lamp annealing (FLA),[442] that can be used to induce the fast crystallization of PVD-deposited solid electrolytes. These techniques are mainly based on a highly energetic light source, and, despite being widely applied in other fields, their application in SSBs remains essentially unexplored.[440–443]

Additional considerations must be kept in mind in the thin-film solid-state electrolyte processing chain: most of the available thin-film deposition equipment is not directly connected to an inert atmosphere that prevents the exposure of the films to ambience. In addition, the characterization of the films also adds exposure time that will affect the film stoichiometry and morphology.[414,420,444] Ambient exposure is also an issue for other techniques, such as pellet processing; however, the larger surface-to-volume ratio in thin films results in a stronger effect on the formation of LiOH and Li$_2$CO$_3$ at the surface of the films. This results in proton exchange with the lattice, negatively affecting the interfacial resistance and overall stability of the film.[415,420] Although this phenomenon has been largely shown to occur preferentially at the surface of bulk-type LLZO pellets, the larger surface-to-volume ratio and reduced thickness of the layers make it a more critical issue in the thin-film form. Although more dedicated equipment minimizing air exposure between deposition and characterization stages is essential, other strategies, such as the aforementioned dopant inclusion, can help to mitigate this effect. For example, doping LLZO films with Al results in a more stable lattice parameter with extended exposure time than for the undoped film, as further corroborated by measuring the Li content in the film.[420]

Overall, the processing of thin-film solid-state electrolytes is challenging because of the very complex interconnection between the different deposition parameters. At this stage, further investigations are needed to correlate the role of dopants, the processing conditions, and the film microstructure and performance at the atomic level by employing the most recent advancements in electron microscopy (especially cryo TEM)[445–447] and atom probe tomography.[448,449] Research efforts in the last few years combining the aforementioned strategies are paving the way towards a better understanding of the deposition conditions and overall improvement of thin-film solid-state electrolyte quality, as summarized in Table S3 (ESI†). The analysis of the literature body presented shows that most studies have investigated the effect of different deposition parameters to achieve dense, homogeneous films and their effects on the ionic and electronic conductivities of the films. For example, it has been shown that, despite the wide distributions of conductivities obtained for LATP, LLZO, and LLTO electrolyte thin films across different PVD methodologies and research groups, amorphous LLTO (conductivity of $\sim$10^{-4} S cm^{-1}) stands out over its polycrystalline counterpart (reflecting more general issues with grain-boundary conduction) and exhibits conductivities similar to that of epitaxial LLTO,[425] whereas LLZO and LATP polycrystalline thin films[405,414,420] exhibit higher ionic conductivities ($\sim$10^{-4}–10^{-5} S cm^{-1} and 10^{-4} S cm^{-1}, respectively) than the amorphous phases reported so far ($\sim$10^{-8}–10^{-7} S cm^{-1} and $\sim$10^{-5} S cm^{-1}, respectively).[342,405,433,434,450,451] These comparisons emphasize the significance of the microstructure: grain boundaries can either assist or impede ion transport depending on their chemistry and continuity, while the amorphous structure avoids grain boundaries but may suffer from lower overall Li ion transport. The research community should focus on the lack of material development and characterization at the atomic level while moving forward to device integration. In particular, amorphous solid electrolytes beyond LiPON exhibit consistently higher conductivities and appear to be promising for the next breakthrough in all-solid-state batteries. Polycrystalline films (or even epitaxial films, although less attractive for the industry) require further understanding of the microstructure and the role of grain boundaries, and solutions are needed at the processing level to overcome the current limitations.

4.2. Chemical vapor deposition of thin-film solid electrolytes

Chemical vapor deposition (CVD) technologies have often been applied for thin-film deposition not only on planar substrates

8962 | *Chem. Soc. Rev.*, 2025, **54**, 8925–9007

This journal is © The Royal Society of Chemistry 2025

but also on complex 3D structures. Their biggest advantage over wet-chemical and PVD processes is the capability to deliver uniform, conformal, pure, and dense thin-film structures, which should, in principle, be highly beneficial for achieving high-performance Li-oxide solid-electrolyte thin films. Among their other advantages, some CVD techniques (*e.g.* atomic layer deposition) usually do not require the high deposition temperature needed for PVD techniques, thereby making CVD favorable for simultaneously depositing multilayers with different thermal stress, *e.g.*, cathode, solid-electrolyte, and anode layers within solid-state thin film battery structures. Further advantages include a moderate deposition rate (1–100 nm min^{-1}) and moderate vacuum deposition conditions. However, the expensive vacuum supplies and equipment and the high cost and toxic ultra-pure precursors make CVD a high-cost solution for large-scale thin-film manufacturing. Moreover, although 5″ wafer-scale high-quality CVD of graphene with thin-film size has been reported,[452] wafer-scale ($>1 \times 1$ cm^2) Li-oxide solid-electrolyte thin films have not been reported to date.

Several CVD methods have been used for Li-oxide solid-electrolyte thin-film deposition, including metal organic chemical vapor deposition (MOCVD),[453] CO2-laser assisted CVD,[454,455] plasma-enhanced MOCVD,[456] thermal atomic layer deposition (ALD),[457] and plasma-assisted ALD.[458] In a typical CVD process, as shown in Fig. 8a, the ultra-pure gaseous precursors, reacting gas (*e.g.*, O_2 or O_3 for oxide growth, NH_3 for nitride growth, N_2 for LiPON growth), and non-reactive carrier gas (*e.g.*, N_2 for nitride growth and Ar for oxide growth) are separately supplied and pre-mixed in a mixing chamber called the precursor delivery system. The precursors then flow simultaneously into the reaction chamber under vacuum conditions, pass over the surface of the heated substrate where they adsorb on the surface, diffuse across it, and then undergo chemical reactions or pyrolysis; subsequently, gaseous by-products are removed from the reaction chamber. The reaction activation energy can be thermal energy (generated through high-temperature or radiant heating), photon energy (generated by a high-power laser), or plasma energy (inert gas plasma produced by electrical energy). CVD methods require an ultra-high base vacuum in the reaction chamber before the gas-phase reaction to ensure the deposition of high-purity thin films. The precursors and related delivery systems also play a determining role in the film quality and performance. The precursors are versatile and can be either solid, liquid, or gaseous but must all be vaporized for the gaseous reaction process, unlike using ceramic targets for RF sputtering[155] and PLD.[414,435] For deposition of Li-oxide solid-electrolyte thin films, ultra-pure metal organic compounds are usually used as the metal-element source because of the low melting point and high volatility (to avoid high-temperature heating of the delivery pipelines) with the required thermal stability. In the precursor mixing chamber, the different vapor pressures or mole ratio of different precursors must also be optimized to obtain the correct composition and stoichiometry, particularly for multi-element compounds. Inducing laser flash evaporation in a delivery

system not only allows for rapid heating of the solid precursors by absorption of infrared laser radiation but can also achieve the stoichiometric growth of multi-element compounds over the entire growth period. Thus, CO_2-laser-assisted CVD combined with laser technology to evaporate solid precursors is used to differentiate the general CVD processes. After that, the deposition pressure (or vacuum of the reaction chamber) and temperature together control the reaction kinetics for thin-film deposition. The deposition pressure for CVD-processed thin films is maintained *via* the precursor gases, reacting gas, and carrier gas, ranging from hundreds to thousands of Pascals, which is more moderate than that for high-vacuum PVD; the deposition temperature is usually several 100 °C and generally below 900 °C, which is typically lower than that of solid-state reaction processes. Furthermore, introducing the plasma technique to activate the reaction by transferring the energy of the plasma to the precursors and then inducing free-radical formation can lead to a lower deposition temperature *via* the radical reaction mechanism, compared with the thermal driving reaction *via* thermal CVD. It is possible to lower the deposition temperature to room temperature when combined with plasma and high-vacuum techniques (for example, the room-temperature deposition of ZnO thin films by high-vacuum plasma-assisted CVD[459]). However, to date, there have been no reports that Li-oxide solid-electrolyte thin films can be deposited at or near room temperature, likely because of the precursor condensation in the reaction chamber at room temperature.

ALD is a sub-set of CVD; however, the tremendous difference is that ALD involves a sequence of surface self-limiting reactions to grow uniform and conformal thin films at low temperature sequentially layer-by-layer through separately delivering gaseous precursors. (In contrast, CVD is a continuous process with linear growth with all the gaseous precursors mixing together and reacting). In a typical ALD process shown in Fig. 8b, each precursor is individually introduced into the reaction chamber with a carrier gas, one at a time (which is called pulse time), and all the precursor gas pulses are separated by carrier gas purge (which is called purge time) to remove any residual gases and by-products before the next sub-cycle. Overall, ALD is a self-terminating process, depositing one atomic layer at a time, depending on a sufficient dose of reactants rather than the controlled flux of reactants in CVD resulting in a continuous process with linear growth. ALD is a very well-established technique for simple binary systems (*i.e.*, TiO_2). However, fundamental knowledge is still needed to understand the complex deposition processes for multi-element compounds (*e.g.*, the quaternary systems LLZO and LLTO), including optimization of each single process and alternating different layers, *e.g.*, Li_2O, La_2O_3, ZrO, and Al_2O_3 layers for Al-LLZO.[460] Briefly, for amorphous thin films (such as LiPON), ALD usually occurs at low temperatures (typically below 300 °C, Table S4, ESI†), where high uniformity and conformity are achieved. These features make it favorable to deposit a thin interfacial layer between the electrode and the electrolyte to improve the stability and performance.[461–463] The

This journal is © The Royal Society of Chemistry 2025

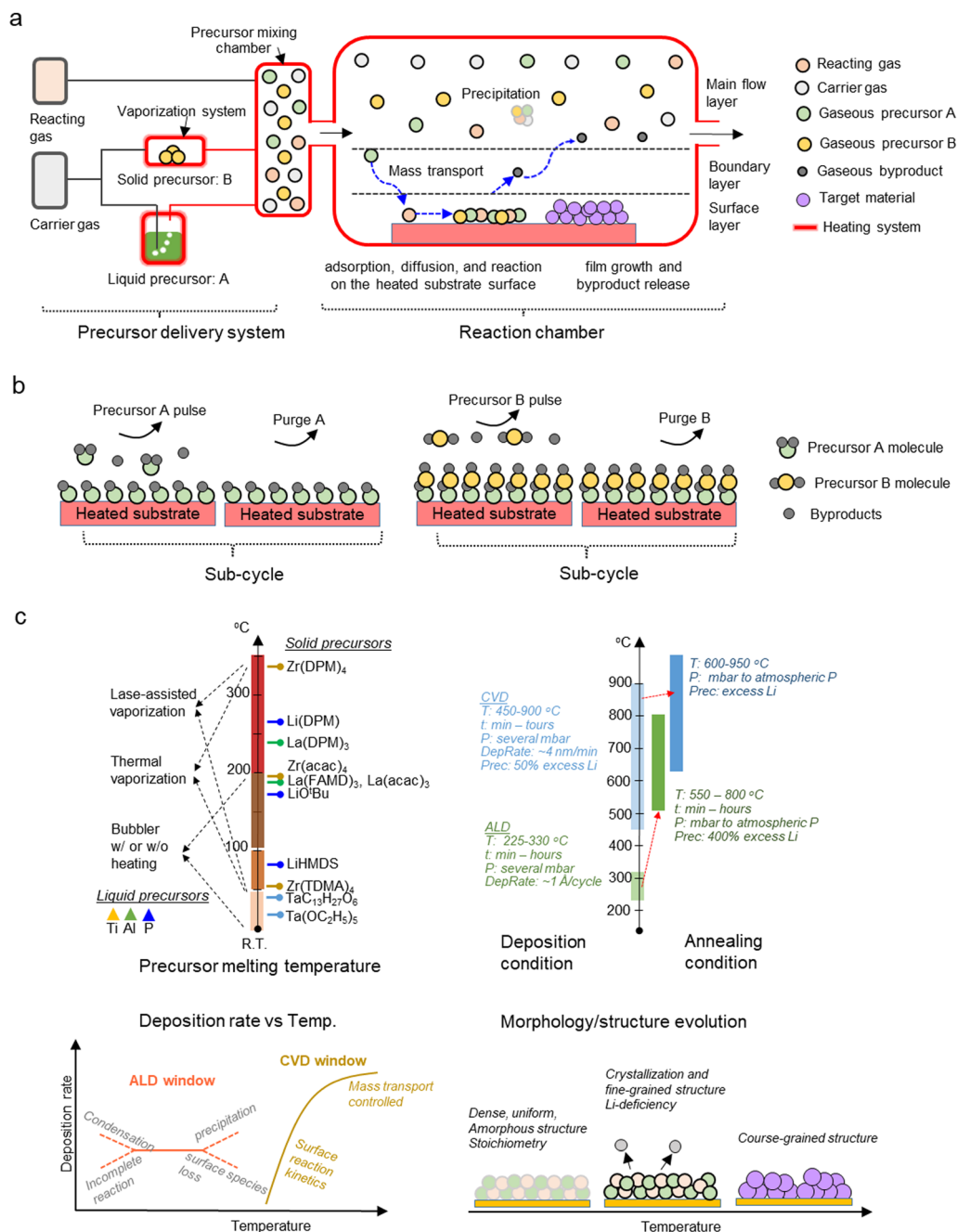*Chem. Soc. Rev.*, 2025, **54**, 8925–9007 | **8963**

Fig. 8 Chemical vapor deposition (CVD) techniques for solid–state electrolyte processing: (a) typical CVD steps from precursors to the target film; (b) typical steps during atomic layer deposition (ALD); and (c) critical processing parameters of solid electrolytes prepared *via* CVD and ALD techniques.

lower deposition temperature can also be beneficial when depositing on flexible substrates for flexible thin-film batteries. To obtain the desired crystallinity in Li-oxide-based solid electrolytes such as LLTO and LLZO, a high-temperature post-annealing step is needed but might lead to some issues such as Li loss, structure/morphology evolution from a dense and amorphous structure to a coarse-grained and crystalline structure, and unwanted reactions between the thin films and substrates. The details are discussed in the parameters section.

To date, solid-electrolyte thin films such as garnet LLZO,[453,454] $Li_5La_3Ta_2O_{12}$ (LLTaO),[455] perovskite LLTO,[457] LiPON,[74,272–275,456] and Li nitride[463] have been deposited *via* CVD or ALD methods. The deposition conditions and film properties are indicated in Table S4 (ESI†). Most of these films were deposited at low temperature in the range of 225–330 °C by ALD and at moderate temperature in the range of 450–700 °C by CVD (Fig. 8c); exhibit dense, uniform, pinhole-free, and even conformal morphology; possess an amorphous or crystalline structure; and exhibit ionic conductivities of 10^{-8}–10^{-5} S cm^{-1}

8964 | *Chem. Soc. Rev.*, 2025, **54**, 8925–9007

This journal is © The Royal Society of Chemistry 2025

(Table S4, ESI†). For LLZO and LLTO, a post-annealing step at 500–800 °C was required to achieve the crystalline phase. Some of these solid-electrolyte thin films have been processed in planar or 3D thin-film batteries, e.g., a solid-state battery fabricated with a $Li_4Ti_5O_{12}$ cathode, a 70-nm-thick ALD LiPON solid electrolyte, and a metallic lithium anode.[465] Among the Li-oxide solid-electrolyte thin films prepared using CVD/ALD, the highest ionic conductivity of 3.8×10^{-5} S cm^{-1} was achieved for cubic $Li_5La_3Ta_2O_{12}$ films via CO_2-laser-assisted CVD at 700 °C, which is only approximately 3.5-times lower than the highest reported value for the bulk sample.[455] The higher Li-ion conductivity can be attributed to the high quality (high density and purity, crystallinity, chemical composition) of the films, as the ionic conductivity not only depends on compositional factors but also on the microstructure. Furthermore, a moderate deposition rate of $\sim$4 nm min^{-1} and a low deposition rate of 0.7–1 Å per cycle (on the order of 0.1 nm min^{-1}) have been observed for CVD and ALD methods, respectively. However, the highest deposition rate of approximately 20 µm h^{-1} ($\sim$333 nm min^{-1}) was achieved for MOCVD-synthesized LLZO films,[453] which is one to two orders of magnitude greater than that of PLD-synthesized LLZO films.[450] However, the poor quality of those LLZO films, including a granular and non-continuous structure and faceted large-sized grains, makes it impossible to build current collectors to test the ionic conductivity. In addition, to ensure the desired crystallinity, one-step high-temperature deposition (e.g., a cubic LLTaO film prepared by CVD at 900 °C[453]) or a two-step low-temperature deposition followed by a post-annealing process (e.g., cubic LLTaO film prepared by CVD at 700 °C and post-annealed at 650 °C,[455] cubic LLZO-Al prepared by ALD at 225 °C and post-annealed at 550 °C[460]) is needed. In this case, Li loss is unavoidable at elevated temperature and often results in a delithiated phase or second phase, granular structure, and coarse-grained morphology; these properties can significantly reduce the ionic conductivity. Considering the Li content, stoichiometry, and crystallinity of CVD/ALD films, the most used strategy is the incorporation of excess Li precursors to compensate for Li loss, thus enabling easy adjustment of the stoichiometry of films with one-step high-temperature deposition. For example, stoichiometric tetragonal LLZO films were obtained by using 50 mol% excess of the Li precursor in a one-step CVD process at 700 °C,[454] which is much more than that for the solid-state process ($\sim$10–20 mol% excess of the Li precursor) for preparing solid-electrolyte pellets because the large surface-to-volume ratio in the thin films induces more Li loss. Another strategy involves a two-step method: low-temperature deposition followed by a post-annealing process. For example, the deposition temperature of amorphous $Li_{6.28}La_3Zr_2O_{12}Al_{0.24}$ (LLZO-Al) can be lowered to 225 °C via a thermal ALD process; then, cubic LLZO-Al is formed by annealing the ALD amorphous film at 555 °C with 400% excess Li precursor (the Li-ion conductivity was not reported).[457] It is worth noting that in the high-temperature-processed crystalline CVD/ALD films, special attention should be paid to the morphology and microstructure, as excess Li evaporation and long-

range diffusion may lead to segregation of the dense structure and disrupt the film continuity, resulting in island or coarse-grained porous morphology, thus degrading the film performance. Such morphological degradation introduces tortuous ion pathways, poor electrode–electrolyte contact, and non-uniform current distribution, ultimately increasing resistance and reducing cycling stability.

In summary, CVD and ALD methods are favorable for the deposition of amorphous to crystalline Li-oxide solid-electrolyte thin films with high uniformity, conformality, purity, and density at low temperature. Especially for conformal deposition onto 3D structures to manufacture 3D thin-film batteries, which is impossible using the aforementioned wet-chemical and PVD processes, ALD is the ultimate choice; it is also ideal for creating protective coatings at interfaces (e.g. towards the cathode or anode for various battery designs). To obtain the desired crystallinity, high-temperature deposition or a post-annealing process is still needed, which can introduce issues of Li loss, morphology/microstructure evolution, and interactions between the films and substrates and, in turn, affect the electrochemical performance of the film. Although some strategies have been developed to compensate for the Li loss, maintain the stoichiometry, and modify the film micro-structure, appropriate deposition conditions are still necessary to obtain high-quality, large-scale solid-electrolyte thin films. Currently, there have been no reports on wafer-scale Li-oxide solid-electrolyte thin films prepared by CVD/ALD; however, wafer-scale semiconducting films (e.g., MoS_2, WS_2) up to 8′ have been prepared by MOCVD and ALD.[466–468] Thus, a better understanding of the deposition conditions–structure–performance relationship is a prerequisite for achieving these goals.

4.2.1. Critical processing parameters of solid-electrolyte deposition via CVD. The CVD and ALD processing parameters, including the selected precursors, gas flow, pressure, substrate temperature, and deposition time, have a critical effect on the film properties (i.e., the composition, thickness, crystallinity, density, and morphology/microstructure) as well as on the film performance such as ionic conductivity. For instance, the deposition temperature and reacting gas partial pressure have been shown to affect the crystal structure of $Li_7La_3Zr_2O_{12}$ thin films when deposited by CO_2-laser-assisted CVD.[454] Considering the complexity of the interdependency of many parameters, different results are often obtained for the same precursor, making comparison of the results from different systems difficult. Thus, a detailed understanding of the CVD/ALD processing is critical to enable the rational design of Li-oxide solid-electrolyte films. The growth of functional films with desired properties requires a good understanding of the relationships between the processing parameters and the resultant structures of the deposited film. We introduce the main processing parameters (Fig. 8c), including (i) precursors, (ii) pressure or reacting gas partial pressure in the reaction chamber, (iii) deposition temperature, and (iv) post-annealing process, and discuss their effects on the film stoichiometry, crystallinity, and morphology and overall electrochemical performance. We

This journal is © The Royal Society of Chemistry 2025

Chem. Soc. Rev., 2025, **54**, 8925–9007 | **8965**

aim to provide links between the chemistry, deposition method, and characteristics of Li-oxide solid-electrolyte films.

(i) Precursors: precursors for Li-oxide solid-electrolyte thin films prepared by CVD and ALD are usually metal–organic compounds because of their low melting/boiling points, as shown in Table S4 (ESI†). To simply and directly deliver the precursors into the reaction chamber, gaseous metal–organic precursors at room temperature are always the first choice but are scarce. Thus, solid and liquid precursors are most often used with thermal vaporization or bubbling. As shown in the table, liquid or very-low-melting-point ($<100\ ^{\circ}C$) precursors are bubbled at room temperature or with low-temperature heating ($<100\ ^{\circ}C$), and the solid precursors with a melting point above $150\ ^{\circ}C$ are heated and melted at temperatures above $150\ ^{\circ}C$. This type of delivery system shows poor mass flow control over the long term; therefore, constant heating of the pipelines is required to prevent precursor condensation. Integration of other techniques such as plasma/laser techniques with the precursor delivery system can widen the precursor pool and promise a constant flow rate of precursors. For instance, the CO_2-laser technique was used to instantaneously vaporize the high-melting-point solid precursors (e.g., Li(TMHD), La(acac), Zr(acac)) by absorption of infrared laser radiation, which has a long wavelength and can be used for direct heating, melting, and vaporization of solids.[454,455] Additionally, the N_2 plasma technique was used to advance nitrogen incorporation into Li_3PO_4 by forming a double bond (P=N–P, doubly coordinated nitrogen) or three single bonds (P–N<, triply coordinated nitrogen) during the ALD process.[74,274]

To deposit multi-element compounds such as quaternary systems (e.g., LLTO, LLZO), the precursors must be carefully selected to avoid unwanted reactions, incompatible temperature requirements, and impurities. In general, each element in the target compound has its own precursor; however, it is also possible for two elements in the target compound to be derived from one precursor. For instance, the simultaneous incorporation of phosphorus and nitrogen in a LiPON film has been achieved using a single-source precursor of diethyl phosphoramidate (DEPA, $H_2NP(O)(OC_2H_5)_2$)), and the obtained $Li_{0.95}PO_{3.00}N_{0.60}$ film exhibited an ionic conductivity of $6.6 \times 10^{-7}\ S\ cm^{-1}$ ($25\ ^{\circ}C$) and an activation energy of $0.55\ eV$.[469] Using a single precursor (e.g., lithium hexamethyldisilazide (LiHMDS) containing Li and Si cations, diethyl phosphoramidate (DEPA) containing P and N elements) can simplify the overall ALD process but also create possible precursor redundancy during cycling.[24,469] Furthermore, incomplete decomposition of the precursors results in unwanted components appearing as impurities incorporated into the grown films, which can affect the film properties. For instance, carbon residues were induced in $Li_{0.32}La_{0.30}TiO_z$ ALD films due to the incomplete decomposition of the precursor, which were as little as 1.9 at% when using LiO^{t}Bu with less carbon in comparison with Li(thd) with more carbon.[457] As another example, a trimethylphosphate (TMP) precursor could not fully react with LiO^{t}Bu-terminated surface ligands, resulting in carbon residue in LiPON films.[458] The residues in the grown films have been characterized by XPS or time-of-flight elastic recoil detection analysis (TOF-ERDA); however, understanding of the effect of the residues on the film morphology, microstructure, and properties remains lacking. In addition, the precursor delivery order for ALD processes not only affects the film composition and purity but also the microstructure and morphology. For instance, the amorphous $Li_{0.32}La_{0.3}TiO_z$ film with the precursor delivery order of (TiCl$_4$ + H$_2$O)–(La(thd)$_3$ + O$_3$)–(LiO^{t}Bu + H$_2$O) exhibited improved surface smoothness and higher uniformity than the film with the delivery order of (TiCl$_4$ + H$_2$O)–(LiO^{t}Bu + H$_2$O)–(La(thd)$_3$ + O$_3$).[457] The effect of the precursor delivery order (or each precursor's reaction order) on the electrochemical performance of the film has not been discussed. Most importantly, because of the different reaction energy from different surface termination, some precursors may only be reactive to the specific surface termination. Even when using the same precursors, incorrect surface-terminated species will not initiate the next sub-cycle reaction. Thus, a thorough understanding of the effects of precursors, including the coordinating organic-functional groups, physical properties, and delivery order, on the morphology, composition, and electrochemical properties is still needed to pursue high-quality Li-oxide solid-electrolyte films.

(ii) Total pressure or reacting gas partial pressure in the reaction chamber: before delivery of the precursors, the reaction chamber is usually pumped down to a maximum pressure of $<1.33 \times 10^{-7}$ mbar to remove any potential contamination. The total pressure of a CVD chamber is stabilized with gaseous precursors, reacting gas, and non-reactive carrier gas and is maintained within a range of several to tens of mbar to keep all the precursors vaporized. A high total pressure will induce a low gas-flow velocity (inversely related to the pressure) and a thick boundary layer, which limit precursor diffusion into the substrate surface as well as by-product diffusion away from the surface; thus, the chemical-reaction kinetics is mass-transport controlled. At low pressure, the surface chemical reaction is the growth-rate determining step and the mass transport is far less critical than at high pressure. When lowering the total pressure at the expense of the partial pressure of the gaseous precursors, the surface chemical-reaction kinetics is proportional to the partial pressure of the gaseous precursors. This means that both nucleation rate and uniformity of initial film growth are directly impacted by precursor availability (mass transport) dynamics. Overall, the total pressure, reacting gas partial pressure, and partial pressure of the gaseous precursors all affect the chemical-reaction kinetics, surface nucleation, and subsequent film growth, thereby affecting the film stoichiometry, structure, and morphology.[453,454] For instance, lowering the total pressure from 20 to 5 mbar resulted in a microstructure change from a coarse-grained to a fine-grained structure of garnet-type $Li_5La_3Ta_2O_{12}$.[455] Reducing only the partial pressure of the gaseous precursor (Mo(CO)$_6$) from 1×10^{-3} to 5.6×10^{-5} mbar while keeping the total pressure constant induced a lower growth rate (from 1.3 to 0.15 nm min^{-1}) and higher conformality of MoS$_2$.[467] Reducing the partial pressure of the reacting oxygen gas from 40% to 8% induced the formation of a Li-poor

8966 | Chem. Soc. Rev., 2025, 54, 8925–9007

This journal is © The Royal Society of Chemistry 2025

phase with fluorite-type related structure in a polycrystalline tetragonal $Li_7La_3Zr_2O_{12}$ film.[454] Thus, reducing the total pressure by reducing the carrier gas flow is beneficial to maintain the growth rate and film properties of CVD-processed films. ALD is a self-limiting reaction; the surface saturated reaction will stop once the surface reactive sites are entirely depleted. Higher pressure induces a high conversion of surface sites, resulting in a shorter cycle time to complete the surface reaction and may thus lead to a high deposition rate, uniformity, and conformity. For instance, upon increasing the total pressure from 0.267 to 1.333 mbar, the deposition rate of ALD-processed Al_2O_3 thin films increased from 0.89 Å per cycle to 0.96 Å per cycle, and better uniformity and higher conformity were observed.[470] However, the effect of the total pressure on the deposition rate and film properties of solid electrolytes has hardly been investigated. The total pressure is usually set at several mbar to enable vaporization of all the precursors. For example, the reactor pressure of 3 mbar can be applied for vaporization of the solid precursors $La(thd)_3$, LiO^tBu, TMA, and $TiCl_4$ at 225 °C.[457] In summary, careful tuning of total and partial pressures allows for balancing precursor delivery, film uniformity, and microstructural evolution, especially in multi-component Li-oxide systems where precise stoichiometry is critical for ionic conductivity.

(iii) Deposition temperature: the deposition temperature has a crucial effect on the crystallinity, morphology, and Li content of Li-oxide solid-electrolyte thin films. As CVD methods rely on gas-phase chemical reaction, the decomposition temperature of the precursors and the activation energy of the surface chemical reaction determine the lowest deposition temperature, and the homogeneous bulk reaction resulting in the gas-phase precipitation determines the highest deposition temperature. In a general thermal CVD, at low deposition temperature and low pressure, the surface reaction kinetics is the limiting step because of the surplus of reactants at the surface; in contrast, at high deposition temperature and high pressure, mass transport with the diffusion of reactants through the boundary layer is the limiting step because of the lower gas velocity at higher pressure and faster gas-phase precipitation at higher temperature.[471] Metal–organic precursors for Li-oxide solid-electrolyte thin films are thermally stable, thus having the lowest deposition temperature as high as 450 °C, as shown in Table S4 (ESI†). Increasing the deposition temperature of CVD not only changes the crystallinity and morphology of the grown films but also introduces some problems such as Li loss, delithiated phases, and microstructure evolution.[455] For example, crystal-structure evolution of $Li_7La_3Zr_2O_{12}$ films by MOCVD was observed from a tetragonal structure (800 °C) to a cubic structure (950 °C) to a delithiated phase $La_2Zr_2O_7$ (1000 °C) with increasing deposition temperature.[453] In addition to crystal-structure changes, morphology changes of $Li_5La_3Ta_2O_{12}$ films were also observed from amorphous-like to fine- and coarse-grained to coarse-grained with particulates on top upon increasing the deposition temperature from 600 to 900 °C.[455] As mentioned above, using plasma to activate the chemical reaction can significantly lower the deposition temperature by opening up a new reaction pathway such as radical reaction. For instance, the deposition temperature of amorphous LiPON was lowered to 180 °C by introducing N_2–H_2–Ar plasma, and the obtained film exhibited comparable ionic conductivity ($\sim 10^{-6}$ S cm^{-1}) to other films deposited by MOCVD and RF sputtering.[456] To maintain the Li content and desired stoichiometry of Li-oxide solid-electrolyte films deposited at high temperature, tuning the mole ratio of Li precursors (usually, a lithium excess of 50% mol) is preferred in CVD.[455,472] Proper optimization of CVD parameters such as the reacting pressure, deposition temperature, and molar ratio of precursors can be used to precisely control the film stoichiometry, structure, and morphology.

For ALD, the deposition temperature must be not only high enough to activate the surface chemical reaction and avoid condensation of the gaseous precursors on the substrate surface but also low enough to avoid self-decomposition of the precursors during adsorption processes. The deposition temperature affects the crystallinity of the grown films, as they undergo phase transition from an amorphous to a crystalline phase or from a crystalline phase to another crystalline phase at characteristic temperatures.[473] Usually, a temperature of 225–300 °C is selected as the deposition temperature for ALD Li-oxide solid-electrolyte thin films (as shown in Table S4, ESI†), which falls within the ALD window for all the sub-cycles of different precursors. Thus, an amorphous structure is always obtained because of the low deposition temperature. For instance, amorphous Li_3N,[474] Li-tantalite ($Li_{5.1}TaO_z$),[475] Li_2O–Al_2O_3 ($Li_{1.6}Al_{1.0}O_z$),[476] Li_3PO_4,[477,478] Li silicate ($Li_{2.0}SiO_{2.9}$),[479] LLZO,[460] LLTO,[457] and LiPON[465] films were successfully deposited at 225–300 °C. In terms of multi-element compounds, stoichiometry of the grown films can be obtained by simply tuning each ALD sub-cycle. Therefore, ALD is favorable for the deposition of amorphous films with the desired stoichiometry of multi-element compounds. For example, stoichiometric $Li_{6.28}La_3Zr_2O_{12}Al_{0.24}$ with an amorphous structure was deposited on a Si substrate at 225 °C by tuning and combining each sub-cycle of Li_2O, La_2O_3, ZrO_2, and Al_2O_3. The obtained films with high density and uniformity and low carbon residue content (<1 at%) exhibited an ionic conductivity of 1.2×10^{-6} S cm^{-1} at 100 °C with an activation energy of 0.63 eV.[460] If a crystalline phase is desired, a high-temperature post-annealing step should be performed. In this case, the morphology and Li content will be changed because of Li loss at elevated temperature. The Li content in the grown films can be increased by simply increasing the dose of the Li precursor to compensate for the Li loss during post-annealing processes. The effect of post-annealing will be discussed in the following section. Furthermore, the effects of the deposition temperature on the deposition rate, impurity content, and film orientation have been investigated for semiconducting materials, e.g., Al_2O_3,[480] but have barely been studied for Li-oxide solid electrolytes, potentially due to the relatively new application of Li-oxide solid electrolytes and the complexity of their multi-element composition. Regardless of the crystallinity, the

This journal is © The Royal Society of Chemistry 2025

Chem. Soc. Rev., 2025, 54, 8925–9007 | 8967

deposition temperature of ALD processes is much lower than that of PLD, wet-chemical, and solid-state processes.

(iv) Post-annealing: as mentioned above, ALD processes are typically performed below 300 °C, which results in amorphous films. To obtain a high ionically conductive crystalline phase (*e.g.*, cubic garnet LLZO and cubic perovskite LLTO), post-annealing at high temperature is generally performed. The post-annealing conditions will affect the composition and microstructure of Li-oxide solid-electrolyte films through Li evaporation, which will in turn affect the ionic/electronic conductivity. For instance, a stoichiometric structure of crystalline $Li_{0.33}La_{0.557}TiO_3$ was obtained after annealing the stoichiometric structure of amorphous $Li_{0.32}La_{0.30}TiO_z$ at 800 °C in O_2 for 3 h.[457] Simultaneously, a titanium-containing second phase was obtained in the annealed films due to the Li loss. To mitigate the Li loss and tune the composition of annealed films, excess Li content in the grown films is needed, which means excess Li precursors are required during deposition of the amorphous film. Notably, much more Li excess is needed in thin films than in bulk electrolytes (typically 10–20 mol%) because of the large ratio of surface to depth in thin films. For instance, an excess Li content of 400 mol% was needed to obtain the cubic phase of $Li_{6.28}La_3Zr_2O_{12}Al_{0.24}$ by annealing the grown films at 555 °C.[460] However, evaporation and long-range diffusion of excess Li during annealing can lead to the segregation of the dense film into a granular structure or even cracks, thus disrupting the film continuity and affecting the ionic conductivity. ALD offers the promise of low-temperature fabrication of amorphous thin films. Tuning the stoichiometry of crystalline structures with post-annealing at moderate temperature is possible; however, the microstructural evolution of the thin films during annealing remains a major issue.

In short, CVD and ALD are versatile techniques for depositing amorphous Li-oxide solid-electrolyte thin films under low temperature and moderate vacuum conditions. Moreover, the morphology and structure are well controlled, including the stoichiometry, density, conformality, and uniformity. However, there are several challenges regarding the crystallinity, microstructure, and ionic conductivity, especially for crystalline Li-oxide solid-electrolyte CVD/ALD films. The possibility of high conformal deposition positions CVD and ALD as promising thin-film coating processes for complex 3D substrates for 3D all-solid-state thin-film batteries. Further challenges include the inherent low deposition rate, which is on the order of 0.1 nm min^{-1} for ALD and tens of nm min^{-1} for CVD, and the expensive and toxic ultra-pure precursors with low operability, which inhibit the process scalability. Most importantly, Li loss and the resulting granular structure at elevated temperature are unavoidable. Two strategies have been used to resolve the Li loss issue: the use of an excess amount of Li precursors and lowering of the processing temperature through combination with plasma and laser techniques. In addition to the developed strategies, new methods need to be investigated to resolve the Li loss accompanied by structure evolution. To date, CVD/ALD methods are more popular for coating a thin protective layer on

the surface of electrode materials to resolve interfacial issues in all-solid-state batteries.[481–483]

5. Processing metrics for high-performance oxide-based solid electrolytes

Based on the detailed discussion and data for each individual fabrication method, namely solid-state processing (Section 2), wet-chemical solution processing (Section 3), and vapor deposition technologies (Section 4), we would now like to discuss the advantages and disadvantages of each processing method and present an overview of the major processing metrics relevant to obtaining high Li-ion conducting solid-state Li oxide electrolytes (LLZO, LLTO, LATP/LAGP, and LiPON). Previous reviews on Li oxide processing often examine individual methods in isolation, requiring readers to assess different processing metrics for each technique separately. This section aims to provide a comprehensive overview, offering a unified evaluation rubric to help select the most suitable techniques and relevant parameters for various material development objectives. Moreover, by addressing these parameters collectively, we emphasize their interdependence—some relationships are applicable broadly across all techniques, while others are unique to specific methods. This integrated approach provides a clearer understanding of how the factors interact, enabling readers to make more informed decisions when optimizing processing conditions for each technique. The following general processing metrics are considered: processing temperature, chemistry of the precursors, dopants and stoichiometry, and atmosphere and pressure to synthesize a Li-based oxide electrolyte ceramic.

5.1. Processing temperature

5.1.1. Processing temperature for powder calcination. Solid-state processing relies on the physical mixing of precursor powders and subsequent ionic diffusion activation at a high temperature across solid particles.[175] Here, the ionic carriers of the precursors should diffuse across their particle boundaries only through slow solid diffusion to form a new solid compound. Moreover, the precursors, mostly metal oxides, for solid-state synthesis require high decomposition temperatures up to 750 °C (Li_2CO_3 decomposition). Therefore, a high calcination temperature with a long holding time is essential to obtain the desired phase electrolyte powders *via* the solid-state route. Despite the high temperature requirements, the early development of Li oxide electrolytes has often relied on solid-state methods due to their relative simplicity. The calcination of LLZO typically starts at 750 °C with the tetragonal phase and generally requires a temperature of above 950 °C to stabilize the highly conductive cubic phase.[198–200] The calcination of LLTO occurs at temperatures over 800 °C to remove unfavorable secondary phases,[484,485] and that of LATP requires a temperature above 700 °C[183] to decompose the solid precursors and obtain pure phases. Although temperature requirements to

8968 | *Chem. Soc. Rev.*, 2025, **54**, 8925–9007

This journal is © The Royal Society of Chemistry 2025

produce phase-pure electrolytes have been suggested, there are still limited reports on the optimum calcination protocols for each electrolyte. For instance, the calcination temperatures for cubic LLZO vary widely from 900 to 1130 °C, and the duration also ranges from 3 to 12 h. In general, higher temperatures allow for shorter duration, while lower temperatures require longer dwell times, but not all studies consistently followed this trend. Additionally, some works used a single calcination, whereas others conducted multiple calcinations to prepare the same phase powders.[486] Solid-state methods allow an easy development of complex Li solid-oxide electrolytes and enable large volume scaling. However, the high temperature and long duration deteriorate the practicality in production; therefore, temperature optimization would be beneficial to boost the advantage of solid-state processing.

To decrease the processing temperature, alternative routes based on wet-chemical solution processing have been studied to synthesize the solid-electrolyte powders.[259,261,342] Wet-chemical solution processing methods such as sol–gel or Pechini methods enable the formation of ceramic powders from a solution of dissolved precursors. Because the lattice diffusion between precursors proceeds directly in the liquid/gel state, a lower calcination temperature is generally needed compared to that required for solid-state synthesis methods. In addition, common precursors used for sol–gel processing have lower decomposition temperatures (e.g., 550 °C for $LiNO_3$), promoting the calcination at lower temperature. For example, van den Broek et al. applied the sol–gel route to calcine and synthesize cubic LLZO at 650 °C, which is 100–300 °C lower than that of the solid-state methods.[487] In addition, the phase homogeneity of LLZO powders can be improved with sol–gel processing (pure cubic phase at 950 °C), whereas the solid-state method produces a mixture of cubic and tetragonal powders at the same temperature.[488] In the case of sol–gel-based LLTO synthesis, the calcination temperature can be decreased down to 650 °C,[489] whereas the solid-state-based method requires a temperature of 800 °C or above to achieve the same phase.[490]

Overall, solid-state reactions are easy to develop and economical as they are based on inexpensive precursors but require high calcination temperature. Solution-based methods can produce high-purity and homogeneous powder products; however, the reactions are relatively complex to control.[491] Due to their distinctive advantages and drawbacks, there exists no standardized powder processing route for Li solid-electrolyte materials. In addition, there are other promising powder synthesis methods (e.g., fluid-solid reactions, drying/precipitation, hydrothermal synthesis, emulsion process, microwave synthesis, and plasma synthesis) that have the potential to overcome the drawbacks and further reduce the calcination temperature. These methods, however, have not yet been systematically studied for Li solid-electrolyte powder syntheses.

5.1.2. Processing temperature to sinter dense pellets. Different powder properties also affect the final sintering temperature and time for Li-oxide electrolytes. A cold-pressed LLZO green body from solid-state reactions requires sintering at 1050–1250 °C for 2–36 h to achieve a high enough relative density ($>95\%$).[202,492,493] LLTO should reach up to 1350 °C during the sintering process and realize a high-density and pure-tetragonal-phase pervoskite.[166,250] Sintering temperatures not only play a key role in forming a favorable dense microstructure but also influence Li^+ conductivity by altering the mesoscopic ordering for ion percolation pathways.[249] At sufficiently high temperatures, grain growth leads to improved neck formation between particles, enhancing Li^+ transport across grain boundaries by reducing the boundary area. NASICON-type LATP requires a temperature of higher than 1100 °C to obtain high-ionic-conducting (7×10^{-4} S cm^{-1}) electrolyte pellets based on high-density and interconnected Li^+ conduction pathways.[494,495] However, increasing the sintering temperature and duration will in general trigger Li evaporation while processing the solid electrolytes.[251] For example, the pyrochlore lanthanum zirconate ($La_2Zr_2O_7$) phase can form due to excessive Li loss of LLZO. Any temperature above 1250 °C results in a significant Li loss and forms the Li-deficient pyrochlore secondary phase, decreasing the total conductivity of LLZO pellets.[252,496] Similarly, Li loss of LLTO can trigger the formation of Li-deficient TiO_2 or $La_2Ti_2O_7$ secondary phases above 1350 °C.[213] Therefore, there exist optimal sintering temperature ranges to balance faster ionic diffusion to achieve higher density and lower Li evaporation to obtain phase-pure electrolyte materials.[497]

To further decrease the sintering temperature, time, and costs, solution-based powder production could also be beneficial based on the smaller electrolyte particle sizes. The solution-based method is easy to control the size and morphology of the powder particles. The mechanism of powder synthesis via the sol–gel process includes two key steps: hydrolysis and polycondensation.[498] By controlling the condensation rates, the electrolyte particle size can be tuned from few tens of nanometers to a few microns.[499] Smaller particles generally have a greater driving force for densification and grain growth due to the larger surface area of the green body.[202] Therefore, lower sintering temperatures (900–1100 °C) and shorter heat-treatment times (<12 h) are required for Li oxide powders from solution-based routes,[248,281,500] compared to those synthesized via a solid-state reaction process.[496] For example, with a sol–gel method to produce the electrolyte powders, cubic-phase highly dense (96.4%) LLZO pellets can be obtained by sintering at 1040 °C for 3 h. This processing temperature is approximately 10–210 °C lower than that for ceramics from solid-state reactions.[501] Similarly, a LLZO pellet was successfully sintered within a greatly reduced time of 20 min at the same temperature (1130 °C), enabled by a 100-nm-sized nano-powder synthesized through the sol–gel processing route.[201]

Some advanced sintering techniques can also be employed to decrease the sintering temperature further by promoting the mass transport with external bias (e.g., pressure, electric field). For instance, hot-pressing studies with LLZO pellets were successful in reducing the sintering temperature down to 1000 °C,[502] which is 50–250 °C lower than that for cold-pressed samples. SPS techniques using LATP electrolytes also used lower temperature (1000 °C) than conventional sintering

This journal is © The Royal Society of Chemistry 2025

Chem. Soc. Rev., 2025, 54, 8925–9007 | 8969

(1080 °C).[215,268] As lowering the sintering temperature was shown to be important for maintaining the pure phase of the electrolytes, systematic optimization studies combining these techniques would be encouraging to further reduce the pellet sintering temperature.

5.1.3. Processing temperature for film production. Wet-chemical solution processing enables the fabrication of thin-to-thick films from solution using techniques such as dip coating, spin coating, sequential deposition synthesis, or spray pyrolysis. In this case, the classic calcination and sintering steps are not needed, as a direct transfer from the liquid precursor to a solidified body *via* condensation, nucleation, and growth can be achieved. As a consequence, these synthesis routes do not require a high processing temperature and long processing time compared to the powder-based tape processing methods (*e.g.*, tape casting). The solution-based techniques commonly require solidification below 400 °C and phase stabilization at temperatures between 500 and 1000 °C for most Li-electrolyte films with a duration of a few minutes to hours.[503] For instance, an amorphous LLTO film was prepared using a spin-coating method at 500 °C after 350 °C of solidification,[282] and crystalline phases of LLTO were formed between 700 and 900 °C.[348,355] Similarly, sequential deposition synthesis of a LLZO thick film can be performed at 280–350 °C for film deposition, 350–550 °C for salt decomposition, and 550–800 °C for phase stabilization, resulting in a crystalline cubic LLZO film above 750 °C.[308,316] Both temperatures are much lower than those for producing LLZO (>1050 °C) and LLTO (∼1350 °C) electrolyte pellets. Even though the trials to decrease the processing temperature were effective, the techniques are still not free from the common problems of Li loss once exposed to high temperature.[342] Such Li volatility can lead to stoichiometric imbalance, which degrades ionic transport by forming electrically insulating or low-conductivity secondary phases. For instance, increasing the annealing temperature of the LLZO film above 850 °C causes severe Li loss and yields the La$_2$Zr$_2$O$_7$ phase.[318] Zhu and co-workers developed time–temperature–transformation (TTT) diagrams specific to the chemistry and precursors used, providing guidance on phase stability and optimal time–temperature conditions during post-annealing (Fig. 9).[309] Further investigations aimed at providing a comprehensive understanding of how temperature affects stoichiometry and phase formation are recommended to optimize the processing conditions for wet-chemically derived films.

In thin-film processing using vapor deposition techniques, the electrolytes are more sensitive to the substrate temperature because of the short diffusion length of the film; it is easy to reach the phase but there is a risk of losing stoichiometry.[504] Generally, processing temperatures for vapor deposition techniques are lower than those for solid-state processing or wet-chemical solution-processing methods. This is because the high energy of the depositing particles enables the stabilization of out-of-equilibrium phases, supporting the synthesis of the desired phase at low temperature. A crystalline LLZO film can be obtained when the deposition temperature is above 500 °C using PLD.[342] The deposition temperature can be further
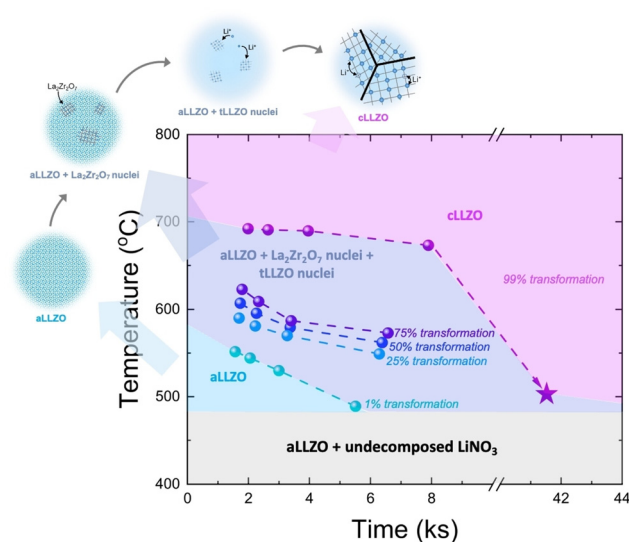
Fig. 9 Time–temperature–transformation (TTT) diagram for LLZO transforming from the amorphous to crystalline cubic phase. The 1%, 25%, 50%, 75%, and 99% iso-phase lines are presented. Specifically, the 1%, 50% and 99% iso-phase lines are indicated as the beginning, mid-point, and final stage of the phase transformation from amorphous to crystalline cLLZO. The annealing condition of 500 °C, 10 h is highlighted. Schematic illustrations of the phase compositions at each crystallization stage are provided. cLLZO, cubic phase LLZO; tLLZO, tetragonal LLZO; aLLZO, amorphous LLZO. Reproduced with permission ref. 309.

decreased down to 300 °C if an additional annealing step is introduced.[414] A crystalline perovskite LLTO thin film can be obtained at approximately 750–850 °C using the same technique.[415] A polycrystalline LATP film was prepared at 700 °C, and the ionic conductivity was further enhanced with annealing at 800 °C.[505] The same benefit of processing-temperature reduction is also achievable with CVD/ALD processes, generally requiring low processing temperatures ranging from 200 to 950 °C: 225–330 °C for ALD and 450–950 °C for CVD for LLZO and LLTO, respectively.[453,506] For example, the crystallization and phase transformation of a LLZO film were observed at 800 °C for the tetragonal phase and 950 °C for the cubic phase.[453] A LLTO thin film was deposited at 600–900 °C[455] using MOCVD methods. Despite the benefit of temperature reduction, the ionic conductivity of the Li-oxide thin films is reduced by several orders of magnitude compared with that of the bulk electrolytes. For example, a 170-nm LLTO film grown by PLD exhibited a room-temperature ionic conductivity of 2.2×10^{-6} S cm^{-1}, which is two to three orders of magnitude lower than that of pellet-based electrolytes (∼10^{-3} S cm^{-1}).[415] There are no clear explanations for the conductivity drop; however, one possible reason could be the high Li volatility causing the formation of non-stoichiometric films during deposition.[414] The phase of film electrolytes can also be easily changed because of the active Li loss at high deposition temperature. In LLZO thin-film electrolytes prepared using PLD, a Li-deficient La$_2$Zr$_2$O$_7$ phase emerged above the substrate temperature of 750 °C. In addition, a LLZO film prepared using MOCVD exhibited severe Li loss above 1000 °C. Both these

8970 | *Chem. Soc. Rev.*, 2025, **54**, 8925–9007

This journal is © The Royal Society of Chemistry 2025

phenomena lead to a decrease in the total ionic conductivity.[453] Therefore, the film processing temperature should be carefully optimized to achieve balance between the phase evolution and lithiation degree of the samples.

5.2. Chemistry of precursors and solvents

Precursors directly affect the phases and microstructures of the solid electrolytes. However, the unique thermodynamic nature such as the solubility, chemical reactivity, and decomposition energy of each precursor has not been investigated in a thorough manner. For solid-state processing, base cations are supplied as ionic compounds with oxide (O^{2-}), hydroxide (OH^-), carbonate (CO_3^{2-}), nitrate (NO_3^-), acetate ($COOH^-$), or other anion groups.[507–509] Generally, the precursors first undergo thermal decomposition reactions from their original anionic composition into oxides before formulating electrolyte grains. Hood and co-workers have roughly estimated the reaction thermodynamics of different precursors based on their decomposition temperature.[318] In a more systematic manner, the reaction Gibbs free energy of thermal decomposition should be considered to evaluate the conversion reactions of the precursors into the oxides. For example, LiOH has the lowest Gibbs free energy change at 1000 °C among LiOH, Li_2CO_3, and $LiNO_3$ and is favorable to employ to promote the conversion reaction to highly conducting LLZO.[507] The choice of precursors also critically influences the quality of wet-chemical powder processing. The crucial part in wet-chemical solution processing is to prepare a well-mixed high-quality solution; therefore, metal carboxylates ($COOR^-$) and alkoxides (OR^-) are often used as the anion pair because of their high solubility in organic solvents. Because of the strict limitation in terms of solubility to select precursors, there is a relatively limited number of salt precursors that can be employed for solution-based processing.

Similarly, selecting appropriate solution components for wet-chemically produced film electrolytes is crucial. Many salt anions used in these routes, including nitrates (NO_3^-), nitrides (N_3^-), carboxylates ($COOR^-$), alkoxides(OR^-), or even halides (X^-), commonly require high decomposition temperatures,[318] often necessitating solvents with equally high thermal stability to ensure the complete conversion of reactants. Unfortunately, achieving these properties typically relies on organic solvents, which are often heavy, viscous, and sometimes hazardous.[318] Exploring alternative precursor chemistries with lower decomposition temperatures is critical to more efficiently drive the conversion from precursors to metal oxides. The choice of precursors critically influences the quality of wet-chemical powder processing, as well as the specific TTT diagrams governing phase formation and crystallization. These aspects yet remain a relatively underexplored area in ceramic science. In addition, the thermal-decomposition mechanism of precursors can also affect the final phase and ionic conductivity of electrolytes. For instance, the ionic conductivity of the LLTO film prepared from all-alkoxide precursors was 1.78×10^{-5} S cm^{-1}, whereas that prepared from an acetate and alkoxide mixture was only 1.86×10^{-7} S cm^{-1}. The difference

was attributed to the different thermal decomposition mechanisms of alkoxides and acetates; the acetates decomposed with a two-step reaction via carbonate formation and formed a phase with low ion conduction.[285] Lastly, controlling the drying process is also both essential and challenging to prevent cracks during film formation. Regardless of the film production techniques employed, effectively managing shrinkage and volume changes as different metal salts convert into multicomponent metal oxides is vital for achieving the desired microstructure. As such, both the solubility and decomposition properties should be simultaneously considered, resulting in greater complexity to discover and evaluate electrolyte precursors.

Precursor selection for vapor deposition methods, particularly CVD processes, is also important to induce facile chemical flow in the deposition system. Generally, precursors with low melting and vaporization temperatures are favored, including organic (O^tBu^-,[506] dpm^-,[453] thd^{-506}) or halide (Cl^{-506}) anion groups. Liquid or gas phase precursors would also be recommended; however, the candidates are too scarce, considering the heavy nature of metal elements. To deposit phase-pure multi-element Li electrolyte compounds, the precursor chemistry and delivery order are vital. Recalling from the previous section, some anion groups (thd^-) leave more carbon residue than others (O^tBu^-) due to the incomplete decomposition during deposition, which affects the microstructure and chemistry of the film products.[458,506] In addition, the delivery order of the precursors can change the electrochemical properties of CVD films, as the step-wise decomposition of precursors produces different surface chemistries on the film, affecting the reaction thermodynamics and later film homogeneity.[506] Thus, obtaining a deeper understanding of the effect of the organic-functional anion groups and their decomposition reactions is important to ensure favorable microstructure and chemistry of CVD-grown films.

Solvent combination with precursor chemistry can play significant roles in some processing routes utilizing solvents. In solid-state reaction routes, organic solvents like ethanol and 2-propanol are commonly used during powder processing to reduce interparticle friction and ensure uniform mixing of solid precursors. Aqueous solvents cannot be widely applied because they react with solid oxides and cause ion exchange of Li^+/H^+, creating a thermally unstable electrolyte and ionically insulating by-product (lithium hydroxide: LiOH).[508–511] Recently, the selection of solvents with surfactants was proven to be effective to change the distribution of the electrolyte particle size, later affecting the densification process. Wood and colleagues showed that the combination of acetonitrile with surfactants can reduce the LLZO powder particle size down to 220 nm and result in a high pellet density at a lower sintering temperature of 1000 °C.[191] As such, solvent selection can affect the chemistry and microstructure of the final electrolyte products in solid-state processing. In addition, solvents affect the uniformity of materials for solution-based processing such as sol–gel synthesis, electrospinning, or sequential deposition synthesis.[512] The solvent serves substantial roles in terms of the (i) dissolution of precursors, (ii) diffusion of the reactants, (iii) nucleation of crystallites, and (iv) crystal growth from the

This journal is © The Royal Society of Chemistry 2025

Chem. Soc. Rev., 2025, 54, 8925–9007 | 8971

nuclei in metal oxide processing.[513,514] In general, solvents such as 1-propanol, 2-methoxyethanol, and citric/nitric/acetic acids are used based on the high solubility of the precursors. The evaporation temperature of the solvents has been shown to be important to maintain a uniformly mixed solution during thermal decomposition steps. However, our understanding of the effect of the solvent on the chemistry of the final Li-oxide electrolytes remains limited compared to this knowledge for electrode processing. To facilitate the market entry of the oxide electrolytes produced through solution-based wet chemical methods, extensive exploration of precursor screening and test synthesis is required. This includes investigating the use of environmentally friendly organic materials and reagents in the manufacturing process.

5.3. Li stoichiometry and dopants

Controlling the stoichiometric ratio of precursors is the knob to manipulate the phase and microstructure of solid electrolytes.[515] One of the well-known approaches to compensate for Li loss during sintering is to provide an excess stoichiometric amount of Li precursors for synthesizing the solid electrolytes. Li evaporation initiates from interfacial regions such as grain boundaries and expands into the surface of grains;[516] excessive Li precursor usage can prevent secondary phase formation and decrease the resistance of grains and grain boundaries.[250,251] However, when the excess Li is more than enough, some of the Li will gather in the grain-boundary region. For example, in LLZO, excessive Li can cause a decrease in the relative density and ionic conduction.[247] Many studies indicate that sintering ~1-mm-thick pellets from both solid-state processing and solution-based powder synthesis requires 10–20 wt% excess Li,[244,245] where additional Li can be introduced either during the precursor stage or added separately prior to the sintering process. For different processing techniques, further addition of excess Li is sometimes required to compensate for Li evaporation. Wet-chemical-derived films are more readily adapted to the Li level in the final film state, as adjustments can be easily made at the precursor mixture stage. For example, flame spray pyrolysis requires 50 wt% excess Li to balance the Li stoichiometric amount,[236] and 30 mol% excess Li was selected for nebulized spray pyrolysis studies, all added in the precursor solutions.[245] Moreover, if the film does not require additional annealing and the deposition temperature remains low, optimal stoichiometry can also be achieved without the need for excess Li.[318] Thin films prepared from vapor deposition techniques are more vulnerable to Li loss due to their short diffusion length to the grain boundaries. The targets for PVD generally contain 10–20 wt% excess Li.[415] An additional Li source can be incorporated using multilayer deposition techniques, which introduce a Li-rich interlayer (such as Li_3N or Li_2O) between the electrolyte layers. These layers decompose during the post-annealing process, further compensating for the Li evaporation.[414] Lastly, a similar approach is needed for CVD, with the addition of 50 wt% to 400 wt% excess Li precursors for film fabrication.[472,506]

Dopants are frequently added in solid electrolytes to stabilize a favorable microstructure or phase of the solid electrolytes and improve the ionic conductivity.[321,517–519] Dopants, incorporated by substituting for a base element of the electrolytes, can be supplied as precursors alongside the base precursors when processing solid-oxide electrolytes. The ionic conductivity of an electrolyte is proportional to the charge-carrier concentration and the mobility of the charged ion. Heterogeneous atom doping can affect the Li-ion conductivity either by manipulating the lattice structure or by creating additional Li ionic carriers. This effect is not confined to a single processing method; rather, it is applicable across all range of techniques. For example, doping of large cations (Sr and Ba) at La sites of LLTO increases the ionic conductivity because large-sized dopant ions expand the lattice, enlarging the bottleneck size for Li^+ migration and promoting the Li-ion mobility.[243,520] Similarly, the Al^{3+} cation in the LATP system can be replaced by trivalent cations (Ga, Sc, Y) of larger ionic radii, which increases the lattice parameter and Li-ion conductivity.[521,522] In LLZO electrolytes, divalent doping (Sr and Ba) at the La site increases the Li-ion mobility in a similar way by enlarging the crystal lattice.[523,524] In contrast, hetero-valent dopants contribute to the enhanced conductivity typically by increasing ionic carrier concentration. Trivalent dopants (Al, Ga) substitute for Li^+ and provide Li vacancies in the LLZO crystal lattice to ensure charge neutrality of the crystal lattice.[525,526] Doping of supervalent cations (Ta, Nb, Sb, Bi) at the Zr site increases Li vacancy population as well as affecting disorderliness in the framework,[518,519,527] both of which positively affect ionic conductivity from carrier (Li vacancy) enrichment. Dopants can not only enhance the ionic conductivity but also reduce the processing temperature. The ease of Li^+ diffusion in doped electrolyte materials can stabilize the pure phase and aid in the formation of dense electrolytes under lower processing temperature. Fast-ion-conducting Al-doped LLZO phases ($\sim 3 \times 10^{-4}$ S cm^{-1}) were achieved with a final sintering temperature of <1100 °C.[528] Ga was also found to stabilize a similar cubic phase at a low synthesis temperature of approximately 1000 °C and a sintering temperature of approximately 1100 °C.[525] Despite their proven benefits in enhancing ionic conductivity and lowering processing temperatures, the fundamental understanding of dopant behavior in these materials remains limited. For example, although Al and Ga migrate to the same lattice site of LLZO, their segregation tendencies to the grain boundary are significantly different, forming different microstructures.[529] Different segregation trends of dopants can influence the defect distribution and electrochemical properties of Li oxide electrolytes. For instance, Chu and colleagues demonstrated that the incorporation of Ta in LLZO promotes its segregation and alters the space charge distribution at the grain boundaries. This segregation effect subsequently modifies the local ionic conductivity and electronic conductivity of the grain boundaries, affecting the short-circuit endurance of the electrolytes.[209] In addition, some dopants can cause different grain-growth behavior (i.e., abnormal grain growth in Ga-doped LLZO[207]). Other dopants can cause electrochemical

8972 | Chem. Soc. Rev., 2025, 54, 8925–9007

This journal is © The Royal Society of Chemistry 2025

decomposition that instigates a detrimental failure of the electrolyte (i.e., Nb reduction in Nb-doped LLZO).[530] Therefore, careful approaches in dopant selection are required based on thorough investigations of multiple factors other than the ionic conductivity or processing temperature.
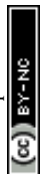
5.4. Atmosphere and pressure

In general, Li oxide electrolytes produced by solid-state synthesis, wet-chemical processing, and vapor deposition techniques should be either fully fabricated or treated at the final stage in a moisture-free atmosphere. This is necessary due to the high reactivity of Li^+ with the H^+ from moisture, which can significantly reduce the Li-ion conductivity.[531] For example, the exchanged protons distort the Li–O octahedral bond of LLZO and reduce the occupancy of Li on the octahedral sites of the bulk phase, which leads to fewer mobile Li ions in the crystal lattices. After ion exchange, the amorphous phase such as $LiAlO_2$ can be formed from Li^+ extracted from the lattice and dissolved into the grain boundaries, which acts as an ion-blocking layer at the boundaries. As such, H^+ not only reacts with bulk grains but also with grain boundaries, lowering the total (bulk + grain-boundary) conductivities of the garnets.[534] Moreover, lithium hydroxide (LiOH), a side product obtained by switching the cation, also accelerates the formation of highly insulating lithium carbonate (Li_2CO_3) and passivates both surfaces and grain boundaries of Li-oxide electrolytes, deteriorating Li^+ transport at various interfaces.[533] To minimize impurities from ambient air exposure, it is essential to limit contact with water and CO_2 during processing. A post-treatment step is also recommended to remove any impurities that may have formed. Pure oxygen (O_2) sintering can meaningfully enhance both the density and ionic conductivity of Li oxide solid electrolytes. Flowing O_2 is known to facilitate sintering by filling the pores with pure O_2. The subsequent disappearance of pores is facilitated by the good solubility and diffusivity of oxygen through atomic O migration via lattice diffusion or vacancy transport.[210] An overall ionic conductivity of LLZO as high as 7.4×10^{-4} S cm^{-1} was achieved, higher than that of materials sintered in other atmospheres.[210] In addition, sintering under flowing pure oxygen prevents Li^+/H^+ exchange in Li-oxide electrolytes and reduces secondary phase formation.[534] Then, the grain-boundary conductivity of LLTO electrolytes increased upon replacing the atmosphere of air (1.5×10^{-5} S cm^{-1}) with oxygen (7.4×10^{-5} S cm^{-1}).[502] Except for reports on oxygen sintering, there have been few phenomenological trends observed with other gas atmospheres. Employing an argon (Ar) atmosphere during sintering was shown to be effective for achieving the phase evolution of Li-oxide electrolytes. For Ta-doped LLZO, a pure cubic phase was obtained when sintering at 1150 °C for 10 h under an Ar atmosphere (2.21×10^{-5} S cm^{-1}), whereas some tetragonal phase was formed for the air-sintered samples (2.08×10^{-5} S cm^{-1}).[535] Moreover, Paolella and co-workers were able to control the thermal decomposition equilibrium of the precursors by controlling the atmosphere carbon dioxide (CO_2). By increasing the CO_2 partial pressure, the Li_2CO_3 decomposition rate could be slowed down and the

Li loss was reduced during the high-temperature calcination.[251] Lastly, previous studies on oxygen-ion and proton-conducting oxides have indicated that processing atmospheres can also impact defect distribution and ionic conductivity in electrolytes. Li oxides are expected to behave similarly, given their favorable exchange of lattice oxygens with the surrounding environment.[536] LLZO pellets produced via solid-state methods exhibited a clear dependency of their bulk electrical properties on oxygen partial pressure. The authors showed that Li^+ ion conductivity increased as oxygen partial pressure decreased, due to the dynamic variation in Li vacancy concentration within the lattice. This effect was observed not only at high temperatures (>300 °C), but also at lower temperatures (~ 90 °C), underscoring the critical role of the oxygen environment in influencing charge carrier equilibrium.[219] Similarly, LLTO pellets exhibited improved ionic conductivity at the grain boundaries when sintered under low oxygen pressure atmospheres.[217] This enhancement was possible due to the increased electron population from oxygen vacancy formation, which had a selective effect on the grain boundary conduction. Despite some early demonstrations, there are a limited number of studies examining the effects of processing atmosphere beyond its influence on the bulk microstructure and phase; therefore, further exploration in this area is highly recommended.

Next, the processing pressure is another important parameter that should be carefully tuned depending on the processing methods. Employing enough pressure during the sintering process helps to reduce the amount of Li evaporation and stabilizes the stoichiometric structures.[259,261] Electrolytes can be sintered using special processing techniques such as hot pressing, field-assisted sintering technique (FAST), or SPS, which commonly leverage the benefit of applied pressure. For instance, hot-pressing sintering simultaneously applies heat and pressure. A cubic-phase LLZO pellet can be fabricated by hot pressing the pellet green body at 40 MPa for 1 h under flowing Ar, requiring relatively low temperature and short duration.[246] However, applying high pressure during the material fabrication often results in remaining residual stress, which affects the properties of oxide electrolytes. Ta-doped LLZO, prepared by SPS (with a pressure of 25 MPa), exhibited a residual stress of more than 200 MPa, causing the distortion of X-ray diffraction profiles.[537] The effect of residual stress on material properties has not been clearly understood in Li-oxide electrolytes. However, residual stress has been reported to influence the mechanical hardness[538] and local ionic conductivity,[537,539] of electrolytes, and thus should be carefully considered.

In vapor deposition techniques, especially for CVD, all the precursors are in the gaseous phase and should be ultra-pure. The atmosphere for CVD is composed of the precursor gases, reacting gases (O_2 or O_3 for oxides, N_2 for LiPON growth), and carrier gases (Ar for oxide and LiPON growth), which are premixed in a chamber and flow simultaneously in the deposition chamber. For example, LiPON ALD films can be deposited at 250 °C using a gas mixture of lithium tert-butoxide (LiO^{t}Bu),

This journal is © The Royal Society of Chemistry 2025

Chem. Soc. Rev., 2025, 54, 8925–9007 | 8973

TMP, N_2 reacting gas, and Ar carrier gas, resulting in a 20 to 80 nm film with an ionic conductivity of 1.45×10^{-7} S cm^{-1}.[458] Moreover, thin-film electrolytes are more susceptible to changes in their stoichiometry and morphology under ambient air due to the high surface to bulk ratio of the film; therefore, the processing pressure should be carefully controlled as compared to pellet-type electrolytes. In vapor deposition techniques such as sputtering or PLD, too low a deposition pressure increases the mean free path of evaporated materials and promotes mobility of surface adatoms, resulting in a rough surface of film electrolytes.[540] In contrast, too high a background pressure decreases the kinetic energy of ejected species, resulting in the loss of a larger amount of the target by scattering to wider angles.[541] Wang and colleagues demonstrated that the surface morphology of a LiMn$_{1.5}$Ni$_{0.5}$O$_4$ (LMNO) electrode film changed upon increasing the background pressure from 0.2 to 0.3 mbar, and the roughness noticeably increased over 0.3 mbar.[542] Similarly, the optimum pressure still needs to be studied for electrolyte films, considering the laser fluence, target–substrate distance, and deposition temperature. In addition to the total pressure, the oxygen partial pressure during PVD or CVD processing can affect the microstructure of oxide electrolytes.[436,472] In LLTO thin films, Ti^{4+} cations reduce to Ti^{3+}, creating oxygen vacancies at low oxygen pressure and increasing the local electronic conductivity.[436] For example, the electronic conductivity of LLTO thin-film is relatively high at 4.0×10^{-5} S cm^{-1} under a lower atmospheric pressure of 5×10^{-6} Torr, while high pressure (0.1 Torr) can decrease the electronic conductivity to 3.5×10^{-11} S cm^{-1}.[423,429] Also in CVD, a tetragonal-phase LLZO film was successfully deposited at 700 °C with an O_2 partial pressure of 40% among the total gas flow, whereas if the oxygen partial pressure was reduced to 8%, a Li-poor fluorite-type phase was instead formed.[472] Therefore, adequate pressure should be used to obtain pure and dense thin-film electrolytes.[453,543]

To aid in the comparison of different synthesis strategies for oxide Li-ion conductors, Table S5 (ESI†) summarizes representative examples of Li-oxide electrolyte thin- and thick-films fabricated via various wet-chemical and vapor-phase techniques. The table highlights key processing metrics—precursor chemistry, dopants and stoichiometry, synthesis temperature, atmosphere and pressure, and film thickness—alongside the measured room-temperature ionic conductivities. This comparative overview is intended to help identify promising material-processing combinations that balance performance with practical considerations such as process scalability, thermal budget, and structural integrity. For benchmarking, data for bulk ceramics processed via tape casting have also been included to reflect practically relevant configurations for multi-layer battery devices, while pellet-based metrics are excluded due to their excessive thickness and limited applicability.

While lab-scale demonstrations of solid-state electrolytes have shown great promise, large-scale manufacturing of all-solid-state batteries (ASSBs) remains a significant challenge due to differences in processing routes and infrastructure compatibility with existing Li-ion battery production lines (Table S6, ESI†).

Following this processing-focused discussion of solid electrolytes, we now turn to full-cell configurations, where the compatibility between solid-state electrolytes and electrode materials—along with composite cathode preparation and interfacial design—plays a critical role in overall battery performance.

6. Processing Li-metal-oxide-based solid-state batteries

Oxide solid electrolytes with thicknesses ranging from 1000 μm down to 0.1 μm can be processed using one of the following major methods: solid-state processing (1 μm–1 mm; Section 2), wet-chemical deposition (0.1–10 μm, Section 3), or vacuum-based deposition (<1 μm, Section 4) (Fig. 4). Such processing methods, which differ in terms of thickness range, processing temperature, and scalability, have a direct effect on the full-cell design for the integration of the oxide electrolyte with the cathode and Li-metal anode. While it is preferable for the solid electrolyte to be as thin as possible (while still maintaining the desired properties and functionality) and the anode to be based on a high-capacity material, the cathode composite is the most voluminous component of the battery cell, and the design of the cathode, including the use of a small amount of liquid/gel electrolyte as the catholyte or anolyte, largely determines the battery performance (areal capacity, gravimetric and volumetric energy). It is thus critical to evaluate the optimal cathode composite material, composition, size/distribution, and thickness to allow for high loading of the active material while maintaining sufficient ionic and electronic conductivity (low tortuosity) to ensure high capacity and charging rates. In a bulk-type SSB, typical components include a 100 μm-thick cathode, a 1–20-μm electrolyte, a 1–30-μm Li anode (formed after charging), and a 10 μm-thick current collector (Fig. 3).[544] In contrast, the total thickness of a thin-film battery unit cell is on the order of 1 μm, consisting of several-hundred-nanometer-thick electrodes, a few-hundred-nanometer-thick electrolyte, and a CC.

To date, benchmark SSB materials and architectures remain unclear, and the fabrication of Li-metal-oxide-based SSB designs entails several challenges related to the high-elastic-modulus Li oxides and the additional high-temperature processing necessary to improve the cathode/electrolyte contact area. First, mechanical degradation due to cracking must be considered, which is affected by interfacial stresses due to the mismatch in the thermal expansion coefficient between the electrolyte and cathode components during heat treatment.[545,546] Second, there is the risk of interdiffusion and undesired interphase formation, e.g., the formation of La$_2$Zr$_2$O$_7$ and LaCoO$_2$ between the LLZO electrolyte and the LCO cathode, which significantly increase the interfacial resistance.[547,548] Third, electrochemical and mechanical interfacial degradation during cycling due to limited

8974 | Chem. Soc. Rev., 2025, **54**, 8925–9007

This journal is © The Royal Society of Chemistry 2025

electrochemical stability of electrolyte materials and/or volume expansion of electrode materials must be considered.[549,550] In addition, the challenges associated with using lithium metal as an anode material, including the formation and propagation of Li dendrites, will require further understanding of the fundamental mechanisms and innovative ideas to mitigate or manage short-circuit failure due to dendrite propagation.[551] Therefore, careful selection of battery materials, design, and processing routes for Li-metal-oxide-based SSBs is crucial for capacity utilization, rate performance, and lifetime. In this section, we discuss the general processing metrics for electrode/electrolyte interfaces during cell fabrication, and possible cell architectures, design-specific processing methods, challenges, and mitigating solutions are examined for both bulk-type batteries and thin-film batteries.

6.1. Bulk-type solid-state batteries

For bulk-type solid-state batteries, the cathode and/or cathode/electrolyte can be prepared *via* either wet or dry processing.[24] The first approach, which has the highest commercial maturity and is also used to produce cathode sheets for LIBs, is based on the mixing of the cathode active material (CAM) with a binder (*e.g.*, PVDF, PVB), a solvent (*e.g.*, NMP, IPA, ethanol), and potentially surfactants (to adjust for viscosity) and/or electronic conductive additives (*e.g.*, carbon). Nonetheless, the broad knowledge about cathode sheet production gained through the development of LIB production is not entirely compatible as no solid-electrolyte component was accounted for in the process. In SSBs, the solid electrolyte is also added to the slurry; however, the brittle nature of oxides necessitates the introduction of a high-temperature sintering step to secure maximum electrolyte–CAM phase contacts and achieve improved Li-ion transport, low grain boundary resistance and low overall porosity of the composite cathode. Nonetheless, the high-temperature processing step may lead to side reactions due to CAM decomposition and high interfacial resistance and may increase processing costs. Avoiding the sintering step by using low-melting-point sintering agents (*e.g.*, Li_3BO_3)[278,552] was suggested to reduce the sintering temperature from 1050 °C to 700–750 °C but had the consequences of decreased active material loading and high interfacial resistance.[553,554] The carbon decomposes or burns out at temperatures as low as 500 °C in oxygen-containing atmospheres, restricting the direct use of carbon-based conductive additives in standard oxide-SSB processing. The cathode composite may also serve as a mechanical support for the deposition of a dense and thin oxide solid electrolyte (<20-µm thickness) with one of the following anode architectures: Li-free, dense Li layer, or scaffold-type design to accommodate the volume changes associated with stripping/plating of Li metal during cell discharge/charge. A porous/dense/porous tri-layer scaffold-type design has also been proposed to accommodate the anode and cathode from two sides of the dense solid electrolyte but suffers from low cathode loading and thus low cathode areal capacities. An alternative processing route is dry processing (extrusion, dry calendaring, dry spraying, *etc.*), which obviates the need for the time- and space-consuming solvent drying associated with wet chemical processing. Such processes show promise for soft sulfide solid electrolytes[339,555,556] but may be challenging to develop for oxide-based composite cathodes unless used as a coating technique for the CAM.[557] The introduction of the oxide-based solid electrolyte to the cathode remains an unresolved processing challenge and is thus the major focus of this section.

6.1.1. Processing metrics of the electrolyte/cathode. The cathode composition for bulk-type batteries is typically a composite of an active material (*e.g.* $LiCoO_2$, LCO), an ion conductor (*e.g.* garnet $Li_7La_3Zr_2O_{12}$, LLZO), and an electronic conductor (if the electronic conductivity of the active material is insufficient).[40,85,558,559] In the ideal composite cathode, the two phases of cathode and electrolyte must be 3D connected with a high packing density, ensuring continuous conducting pathways for Li-ion and electron flow during the charging/discharging process.[560] The cathode performance is determined by the degree of charge and mass transport (*i.e.* mixed ionic and electronic conductivities) within the composite cathode.[561] Ions are transported through the electrolyte, and electron paths are usually provided by the partial electronic conductivity of the active cathode materials or/and a small fraction of conductive additives.

The selection of electronically conductive additives in bulk-type oxide-based solid-state batteries is a critical factor that directly influences processing strategies. While carbon-based additives such as carbon black are widely used in lithium-ion cathodes to ensure percolating electronic pathways, they are often incompatible with the high-temperature sintering (>700 °C) required for densifying oxide-based solid electrolytes and cathodes, and their interfaces. Carbon decomposes or combusts above 500 °C in oxidizing environments, leading to poor or little electrical connectivity in the final cathode. To address this, alternative strategies have been proposed. These include low-temperature sintering in inert or reducing atmospheres (*e.g.*, Ar or Ar/H_2), where carbon decomposition can be suppressed, allowing retention of electronic pathways. Another approach is the use of thermally stable oxide-based conductors such as indium tin oxide (ITO), which can be co-sintered with cathode and electrolyte materials. For example, a composite cathode consisting of NMC811, $LiBO_x$ glass, and ITO has been shown to retain conductivity after high-temperature treatment.[562] Alternatively, electronic conductors can be introduced post-sintering through infiltration methods.[563] More recently, a promising strategy has gained attention: redesigning the cathode composition to include materials with inherently high levels of mixed ionic and electronic conductivity (MIEC).[564–566] This eliminates the need for separate conductive additives, potentially enhancing interfacial stability and long-term performance. This concept parallels the transition from electronically conductive $La_{1-x}Sr_xMnO_{3\pm\delta}$ to MIEC $La_{1-x}Sr_xCo_{1-y}Fe_yO_{3\pm\delta}$ in solid oxide fuel cells and is being actively explored for all-solid-state battery cathodes.

If assuming that the Li/electrolyte interfacial impedance is not a limiting step for the overall cell resistance, then the

This journal is © The Royal Society of Chemistry 2025

Chem. Soc. Rev., 2025, **54**, 8925–9007 | **8975**

overall cathode impedance determines the polarization resistance or overpotential during charge and discharge. In general, the electrolyte/cathode interface has several key requirements to achieve good cathode performance. The first criterion is a mechanically, chemically, and electrochemically stable interface between the electrolyte and the cathode to achieve a rechargeable battery that delivers the expected specific capacity during initial and long cycling at given test parameters.[567,568] Such interfacial contact is typically made through the densification process, starting with casting (similar to deposition or coating) and lamination (similar to calendaring) and followed by sintering to physically connect the cathode/electrolyte. Conventionally, the oxide electrolyte requires a high temperature to densify interfacial bonding with other oxides, *i.e.*, the CAM, and thus, there are thermodynamic driving forces for chemical mixing at the interface, which can lead to undesired interphase formation. Therefore, the initial selection of the electrolyte and cathode material should be based on their good chemical compatibility while allowing interfacial densification. Another interfacial instability mechanism is the electrochemical decomposition of the catholyte (solid electrolyte in cathode composite) beyond its oxidation potential. LLZO, LLTO, and LATP/LAGP have theoretical oxidation potentials of 2.9, 3.7, and 4.2 V, respectively.[569] Beyond these potentials, the electrolytes and catholytes are subjected to oxidation into undesired interphases that are ionically and/or electronically insulating, which increases the cathode impedance and overpotential. Depending on the nature of the interphase, however, it can stabilize the interface. The areal specific resistance (ASR) can be used as a measure to characterize the interfacial stability related to the initial performance of SSBs.[28,558,559,570,571] The target ASR values from a cell comprising the cathode/electrolyte/anode is less than 40 Ω cm^2 to allow cycling at 1C with more than 90% energy efficiency.[572] Below, we specifically focus on the processing metrics that can affect the composition and microstructure of the cathode composite and cathode/electrolyte interfaces. We mainly exemplify the conventional oxide composite processing followed by sintering at high temperature to discuss the metrics, including the (i) chemistry and compatibility, (ii) temperature and time, and (iii) atmosphere.

(i) Chemistry and compatibility: the selection of the initial chemistry of the cathode components plays a decisive role in controlling the interdiffusion at electrolyte/cathode interfaces during processing, especially that involving elevated temperature. If other insulating compounds form at the interface, the as-fabricated cells will exhibit a high overpotential or ASR. As a result, the theoretically expected specific capacity (100% utilization) of the active materials cannot be achieved even at low current density (*e.g.* < 0.1 mA cm^{-2}) at room temperature. Such chemical incompatibility can be resolved *via* compositional tuning of the solid electrolyte, which can therefore improve the cell impedance and specific capacity. For example, Ohta *et al.* studied the effect of Sr (x = 0–1) in LLZO (Li$_{6.4}$Al$_{0.2}$)(La$_{3-x}$,Sr$_x$)(Zr$_{2-x}$,Nb$_x$)O$_{12}$ on the chemical compatibility with NMC111 (LiNi$_{1/3}$Mn$_{1/3}$Co$_{1/3}$O$_2$) and battery performance.[554] Above Sr substitutions of 0.1, the formation of La-containing

interphases such as LaNiO$_3$ and La$_2$(Ni$_{0.5}$Li$_{0.5}$)O$_4$ is prevented, resulting in an order-of-magnitude lowered ASR and a significant increase in cathode utilization compared to that of LLZO with Sr = 0. Likewise, a core–shell structure (Sr-rich, La-deficient shell in the above case) of a solid electrolyte can suppress undesired chemical reaction by substituting the stable cation in the shell, thus working as a diffusion barrier during high-temperature sintering.

(ii) Temperature and time: the temperature is the main thermodynamic driving force for both densification (*i.e.*, microstructure) and elemental interdiffusion (*i.e.*, chemical compatibility) in oxide-based cathode composite fabrication. The densification temperature of the oxide electrolyte and oxide active material composite is mostly determined by the electrolyte due to it having a higher melting point than common oxide active materials. In conventional solid-state sintering using pre-calcined powders, densification typically requires high temperatures (>1000 °C) for several hours. However, many cathode composite systems—such as LLZO, LLTO, and LATP combined with NMCs or LFP—suffer from poor chemical compatibility at these conditions, posing a major technical barrier to the development of oxide-based solid-state batteries.[573] Additionally, some Li-containing compounds (*e.g.* LLZO:Al) are subjected to the increased vapor pressure of Li (in the form of Li$_2$O) at elevated temperature (>900 °C) and become Li-deficient La$_2$Zr$_2$O$_7$ phases, impeding overall densification.[574] Excess Li sources, typically 10–20 wt%, are used in starting precursors to balance the Li loss during LLZO synthesis.[575] To achieve densification and chemical compatibility at the cathode/electrolyte interface at reduced temperature and time, other ceramic processing approaches with alternative ceramic processing approaches that apply external sintering forces, such as spark plasma sintering (SPS), can be employed. One of the earliest examples of prototype bulk-type solid-state batteries was assembled using SPS, where a thick electrolyte pellet of Li$_{1.5}$Al$_{0.5}$Ge$_{1.5}$(PO$_4$)$_3$ was co-sintered with Li$_3$V$_2$(PO$_4$)$_3$ as the cathode and carbon as the anode.[576] This configuration demonstrated stable cycling and promising electrochemical performance, achieving a surface capacity of $\approx$ 2.2 mAh cm^{-2}. While the thick electrolyte limits practical energy density, this co-pressed structure is useful for laboratory-scale evaluation and highlights the versatility of pressure-assisted sintering routes. For the cathode composite of LCO/LLZO, good densification with limited chemical interdiffusion has been demonstrated using FAST/SPS[577] and UHS.[270] The addition of sintering additives helps to reduce the required densification temperature by promoting liquid-phase sintering and accelerating the kinetics of densification compared with that of pure solid-state sintering. A common sintering additive of Li$_3$BO$_3$ (LBO) or slightly modified LBO (*e.g.* Li$_{2.3}$C$_{0.7}$B$_{0.3}$O$_3$) compound has been used to densify the cathode composite at temperatures between 700 °C and 800 °C.[553,578]

(iii) Atmosphere: the gas environment has been shown to be one of the critical parameters for cathode/electrolyte interfacial stability during processing. LATP and LLTO are intrinsically stable in ambient air, whereas LLZO forms a Li$_2$CO$_3$ layer on

8976 | *Chem. Soc. Rev.*, 2025, **54**, 8925–9007

This journal is © The Royal Society of Chemistry 2025

the surface as it reacts with $H_2O(g)$ and $CO_2(g)$ at room temperature. For NMC/LLZO interfaces, several studies have confirmed the formation of a second phase in air at temperatures above 500 °C.[553,579] To isolate the contributions to interfacial degradation, Kim *et al.* tested the effect of gas composition (air, oxygen, nitrogen, carbon dioxide) and humidity on the interphase formation at temperatures between 300 °C and 700 °C.[580] Dry oxygen was shown to be the most suitable atmosphere to sinter the NMC/LLZO interface, delivering better interface stability (without second-phase formation up to 700 °C) and a lower ASR of 130 Ω cm^2 than nitrogen, carbon dioxide, and humidified O_2.

6.1.2. Processing bulk-type batteries: electrolyte-supported, cathode-supported, and other cell designs. The procedure of tape-casting, lamination, and sintering has been demonstrated to result in the successful fabrication of 25-μm-thick, dense, free-standing LLZO electrolytes with ionic conductivities as high as 1 mS cm^{-1}.[46,201,581] However, such thin ceramics (10–30-μm thick) (Fig. 10a) may experience cracking during further processing steps. Moreover, the Li-ion pathway should be secured by developing good bonding between the catholyte, electrolyte, and anolyte without disconnection. One of the cell components (catholyte, anolyte, cathode composite (CC)) should thus be selected to withstand mechanical failure with good charge transport and stabilize the cell robustness, similar to how an organic binder serves as a mechanical binder in the LIB system.

6.1.2.1. Bi- or trilayer electrolyte-supported cell. One strategy is to prepare the cell with an additional porous LLZO anolyte and/or catholyte to fabricate a bi- or trilayer framework (porous|dense LLZO or porous|dense|porous LLZO (Fig. 10b)). The trilayer LLZO electrolyte composed of a 20-μm-thick dense LLZO film sandwiched between two 50-μm-thick porous LLZO films was shown to enhance the mechanical strength (breaking force) by 10 times compared with that of a 20-μm-thick free-standing dense LLZO film (Fig. 10c).[101] The trilayer Li–LLZO–Li symmetric cell configuration demonstrates extremely high-rate Li cycling up to 60 mA cm^{-2} and high capacity per cycle of up to 30 mAh cm^{-2} without external pressure and dendrite formation.[582] For the full cell, conventional liquid containing the NMC cathode composite with an areal capacity of 2.3 mAh cm^{-2} has been assembled with the LLZO framework, demonstrating successful cycling over 500 times at a current density of 2.3 mA cm^{-2} and over 350 times at a current density of 1.15 mA cm^{-2} and delivering 72% and 89% of the nominal capacity of the cathode, respectively (Fig. 10d). Despite the promising performance of hybrid oxide batteries based on the LLZO framework, there have been limited studies on an all-oxide cell architecture without a liquid electrolyte and with large cell footprint (*e.g.*, 5 × 5 cm^2 or larger).

Another opportunity for the fabrication of a full cell using the trilayer LLZO-electrolyte-supported framework is infiltration of the cathode active materials into the porous catholyte with post-annealing to obtain crystallized and densified cathode active materials on the catholyte without the addition of a liquid electrolyte[583,584] (Fig. 10e). Earlier works reported interfacial densification between the porous LLZO catholyte and cathode active materials at low annealing temperatures of 600–740 °C with promising initial cycling capacities.[583,584] However, because the active materials are synthesized from the precursor solution inside the pores in the porous scaffold, multiple infiltration and heating processes are often repeated to increase the active material loading and to establish continuous electronic pathways throughout the active materials.[584] The typically achieved cathode loading remains as low as a few mg cm^{-2} or less than 1 mAh cm^{-2}.[584,585] To improve the cathode loading, a highly porous catholyte together with multiple infiltration-heating processes is needed. Fabrication of a highly porous LLZO catholyte (more than 70 vol%) has been achieved using the freeze-tape-casting process,[581] which can be potentially used for preparing high-loading oxide cathode composites. Another challenge for high-loading cathodes using infiltration is the large volume change from the liquid (starting precursors) to solid (active material) during the annealing process. Despite multiple infiltrations, this process may not be suitable for the fabrication of nearly dense cathodes because of the remaining pores.[585]

Similarly, bilayer LLZO electrolytes with a total thickness of 105 μm (including a 35-μm-thick dense layer and the 70-μm-thick porous anolyte) have been shown to be an alternative electrolyte-supported framework as they also provide adequate mechanical strength.[237] The bilayer architecture consists of a dense side for the high loading cathode with a liquid catholyte and a porous anolyte for Li deposition.[586] To fabricate the cathode composite without the liquid catholyte, one can screen print slurry/paste on the bilayer, followed by sintering of the cathode composite onto the dense side of the bilayer (Fig. 10e). This is a feasible approach as successful co-sintering of layered oxides ($LiCoO_2$, $LiNiMnCoO_2$) with LLZO has been demonstrated with a sintered LLZO pellet.[553,554,578,587] In general, the composite slurry/ink includes active material powder (LCO or NMC), LLZO, and binder solution, which is screen-printed onto the sintered LLZO pellet (300–1000 μm in thickness) and co-sintered at elevated temperature (700–1050 °C) to densify the cathode composite of 20–100-μm thickness. If Li_3BO_3 (LBO) additive is added to the slurry, the sintering temperature can be reduced to 700–750 °C from 1050 °C.[553,554] It has also been shown that the introduction of $Li_{e.3}C_{0.7}B_{0.3}O_3$ (LCBO) into the LCO/LLZO mixed cathode results in a low interfacial resistance due to LCBO possessing a higher ionic conductivity than LBO.[578] In addition, the active material loading can be adjusted by modifying the composition ratio in the slurry and/or the printed thickness. For example, the LCO loading achieved was 1.0 mg cm^{-2} in the 20-μm-thick LCO–LLZO–$Li_{2.3}C_{0.7}B_{0.3}O_3$ cathode composite[578] but 12.6 mg cm^{-2} (areal capacity of up to 1.63 mAh cm^{-2}) in the 50-μm-thick LCO–LLZO cathode composite,[587] and the NMC loading was 5.7 mg cm^{-2} (areal capacity of up to 0.7 mAh cm^{-2}) in the 100-μm-thick NMC811–LLZO–LBO cathode composite.[553] Such examples of achieving a good areal capacity and the desired thicknesses indicate that this method may allow processing of

This journal is © The Royal Society of Chemistry 2025

Chem. Soc. Rev., 2025, **54**, 8925–9007 | **8977**
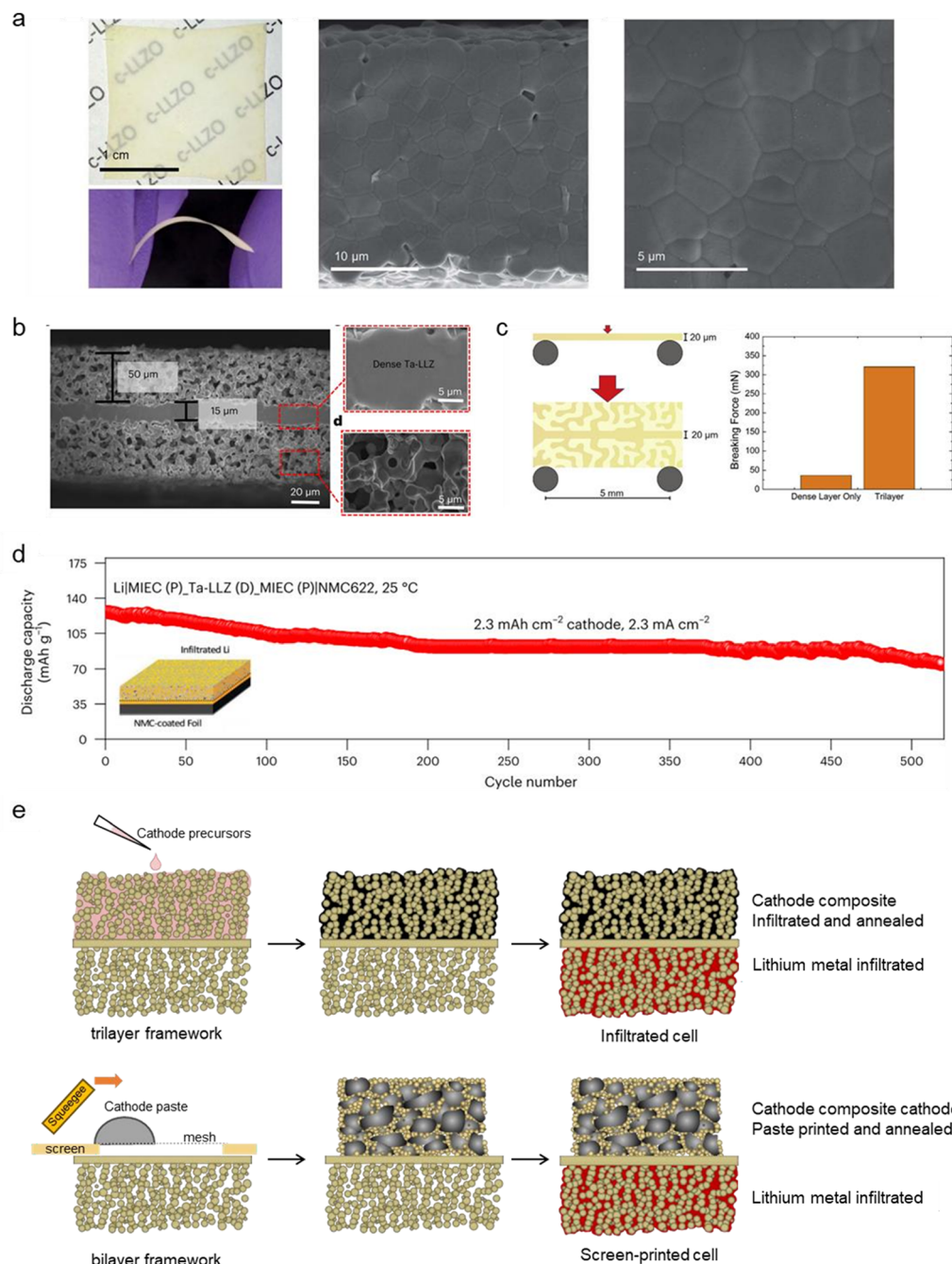
Fig. 10 Recent progress in the electrolyte-supported cell architecture and potential processing scenarios for all solid-state batteries. (a) Translucent, flexible, sintered cubic-LLZO free-standing film. Reproduced with permission ref. 202. (b) Trilayer porous|dense|porous LLZO. (c) Comparison of mechanical strength (breaking force) between the porous (50 mm)|dense (20 mm)|porous LLZO (50 mm) and dense LLZO (20 mm). Reproduced with permission ref. 101. (d) Cycling performance of the electrolyte-supported full cell with a NMC cathode composite (liquid catholyte). Reproduced with permission ref. 582. (e) Potential processing routes for an infiltrated and screen-printed (all solid-state) cell using an electrolyte-supported cell framework.

such cathode composites in the bilayer LLZO electrolyte-supported framework.

6.1.2.2. Composite cathodes as self-supported cells. Tape-casting and sintering: the cathode-supported architecture employs a dense cathode composite of 45–200-μm thickness

as a mechanical support, where the electrolyte can be either (i) deposited directly on top of the composite cathode or (ii) co-processed together with the cathode composite.[573] Both strategies can be attractive in terms of the overall mechanical stability of the cell compared to electrolyte-supported frameworks due to the thick and dense mechanical support. Thus, a

battery cell and pack (series of cells connected for desired energy) might withstand mechanical shock/cracking with increased cell footprint. The main challenge of developing a cathode-supported cell architecture is the limited success of fabricating a cathode composite that is fully dense, practically thin, scaled in area, and electrochemically functional. The limited success reported stems from the chemical compatibility issue, as discussed in previous sections. Only recently, a cathode chemistry consisting of a layered cathode, *e.g.*, $LiCoO_2$ (LCO), together with $Li_{6.45}Al_{0.05}La_3Zr_{1.6}Ta_{0.4}O_{12}$ has been shown to possess a reaction-free interphase and dense microstructure

(relative density > 90%) when fabricated using the tape-casting process followed by conventional sintering at 1050 °C in air (Fig. 11a).[588] This method resulted in free-standing membranes with a thickness range of 70–200 μm, demonstrating the capability of fabricating an ideal cathode composite thickness range with a high loading capability of up to 4.8 mAh (Fig. 11b). By implementing a concentration gradient of LLZO and LCO over the 100-μm-thick cathode composite, the membrane was able to achieve a high active material utilization (99%, 2.8 mAh cm^{-2}) together with a bilayer electrolyte (50-μm-thick PEO and 200-μm-thick LLZO pellet) and a Li-metal anode
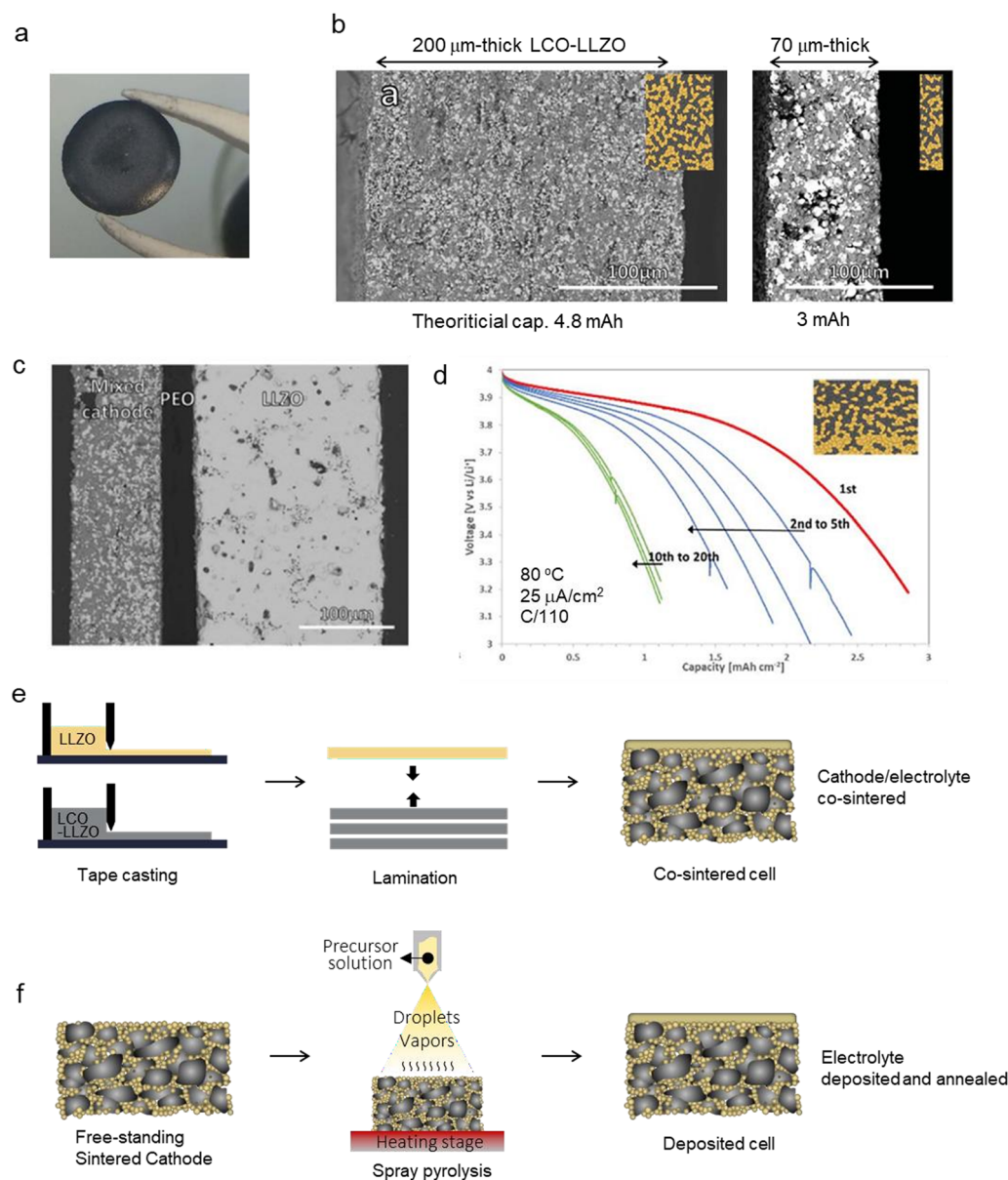
Fig. 11 Recent progress in the cathode-supported cell architecture and the potential processing scenario for all solid-state batteries. (a) As-sintered $LiCoO_2$–LLZO composite cathode (free-standing or self-supported). (b) Cross-sectional SEM micrograph of 200 μm-thick (theoretical capacity: 4.8 mAh) and 70 μm-thick (theoretical capacity: 3 mAh) composite cathodes. (c) and (d) Tested model hybrid cell including the LCO–LLZO composite cathode, PEO as the catholyte, and LLZO as the separator. (d) Discharge curves of the 100 μm-thick composite cathode, showing nearly 100% utilization of capacity with the Li metal anode. (a)–(d) Reproduced with permission ref. 588. (e) and (f) Potential processing routes for the co-sintered and deposited (all solid-state) cathode half-cell.

This journal is © The Royal Society of Chemistry 2025

Chem. Soc. Rev., 2025, **54**, 8925–9007 | **8979**

(Fig. 11c and d).[588] Nonetheless, several studies have reported the undesired reaction between LCO and LLZO such as the formation of $La_2Zr_2O_7$ or $LaCoO_3$ during high-temperature processing.[589–591] It should also be noted that particle size affects the reactivity. An ideal cathode composite requires small LLZO particles (several 100 nm) as ion-conduction pathways into the composite cathode to achieve high CAM loadings; however, this modification results in increased reactivity, thereby promoting secondary phase formation.[591] Further research is necessary to clarify the effect of the specific composition (i.e., doping) and particle size of the LLZO electrolyte on the chemical compatibility with common cathode active materials (e.g., LCO, NMC) and achievable capacity during battery cycling. For characterization of the interphase, both XRD and Raman spectroscopy should be used to identify the secondary phase formation as Co diffusion into LLZO is difficult to detect using XRD.[589] In addition, more advanced techniques such as TOF-SIMS,[592] XPS,[589] TEM-EDS,[593] XAS,[594] XANES, and EXAFS[579] can be used to capture a minor phase. Based on the practice above, more effort should be focused on discovering new chemically compatible cathode chemistries and feasible processing methods for fabrication of electrochemically functional self-supported cathode composites.

Spray pyrolysis: another strategy to prepare a self-supporting composite cathode for a cathode-supported cell design is the spray pyrolysis technique. In principle, spray pyrolysis (e.g., sequential deposition synthesis; SDS) can be tailored to other chemistries, including cathode deposition, by consideration of the points mentioned in Section 3: (i) precursor salt chemistry, (ii) solvent, and (iii) solution pH and concentration. For typical cathodes (e.g., $LiCoO_2$ or $LiNi_xMn_yCo_zO_2$), each of the precursor salts must be chemically stable in solution with each other. The chemical compatibility should also be considered when selecting the solvents of the system in addition to selecting solvents with boiling points near the temperature of the heated substrate. Here, the ideal substrate material is a thin metal foil as the CC (e.g., aluminum or stainless foil).[442] The concentration of the cathode precursor salts should be determined in the same manner as one might determine the concentration of electrolyte precursor salts. The fabrication of composite cathodes that contain both the CAM and electrolyte may present a challenge. The design objective of composite cathodes is to obtain a dense microstructure with electronic and ionic percolation without phase mixing or interfacial reactions to increase the capacity utilization. However, if the precursor salts of both the cathode and electrolyte are in the same solution, there is a large opportunity for chemical compatibility complications. Instead, to create a composite cathode, there is the possibility of employing co-deposition, where each solution (the cathode solution and electrolyte solution) is atomized through different spray heads onto the same substrate at the same time or sequentially. This tactic avoids chemical compatibility complications between the two solutions but presents the added challenge of orienting both spray heads to the same substrate as well as ensuring that each distribution of droplets uniformly coats the substrate. In addition, if a simultaneous deposition

approach is used, possible reactions forming phases other than the pure phase (e.g., LLZO and LCO) and whether the desired material forms at all must be considered. The composite film must be carefully evaluated in terms of density, elemental distribution, active material loading, and electrical and ionic conductivity to ensure that this novel co-deposition strategy achieves the goals of composite electrodes. In principle, each of these challenges may be overcome to achieve a promising cathode composite via spray pyrolysis or SDS that would be very challenging to achieve using another wet-chemical method.

Aerosol deposition: for the production of LIBs, the use of further processing techniques such as solvent-free or solvent-reduced technologies can also be considered. First, the CAM, SE, additives, and a binder can be heated in an extruder to form a viscous mixture that can then be extruded and calendared onto a CC. Second, the CAM and SE together with different additives and a binder can be processed by dry calendaring as a Maxwell-type material. As the mixture exhibits a simple viscoelastic behavior, it can be directly calendared onto a CC. Third, dry spraying techniques can be used to spray a mixture onto a CC followed by hot calendering.[595] One example for the latter is aerosol deposition. The oxide ceramic sub-μm particles become accelerated at room temperature onto a substrate, where they fracture into nanocrystallites and merge into a dense film due to the high impact of the post-launched particles. For example, aerosol deposition was used to deposit NMC and LCO onto LLZO pellets.[596,597] For more practical use, deposition of the cathode should be first performed on thin metallic substrates (e.g., copper) followed by LLZO and Li deposition. Nazarenus et al.[598] fabricated 30-μm-thick LLZO films on copper substrates at room temperature and reported an ionic conductivity of 0.046 mS cm^{-1} after post-annealing at 400 °C for 1 h. For these production methods, the presumed advantages are a reduction in cost and energy because no solvents are used (and therefore the drying process is eliminated) and because aerosol deposition is known to have high deposition rates of up to 1–2 μm min^{-1}.[598] In addition, there are established processing routes for polymer electrolytes, which can be adapted. However, producing uniform films with high microstructural densities and the desired ionic/electronic conductivities remains a challenge. Further research on processing the cathode support is needed, and then, the entire processing chain can be adjusted and examined.[595] Possible processing routes to fabricate self-supported composite cathodes would enable further processing of solid electrolytes on the cathode as a substrate, which will be considered in more detail in the following.

6.1.2.3. Processing of the cathode-supported half-cell. The fabrication of the electrolyte is the next step to make a cathode half-cell configuration (cathode composite/electrolyte bilayer) prior to the fabrication of the Li anode. This can be potentially achieved using the methods used for the self-supported cathode composite, namely tape-casting, spray pyrolysis, or aerosol deposition. We have selected the following processing

8980 | Chem. Soc. Rev., 2025, 54, 8925–9007

This journal is © The Royal Society of Chemistry 2025

strategies as a potential recipe of cathode-supported half-cell architectures:

(i) Co-sintering electrolyte and cathode composite multilayer laminates (Fig. 11e).

(ii) Thin-film electrolyte deposition (*e.g.*, spray pyrolysis) on a self-supported cathode composite (Fig. 11f).

In the tape-casting process for the cathode half-cell fabrication, an electrolyte tape is laminated onto a cathode composite tape with desired pressure and thickness, and then, the laminated tapes (laminates) are placed in a furnace for binder burn-out and a further co-sintering process. The first step removes any inactive ingredients (binder, solvent, and dispersant) used in the slurry for tape-casting and the second step co-densifies the laminates. Even if the use of chemically compatible components is assumed, in general, co-sintering a multilayer ceramic from the tape-casting process involves a high level of complexity as sintering a ceramic multilayer typically results in incomplete densification, warpage, and/or cracking due to the mismatch in the shrinkage and strain rate during sintering.[599–602] The amount of distortion is governed by the sintering strain rate mismatch among the individual layers, the layer thickness ratio, and the viscosity ratio. Applying pressure by mechanical load (*e.g.*, zirconia or alumina setter) to the specimen during co-sintering is a well-known approach to avoid such deformation. Care must be taken when applying the pressure because during sintering, a ceramic is elastic or brittle at low temperature and shows linear viscous behavior at high temperature. Thus, the ideal time for loading is, when the viscosity is sufficiently low to allow creep deformation by viscous flow. To apply the load above a certain temperature, special design of sintering arches is suggested.[599] Nonetheless, one can achieve quite a flat ceramic multilayer cell (*e.g.* anode-supported solid oxide fuel cell) of 55 μm thickness variation in 5 cm by applying mechanical load during sintering process.[600] The effect of applied pressure loads with respect to the composition (*i.e.*, particle size, binder/solvent ratio), thickness, and viscosity of the individual layer on the co-sintering behavior (degree of densification and warpage) of cells should be investigated for optimal load condition. The flatness of the planar cell is crucial for the cell-to-pack performance as a flatter cell offers a greater contact area between the cells, thus maximizing the energy density of the battery pack. Thus, fabrication of a flat unit-cell is very important for commercialization of planar-type Li-metal-oxide-based SSBs.

Another approach is to use the film deposition technique on a self-supported cathode composite (Fig. 11f). For example, the spray pyrolysis method, as opposed to PVD methods, is not dependent on substrate roughness and is able to produce LLZO electrolyte films with a thickness of 1–10 μm at low processing temperatures (<750 °C).[318] However, it should be noted that the as-deposited film is amorphous with ionic conductivities on the order of 10^{-6}–10^{-7} S cm^{-1}.[309] By implementing a post-annealing step, the amorphous LLZO can gradually crystallize as a cubic phase.[309,318,342] Furthermore, there are several degrees of compatibility that must match between spray pyrolysis and the cathode composite substrate. For example, a

100-μm-thick LCO–LLZO sintered cathode composite[588] is a feasible option as a substrate for depositing the LLZO electrolyte using SDS if the sintered substrate is mechanically rigid enough to survive against cracking and convective air currents. The surface roughness should also be considered, especially when depositing films that are only a few micrometers thick. The thickness of the electrolyte should be sufficient to provide a continuous, dense, and uniform film on the cathode substrate. A typical thickness of $\sim$1 μm is needed if the surface roughness is less than 0.5 μm. However, a thicker electrolyte may be needed on a substrate with higher surface roughness. To ensure that the temperature of the cathode substrate is appropriate to decompose the droplets from the spray head, the heat source must be at a higher temperature to account for the convective cooling from the carrier gas. The cathode substrate must be tailored to withstand the higher temperature of the heating source and the thermal gradient within the layer to resist cracking. For example, to fabricate LCO from lithium nitrate and cobalt nitrate (decomposition temperature of 280 °C),[603] the film must reach 400 °C.[604] This is advantageous as the LCO film can be heated to the required temperature and then subsequently cooled to $\sim$300 °C[318] for an independent deposition of the LLZO film. In addition, the thermal conductivity, thinness, and temperature stability of LCO likely result in the temperature of the LCO being sufficient to decompose the LLZO precursors; thus, the desired LLZO layer develops.[605] This step is followed by a post-annealing step to crystallize the amorphous LLZO into the cubic-LLZO phase for high conductivity. The sequence of annealing should be selected to reduce the thermal stresses on both layers to prevent cracking, *e.g.*, applying the electrolyte layer to a high-temperature-sintered cathode composite substrate and heating both at the same time would only sinter the electrolyte layer. If the as-deposited amorphous electrolyte layer is preferred, additional annealing steps can be omitted.

Spray pyrolysis is a promising method to create all-solid-state battery architectures but has not yet been extensively examined in the battery community. Commercially purchased spray pyrolysis equipment can be relatively expensive and is typically custom-made for any given application, leading to greater time and money investment compared to other established methods. For example, a commercial research-scale spray pyrolysis system costs $\sim$120 000 USD; instead, spray nozzles from other fields, *e.g.* automotive, can be repurposed to create a "home-made" spray pyrolysis system at reduced cost but with much greater time investment. A further reason for the lack of widespread application of spray pyrolysis is the infrastructure needed, including a large amount of carrier gas for the multi-hour deposition, a heating source capable of reaching $\sim$400 °C under the convective cooling effect of the spray-head carrier gas, and safe handling of the sometimes corrosive droplets and decomposition products after droplet atomization. In principle, spray pyrolysis can be scaled-up easily by mounting the spray head on a 2D actuator to deposit onto a large substrate; in practice, it is not trivial to maintain uniform film coverage over a large area. A further challenge is

that spray-pyrolyzed films ideally need to be deposited on thin metallic substrates as the films are not mechanically robust enough to be fabricated as free-standing films.

6.1.3. Processing metrics for the lithium–metal anode.

The advantages of lithium metal, often regarded as the ultimate anode material for high-energy-density batteries, have been known for decades.[606,607] Li metal possesses a number of beneficial properties including its highly reducing nature—easily shedding electrons and Li ions, as manifested by the low electrochemical potential (-3.04 V $vs.$ the standard hydrogen electrode), high theoretical capacity (2061 mAh cm^{-3} or 3860 mAh g^{-1}), and low density (0.534 gr cm^{-3} at room temperature). Since the 1970s, tremendous efforts have been placed on the integration of Li metal into batteries; however, the commercial production of Li-metal batteries has been halted by numerous challenges associated with their long-term electrochemical cycling, such as high reactivity, instability of the SEI, and dendrite formation as well as related safety concerns.[606,607] Recently, new opportunities have been presented by highly conductive oxide-based solid electrolytes, some that show good electrochemical compatibility with lithium metal, including garnet-type LLZO and oxynitride LiPON.[608,609] Although these new solid electrolytes show promise for Li-metal batteries, precisely controlling the initial deposition of lithium as well as the interface between the highly reducing anode and the oxide-based solid electrolyte proves challenging.[37,44,610] Accordingly, there are several key requirements for the solid-electrolyte/lithium–metal interface to ensure close-to-ideal performance of all-solid-state batteries. The first is the chemical and electrochemical stability of the solid electrolyte against highly corrosive Li metal. The solid electrolyte should possess excellent chemical stability and low reduction potential $vs.$ Li$^+$/Li or negligible thermodynamic driving forces to be reduced at 0 V. At voltages below the reduction potential, solid electrolytes are decomposed from a stoichiometric compound, leading to undesired phases with either Li$^+$ conductivity lower than that of the solid electrolyte or electronic interphases. This conversion causes an increase in the charge-transport resistance, acting as a barrier for Li-ion transport across the interface. LLZO has one of the lowest reduction potentials of 0.05 V $vs.$ Li$^+$/Li and thus outstanding stability toward Li metal, whereas Ge^{4+}- and Ti^{4+}-containing oxide electrolytes, including perovskite Li$_{3x}$La$_{2/3-x}$TiO$_3$ and Li$_{1.5}$Al$_{0.5}$Ge$_{1.5}$(PO$_4$)$_3$, are decomposed at 1.7 and 2.7 V by Li and form unfavorable electronically conducting interphases. The latter can cause continued side reactions electrochemically and eventual short-circuiting. The next requirement is mechanical stability against volume change during Li cycling. The ideal performance at the solid-electrolyte/Li-metal interface involves the ability to reversibly plate and strip approximately 20 µm of lithium metal. In a planar battery configuration, a 20-µm-thick anode over a 1 cm^2 area could theoretically store 4.12 mAh of electricity; yet, from empirical data, lithium generally non-uniformly deposits and strips at the interface. This often leads to loss of physical contact at the interface.

Another requirement is that lithium metal must favorably adhere to the surface of the solid electrolyte with good lithium wettability. Recently, it was shown that lithium metal favorably wets a number of s-block, p-block, and d-block elements; ΔG_r represents the spontaneity of the reaction between lithium metal and the element of choice at a fixed temperature. Negative values for ΔG_r specify favorable Gibbs formation for newly formed bonds between the element and lithium metal, which boost the lithium wettability at the interface. Overall, by considering chemical/electrochemical and mechanical stability, and wetting properties, Li$^+$ must be able to move reversibly and quickly across the interface together with the solid-electrolyte/lithium–metal interface possessing an area-specific resistance (ASR) of 1 Ω cm^2.[582]

If proper care were maintained during the deposition of lithium–metal anodes, several issues may be overcome during battery operation. Below, we specifically focus on the processing metrics to control the performance of lithium metal as an anode on oxide-based solid electrolytes. These metrics are also discussed considering three methods to form solid-electrolyte/lithium–metal interfaces, namely thermal evaporation, thermal lamination, and in $situ$ plating. Thermal evaporation is a physical vapor deposition process from a lithium source to the target sample under vacuum conditions. Thermal lamination uses a commercially available pre-deposited lithium foil on a copper CC, which is directly applied to the electrolyte-supported or cathode-supported cells, and physical contact is made via heat treatment at near the melting point of lithium. Lithium metal has a melting point of 180.5 °C. The use of heat is one of the most common methods for depositing a lithium–metal anode on solid electrolytes.[611] Finally, lithium metal can be formed or plated in $situ$ solely from the CAM, which does not require excess lithium from thermal evaporation or thermal lamination. We also focus on possible issues that may arise if proper care is overlooked during the deposition of lithium–metal anodes.

6.1.3.1. Precursors.
The deposition of lithium anodes generally starts with lithium metal with a purity $>99.8\%$. In some cases, lithium metal is pre-deposited onto a copper CC using electrodeposition of halogenated lithium salts ($e.g.$, lithium bis(trifluoromethylsulfonyl)imide, lithium hexafluorophosphate) with thicknesses ranging from 1 to 50 µm.[612–614] An electrodeposited lithium anode generally has low purity ($<99\%$) and significantly higher surface roughness than thermally evaporated lithium–metal anodes.

6.1.3.2. Vapor pressure of lithium.
The vapor pressure of lithium metal can be used to direct the deposition of Li-metal anodes onto solid electrolytes or copper CCs using processes such as thermal evaporation. As a bottom-up approach, the advantage of the deposition over physical lamination of lithium is the ability to control the thickness with high microstructural density. Thus, thermal evaporation of lithium metal has been used in thin-film all-solid-state battery research since the 1980s owing to its target thickness of several micrometers and high

8982 | Chem. Soc. Rev., 2025, 54, 8925–9007

This journal is © The Royal Society of Chemistry 2025

packing density of lithium in the film (>0.5 g cm^{-3}).[615] The technique is based on physical deposition, where lithium evaporates under designed thermal and vacuum conditions and then diffuses to and condenses on the unheated surface of the target substrate. The heating source is electrical resistance, an electron beam, or a laser that supplies enough energy to cause the lithium metal to exert vapor pressure and condense onto a solid substrate.[616] Using this technique, the thickness and deposition rate can be easily manipulated by tuning the heating temperature (energy), vacuum level, and the distance between the source and the substrate. For example, Meunier et al. fabricated 5 μm of lithium anode in 5 min under 5×10^{-5} Pa vacuum conditions at a source temperature of 700 K for a thin-film all-solid-battery on a B_2O_3–$0.8Li_2O$–$0.8Li_2SO_4$ solid electrolyte.[1] Similarly, lithium–metal anodes for LiPON-based thin-film batteries were deposited by thermal evaporation with thicknesses between 0.5 and 5 μm.[2–5] In some cases, lithium metal is directly deposited onto copper CCs with thicknesses ranging between 1 and 30 μm; the CC is then thermally laminated to the top surface of the solid electrolyte.

6.1.3.3. Atmosphere. Lithium metal is notoriously reactive with O_2, N_2, CO_2, and H_2O in the air and thus requires special care while being processed into an anode. In fact, lithium reacts faster with N_2, H_2O, and CO_2 to form Li_3N, $LiOH$, and Li_2CO_3 at room temperature. The reaction with O_2 occurs at higher temperature to form Li_2O or Li_2O_2. The formation of these irreversible phases may compromise the deposited capacity of the anode. For thermal lamination, lithium metal must be applied under an inert atmosphere (e.g. ultrapure argon) to avoid any unnecessary oxidation of the lithium metal. For thermal evaporation, the vacuum pressure must be carefully tuned to $<10^{-6}$ Torr; any residual oxygen leads to the formation of lithium oxide during the processing. In some cases, the oxide layer on Li metal can be removed via a polishing procedure under ultrapure argon. It should be noted that species such as H_2O can still migrate into the cell and react with the lithium–metal anode during electrochemical cycling if the anode/current collector is not properly sealed. For instance, H_2O has been shown to directly diffuse through sputtered copper CCs, which were directly deposited onto solid electrolytes in order to plate lithium–metal anodes in situ from the cathode in $Cu/LiPON/LiCoO_2$ cells.[617] In this method, a lithium–metal anode is plated between the solid electrolyte and a copper CC during the initial charge. The key to this method lies in the deposition of a lithium-diffusion-blocking overlayer (on top of the copper CC), which seals the anode from gaseous species (e.g. O_2 and H_2O) and guides the deposition and stripping of lithium metal. This lithium-diffusion-blocking overlayer usually consists of 0.3–1 μm of LiPON or 6 μm of parylene C.[618] To put this metric into perspective, a relatively short cycle life was observed in "lithium-free" battery cells without an O_2-tight overlayer, whereas cells including this overlayer could charge/discharge for over 1000 cycles at 1 mA cm^{-2} and for over 500 cycles at 5 mA cm^{-2} between 4.2 and 3.0 V.[13] These results indicate that even the slightest change in the atmosphere (and any exposure to O_2 or H_2O) can significantly affect the deposition of lithium–metal anodes as well as their long-term performance.

6.1.3.4. Pressure. In some cases, the lithium–metal anode is pressed against the solid electrolyte to form the solid electrolyte/anode interface, followed by heating at >180 °C in most cases to effectively laminate the lithium metal to the surface of the solid electrolyte. When applying pressure to affix the lithium metal to a solid electrolyte, the pressure applied must be low enough to avoid cracking or laceration in the solid electrolyte.

6.1.3.5. Effect of temperature on lithium–metal deposition. In this process, lithium metal is pre-deposited onto a copper CC via extrusion (thicknesses of $\geq$ 20 μm), electrodeposition (thicknesses of 1–50 μm), or evaporation (thicknesses of $\leq$20 μm). Next, the lithium metal is directly laminated on the surface of a solid-state electrolyte by thermally heating the CC/lithium metal to temperatures $\geq$180 °C for $\geq$15 min for lithium to wet the surface.[619,620] Lithium lamination has the obvious advantage of being a relatively fast method that is mass manufacturable; however, one of the main drawbacks of this method is the high cost of thin-metal preparation compared with processing of millimeter-thick lithium foil.

6.1.3.6. Lithium packing density. Lithium metal has a theoretical density of 0.534 g cm^{-3}. Thermal evaporation of lithium–metal anodes onto polished CCs or smooth solid electrolytes results in the highest packing density, close to the theoretical density of lithium. Thermally laminated lithium–metal anodes can have surface roughness or pits, decreasing the total packing density of lithium metal. In "anode-free" batteries, in situ deposited lithium metal gradually redistributes across the interface and, in some cases, dewets from the surface of the solid-electrolyte interface, lowering the packing density of the lithium–metal anode. For instance, wrinkled or pitted surfaces were observed for LiPON-based thin-film batteries.[617] As lithium is cycled between the anode and the cathode, the packing density generally decreases due to the redistribution of lithium and the gradual formation of off phases (e.g. Li_2O). The lithium packing density at the anode can be improved by applying pressure to the entire cell.

6.1.3.7. Interfacial treatment. The chemistry of the solid-electrolyte/lithium–metal interface is among the most important and most difficult to control. Here, highly reducing lithium metal meets the oxide-based solid electrolyte and either wets the surface of the electrolyte or is repelled from the surface. As noted, lithium metal preferentially adheres to several elements; however, with most oxide-based solid electrolytes, such as doped $Li_7La_3Zr_2O_{12}$, $Li_{1+x}Al_xTi_{2x}(PO_4)_3$, and $Li_xLa_{2/3x}TiO_3$, an artificial "lithiophilic" surface layer that is stable with lithium metal is needed to ensure a Li$^+$-conducting and e$^-$-insulating interface. For instance, lithium garnets generally form a surface carbonate (Li_2CO_3), which leads to poor Li wetting. This layer can be removed by a thermal treatment

This journal is © The Royal Society of Chemistry 2025

Chem. Soc. Rev., 2025, **54**, 8925–9007 | **8983**

under argon at 400–600 °C. Another common pretreatment is the addition of an ultrathin buffer layer such as Al_2O_3 or germanium to improve the contact between lithium metal and the solid electrolyte. When lithiated, this interlayer becomes either ionic conducting or mixed ionic and electronic conducting to stabilize the interphase, which is discussed in greater detail with practical examples in the next section.

6.1.4. Processing of lithium–metal anodes, challenges, and mitigation. Li-metal anodes may enable the realization of sought-after high-energy-density SSBs but require the detection and mitigation of lithium dendrites, which can shorten the lifespan of the battery and cause safety issues, and establishment of manufacturing plants with scalable and cost-effective lithium production methods that account for its high reactivity and adhesive properties. A vacuum or inert gas atmosphere (or at least a dry atmosphere) and stringent safety protocols will likely be required to account for the high reactivity of the Li metal with nitrogen, oxygen, and moisture. In the processing chain and independent of the cell-design concept, the Li-anode manufacturing will likely be considered separately from the cathode/solid electrolyte tandem and is visioned to be stacked with the cathode/solid electrolyte half-cell. There are several potential design concepts for Li-metal anodes, e.g., (i) direct application via mechanically extruded lithium (~100-µm thickness) or via molten lithium; (ii) inactive scaffold-supported design; and (iii) Li-free design, where direct Li plating occurs on the CC or on a 3D host structure/CC. The processing of direct Li-metal application can be done via dry extrusion or molten lithium processing. In the former, lithium foil passes through an extruder and several subsequent calendaring steps to reduce its thickness. This technique has shown minimal success in achieving ultrathin Li (<20–30 µm) due to the reactivity and adhesiveness of the lithium metal and may require the use of processing lubricants. In the latter, a scalable and cost-effective technique, lithium is liquefied (T_{melt} (Li) = ~180 °C) and spread on different dense or porous substrates such as a metal CC or inactive porous ceramic solid electrolyte scaffold. At the lab scale, lithium metal is also processed through vaporization or evaporation of Li metal (such as Li evaporation or sputtering); however, these approaches require a vacuum environment in a special chamber and have low throughput with low deposition rates and are thus expensive and inappropriate for large-scale processing. In the inactive scaffold support approach, molten lithium metal is infiltrated on a porous scaffold with a considerably larger surface area compared to a flat electrolyte surface. As a result, the charge-transfer resistance is lowered at the unit surface area at a given current density, and better adhesion and homogeneity is observed compared with a flat solid-electrolyte design.[24,45] Accordingly, high-rate Li plating/stripping up to 10 mA cm^{-2} is possible.[586] More importantly, in the scaffold-based design, the anode does not require external pressure during cycling due to a negligible volume change. Nonetheless, there is an energy penalty due to the additional volume and weight of the porous anolyte as compared to a flat electrolyte. Therefore, a minimal use of the anolyte while

maintaining high-rate performance is an important design consideration for optimizing the cell. An alternative strategy, namely an "anode-free" design, involves the in situ plating of lithium metal on the CC or other anode-supported scaffold during the first charging cycle from the active cathode. This approach obviates the need for either the demanding lithium processing routes or excess lithium and allows the use of the Li ions already stored in the cathode, which are plated as a metal during the formation process, and avoids challenges associated with the handling and shipping of Li-metal foils. Although this relatively new approach is both energy and cost efficient, it is sensitive to irreversible capacity loss if unwanted side reactions occur and may require high stack pressure and complicated pack-level integration considering the large volume changes (if no scaffold is used), estimated at ~19-µm-thick Li metal for the deposition of 4 mAh cm^{-2} Li metal (considering a specific capacity of 3860 mAh g^{-1} and a density of 0.534 g cm^{-3}).

Currently, both the high chemical reactivity of Li metal and dendrite formation during battery operation limit its market potential as an anode material. Only a gradual improvement of the critical current density (CCD, mA cm^{-2}) and/or areal capacity (mAh cm^{-2}) was reported from LLZO-Li symmetrical cell studies, and one of these approaches could be potentially implemented in the future full-cell architecture. For example, Sharafi et al.[621] introduced a procedure to control the surface chemistry of LLZO and decrease impurities such as hydroxide and carbonate, which typically appear on the crystalline LLZO surface upon exposure to air. A decrease of LLZO surface contamination was demonstrated after mechanical (wet) polishing followed by heat treatment at 400–500 °C in Ar and resulted in improved Li wetting of LLZO with a low interfacial resistance of $R_{LLZO/Li}$ ~1 Ohm cm^2 and a CCD$_{R.T.}$ of 0.3–0.7 mA cm^{-2}.[621,622] The removal of contaminated species by laser treatment also translated into interfacial resistance reductions of 44% when testing laser-cleaned lithium metal anodes in a symmetric LLZO–Li cell.[623] In contrast, Han et al.[619] employed a thin-metal oxide interlayer at the Li/LLZO interface to improve the Li wettability. Atomic layer deposition was used to coat a 5.2-nm-thick and conformal Al_2O_3 layer on the surface of a dense and flat LLZO electrolyte. Herein, the Al_2O_3 layer helps the molten Li metal to conformally coat the LLZO surface with no interfacial void space as a result of the thermally lithiated alumina (Li–Al–O compound) interphase stabilization. The low interfacial resistance of $R_{LLZO/Li}$ ~34 Ohm cm^2 (1 Ohm cm^2 in d.c. measurement) was achieved with stable Li cycling under a current density of 0.2 mA cm^{-2} for 90 h. Similarly, thin metallic interlayers (e.g., gold) have also been employed for improved Li wetting[624] by Taylor et al., where a Li–Au intermetallic interphase forms upon lithiation and essentially functions as a mixed ionic and electronic conductor (MIEC). They demonstrated a CCD$_{RT}$ of 0.9 ± 0.7 mA cm^{-2}. The interlayer mainly reduced the standard deviation of CCDs vs. uncoated samples by homogenizing charge transport, therefore preventing hot spots but not greatly affecting the interfacial resistance and absolute CCD values. Despite the success in reducing the interfacial resistance to ~1 Ohm cm^2 by

improving the Li wettability, the Li-metal plating and stripping rates (*i.e.*, CCDs) were still insufficient to satisfy the DOE Fast Charging Goals, which include a plating current density of 10 mA cm^{-2}, per-cycle Li plating of 5 mAh cm^{-2}, and cumulative plating capacity of 10 Ah cm^{-2}.

Additional modification was introduced by Xu *et al.*[625] They intended to increase the surface area of reaction sites for lithium deposition by replacing the dense LLZO, where the reaction only occurs at 2D boundaries (two-phase boundaries: LLZO/Li interface or LLZO/CC interface), to allow for 3D boundaries (triple-phase boundaries (TPBs): LLZO as Li$^+$-conducting/carbon as e-conducting/pores as prereserved space for Li deposition).[530,586,620,625] Herein, the LLZO microstructure is modified with an extended surface area with connected pores. With an applied interlayer and carbon coatings on the porous surface, a 3D porous MIEC anode architecture was developed. In fact, creating a porous LLZO scaffold as an anolyte provides a 40-times-larger surface area of reaction sites compared to a planar cell such that the localized current density at the TPBs is 40 times lower.[101] Accordingly, the charge-transfer resistance is lowered at the unit surface area at a given current density and there is improved adhesion and homogeneity compared to that of a flat SE. Moreover, mechanical stress is accommodated with the 3D porous scaffold, which avoids the need for external pressure. A Li symmetrical LLZO cell with this anode architecture showed cumulative plating over 300 mAh cm^{-2} on each side (600 mAh cm^{-2} total cycling) at 2.5 mA cm^{-2} and CCDs up to 10 mA cm^{-2} without dendrite formation. Furthermore, a 'single-phase' 3D porous MIEC was introduced to further optimize the Li deposition uniformity, thereby avoiding hot spots during high-current cycling. To increase the electronic conductivity of LLZO while maintaining the ionic conductivity, various multivalent transition metals (Nb, Ce, Cr) were doped at the Zr site in Ga:Li$_7$Pr$_3$Zr$_2$O$_{12}$. A carbon-free, ZnO-coated porous MIEC anode showed notable improvement in the CCDs and cycling stability—stable plating/stripping cycle at 60 mA cm^{-2} and CCD up to 100 mA cm^{-2} without dendrite formation. A capacity per cycle of up to 30 mAh cm^{-2} and a Li cumulative capacity of 18.5 Ah cm^{-2} were reported without applied external pressure, far exceeding the DOE Fast Charging Goals.

MIECs as a porous interlayer or 3D scaffold have also been evaluated as a high-performance Li anode concept in other solid-electrolyte chemistries: a Li–Mg alloy anode for the LLZO electrolyte,[626] a Sn–Ni alloy-coated Cu nanowire anode for the PEO electrolyte,[627] and a Ag–C nanocomposite anode for the Li$_6$PS$_5$Cl electrolyte.[628] For example, Im and colleagues revealed how the local microstructure and composition evolve during cycling (Fig. 12a–c).[628,629] During the initial stage of charging, lithiation of silver and carbon nanoparticles occurs within the nanocomposite, resulting in the formation of a Li–Ag alloy and densification of the composite structure. Near the end of charging, lithium begins to deposit—alongside silver—at the interface between the nanocomposite and the current collector. Upon discharge, lithium ions are extracted back to the cathode, and some silver redistributes into the nanocomposite, though a significant portion remains localized near the bottom, forming a silver-rich region. The Li–Ag alloy formation acts as a nucleation template that promotes uniform Li deposition and reduces the propensity for dendritic growth. Furthermore, the Ag–C nanocomposite's inherent mixed ionic and electronic conductivity facilitates continuous contact between the plated lithium, the current collector, and the solid electrolyte. It also functions as a protective buffer layer, mitigating direct reactions between lithium and the argyrodite electrolyte. Optimization of the carbon-to-silver ratio was also found to be critical in accommodating nanoparticle pulverization and re-segregation, resulting in stable long-term cycling without significant degradation. These insights reinforce the role of engineered MIEC scaffolds in achieving stable, dendrite-free lithium metal anodes for sulfide-based solid-state batteries. Theoretical interpretations on how open nanoporous MIEC interlayers manipulate Li deposition and stripping behavior and thereby suppress general instability of the Li anode are discussed in greater detail in a recent review article.[630] Even if the electrochemical and mechanical instability phenomenon of using a Li anode is often associated with the properties of the solid electrolyte, the microstructure and composition of the interface appear to play key roles. As discussed above, a 3D MIEC anode has been shown to avoid the localization of high current densities at hot spots. Homogenizing charge transport for Li cycling was first achieved either by improving the Li wettability or by employing lithiated metal alloy/oxide at the LLZO/Li interface. Additionally, the porous anolyte with extended reaction sites and high electronic conductivity further improves the distribution of local current; thus, extremely high Li plating is possible without the need for carbon coating or external pressure. Finally, minimal use of the anolyte while maintaining high-rate performance is an important design consideration to maximize the volumetric energy density. Based on the conduction properties of MIECs and the open porosity of 3D architectures, 3D MIEC anode architectures are expected to realize reliable Li-metal SSBs by simultaneously achieving high energy density, long-term stability, and rate capability.

6.2. Processing thin-film batteries

The development of ceramic thin-film processing technologies for Li-oxide solid-state electrolytes gave rise to thin-film batteries, representing a promising solution for on-chip integrated energy storage with 3D stacking potential.[631,632] Thin-film SSBs have been intensely researched since the 1990s, after the glass-type Li$_x$PO$_y$N$_z$ (LiPON, $x = 2y + 3z - 5$) electrolyte was invented.[631,633–635] As thin-film components need to be supported by a substrate, careful strategies for stepwise anode–electrolyte–cathode film assembly are required. As each battery component layer requires different processing temperatures to obtain the desired crystalline structure with sufficient Li-ion diffusivity, a component requiring a higher deposition/annealing temperature needs to be deposited before one requiring a lower processing temperature. This approach allows minimization of possible chemical compatibility issues during layer integration. For example, in a LiPON-based thin-film battery
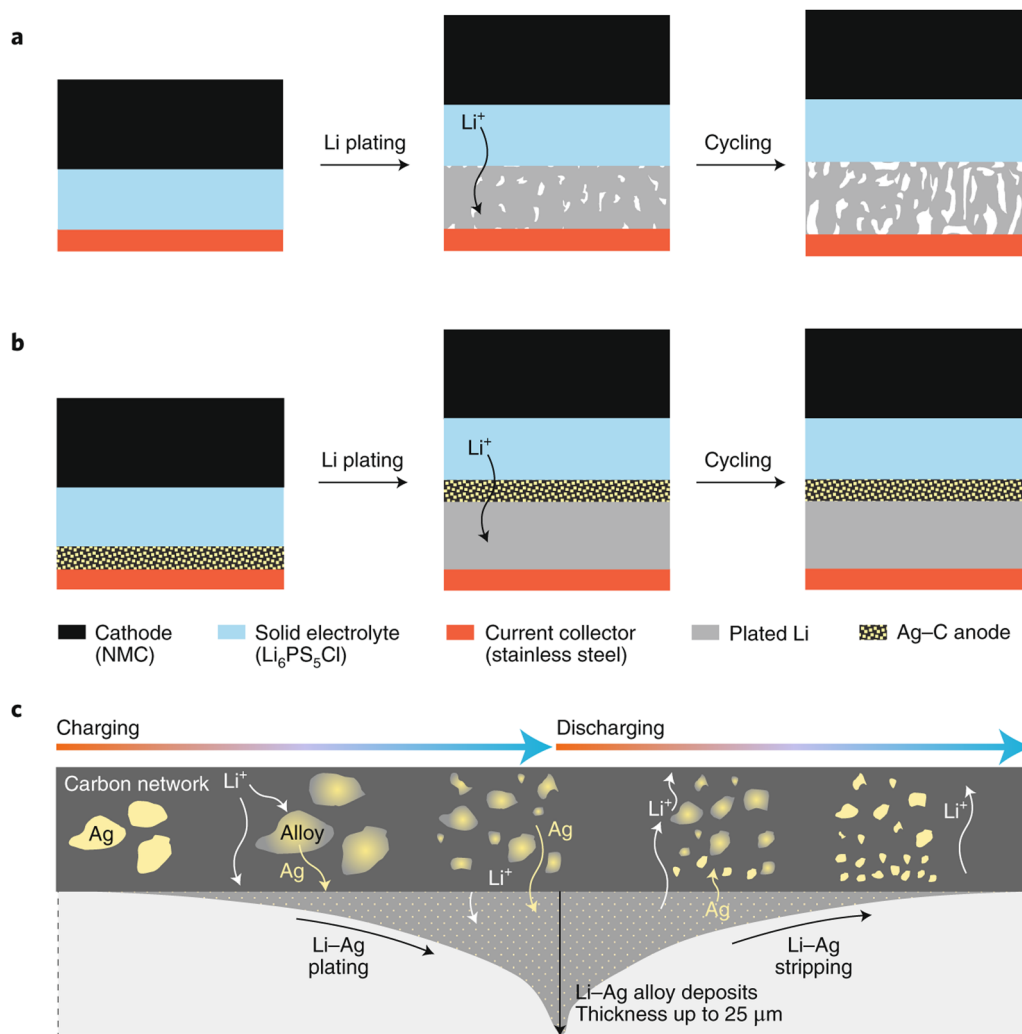
This journal is © The Royal Society of Chemistry 2025

Chem. Soc. Rev., 2025, **54**, 8925–9007 | **8985**

Fig. 12 Morphological effect of the Ag−C nanocomposite anode in ASSLBs. Lithium deposition morphology without (a) and with an Ag−C interlayer (b), and the corresponding mechanism (c) at MIEC−solid electrolyte interfaces, illustrating their effect on plating uniformity and the evolution of silver nanoparticles within the carbon matrix during cycling. Reproduced with permission ref. 631.

system, the $LiCoO_2$ or $LiMn_2O_4$ cathode film is first deposited on the heated substrate at 300–800 °C to induce crystallization and grain growth, followed by deposition of the amorphous LiPON electrolyte and Li-metal anode at room temperature.[635,636] In a similar manner, an amorphous LLZO thin film can be deposited on a cathode layer at room temperature followed by Li-metal anode deposition.[637] For the cubic-phase LLZO electrolyte, which requires a processing temperature above 660 °C,[317] assembly with the cathode layer becomes more complicated. The cathode layer needs to be prepared before depositing the crystalline LLZO not only to avoid the possible chemical reaction at the interface during the LLZO deposition but also to control the crystal orientation of the cathode to achieve the desired Li diffusion path across the cell.[638] Physical shadow masks are typically used to assemble the component layers with desired patterns for planar thin-film batteries. However, the shadow mask does not allow the sizes of batteries below several tens of mm²; nevertheless, microfabrication techniques, such as photolithography and ionic dry etching, can further reduce the footprint of thin-film batteries.[639–642]

6.2.1. 2D structure of a thin-film battery. There are two main planar thin-film SSB architectures: an in-plane[643–645] and a through-plane (stacked)[646–648] design. The in-plane architecture (Fig. 13a) has CCs for both the anode and cathode positioned next to each other on the same substrate, and Li^+ ions are conducted between the cathode and anode metal contacts in-plane. This design was used by the first successfully commercialized solid-state thin-film battery based on LiPON.[401,649] The advantages of this architecture include (i) preventing component short-circuiting (cathode–anode electrode and CC separation), (ii) minimized thermal strain and cracking upon annealing (smaller active contact area between the layers), and (iii) one-step deposition of metal contacts (cathode and anode metal contacts can be deposited on a substrate simultaneously and separated by a gap). However, the long Li^+ diffusion

8986 | *Chem. Soc. Rev.*, 2025, **54**, 8925–9007

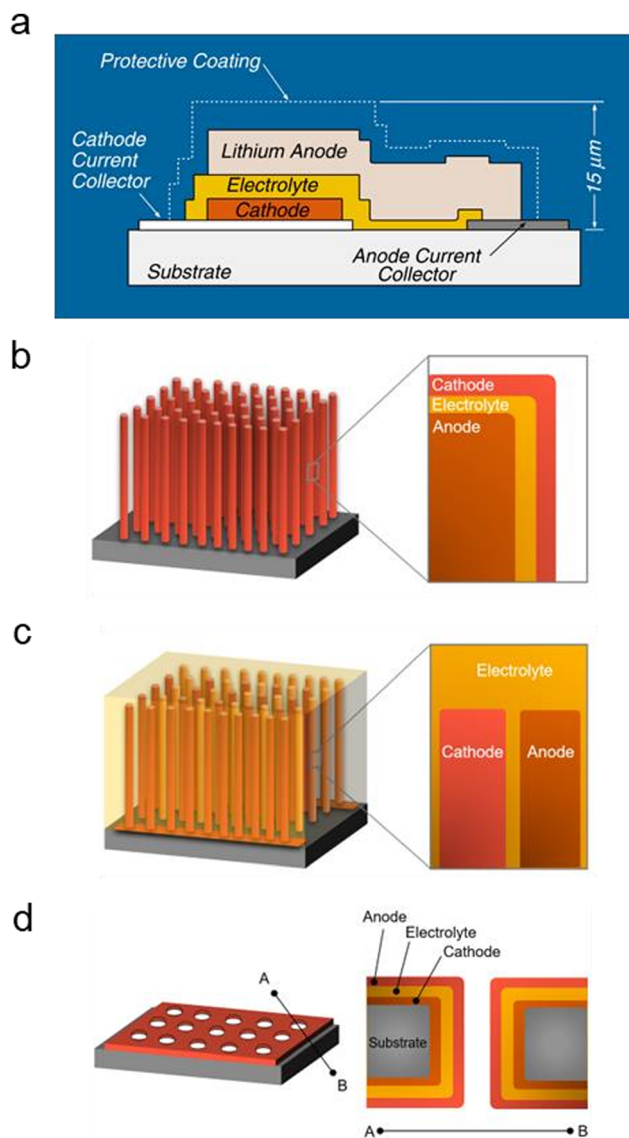This journal is © The Royal Society of Chemistry 2025

Fig. 13 Schematics of different microbattery architectures. (a) 2D in-plane designs and (b)–(d) 3-D designs: 3D microbattery based on nanorods, 3D microbattery based on microchannels, and interdigitated 3D battery, Reproduced with permission ref. 403.

pathway between the cathode and the anode (100 s of μm) and the low contact area of active materials might limit its practical applications, particularly if oxide-based anodes (*e.g.*, spinel $Li_4Ti_5O_{12}$ with low Li^+ diffusion coefficient, $<10^{-6}$ cm^2 s^{-1}, and low electronic conductivity, $<10^{-13}$ S cm$^{-1})$[650,651] are used instead of pure Li metal. The through-plane architecture (Fig. 3) has the CC for the anode placed on top of the anode layer, whereas the CC for the cathode is deposited directly on a substrate, and Li^+ ions are conducted between the stacked metal contacts. It is an alternative design benefiting from (i) the high contact area of active components (leading to higher energy densities) and (ii) the short Li^+-ion diffusion pathway between the cathode and the anode (hundreds of nanometers to hundreds of micrometers, determined by the thickness of

the electrolyte). The shortcomings of this design include higher thermal strain upon annealing, leading to full SSB stack cracking[652] and pinhole formation;[28] increased likelihood of short-circuiting (stacked components); and two-step current collector deposition. For both in-plane and through-plane designs, complicated stack engineering is often required with many additional layers (such as sintering and adhesion layers) to reduce the interfacial resistance.[644]

The choice of the processing route directly controls the electrical, chemical, and mechanical properties of the battery components and ultimately the device performance and determines the potential for scale-up. Thin-film electrodes can be produced by vacuum-based deposition techniques, such as magnetron sputtering, pulsed laser deposition, electron beam evaporation, chemical-vapor deposition, or solution-based deposition techniques, including electrostatic-spray deposition, spray pyrolysis, or sol–gel fabrication.[646,653] To date, fully integrated thin-film battery (microbattery) cell architecture designs, both in-plane and through-plane, have only been realized using sputtering-type techniques and a Li evaporator.[646] We present here an example of a layer-by-layer processing flow based on a single cell of a LiPON-based thin-film battery from Oak Ridge National Laboratory, which consists of the following eight stages: (1) substrate selection, (2) cathode CC deposition, (3) cathode deposition, (4) cathode annealing (optional), (5) anode CC deposition, (6) electrolyte deposition, (7) anode deposition (Li-ion or Li metal), and (8) protective layer deposition.

Substrate selection: MgO, Al_2O_3, quartz glass, and wafer-type coated Si substrates are typically selected as the substrate due to their chemical and thermal stability and lack of metal ion (*e.g.* Mg^{2+}, Al^{3+}) interdiffusion with the metal CC and Li-oxide electrode material upon annealing, showing the highest stability and chemical inertness at higher temperatures ($>700\ °C$).[317,617,635,654–656] However, these substrates are limited by their high thickness (~ 0.5–1 mm), stiffness, and brittleness. The high cost of these substrates also makes them less practical for use in industrial applications. Alternatively, using a flexible metal foil substrate (*e.g.* stainless steel, Cu, Al, Ni) avoids CC deposition.[657–661] However, the material must be stable against thermal treatment such as oxidation or deformation during the entire cell processing (*e.g.* cathode annealing and anode deposition steps). Similarly, a mica or polymer substrate (*e.g.* PDMS) benefits from flexibility but must exhibit thermal and mechanical stability.[645,662]

Cathode current collector deposition, cathode deposition, cathode annealing (optional), and anode current collector deposition: following the substrate selection and preparation (*e.g.*, cleaning pre-treatment), a cathode CC (metal contact) layer is deposited. If an insulating substrate is used, typically a Pt, Au, Cu, Al, or Ni thin layer is deposited on top *via* DC sputtering.[617,662–667] The key challenges here include CC layer delamination (de-wetting) due to poor adhesion to the substrate, which can be suppressed by introducing an adhesion layer of Ti or Cr, and alloying with Li metal from reduced Li^+ ions extracted from the Li-oxide cathode on annealing.[654] In the

This journal is © The Royal Society of Chemistry 2025

Chem. Soc. Rev., 2025, **54**, 8925–9007 | 8987

subsequent step, the cathode layer is deposited, typically using a physical vapor deposition technique. The film of $LiCoO_2$ is the cathode material most frequently used in the fabrication of thin-film batteries due to its exceptional electrochemical performance and thermal and chemical stability as well as relatively less complicated synthesis process compared with other cathode materials. Besides $LiCoO_2$, other cathode films such as $LiMn_2O_4$,[668] $Li(Mn,Ni)_2O_4$,[640] TiO_2,[669] V_2O_5,[156,666,670,671] MoO_x,[672–674] and WO_x,[672] have been explored as well. Thick cathodes are desirable to maximize the active material loading (and hence energy density); however, thicknesses over 1 µm typically lead to crack formation.[675] Furthermore, cathode deposition challenges include chemical instability upon annealing at >500 °C (metal-ion interdiffusion and secondary phase formation at the cathode/electrolyte interface)[592,676] and lattice parameter or thermal expansion coefficient mismatch between the cathode and electrolyte materials, leading to crack and pinhole formation on annealing.[652] Following cathode layer deposition and post-deposition annealing to obtain the desired crystal structure (optional), an anode CC is typically deposited by DC sputtering, which similarly to the cathode CC must exhibit high thermal stability, conductivity, and inertness to Li.

Electrolyte deposition: in the next step, a solid electrolyte layer is deposited, which must be dense, crack- and pinhole-free, and thick enough to avoid short-circuiting, Li dendrite formation, and propagation.[558] Hence, chemical stability of Li-oxide electrolytes makes them promising candidates.[33,677] The key challenge here is to minimize the interfacial interlayer resistance or area-specific resistance (ASR; typically due to insulating interfacial reaction products and/or low cathode/electrolyte contact area) and to achieve good physical interlayer adhesion.[28,558,559] Recently, several studies have employed a LLZO thin film, which has a several-orders-of-magnitude-higher ionic conductivity and wider electrochemical window than LiPON, to design all-solid-state thin-film batteries.[678–681] However, a few technical challenges of fabricating LLZO thin films such as the higher processing temperature and controlling the desired phase and crystallinity have hindered achieving a liquid-free thin-film battery.

Anode deposition (Li-ion or Li metal): finally, anode material deposition is performed, via either RF sputtering (e.g. Si, Al)[654,655,660,682] or Li thermal evaporation (pure Li metal).[634,635,640,664] Due to the high reactivity of Li metal, depositing pure Li metal for the anode layer must be conducted in an inert environment. The anode/electrolyte interface often suffers from high ASR, poor physical interlayer adhesion, and Li dendrite growth along the grain boundaries or cracks in the electrolyte.[28,558] In addition, typically patterning of the CCs, cathode, electrolyte, and anode is achieved via shadow masking to obtain the desired shapes and avoid short-circuiting.[643–645] An anode-free thin-film battery is an alternative structure that does not use an anode layer and instead directly places the metal CC on the electrolyte. During cycling, lithium metal is plated at the interface between the metal and the electrolyte.[617,683] This architecture is beneficial for increasing the energy density and simplifying the assembling process by removing the step of anode layer deposition. However, the major challenges with an anode-free structure are the large volume expansion during Li plating and stripping, causing a structure failure such as cracking and the formation of dead lithium due to the weak binding energy between Li and the anode CC, resulting in a drop of the energy capacity over cycling.[683]

Other solid-state full thin-film battery processing and fabrication challenges include (i) low Li^+ conductivity of a thin-film solid electrolyte (typically $\sim10^{-6}$ S cm^{-1}, orders of magnitude lower compared to that of bulk pellets, $\sim10^{-3}$ S cm^{-1});[401,648,649,684] (ii) thickness range limitation (vacuum fabrication techniques are confined to thicknesses <1 µm,[91] and solution techniques often suffer from densification cracking of ceramic films with thicknesses >1 µm);[685] and (iii) low scalability and throughput, as currently the cell sizes are limited to small geometrical area (<4 cm^2)[686] and time-consuming thin-film fabrication.

6.2.2. 3D structure of a thin-film battery. To further increase the energy density of a thin-film battery, the concept of a 3D architecture of a thin-film battery has been intensively developed. The volumetric energy capacity is determined by the mass loading of the active electrode materials.[687–691] However, the electrode thickness is limited by kinetic restrictions, such as low ionic and electronic conductivity, and structural restrictions, such as film delamination.[687] The structure of 3D thin-film batteries with a large interfacial contact area has been explored to improve the charge-transfer efficiency. Higher energy and power density can also be achieved by increasing the volumetric mass loading of the active electrode materials while keeping the thickness of the component layers small for fast ionic diffusion across the battery components.[692–694] These features lead to improved cycling performance for 3D thin-film batteries compared with that for the planar geometry. In general, 3D thin-film battery architectures (Fig. 13b–d) employ either (i) micro-column structures, where cylindrical templates are used and thin-film battery component layers are sequentially deposited;[660] (ii) micro-channel structures, where channels are etched in the substrate using either shadow masking or photolithography in an initial step followed by filling in of these channels with the thin-film battery constituent materials;[666,695] or (iii) interdigitated 3D battery structures. Although successful works of 3D thin-film battery design are mostly done with a liquid electrolyte and the complex architecture of the electrodes, there are several studies where all the components are solid phase and achieve 3D SSBs.

Fig. 13b displays arrays of columns composed of the substrate, current collectors, active electrode materials, and the electrolyte. Subsequent components are deposited layer-by-layer on the 3D columnar template. The main advantages of this approach include the relatively simple fabrication method and the easily monitored and controlled layer thickness during deposition.[631] However, conformal layer deposition may be challenging if the column arrays are dense and composed of the high-aspect ratio structure, especially during physical vapor

8988 | Chem. Soc. Rev., 2025, **54**, 8925–9007

This journal is © The Royal Society of Chemistry 2025

deposition. The incident flux of the conventional physical vapor deposition technique, such as sputtering or PLD, is directional and normal to the substrate surface, causing poor coverage on the side of the columns.[696] The fragile properties of column structures are also vulnerable to mechanical damage during the charging and discharging process.[631] In Fig. 13c, thin-film battery-component deposited on an etched microchannel substrate are shown. Compared to the architectures shown in Fig. 13b, where individual columns are exposed, the microchannel geometry is mechanically more robust.[666] However, deposition methods are limited to those where the precursors can uniformly access the channels, such as electrodeposition and chemical vapor deposition.[666,695] Monitoring the layer deposition inside the pores cannot be easily achieved. Fig. 13d presents an example of an interdigitated 3D battery structure, which relied on the formation of 3D trenches. The main advantage of 3D trenches is that microchannel substrates are readily available and require relatively simple preparation methods. Besides the examples, 3D SSBs have also been fabricated as various patterns prepared by 3D printing,[697] core–shell nanowires,[692] and textile scaffolds.[101]

The 3D architecture with thin electrode and electrolyte layers is expected to have fast charge and discharge kinetics as well as high capacity due to the effective surface-area enhancement. However, to fully realize these theoretical benefits, significant technological development is still required to address fabrication complexity and performance tradeoffs. For example, the power performance of the 3D SSBs shown is significantly lower than that of similarly prepared 2D planar SSBs composed of LCO, LiPON, and Si as the cathode, electrolyte, and anode, respectively.[660] According to the experimental and computational studies, the major reasons for the poor power performance were the structural inhomogeneity of the 3D structures and uneven internal current density distribution and poor cathode utilization due to the low kinetics in the cathode. This study suggested that improving the electrolyte conductivity to 10^{-5} S cm^{-1} or designing the 3D structure with a constant distance between the anode and the cathode could improve the 3D cell performance. In a more recent study, 3D microchannel SSBs were fabricated using conformal ALD deposition of SnNx, LiPON, and V_2O_5 as the anode, electrolyte and cathode, respectively.[666] The 3D SSB exhibited an order-of-magnitude-higher areal discharge capacity and improved power density compared to a 2D planar SSB assembled using the same battery component materials. However, the energy density was almost an order-of-magnitude lower than that of LiPON-based planar 2D SSBs with 2500-nm thickness of LCO.[635] These contrasting outcomes reflect the sensitive interplay between cell architecture, film thickness, and material utilization. While 3D designs can boost areal capacity and power output through increased active surface area, their total energy density can be compromised by dead volume, limited cathode loading, or incomplete filling of high-aspect-ratio structures. Therefore, rational geometric design, combined with advanced conformal deposition methods and optimized component materials, is essential to achieve the predicted

advantages of 3D architectures without sacrificing volumetric performance.

Overall, the development of Li-ion solid-state thin-film batteries is an area of ongoing research, with scientists and engineers constantly seeking to improve their performance characteristics through new cell designs and fabrication methods. The use of 3D structures in thin-film battery design offers great potential for meeting the increasingly demanding requirements of wireless microdevices, which have seen their footprint decrease while their required power and energy densities increase.

7. Outlook and perspective

The global energy consumption across all sectors in 2023 worked out to a staggering 172 Peta-watt-hour per year, ~82% of which originated from fossil fuels.[698] Across all sectors, in the US, this corresponds to roughly 35% for industrial applications, 36% for transportation, and the remaining 29% for residential and commercial heating and cooling budgets.[699] Most of the energy used for transportation (90%) comes from petroleum, which accounts for 23% of the global-energy-related CO_2 emissions.[699] As energy-storage systems, batteries are needed because of the rapid rise of electric mobility and to store energy from renewable resources (i.e., solar, wind). As such, batteries play a crucial role in combating climate change and achieving ambitious goals such as that of the European Commission's goal to reduce greenhouse gas emissions by 55% below 1990 levels by 2030, phasing out new passenger cars and light commercial vehicles with internal combustion engines starting in 2035, and creating a carbon-neutral economy in the EU by 2050.[700] By 2030, ~90% of battery demand will be in road transport and more than 300 Gigafactories are forecasted to be built in the US (~0.8 TWh by LG Chem, SK innovation, Panasonic, Envision AESC, CATL, etc.), Europe (~1 TWh by Tesla, Northvolt, PowerCo SE, CATL, etc.), and China (~2.6 TWh by BYD, CATL, EVE, Tesla, LG Chem, etc.) to produce >4 TWh of the needed cell capacity. Today's battery demand is dominated by China with 3 in every 10 light vehicles bought in 2023 being battery electric or plug-in hybrid vehicles, whereas Europe and the USA still have to catch up in their contribution and market shares. China does not possess a significant amount of the relevant raw materials; however, in the past decade, it has been heavily subsidizing its battery value chain, investing in processing steps and cell components and manufacturing and thus owning a more mature battery supply chain. The EU and USA may experience delays in global EV adoption due to major challenges such as lack of infrastructure and local supply chain and recycling capabilities but have recently established new policies to serve as a catalytic factor to spur investments. The US has established several policies that support both the supply and demand of the battery market: (i) the Bipartisan Infrastructure Law, the largest federal investment in public transportation, which includes over $18 billion in investments to reduce emissions through

This journal is © The Royal Society of Chemistry 2025

Chem. Soc. Rev., 2025, 54, 8925–9007 | 8989

electrification of vehicles; (ii) the Inflation Reduction Act, which offers a variety of game-changing tax-related credits across the clean energy sector that can potentially reduce battery-pack costs by $\sim$27% and thus support local (or allied) cell manufacturing and supply chain. In the EU, the European's Green Deal and the Net Zero Industry Act have the aims of domestically producing 85% of batteries and boosting their recycling. The EU has adopted new agnostic battery regulations for batteries placed on the EU market (produced or imported) and starting in 2026/2027, the ''Battery Passport'', a digital document that contains comprehensive labeling and information on the battery components, carbon footprint, and recycled content, among other information, is expected to be implemented in all batteries with capacities larger than 2 kWh and should serve as a strong foundation for current and future recycling efforts.

The key metrics of batteries for stringent EV applications include the safety, costs, range, performance per volume, and extended shelf and cycle life,[4] which may translate into the following requirements at the cell level: (i) safe and effective operation at −30 to 100 °C[4] under minimal (preferably without) stack pressure ($\sim$ 1 MPa but ideally below 0.1 MPa); (ii) competitive energy densities ($\sim$400 Wh kg^{-1} and 1000 Wh L^{-1}), fast charging rates ($>$1C and preferably as high as 3–6C), and extended cycle life; (iii) cost-effective and scalable processing and manufacturing, preferably compatible with current Li-ion battery processing routes (and incorporated as 'drop-in' technologies); (iv) material costs and supply chains; and potentially (v) recycling of battery components. Different vehicle segments will most likely dictate the required level of technological innovation. Throughout the last decade, cathode technology has been the main driver for the incremental energy-density improvements of LIBs. Although entry-level EVs, required to deliver cost-competitive battery solutions, can adopt Li-ion technologies with LFP/LMFP cathodes and Na-ion technologies, mid-level EVs, required to support fast-charging solutions, can adopt LIBs with variations of NMC/NCA or even use Ni- and Co-free chemistries such as LFP. Premium vehicles typically adopt the latest battery innovation and are currently based on Li-ion technologies with NMC/NCA cathodes; however, the desired significant enhancement in battery performance will require the implementation of advanced solid state electrolyte ceramic technologies towards higher energy densities enabling the use of high-capacity anodes (Li metal or Si), cathodes (sulfur-based), and/or solid-state electrolytes (which eliminate the need for a liquid electrolyte). All solid or quasi-solid ($\leq$5% liquid/gel electrolyte), or hybrid ($\sim$5%–10% liquid/gel electrolyte) electrolytes may be the optimal intermediate solution or perhaps the ultimate one.

Hybrid and solid-state batteries, where liquid electrolytes are replaced with a solid electrolyte with a high (close to unity) Li-ion transference number, are one of the leading technologies targeting EV applications. These may possess fast charging capabilities and high power densities due to their potential combination with high-voltage cathodes and Li-metal anodes. Moreover, the possible bi-polar stacking configuration (series connection of battery cells), where the cathode and anode materials are coated from each side of the current collector, may also contribute to high output voltage and high energy density. Nonetheless, SSBs are also prone to various material and interfacial stability and processing challenges. The cathode–electrolyte solid–solid interface requires satisfactory interfacial contact to allow for percolated electron and Li$^+$-ion transport at the interface. For oxides, it is typically challenging to establish a good solid–solid interface with high ionic conductivity and low interfacial resistance to secure high overall performance. Importantly, the cathode–solid electrolyte interfaces should have chemical, electrochemical, and electrochemo-mechanical stability during battery operation; however, the stiff nature of the materials coupled with volume changes during discharge–charge cycles hampers the interfacial contact between the materials, leading to contact loss and microstructural cracking. On the other hand, the integration of an oxide-based cathode composite and the mechanically stiff solid electrolyte may obviate the need for external stacking pressure, as currently required for sulfide-based SSBs, or at least require relatively low stacking pressure.[701] The development of oxide-based Li-metal SSBs is also associated with dendrite propagation, short-circuits, and safety concerns related to the risk of thermal runaway. It thus remains unclear how the safety risk is reduced with the replacement of LIBs with Li-metal-based SSBs. However, if SSBs would show a clear advantage of lower safety risks, which may reduce the current stringent thermal management and engineering safety components, their volumetric and gravimetric energy would potentially increase even further at the pack level. In cases where all major requirements are met, especially the competitive performance metrics, widespread commercialization of SSBs will largely depend on their material, processing, and manufacturing costs, the last of which might mandate energy-demanding processing routes with low-scalability prospects in the case of oxide-based SSBs. Although such a cost estimation is complicated considering the low level of technological maturity, it has been previously estimated that the material value of oxide solid electrolytes (e.g., LLZO, LLTO, LATP), without their processing-related costs, is already similar to or higher than that of liquid electrolytes, which leaves minimal wiggle room for their processing costs and almost surely eliminates technologies that are based on high-temperature sintering steps.[24,48] The Achilles heel of the oxide solid electrolytes is thus the high-temperature sintering processes that are typically required to maintain good physical contact between oxide-based cell components. Alternative low-temperature wet-chemical solution processing routes (e.g., sequential deposition synthesis) are still at an early stage of development and may potentially enable the introduction of oxide-based coating in a non-oxide SSB at a low price-tag, where a high stability against Li metal is needed. In addition, oxide-based solid electrolytes are typically associated with room-temperature ionic conductivities below 1 mS cm^{-1}, which are sufficient for some thickness ranges but are still considered low, especially for incorporation in a composite cathode, where tortuosity may reduce the effective conductivity of the solid

8990 | Chem. Soc. Rev., 2025, 54, 8925–9007

This journal is © The Royal Society of Chemistry 2025

electrolyte even further, requiring approximately order-of-magnitude-higher effective ionic conductivities.[116] The development of a dense (>99%) and thin (1–20 μm) solid electrolyte capable of being integrated into sheet-to-sheet processing requires attention in the development of oxide-based SSBs or for future hybrid battery types. For context, LIB manufacturing has a 35–80 m min^{-1} throughput for the coating process (accounting for ~15% of the cost/year and 1.4% of the energy consumption per cell per kWh),[702] which is higher by several orders of magnitude compared to the techniques presented in the paper. Unlike for LIBs,[703] there are no performance and cost modeling tools available for SSBs considering the low maturity level of this technology, making it difficult to provide any reliable production time, cost, scale-up, and performance forecasts and expectations.

How can battery cost be reduced without compromising battery performance? Theoretically, a combination of regulations, enforcement, and financial incentives alongside manufacturing improvement (higher throughput, lower scrap rate, etc.), cell chemistry improvement, reduction of material cost through the investment of battery and automotive makers in raw materials through long-term agreements with material providers and in mining and refinement projects, among other approaches, could reduce battery cost. Although battery prices highly rely on the prices of commodities (depending on their capacity and availability), great uncertainties remain, mainly due to unclear future battery capacity requirements.[8] For example, the prices of Li have decoupled from their production costs since ~2015, the year EVs went mainstream. Reduced manufacturing costs can be achieved by lowering the processing temperature and duration and by ensuring smooth technology transition ('drop-in' technologies) by selecting electrode-production and cell-assembly routes that are similar to those of current technologies used in gigafactories, among other approaches. Design principles incorporating interface engineering (e.g., coating layers, additives, sintering aids), new battery designs (e.g., bi-layers and tri-layers of porous and dense ceramic structures) and advanced processing techniques (ultra-high-temperature sintering) are some of the innovative approaches recently proposed to realize all SSBs. Nonetheless, such approaches typically introduce additional complexities to the system and are not feasible to manufacture at scale; in addition, understanding of the chemo-electro-mechanical performance under diverse conditions such as varied temperature and stack pressure is lacking. Using wet-chemical manufacturing techniques ("from powder to slurries to film") such as tape-casting and blade coating of slurries, which are transferable from the LIB production line, will be highly advantageous to facilitate scale-up (also still costly and considered to account for 50% of the power consumption[704] due to costly drying processes). However, once a sintering step is needed, this transition is questionable. Dry battery electrode technology ("from powder to film") in SSBs is an emerging concept and technology that would eliminate toxic solvents (only using the active material and a low binder content), increasing the throughput by two to three times and having the potential to reduce the

energy consumption by 20–30%. Such technology can produce flexible and thick high-energy electrodes (>4 mAh cm^{-2}) and robust solid electrolyte coatings (<50 μm) that are compatible with roll-to-roll manufacturing.[704] The dry battery electrode technique is still in its infancy, presenting challenges in terms of adhesion, binder selection, mixing, interfacial stability, optimization, and scale-up, thereby requiring further research and development.

Reduction in material costs can also be achieved by replacing costly elements or potentially through recycling. Relying on abundant, sustainable, ecologically recyclable, and inexpensive materials that are easy to process and can be found in stable countries is an ultimate desire. Looking at the periodic table, several tens of possibilities may align with these criteria, resulting in billions of possible combinations considering that battery materials are typically composed of 4–5 elements. Identifying and exploring new materials and the processing space for battery applications is an important step towards the development of next-generation energy-storage applications. Here, combining high-throughput automated ceramic synthesis (when possible), data management, data mining, autonomous material characterization, and data analysis guided by artificial intelligence (AI) and machine learning (ML) will aid in reinventing the way research is conducted. Although recycling and life-cycle assessments can indicate the most and least promising recyclable chemistries, the lack of standardization, legislation, business models, collection infrastructure, and technology limits their potential impact. The breadth of Li-battery chemistries and uncertainties regarding the dominating LIB compositions and chemistries, not only at the cathode level (LCO, LMO, NMC, NCA, LFP) and anode level (carbon/graphite, Si, Li, LTO) but also with the introduction of solid electrolytes (oxides, sulfides, polymers, or a combination thereof), complicate the task of recycling feasibility even further. Nevertheless, given that SSBs are only in their initial research and development stage, sustainable design, processing, and scalable recycling approaches should be considered concurrently to ensure sustainable handling of EOL batteries. Although the use of a Li-metal anode has the potential to increase the overall cell energy densities of SSBs, the anode-free concept also offers tantalizing advantages with respect to the recycling process as it eliminates the need for an anode within the cell and thus for its recovery. Yet, safety precautions must be placed to secure safe handling in the case of potential Li-metal residues. It is thus clear, also from the recyclability point of view, that focusing on research and development of battery technologies with higher specific energies towards decreasing the Li material intensity value (g/Wh) should be pursued and intensified to reduce the worldwide cumulative Li demand. Alternatively, identifying chemistries that avoid using Co and other CRMs and post-Li batteries based on abundant materials that are not considered CRMs, such as sodium, magnesium, aluminum, and calcium, should also be pursued.[8,124] The recycling of EOL batteries could be a viable strategy to narrow the gap between supply and demand by increasing the supply of battery-related critical raw materials and mitigating potential price fluctuations. The effect of

This journal is © The Royal Society of Chemistry 2025

Chem. Soc. Rev., 2025, 54, 8925–9007 | 8991

recycling of EOL batteries on the fraction of materials needed for Li batteries for EVs remains unclear, exemplified by the different estimations that sometimes lead to contradicting results.[8,140] Although some estimations indicate that with increasing global production capacity for Li, Co, Ni, *etc.*, recycling will likely play only a minor role in reducing the primary material demand, the life-cycle perspective also has an environmental importance considering materials that are not recycled at their EOL end up buried in landfills.

A closing note. The key to the success of SSBs will rely on long-term performance improvement (specific capacity and power), economic manufacturing routes and overall cost, material availability, and safety. A fundamental understanding of the transport properties, volume changes, Li dendrite propagation, and decomposition reactions at the interfaces is key to mitigating the current limitations of SSBs and progressing towards novel cell concepts. The large-scale manufacturing of SSBs must also be addressed. Extensive work has been conducted to develop a solid-state electrolyte with high stability towards the cathode and anode interfaces; however, the integration of solid electrolytes into hybrid and full SSB cells and their manufacture at low processing costs, with respect to future SSB chemistries, designs, processing, and manufacturing scalability, remain still a challenge. When promising preliminary performance data are presented, it is also important to consider other factors such as the raw materials used and the scalability of the technology and to avoid over-extrapolation and false promises. Although economics will be the dominating factor in determining battery-technology implementation in the EV market, the environmental and social considerations, including lower greenhouse gas emissions, less exploitation of ecological resources, less human exposure to mining toxic materials, lower waste disposal in the landfills of third-world countries, as well as fewer human rights violations, should also lead to a regulatory drive to maintain closed-loop battery manufacturing with recycling at the EOL.

Conflicts of interest

The authors declare no competing interests.

Data availability

The authors declare no data/software citations.

Acknowledgements

References

1 C. Diaz, 1 in 7 cars sold globally now is electric, https://www.weforum.org/agenda/2023/03/ev-car-sales-energy-environment-gas/#:~:text=Globalsales of electric cars, International Energy Agency (IEA).
2 Tesla Model S Plaid, https://ev-database.org/car/1405/Tesla-Model-S-Plaid.
3 X.-G. Yang, T. Liu and C.-Y. Wang, *Nat. Energy*, 2021, **6**, 176–185.
4 A. B. Cohn, C. Underwater and H. Preserves, *Nat. Commun.*, 2023, **14**, 420.
5 L. Mauler, F. Duffner, W. G. Zeier and J. Leker, *Energy Environ. Sci.*, 2021, **14**, 4712–4739.
6 Battery Pack Prices Fall to an Average of $132/kWh, But Rising Commodity Prices Start to Bite, https://about.bnef.com/blog/battery-pack-prices-fall-to-an-average-of-132-kwh-but-rising-commodity-prices-start-to-bite/.
7 V. Henze, Lithium-ion Battery Pack Prices Rise for First Time to an Average of $151/kWh, https://about.bnef.com/blog/lithium-ion-battery-pack-prices-rise-for-first-time-to-an-average-of-151-kwh/.
8 C. Xu, Q. Dai, L. Gaines, M. Hu, A. Tukker and B. Steubing, *Commun. Mater.*, 2020, **1**, 99.
9 US Department of Energy, Batteries 2021 Annual Progress Report, 2021.
10 J. Amici, P. Asinari, E. Ayerbe, P. Barboux, P. Bayle-Guillemaud, R. J. Behm, M. Berecibar, E. Berg, A. Bhowmik, S. Bodoardo, I. E. Castelli, I. Cekic-Laskovic, R. Christensen, S. Clark, R. Diehm, R. Dominko, M. Fichtner, A. A. Franco, A. Grimaud, N. Guillet, M. Hahlin, S. Hartmann, V. Heiries, K. Hermansson, A. Heuer, S. Jana, L. Jabbour, J. Kallo, A. Latz, H. Lorrmann, O. M. Løvvik, S. Lyonnard, M. Meeus, E. Paillard, S. Perraud, T. Placke, C. Punckt, O. Raccurt, J. Ruhland, E. Sheridan, H. Stein, J. M. Tarascon, V. Trapp, T. Vegge, M. Weil, W. Wenzel, M. Winter, A. Wolf and K. Edström, *Adv. Energy Mater.*, 2022, **12**, 2102785.
11 Y. Lu, X. Rong, Y. S. Hu, L. Chen and H. Li, *Energy Storage Mater.*, 2019, **23**, 144–153.
12 L. Goldie-Scot, A Behind the Scenes Take on Lithium-ion Battery Prices, https://about.bnef.com/blog/behind-scenes-take-lithium-ion-battery-prices/.

8992 | *Chem. Soc. Rev.*, 2025, **54**, 8925–9007

This journal is © The Royal Society of Chemistry 2025

13 N. Shirouzu and P. Lienert, Tesla's secret batteries aim to rework the math for electric cars and the grid, https://www.reuters.com/article/us-autos-tesla-batteries-exclusive/exclusive-teslas-secret-batteries-aim-to-rework-the-math-for-electric-cars-and-the-grid-idUSKBN22Q1WC.

14 Top 10 Energy Storage Trends in 2023, https://about.bnef.com/blog/top-10-energy-storage-trends-in-2023/.

15 N. Bullard, *Electric Car Price Tag Shrinks Along With Battery Cost*, https://about.bnef.com/blog/bullard-electric-car-price-tag-shrinks-along-battery-cost/.

16 International Energy Agency (IEA), Global EV Outlook 2022 Securing supplies for an electric future, 2022.

17 D. Harrison, Electric Vehicle Battery Supply Chain Analysis, 2021.

18 K. Liu, Y. Liu, D. Lin, A. Pei and Y. Cui, *Sci. Adv.*, 2018, 4, eaas9820.

19 P. J. Mankowski, J. Kanevsky, P. Bakirtzian and S. Cugno, *Burns*, 2016, 42, e61.

20 N. Niese, Battery Market Trends by Boston Consulting Group, 2023.

21 G. Harper, R. Sommerville, E. Kendrick, L. Driscoll, P. Slater, R. Stolkin, A. Walton, P. Christensen, O. Heidrich, S. Lambert, A. Abbott, K. Ryder, L. Gaines and P. Anderson, *Nature*, 2019, 575, 75–86.

22 K. J. Huang, G. Ceder and E. A. Olivetti, *Joule*, 2021, 5, 564–580.

23 K. B. Hatzell and Y. Zheng, *MRS Energy Sustain.*, 2021, 8, 33–39.

24 A. Schmaltz, W. T. Thomas; L. Weymann; P. Voß and C. T. Neef, Solid-State Battery Roadmap, 2022, 1–112.

25 Y. Kato, S. Hori, T. Saito, K. Suzuki, M. Hirayama, A. Mitsui, M. Yonemura, H. Iba and R. Kanno, *Nat. Energy*, 2016, 1, 16030.

26 P. Albertus, S. Babinec, S. Litzelman and A. Newman, *Nat. Energy*, 2018, 3, 16.

27 J. Li, C. Ma, M. Chi, C. Liang and N. J. Dudney, *Adv. Energy Mater.*, 2015, 5, 1–6.

28 T. Famprikis, P. Canepa, J. A. Dawson, M. S. Islam and C. Masquelier, *Nat. Mater.*, 2019, 18, 1278–1291.

29 J. Sakamoto, *Handbook of Solid State Batteries*, 2015, pp. 391–414.

30 J. C. Bachman, S. Muy, A. Grimaud, H. H. Chang, N. Pour, S. F. Lux, O. Paschos, F. Maglia, S. Lupart, P. Lamp, L. Giordano and Y. Shao-Horn, *Chem. Rev.*, 2016, 116, 140–162.

31 Y. Meesala, A. Jena, H. Chang and R.-S. Liu, *ACS Energy Lett.*, 2017, 2, 2734–2751.

32 C. Yang, K. Fu, Y. Zhang, E. Hitz and L. Hu, *Adv. Mater.*, 2017, 29, 1–28.

33 A. Manthiram, X. Yu and S. Wang, *Nat. Rev. Mater.*, 2017, 2, 1–16.

34 K. Takada, *J. Power Sources*, 2018, 394, 74–85.

35 X. Judez, H. Zhang, C. Li, G. G. Eshetu, J. A. González-Marcos, M. Armand and L. M. Rodriguez-Martinez, *J. Electrochem. Soc.*, 2018, 165, A6008–A6016.

36 D.-H. Liu, Z. Bai, M. Li, A. Yu, D. Luo, W. Liu, L. Yang, J. Lu, K. Amine and Z. Chen, *Chem. Soc. Rev.*, 2020, 49, 2869–2885.

37 F. Han, Y. Zhu, X. He, Y. Mo and C. Wang, *Adv. Energy Mater.*, 2016, 6, 1–9.

38 S. A. Pervez, M. A. Cambaz, V. Thangadurai and M. Fichtner, *ACS Appl. Mater. Interfaces*, 2019, 11, 22029–22050.

39 A. Banerjee, X. Wang, C. Fang, E. A. Wu and Y. S. Meng, *Chem. Rev.*, 2020, 120, 6878–6933.

40 K. Kerman, A. Luntz, V. Viswanathan, Y.-M. Chiang and Z. Chen, *J. Electrochem. Soc.*, 2017, 164, A1731–A1744.

41 H. Lee, P. Oh, J. Kim, H. Cha, S. Chae, S. Lee and J. Cho, *Adv. Mater.*, 2019, 31, 1–26.

42 Q. Liu, Z. Geng, C. Han, Y. Fu, S. Li, Y. He, F. Kang and B. Li, *J. Power Sources*, 2018, 389, 120–134.

43 B. J. Smith, G. M. Phillip, M. E. Sweeney, A. J. Samson, K. Hofstetter, S. Bag, V. Thangadurai, B. J. Smith, G. M. Phillip, M. E. Sweeney, A. J. Samson, K. Hofstetter, S. Bag and V. Thangadurai, *Energy Environ. Sci.*, 2019, 12, 2957–2975.

44 C. Wang, K. Fu, S. P. Kammampata, D. W. Mcowen, A. J. Samson, L. Zhang, G. T. Hitz, A. M. Nolan, E. D. Wachsman, Y. Mo, V. Thangadurai and L. Hu, *Chem. Rev.*, 2020, 120, 4257–4300.

45 K. J. Kim, M. Balaish, M. Wadaguchi, L. Kong and J. L. M. Rupp, *Adv. Energy Mater.*, 2021, 11, 2002689.

46 H. Shen, E. Yi, M. Amores, L. Cheng, N. Tamura, D. Y. Parkinson, G. Chen, K. Chen and M. Doeff, *J. Mater. Chem. A*, 2019, 7, 20861–20870.

47 A. Banerjee, X. Wang, C. Fang, E. A. Wu and Y. S. Meng, *Chem. Rev.*, 2020, 120, 6878–6933.

48 M. Balaish, J. C. Gonzalez-Rosillo, K. J. Kim, Y. Zhu, Z. D. Hood and J. L. M. Rupp, *Nat. Energy*, 2021, 6, 227–239.

49 P. H. L. Notten, F. Roozeboom, R. A. H. Niessen and L. Baggetto, *Adv. Mater.*, 2007, 19, 4564.

50 C. Chen, Q. Li, Y. Li, Z. Cui, X. Guo and H. Li, *ACS Appl. Mater. Interfaces*, 2018, 10, 2185–2190.

51 D. Molina, D. M. Piper, T. A. Yersak and S. Lee, *J. Electrochem. Soc.*, 2013, 160, A77.

52 M. Yamamoto, Y. Terauchi, A. Sakuda and M. Takahashi, *Sci. Rep.*, 2018, 8(2), 1212.

53 D. H. S. Tan, Y. Chen, H. Yang, W. Bao, B. Sreenarayanan, J. Doux, W. Li, B. Lu, S. Ham, B. Sayahpour, J. Scharf, E. A. Wu, G. Deysher, H. E. Han, H. J. Hah, H. Jeong, J. B. Lee, L. Si and L. Si, *Science*, 2021, 373, 1494–1499.

54 C. Heubner, S. Maletti, H. Auer, J. Hüttl, K. Voigt, O. Lohrberg, K. Nikolowski, M. Partsch and A. Michaelis, *Adv. Funct. Mater.*, 2021, 16, 2106608.

55 H. Huo and J. Janek, *ACS Energy Lett.*, 2022, 7, 4005–4016.

56 K. V. Kravchyk, H. Zhang, F. Okur and M. V. Kovalenko, *Acc. Mater. Res.*, 2022, 3, 411–415.

57 V. Thangadurai, J. Schwenzel and W. Weppner, *Ionics*, 2005, 11, 11–23.

58 V. Thangadurai, S. Narayanan and D. Pinzaru, *Chem. Soc. Rev.*, 2014, 43, 4714–4727.

59 F. Han, Y. Zhu, X. He, Y. Mo and C. Wang, *Adv. Energy Mater.*, 2016, 6, 1–9.

60 S. Ohta, T. Kobayashi and T. Asaoka, *J. Power Sources*, 2011, 196, 3342–3345.

This journal is © The Royal Society of Chemistry 2025

Chem. Soc. Rev., 2025, 54, 8925–9007 | 8993

61 V. Thangadurai, D. Pinzaru, S. Narayanan and A. K. Baral, *J. Phys. Chem. Lett.*, 2015, DOI: **10.1021/jz501828v**.

62 M. J. Wang, E. Kazyak, N. P. Dasgupta and J. Sakamoto, *Joule*, 2021, **5**, 1371–1390.

63 R. Chen, M. Adelaide, J. Lu, L. Chen, R. Chen, A. M. Nolan, J. Lu, J. Wang, X. Yu and Y. Mo, *Joule*, 2020, **4**, 812–821.

64 C. Singer, H. C. Töpper, T. Kutsch, R. Schuster, R. Koerver and R. Daub, *ACS Appl. Mater. Interfaces*, 2022, **14**, 24245–24254.

65 Y. Deng, C. Eames, B. Fleutot, R. David, J. N. Chotard, E. Suard, C. Masquelier and M. S. Islam, *ACS Appl. Mater. Interfaces*, 2017, **9**, 7050–7058.

66 T. Okumura, S. Taminato, Y. Miyazaki, M. Kitamura, T. Saito, T. Takeuchi and H. Kobayashi, *ACS Appl. Energy Mater.*, 2020, **3**, 3220–3229.

67 L. Wei, S. T. Liu, M. Balaish, Z. Li, X. Y. Zhou, J. L. M. Rupp and X. Guo, *Mater. Today*, 2022, **58**, 297–312.

68 X. Liu, Z. Xiao, H. Peng, D. Jiang, H. Xie, Y. Sun, S. Zhong, Z. Qian and R. Wang, *Chem. – Asian J.*, 2022, **17**, e202200929.

69 W. Liao and C. Liu, *ChemNanoMat*, 2021, **7**, 1177–1187.

70 L. Z. Fan, H. He and C. W. Nan, *Nat. Rev. Mater.*, 2021, **6**, 1003–1019.

71 R. C. Agrawal and G. P. Pandey, *J. Phys. D:Appl. Phys.*, 2008, **41**, 223001.

72 C. F. N. Marchiori, R. P. Carvalho, M. Ebadi, D. Brandell and C. M. Araujo, *Chem. Mater.*, 2020, **32**, 7237–7246.

73 H. Zhang, F. Chen, O. Lakuntza, U. Oteo, L. Qiao, M. Martinez-Ibañez, H. Zhu, J. Carrasco, M. Forsyth and M. Armand, *Angew. Chem., Int. Ed.*, 2019, **58**, 12070–12075.

74 L. E. Marbella, S. Zekoll, J. Kasemchainan, S. P. Emge, P. G. Bruce and C. P. Grey, *Chem. Mater.*, 2019, **31**, 2762–2769.

75 S. Sand, J. L. M. Rupp and B. Yildiz, *Chem. Soc. Rev.*, 2025, **54**, 178–200.

76 Blue Solutions Bollore, Battery Technology, **https://www.blue-solutions.com/en/battery-technology/**.

77 P. Adeli, J. D. Bazak, K. H. Park, I. Kochetkov, A. Huq, G. R. Goward and L. F. Nazar, *Angew. Chem., Int. Ed.*, 2019, **58**, 8681–8686.

78 Z. Zhang, Y. Shao, B. Lotsch, Y. S. Hu, H. Li, J. Janek, L. F. Nazar, C. W. Nan, J. Maier, M. Armand and L. Chen, *Energy Environ. Sci.*, 2018, **11**, 1945–1976.

79 N. Kamaya, K. Homma, Y. Yamakawa, M. Hirayama, R. Kanno, M. Yonemura, T. Kamiyama, Y. Kato, S. Hama, K. Kawamoto and A. Mitsui, *Nat. Mater.*, 2011, **10**, 682–686.

80 R. Kanno, T. Hata, Y. Kawamoto and M. Irie, *Solid State Ionics*, 2000, **130**, 97–104.

81 L. J. Miara, G. Ceder, J. C. Kim, S. P. Ong, Y. Wang, Y. Mo and W. D. Richards, *Nat. Mater.*, 2015, **14**, 1026–1031.

82 L. Zhou, A. Assoud, Q. Zhang, X. Wu and L. F. Nazar, *J. Am. Chem. Soc.*, 2019, **141**, 19002–19013.

83 F. Walther, R. Koerver, T. Fuchs, S. Ohno, J. Sann, M. Rohnke, W. G. Zeier and J. Janek, *Chem. Mater.*, 2019, **31**, 3742–3755.

84 S. Wang, Y. L. Ruyi Fang, C. X. Yuan Liu, F. H. Richter and C.-W. Nan, *J. Mater.*, 2021, **7**, 209–218.

85 Y. Xiao, Y. Wang, S. H. Bo, J. C. Kim, L. J. Miara and G. Ceder, *Nat. Rev. Mater.*, 2020, **5**, 105–126.

86 J. Wu, L. Shen, Z. Zhang, G. Liu, Z. Wang, D. Zhou, H. Wan, X. Xu and X. Yao, *All-Solid-State Lithium Batteries with Sulfide Electrolytes and Oxide Cathodes*, Springer, Singapore, 2021, vol. 4.

87 O. G. Gromov, G. B. Kunshina, A. P. Kuz'min and V. T. Kalinnikov, *Russ. J. Appl. Chem.*, 1996, **69**, 385–388.

88 W. J. J. Kwon, H. Kim, K. N. N. Jung, W. Cho, S. H. H. Kim, J. W. W. Lee and M. S. S. Park, *J. Mater. Chem. A*, 2017, **5**, 6257–6262.

89 J. Kim, J. Kim, M. Avdeev, H. Yun and S. J. Kim, *J. Mater. Chem. A*, 2018, **6**, 22478–22482.

90 S. Qin, X. Zhu, Y. Jiang, M. Ling, Z. Hu and J. Zhu, *Appl. Phys. Lett.*, 2018, **112**, 113901.

91 A. J. Samson, K. Hofstetter, S. Bag and V. Thangadurai, *Energy Environ. Sci.*, 2019, **12**, 2957–2975.

92 K. Yang, L. Chen, J. Ma, Y. He and F. Kang, *InfoMat*, 2021, **3**, 1195–1217.

93 L. J. Miara, W. D. Richards, Y. E. Wang and G. Ceder, *Chem. Mater.*, 2015, **27**, 4040–4047.

94 W. D. Richards, L. J. Miara, Y. Wang, J. C. Kim and G. Ceder, *Chem. Mater.*, 2016, **28**, 266–273.

95 Y. Zhu, X. He and Y. Mo, *J. Mater. Chem. A*, 2015, **4**, 1–14.

96 T. Yoshinari, R. Koerver, P. Hofmann, Y. Uchimoto, W. G. Zeier and J. Janek, *ACS Appl. Mater. Interfaces*, 2019, **11**, 23244–23253.

97 Y. Xiao, L. J. Miara, Y. Wang and G. Ceder, *Joule*, 2019, **3**, 1252–1275.

98 K. J. Kim and J. L. M. Rupp, *Energy Environ. Sci.*, 2020, **13**, 4930–4945.

99 S. Randau, D. A. Weber, O. Kötz, R. Koerver, P. Braun, A. Weber, E. Ivers-Tiffée, T. Adermann, J. Kulisch, W. G. Zeier, F. H. Richter and J. Janek, *Nat. Energy*, 2020, **5**, 259–270.

100 J. Schnell, F. Tietz, C. Singer, A. Hofer, N. Billot and G. Reinhart, *Energy Environ. Sci.*, 2019, **12**, 1818–1833.

101 G. T. Hitz, D. W. McOwen, L. Zhang, Z. Ma, Z. Fu, Y. Wen, Y. Gong, J. Dai, T. R. Hamann, L. Hu and E. D. Wachsman, *Mater. Today*, 2019, **22**, 50–57.

102 E. Yi, H. Shen, S. Heywood, J. Alvarado, D. Y. Parkinson, G. Chen, S. W. Sofie and M. M. Doeff, *ACS Appl. Energy Mater.*, 2020, **3**, 170–175.

103 K. Xu, *Chem. Rev.*, 2004, **104**, 4303–4418.

104 D. R. Rajagopalan Kannan, P. K. Terala, P. L. Moss and M. H. Weatherspoon, *Int. J. Electrochem.*, 2018, 1–7.

105 X. Lin, M. Salari, L. M. R. Arava, P. M. Ajayan and M. W. Grinstaff, *Chem. Soc. Rev.*, 2016, **45**, 5848–5887.

106 S. Wu, R. Xiong, H. Li, V. Nian and S. Ma, *J. Energy Storage*, 2020, **27**, 101059.

107 X. Lin, M. Salari, L. M. R. Arava, P. M. Ajayan and M. W. Grinstaff, *Chem. Soc. Rev.*, 2016, **45**, 5848–5887.

108 Z. Jiang, S. Wang, X. Chen, W. Yang, X. Yao, X. Hu, Q. Han and H. Wang, *Adv. Mater.*, 2020, **32**, 1906221.

8994 | *Chem. Soc. Rev.*, 2025, **54**, 8925–9007

This journal is © The Royal Society of Chemistry 2025

109 J. Akimoto, Y. Gotoh and Y. Oosawa, *J. Solid State Chem.*, 1998, **141**, 298–302.

110 U. A. Stival, I. B. C. Gallo, C. F. N. Gonin, S. L. Reis, R. L. Grosso, J. B. Kosctiuk, M. G. S. Franchetti, B. Leão, F. E. R. Oliveira, A. Souza, H. R. Freitas, R. S. Monteiro, L. S. Parreira and M. A. C. Berton, *J. Energy Storage*, 2023, **72**, 108706.

111 Y. Ye, Y. Zhao, T. Zhao, S. Xu, Z. Xu, J. Qian, L. Wang, Y. Xing, L. Wei, Y. Li, J. Wang, L. Li, F. Wu and R. Chen, *Adv. Mater.*, 2021, **33**, 1–10.

112 N. Ohta, K. Takada, L. Zhang, R. Ma, M. Osada and T. Sasaki, *Adv. Mater.*, 2006, **18**, 2226–2229.

113 J. Auvergniot, A. Cassel, J. B. Ledeuil, V. Viallet, V. Seznec and R. Dedryvère, *Chem. Mater.*, 2017, **29**, 3883–3890.

114 J. A. Lewis, F. J. Q. Cortes, M. G. Boebinger, J. Tippens, T. S. Marchese, N. Kondekar, X. Liu, M. Chi and M. T. McDowell, *ACS Energy Lett.*, 2019, **4**, 591–599.

115 J.-G. Z. Brian, D. Adams, J. Zheng, X. Ren and W. Xu, *Adv. Energy Mater.*, 2018, **8**, 1702097.

116 A. Bielefeld, D. A. Weber and J. Janek, *ACS Appl. Mater. Interfaces*, 2020, **12**, 12821–12833.

117 S. Y. Park, J. Jeong and H. C. Shin, *Appl. Sci.*, 2022, **12**, 12692.

118 M. B. Dixit, M. Regala, F. Shen, X. Xiao and K. B. Hatzell, *ACS Appl. Mater. Interfaces*, 2019, **11**, 2022–2030.

119 A. Neumann, T. R. Hamann, T. Danner, S. Hein, K. Becker-Steinberger, E. Wachsman and A. Latz, *ACS Appl. Energy Mater.*, 2021, **4**, 4786–4804.

120 C. Gohd, Elon Musk: 100 Tesla Gigafactories Could Power the Entire World, **https://futurism.com/elon-musk-100-tesla-gigafactories-could-power-entire-world**.

121 Z. Yan, H. Jin, V. Waldersee, B. Klayman, K. Krolicki and N. Zieminski, Tesla output forecast shows jump in Q4, growth through 2023 sources, **https://www.reuters.com/business/autos-transportation/exclusive-tesla-output-forecast-shows-jump-q4-growth-through-2023-sources-2022-09-30/**.

122 E. A. Olivetti, G. Ceder, G. G. Gaustad and X. Fu, *Joule*, 2017, **1**, 229–243.

123 L. Schwich, M. Küpers, M. Finsterbusch, A. Schreiber, D. Fattakhova-Rohlfing, O. Guillon and B. Friedrich, *Metals*, 2020, **10**, 1–19.

124 G. A. Blengini, C. E. L. Latunussa and U. Eynard, Study on the Eu's list of critical raw materials - Critical raw materials factsheets, 2020.

125 C. Helbig, A. M. Bradshaw, L. Wietschel, A. Thorenz and A. Tuma, *J. Clean. Prod.*, 2018, **172**, 274–286.

126 K. Schneider and D. Goldmann, Oxide-based lithium solid-state batteries from a recycling perspective, Conference proceedings, 16. Recy & DepoTech-Konferenz, 2022, pp. 381–386.

127 Harvard School of Public Health, The dangers of cobalt mining in the Congo.

128 L. Boyle, Cobalt mining for Big Tech is driving child labor, deaths in the Congo.

129 M. Chen, X. Ma, B. Chen, R. Arsenault, P. Karlson, N. Simon and Y. Wang, *Joule*, 2019, **3**, 2622–2646.

130 E. Pickrell, Forbes, 2022.

131 CSR Euorpe, The Raw Material Outlook Platform, **https://www.rawmaterialoutlook.org/**.

132 showtheplanet inc., Daily Metal Prices, **https://www.dailymetalprice.com/**.

133 K. Habib, S. T. Hansdóttir and H. Habib, *Resour. Conserv. Recycl.*, 2020, **154**, 104603.

134 Benchmark Source, More than 300 new mines required to meet battery demand by 2035, **https://source.benchmarkminerals.com/article/more-than-300-new-mines-required-to-meet-battery-demand-by-2035**.

135 K. V. Kravchyk, D. T. Karabay and M. V. Kovalenko, *Sci. Rep.*, 2022, **12**, 1–10.

136 A. Kwade, M. Möller, J. Müller, J. Hesselbach, S. Zellmer, S. Doose, J. Mayer, P. Michalowski, M. Powell and S. Breitung-Faes, *KONA Powder Part. J.*, 2023, 50–73.

137 R. P. Navarro, P. Seidel, M. Kolk, A. Krug and L. Lenz, European Battery Recycling: An Emerging Cross-Industry Convergence, 2022.

138 Li-ion Battery Market by Type, Capacity, Voltage, Industry and Region- Global Forecast to 2031, 2022.

139 L. Azhari, S. Bong, X. Ma and Y. Wang, *Matter*, 2020, **3**, 1845–1861.

140 A. Mayyas, D. Steward and M. Mann, *Sustainable Mater. Technol.*, 2019, **19**, 0–26.

141 J. Neumann, M. Petranikova, M. Meeus, J. D. Gamarra, R. Younesi, M. Winter and S. Nowak, *Adv. Energy Mater.*, 2022, **12**, 2102917.

142 H. E. Melin, *Circular Energy Storage*, 2019, **1**, 1–57.

143 Y. Zhao, O. Pohl, A. I. Bhatt, G. E. Collis, P. J. Mahon, T. Rüther and A. F. Hollenkamp, *Sustain. Chem.*, 2021, **2**(1), 167–205.

144 O. V. Martĺnez, J. Valio, A. Santasalo-aarnio, M. Reuter and R. Serna-guerrero, *Batteries*, 2019, **5**(4), 68.

145 X. Ma, L. Azhari and Y. Wang, *Chem*, 2021, 7, 2843–2847.

146 D. H. S. Tan, P. Xu and Z. Chen, *MRS Energy Sustain.*, 2020, **7**, 1–23.

147 D. H. S. Tan, P. Xu, H. Yang, M. Cheol Kim, H. Nguyen, E. A. Wu, J. M. Doux, A. Banerjee, Y. S. Meng and Z. Chen, *MRS Energy Sustain.*, 2020, **7**, 1–21.

148 A. Sharafi, S. Yu, M. Naguib, M. Lee, C. Ma, H. M. Meyer, J. Nanda, M. Chi, D. J. Siegel and J. Sakamoto, *J. Mater. Chem. A*, 2017, **5**, 13475–13487.

149 Grand View Research, Battery Market Size, Share & Trends Analysis Report By Product (Lead Acid, Li-ion, Nickle Metal Hydride, Ni-Cd), By Application, By End-use, By Region, And Segment Forecasts, 2023–2030, 2023.

150 Grand View Research, Solid State Battery Market Size, Share & Trends Analysis Report By Application (Energy Harvesting, EVs), By Battery Type (Thin Film, Portable Batteries), By Capacity (Below 20 mAh, Above 500 mAh), And Segment Forecasts, 2021–2028, 2020.

151 Grand View Research, Thin Film Battery Market Size, Share & Trends Analysis Report By Voltage (Below 1.5 V, Above 3 V), By Battery Type (Disposable, Rechargeable), By Application

This journal is © The Royal Society of Chemistry 2025

Chem. Soc. Rev., 2025, **54**, 8925–9007 | 8995

(Medical, Smart Cards, Wearables), And Segment Forecasts, 2020–2027, 2019.

152 E. Cohen, S. Menkin, M. Lifshits, Y. Kamir, A. Gladkich, G. Kosa and D. Golodnitsky, *Electrochim. Acta*, 2018, **265**, 690–701.

153 Bollore, Electricity storage and systems, https://www.bollore.com/en/activites-et-participations-2/stockage-delectricite-et-systemes/blue-solutions-films-plastiques/, (accessed 19 April 2023).

154 Volta Foundation, The Battery Report 2022, 2023.

155 J. B. Bates, N. J. Dudney, G. R. Gruzalski, R. A. Zuhr, A. Choudhury, C. F. Luck and J. D. Robertson, *Solid State Ionics*, 1992, **56**, 53–56.

156 J. B. Bates, N. J. Dudney, G. R. Gruzalski, R. A. Zuhr, A. Choudhury, C. F. Luck and J. D. Robertson, *J. Power Sources*, 1993, **43**, 103–110.

157 B. Wang, J. B. Bates, F. X. Hart, B. C. Sales, R. A. Zuhr and J. D. Robertson, *J. Electrochem. Soc.*, 1996, **143**, 3203.

158 V. Lacivita, A. S. Westover, A. Kercher, N. D. Phillip, G. Yang, G. Veith, G. Ceder and N. J. Dudney, *J. Am. Chem. Soc.*, 2018, **140**, 11029–11038.

159 V. Lacivita, N. Artrith and G. Ceder, *Chem. Mater.*, 2018, **30**, 7077–7090.

160 A. R. West, *Solid state chemistry and its applications*, John Wiley & Sons, 2014.

161 S. J. Cho, M. J. Uddin and P. Alaboina, *Review of Nanotechnology for Cathode Materials in Batteries*, Elsevier Inc, 2017.

162 S. Afyon, F. Krumeich and J. L. M. Rupp, *J. Mater. Chem. A*, 2015, **3**, 18636–18648.

163 D. Sarkar, Nanostructured ceramics: characterization and analysis, 2018.

164 M. N. Rahaman, Ceramic processing and sintering, 2003.

165 P. D. Ownby, in *Oxidation State Control of Volatile Species in Sintering*, ed. G. C. Kuczynski, Springer, 1972, vol. 6, pp. 431–437.

166 Y. Inaguma, C. Liquan, M. Itoh, T. Nakamura, T. Uchida, H. Ikuta and M. Wakihara, *Solid State Commun.*, 1993, **86**, 689–693.

167 R. Murugan, V. Thangadurai and W. Weppner, *Angew. Chem., Int. Ed.*, 2007, **46**, 7778–7781.

168 H. Aono, E. Sugimoto, Y. Sadaoka, N. Imanaka and G. Y. Adachi, *J. Electrochem. Soc.*, 1990, **137**, 1023–1027.

169 K. Senevirathne, C. S. Day, M. D. Gross, A. Lachgar and N. A. W. Holzwarth, *Solid State Ionics*, 2013, **233**, 95–101.

170 D. Sarkar, Ceramic Processing: Industrial Practices, 2019.

171 P. G. Debenedetti and F. H. Stillinger, *Nature*, 2001, **410**, 259.

172 P. J. Skrdla, P. D. Floyd and P. C. Dell'Orco, *Phys. Chem. Chem. Phys.*, 2017, **19**, 20523–20532.

173 B. Lee and S. Komarneni, *Chemical Processing of Ceramics*, 2005.

174 R. Chen, Q. Li, X. Yu, L. Chen and H. Li, *Chem. Rev.*, 2020, **120**, 6820–6877.

175 W. D. Kingery, H. K. Bowen and D. R. Uhlmann, *Introduction to ceramics*, John wiley & sons, 1976, vol. 17.

176 R. P. Rao, W. Gu, N. Sharma, V. K. Peterson, M. Avdeev and S. Adams, *Chem. Mater.*, 2015, **27**, 2903–2910.

177 J. L. Allen, J. Wolfenstine, E. Rangasamy and J. Sakamoto, *J. Power Sources*, 2012, **206**, 315–319.

178 M. H. Bhat, A. Miura, P. Vinatier, A. Levasseur and K. J. Rao, *Solid State Commun.*, 2003, **125**, 557–562.

179 G. B. Kunshina, I. V. Bocharova and E. P. Lokshin, *Inorg. Mater.*, 2015, **51**, 369–374.

180 A. D. Robertson, S. G. Martin, A. Coats and A. R. West, *J. Mater. Chem.*, 1995, **5**, 1405–1412.

181 A. A. Shibkova, A. A. Surin, Z. S. Martem'yanova, V. I. Voronin, A. P. Stepanov, I. V. Korzun, L. A. Blaginina and V. P. Obrosov, *Glass Ceram.*, 2007, **64**, 124–128.

182 H. Jena, K. V. G. Kutty and T. R. N. Kutty, *J. Mater. Sci.*, 2005, **40**, 4737–4748.

183 T. Zangina, J. Hassan, K. A. Matori, R. S. Azis, U. Ahmadu and A. See, *Results Phys.*, 2016, **6**, 719–725.

184 X. Huang, Y. Lu, J. Jin, S. Gu, T. Xiu, Z. Song, M. E. Badding and Z. Wen, *ACS Appl. Mater. Interfaces*, 2018, **10**, 17147–17155.

185 J. Zhang, N. Zhao, M. Zhang, Y. Li, P. K. Chu, X. Guo, Z. Di, X. Wang and H. Li, *Nano Energy*, 2016, **28**, 447–454.

186 P. Barai, T. Fister, Y. Liang, J. Libera, M. Wolfman, X. Wang, J. Garcia, H. Iddir and V. Srinivasan, *Chem. Mater.*, 2021, **33**, 4337–4352.

187 W. H. Rhodes, *J. Am. Ceram. Soc.*, 1981, **64**, 19–22.

188 K. Uchino, E. Sadanaga and T. Hirose, *J. Am. Ceram. Soc.*, 1989, **72**, 1555–1558.

189 K. Yoshima, Y. Harada and N. Takami, *J. Power Sources*, 2016, **302**, 283–290.

190 J.-M. Lee, T. Kim, S.-W. Baek, Y. Aihara, Y. Park, Y.-I. Kim and S.-G. Doo, *Solid State Ionics*, 2014, **258**, 13–17.

191 M. Wood, X. Gao, R. Shi, T. W. Heo, J. A. Espitia, E. B. Duoss, B. C. Wood and J. Ye, *J. Power Sources*, 2021, **484**, 1–30.

192 R. L. Coble, *J. Appl. Phys.*, 1961, **32**, 787–792.

193 M. S. Diallo, T. Shi, Y. Zhang, X. Peng, I. Shozib, Y. Wang, L. J. Miara, M. C. Scott, Q. H. Tu and G. Ceder, *Nat. Commun.*, 2024, **15**, 858.

194 R.-J. Chen, M. Huang, W.-Z. Huang, Y. Shen, Y.-H. Lin and C.-W. Nan, *Solid State Ionics*, 2014, **265**, 7–12.

195 M. Huang, T. Liu, Y. Deng, H. Geng, Y. Shen, Y. Lin and C. W. Nan, *Solid State Ionics*, 2011, **204–205**, 41–45.

196 C. Herring, *J. Appl. Phys.*, 1950, **21**, 301–303.

197 R. Takano, K. Tadanaga, A. Hayashi and M. Tatsumisago, *Solid State Ionics*, 2014, **255**, 104–107.

198 W. Xue, Y. Yang, Q. Yang, Y. Liu, L. Wang, C. Chen and R. Cheng, *RSC Adv.*, 2018, **8**, 13083–13088.

199 H. Buschmann, J. Dölle, S. Berendts, A. Kuhn, P. Bottke, M. Wilkening, P. Heitjans, A. Senyshyn, H. Ehrenberg, A. Lotnyk, V. Duppel, L. Kienle and J. Janek, *Phys. Chem. Chem. Phys.*, 2011, **13**, 19378–19392.

200 R. Murugan, V. Thangadurai and W. Weppner, *Angew. Chem., Int. Ed.*, 2007, **46**, 7778–7781.

201 E. Yi, W. Wang, J. Kieffer and R. M. Laine, *J. Power Sources*, 2017, **352**, 156–164.

8996 | *Chem. Soc. Rev.*, 2025, **54**, 8925–9007

This journal is © The Royal Society of Chemistry 2025

202 L. Cheng, J. S. Park, H. Hou, V. Zorba, G. Chen, T. Richardson, J. Cabana, R. Russo and M. Doeff, *J. Mater. Chem. A*, 2014, **2**, 172–181.

203 X. Wang and I. Chen, *Nature*, 2000, **404**, 168–171.

204 X. Huang, T. Xiu, M. E. Badding and Z. Wen, *Ceram. Int.*, 2018, **44**, 5660–5667.

205 J. L. M. Rupp, A. Infortuna and L. J. Gauckler, *Acta Mater.*, 2006, **54**, 1721–1730.

206 S. Guo, Y. Li, H. Zhang, Z. Cao, L. Wang and G. Li, *Ceram. Int.*, 2024, **50**, 559–565.

207 J. Su, X. Huang, Z. Song, T. Xiu, M. E. Badding, J. Jin and Z. Wen, *Ceram. Int.*, 2019, **45**, 14991–14996.

208 H. El Shinawi and J. Janek, *J. Power Sources*, 2013, **225**, 13–19.

209 H. Chu, *et al.*, Under review.

210 Y. Li, Z. Wang, C. Li, Y. Cao and X. Guo, *J. Power Sources*, 2014, **248**, 642–646.

211 M. Itoh, Y. Inaguma, W. H. Jung, L. Chen and T. Nakamura, *Solid State Ionics*, 1994, **70–71**, 203–207.

212 C. W. Ban and G. M. Choi, *Solid State Ionics*, 2001, **140**, 285–292.

213 W. Brennan, V. Blair and J. Marsico, Density Optimization of Lithium Lanthanum Titanate Ceramics for Lightweight Lithium-Air Batteries, 2014.

214 M. Vinnichenko, K. Waetzig, A. Aurich, C. Baumgaertner, M. Herrmann, C. W. Ho, M. Kusnezoff and C. W. Lee, *Nanomaterials*, 2022, **12**, 3178.

215 K. Waetzig, C. Heubner and M. Kusnezoff, *Crystals*, 2020, **10**, 408.

216 R. Raj and J. Wolfenstine, *J. Power Sources*, 2017, **343**, 119–126.

217 H. Chu, *et al.*, Under review.

218 H. K. Tian, B. Xu and Y. Qi, *J. Power Sources*, 2018, **392**, 79–86.

219 X. Zhan, S. Lai, M. P. Gobet, S. G. Greenbaum and M. Shirpour, *Phys. Chem. Chem. Phys.*, 2018, **20**, 1447–1459.

220 F. D. D. Han, A. S. S. Westover, J. Yue, X. L. L. Fan, F. Wang, M. F. F. Chi, D. N. N. Leonard, N. J. Dudney, H. Wang and C. S. S. Wang, *Nat. Energy*, 2019, **4**, 187–196.

221 W. E. Tenhaeff, E. Rangasamy, Y. Wang, A. P. Sokolov, J. Wolfenstine, J. Sakamoto and N. J. Dudney, *ChemElectroChem*, 2014, **1**, 375–378.

222 Y. Kim, H. Jo, J. L. Allen, H. Choe, J. Wolfenstine and J. Sakamoto, *J. Am. Ceram. Soc.*, 2016, **99**, 1367–1374.

223 Y. Jin and P. J. McGinn, *J. Power Sources*, 2013, **239**, 326–331.

224 W. Xia, B. Xu, H. Duan, Y. Guo, H. Kang, H. Li and H. Liu, *ACS Appl. Mater. Interfaces*, 2016, **8**, 5335–5342.

225 F. Shen, M. B. Dixit, X. Xiao and K. B. Hatzell, *ACS Energy Lett.*, 2018, **3**, 1056–1061.

226 C. Wang, Z.-G. Liu, P.-P. Lin, X. Xu, F.-G. Lu, J.-C. Lin, P. He and T.-S. Lin, *Appl. Surf. Sci.*, 2022, **575**, 151762.

227 G. Yan, S. Yu, J. F. Nonemacher, H. Tempel, H. Kungl, J. Malzbender, R. A. Eichel and M. Krüger, *Ceram. Int.*, 2019, **45**, 14697–14703.

228 H. Y. Li, B. Huang, Z. Huang and C. A. Wang, *Ceram. Int.*, 2019, **45**, 18115–18118.

229 J. Ma and L. C. Lim, *J. Eur. Ceram. Soc.*, 2002, **22**, 2197–2208.

230 J. H. Cho, K. Kim, S. Chakravarthy, X. Xiao, J. L. M. Rupp and B. W. Sheldon, *Adv. Energy Mater.*, 2022, **12**, 1–15.

231 B. Timurkutluk and S. Dokuyucu, *Ceram. Int.*, 2018, **44**, 17399–17406.

232 B. Timurkutluk, S. Celik and E. Ucar, *Ceram. Int.*, 2019, **45**, 3192–3198.

233 M. Jabbari and J. Hattel, *Mater. Sci. Technol.*, 2014, **30**, 283–288.

234 M. Jabbari, R. Bulatova, A. I. Y. Tok, C. R. H. Bahl, E. Mitsoulis and J. H. Hattel, *Mater. Sci. Eng., B*, 2016, **212**, 39–61.

235 R. A. Jonson, E. Yi, F. Shen and M. C. Tucker, *Energy and Fuels*, 2021, **35**, 8982–8990.

236 E. Yi, W. Wang, J. Kieffer and R. M. Laine, *J. Mater. Chem. A*, 2016, **4**, 12947–12954.

237 K. Fu, Y. Gong, G. T. Hitz, D. W. McOwen, Y. Li, S. Xu, Y. Wen, L. Zhang, C. Wang, G. Pastel, J. Dai, B. Liu, H. Xie, Y. Yao, E. D. Wachsman and L. Hu, *Energy Environ. Sci.*, 2017, **10**, 1568–1575.

238 D. Hanft, J. Exner and R. Moos, *J. Power Sources*, 2017, **361**, 61–69.

239 A. Cheol-Woo, C. Jong-Jin, R. Jungho, H. Byung-Dong, K. Jong-Woo, Y. Woon-Ha, C. Joon-Hwan and P. Dong-Soo, *J. Electrochem. Soc.*, 2015, **162**, 60–63.

240 J. J. Choi, J. H. Choi, J. Ryu, B. D. Hahn, J. W. Kim, C. W. Ahn, W. H. Yoon and D. S. Park, *J. Eur. Ceram. Soc.*, 2012, **32**, 3249–3254.

241 J. Akedo, *J. Am. Ceram. Soc.*, 2006, **89**, 1834–1839.

242 J. J. Choi, C. W. Ahn, J. Ryu, B. D. Hahn, J. W. Kim, W. H. Yoon and D. S. Park, *J. Korean Phys. Soc.*, 2016, **68**, 12–16.

243 Y. Inaguma, L. Chen, M. Itoh and T. Nakamura, *Solid State Ionics*, 1994, **70–71**, 196–202.

244 H. Imagawa, S. Ohta, Y. Kihira and T. Asaoka, *Solid State Ionics*, 2014, **262**, 609–612.

245 R. Djenadic, M. Botros, C. Benel, O. Clemens, S. Indris, A. Choudhary, T. Bergfeldt and H. Hahn, *Solid State Ionics*, 2014, **263**, 49–56.

246 E. Rangasamy, J. Wolfenstine and J. Sakamoto, *Solid State Ionics*, 2012, **206**, 28–32.

247 X. Huang, Y. Lu, H. Guo, Z. Song, T. Xiu, M. E. Badding and Z. Wen, *ACS Appl. Energy Mater.*, 2018, **1**, 5355–5365.

248 Y. Shimonishi, A. Toda, T. Zhang, A. Hirano, N. Imanishi, O. Yamamoto and Y. Takeda, *Solid State Ionics*, 2011, **183**, 48–53.

249 C. Ma, Y. Cheng, K. Chen, J. Li, B. G. Sumpter, C. Nan, K. L. More, N. J. Dudney and M. Chi, *Adv. Energy Mater.*, 2016, **6**, 1600053.

250 H. Geng, J. Lan, A. Mei, Y. Lin and C. W. Nan, *Electrochim. Acta*, 2011, **56**, 3406–3414.

251 A. Paolella, W. Zhu, G. Bertoni, S. Savoie, Z. Feng, H. Demers, V. Gariepy, G. Girard, E. Rivard, N. Delaporte, A. Guerfi,

This journal is © The Royal Society of Chemistry 2025

Chem. Soc. Rev., 2025, **54**, 8925–9007 | 8997

H. Lorrmann, C. George and K. Zaghib, *ACS Appl. Energy Mater.*, 2020, **3**, 3415–3424.

252 Y. Chen, E. Rangasamy, C. R. Dela Cruz, C. Liang and K. An, *J. Mater. Chem. A*, 2015, **3**, 22868–22876.

253 Z. Huang, K. Liu, L. Chen, Y. Lu, Y. Li and C. A. Wang, *Int. J. Appl. Ceram. Technol.*, 2017, **14**, 921–927.

254 D. Rettenwander, G. Redhammer, F. Preishuber-Pflügl, L. Cheng, L. Miara, R. Wagner, A. Welzl, E. Suard, M. M. Doeff, M. Wilkening, J. Fleig and G. Amthauer, *Chem. Mater.*, 2016, **28**, 2384–2392.

255 Y. Li, J. T. Han, C. A. Wang, H. Xie and J. B. Goodenough, *J. Mater. Chem.*, 2012, **22**, 15357–15361.

256 X. Huang, Z. Song, T. Xiu, M. E. Badding and Z. Wen, *J. Mater.*, 2019, **5**, 221–228.

257 S. Yu and D. J. Siegel, *Chem. Mater.*, 2017, **29**, 9639–9647.

258 J. Wolfenstine, J. Sakamoto and J. L. Allen, *J. Mater. Sci.*, 2012, **47**, 4428–4431.

259 J. Wolfenstine, J. L. Allen, J. Read, J. Sakamoto and G. Gonalez-Doncel, *J. Power Sources*, 2010, **195**, 4124–4128.

260 Y. Zhang, F. Chen, R. Tu, Q. Shen, X. Zhang and L. Zhang, *Solid State Ionics*, 2016, **284**, 53–60.

261 Z. Yanhua, C. Fei, T. Rong, S. Qiang and Z. Lianmeng, *J. Power Sources*, 2014, **268**, 960–964.

262 S. W. Baek, J. M. Lee, T. Y. Kim, M. S. Song and Y. Park, *J. Power Sources*, 2014, **249**, 197–206.

263 M. M. Ahmad, *Nanoscale Res. Lett.*, 2015, **10**, 1–10.

264 C. Wang, W. Ping, Q. Bai, H. Cui, R. Hensleigh, R. Wang, A. H. Brozena, Z. Xu, J. Dai, Y. Pei, C. Zheng, G. Pastel, J. Gao, X. Wang, H. Wang, J. Zhao, B. Yang, X. Zheng, J. Luo, Y. Mo, B. Dunn and L. Hu, *Science*, 2020, **526**, 521–526.

265 F. Chen, S. Cao, X. Xiang, D. Yang, W. Zha, J. Li, Q. Shen and L. Zhang, in Proceedings of the 42nd International Conference on Advanced Ceramics and Composites, Ceramic Engineering and Science Proceedings, 2018, p. 223.

266 I. N. David, T. Thompson, J. Wolfenstine, J. L. Allen and J. Sakamoto, *J. Am. Ceram. Soc.*, 2015, **98**, 1209–1214.

267 R. Kali and A. Mukhopadhyay, *J. Power Sources*, 2014, **247**, 920–931.

268 C. M. Chang, Y. Lee, S. H. Hong and H. M. Park, *J. Am. Ceram. Soc.*, 2005, **88**, 1803–1807.

269 K. Waetzig, A. Rost, C. Heubner, M. Coeler, K. Nikolowski, M. Wolter and J. Schilm, *J. Alloys Compd.*, 2020, **818**, 153237.

270 W. Ping, C. Wang, R. Wang, Q. Dong, Z. Lin and A. H. Brozena, *Sci. adv.*, 2020, **6**, eabc8641.

271 J. Guo, H. Guo, A. L. Baker, M. T. Lanagan, E. R. Kupp, G. L. Messing and C. A. Randall, *Angew. Chem., Int. Ed.*, 2016, **55**, 11457–11461.

272 H. Guo, A. Baker, J. Guo and C. A. Randall, *ACS Nano*, 2016, **10**, 10606–10614.

273 J. H. Seo, H. Nakaya, Y. Takeuchi, Z. Fan, H. Hikosaka, R. Rajagopalan, E. D. Gomez, M. Iwasaki, J. H. Randall CA.Seo, H. Nakaya, Y. Takeuchi, Z. Fan, H. Hikosaka, R. Rajagopalan, E. D. Gomez, M. Iwasaki and C. A. Randall, *J. Eur. Ceram. Soc.*, 2020, **40**, 6241–6248.

274 W. Lee, C. K. Lyon, J. H. Seo, R. Lopez-Hallman, Y. Leng, C. Y. Wang, M. A. Hickner, C. A. Randall and E. D. Gomez, *Adv. Funct. Mater.*, 2019, **29**, 1807872.

275 R. Mahbub, K. Huang, Z. Jensen, Z. D. Hood, J. L. M. Rupp and E. A. Olivetti, *Electrochem. Commun.*, 2020, **121**, 106860.

276 Y. Li, Y. Cao and X. Guo, *Solid State Ionics*, 2013, **253**, 76–80.

277 A. Mei, X. L. Wang, Y. C. Feng, S. J. Zhao, G. J. Li, H. X. Geng, Y. H. Lin and C. W. Nan, *Solid State Ionics*, 2008, **179**, 2255–2259.

278 K. Tadanaga, R. Takano, T. Ichinose, S. Mori, A. Hayashi and M. Tatsumisago, *Electrochem. Commun.*, 2013, **33**, 51–54.

279 R. A. Jonson and P. J. McGinn, *Solid State Ionics*, 2018, **323**, 49–55.

280 Y. Jin and P. J. McGinn, *J. Power Sources*, 2011, **196**, 8683–8687.

281 N. Janani, C. Deviannapoorani, L. Dhivya and R. Murugan, *RSC Adv.*, 2014, **4**, 51228–51238.

282 Z. F. F. Zheng, S. D. D. Song and Y. Wang, *Solid State Ionics*, 2016, **287**, 60–70.

283 T. Teranishi, Y. Ishii, H. Hayashi and A. Kishimoto, *Solid State Ionics*, 2016, **284**, 1–6.

284 K. Kitaoka, H. Kozuka, T. Hashimoto and T. Yoko, *J. Mater. Sci.*, 1997, **32**, 2063–2070.

285 Z. Zheng, Y. Zhang, S. Song and Y. Wang, *RSC Adv.*, 2017, **7**, 30160–30165.

286 E. J. van den Ham, N. Peys, C. De Dobbelaere, J. D'Haen, F. Mattelaer, C. Detavernier, P. H. L. Notten, A. Hardy and M. K. Van Bael, *J. Solgel Sci. Technol.*, 2015, **73**, 536–543.

287 J. F. Ihlefeld, P. G. Clem, B. L. Doyle, P. G. Kotula, K. R. Fenton and C. A. Apblett, *Adv. Mater.*, 2011, **23**, 5663–5667.

288 K. P. Abhilash, P. Sivaraj, P. C. Selvin, B. Nalini and K. Somasundaram, *Ceram. Int.*, 2015, **41**, 13823–13829.

289 T. N. H. Le, M. Roffat, Q. N. Pham, S. Kodjikian, O. Bohnke and C. Bohnke, *J. Solgel Sci. Technol.*, 2008, **46**, 137–145.

290 K. Tadanaga, H. Egawa, A. Hayashi, M. Tatsumisago, J. Mosa, M. Aparicio and A. Duran, *J. Power Sources*, 2015, **273**, 844–847.

291 M. Bitzer, T. Van Gestel and S. Uhlenbruck, *Thin Solid Films*, 2016, **615**, 128–134.

292 R. J. J. Chen, Y. B. B. Zhang, T. Liu, B. Q. Q. Xu, Y. Shen, Y. H. H. Lin and C. W. W. Nan, *Ceram. Int.*, 2017, **43**, S603–S608.

293 R. J. Chen, M. Huang, W. Z. Huang, Y. Shen, Y. H. Lin and C. W. Nan, *J. Mater. Chem. A*, 2014, **2**, 13277–13282.

294 M. Zarabian, M. Bartolini, P. Pereira-Almao and V. Thangadurai, *J. Electrochem. Soc.*, 2017, **164**, A1133.

295 D. Popovici, H. Nagai, S. Fujishima and J. Akedo, *J. Am. Ceram. Soc.*, 2011, **94**, 3847–3850.

296 X. M. M. Wu, S. Chen, F. R. R. Mai, J. H. H. Zhao and Z. Q. Q. He, *Ionics*, 2013, **19**, 589–593.

297 X. M. Wu, X. H. Li, S. W. Wang, Z. Wang, Y. H. Zhang, M. F. Xu and Z. Q. He, *Thin Solid Films*, 2003, **425**, 103–107.

8998 | *Chem. Soc. Rev.*, 2025, **54**, 8925–9007

This journal is © The Royal Society of Chemistry 2025

298 S. Takase, C. Kubo, R. Aono and Y. Shimizu, *J. Solgel Sci. Technol.*, 2016, **79**, 564–572.

299 R. Inada, K. Ichi Ishida, M. Tojo, T. Okada, T. Tojo and Y. Sakurai, *Ceram. Int.*, 2015, **41**, 11136–11142.

300 X. Zhang, E. Temeche and R. M. M. Laine, *Macromolecules*, 2020, **53**, 2702–2712.

301 M. Vijayakumar, Y. Inaguma, W. Mashiko, M. P. Crosnier-Lopez and C. Bohnke, *Chem. Mater.*, 2004, **16**, 2719–2724.

302 K. V. Kravchyk, G. Brotons, A. G. Belous and O. Bohnke, *Mater. Lett.*, 2014, **137**, 182–187.

303 T. N. H. Le, M. Roffat, Q. N. Pham, S. Kodjikian, O. Bohnke and C. Bohnke, *J. Solgel Sci. Technol.*, 2008, **46**, 137–145.

304 J. Tan and A. Tiwari, *MRS Online Proc. Libr.*, 2012, **1440**, 73–78.

305 X. Chen, T. Cao, M. Xue, H. Lv, B. Li and C. Zhang, *Solid State Ionics*, 2018, **314**, 92–97.

306 I. Kokal, M. Somer, P. H. L. Notten and H. T. Hintzen, *Solid State Ionics*, 2011, **185**, 42–46.

307 Y. Zhu, E. R. Kennedy, B. Yasar, H. Paik, Y. Zhang, Z. D. Hood, M. Scott and J. L. M. Rupp, *Adv. Mater.*, 2024, **36**, 2302438.

308 Y. Zhu, Z. D. Hood, H. Paik, P. B. Groszewicz, S. P. Emge, F. N. Sayed, C. Sun, M. Balaish, D. Ehre, L. J. Miara, A. I. Frenkel, I. Lubomirsky, C. P. Grey and J. L. M. Rupp, *Matter*, 2024, **7**, 500–522.

309 Y. Zhu, M. Chon, C. V. Thompson and J. L. M. Rupp, *Angew. Chem., Int. Ed.*, 2023, **62**, e202304581.

310 H. Nakano, K. Dokko, M. Hara, Y. Isshiki and K. Kanamura, *Ionics*, 2008, **14**, 173–177.

311 M. Schroeder, S. Glatthaar and J. R. Binder, *Solid State Ionics*, 2011, **201**(1), 49–53.

312 G. B. Kunshina, O. G. Gromov, E. P. Lokshin and V. T. Kalinnikov, *Russ. J. Inorg. Chem.*, 2014, **59**, 424–430.

313 S. Duluard, A. Paillassa, L. Puech, P. Vinatier, V. Turq, P. Rozier, P. Lenormand, P. L. Taberna, P. Simon and F. Ansart, *J. Eur. Ceram. Soc.*, 2013, **33**(6), 1145–1153.

314 F. Ma, E. Zhao, S. Zhu, W. Yan, D. Sun, Y. Jin and C. Nan, *Solid State Ionics*, 2016, **295**(1), 7–12.

315 M. Weiss, D. A. Weber, A. Senyshyn, J. Janek and W. G. Zeier, *ACS Appl. Mater. Interfaces*, 2018, **10**(13), 10935–10944.

316 Y. Zhu, J. C. Gonzalez-Rosillo, M. Balaish, Z. D. Hood, K. J. Kim and J. L. Rupp, *Nat. Rev. Mater.*, 2021, **6**, 313–331.

317 R. Pfenninger, M. Struzik, I. Garbayo, E. Stilp and J. L. M. Rupp, *Nat. Energy*, 2019, **4**, 475–483.

318 Z. D. Hood, Y. Zhu, L. J. Miara, W. S. Chang, P. Simons and J. L. M. Rupp, *Energy Environ. Sci.*, 2022, **15**, 2927–2936.

319 C. J. Brinker and G. W. Scherer, *Sol-Gel Science: The Physics and Chemistry of Sol-Gel Processing*, 2013.

320 M. S. Bhuiyan, M. Paranthaman and K. Salama, *Supercond. Sci. Technol.*, 2006, **19**, R1.

321 A. J. Samson, K. Hofstetter, S. Bag and V. Thangadurai, *Energy Environ. Sci.*, 2019, **12**, 2957–2975.

322 C. J. Brinker and G. W. Scherer, *Sol-Gel Science: The Physics and Chemistry of Sol-Gel Processing*, 2013.

323 R. W. W. T. Schneller, M. Kosec and D. Payne, *Chemical Solution Deposition of Functional Oxide Thin Films*, Springer, 2013.

324 K. L. Chopra, R. C. Kainthla, D. K. Pandya and A. P. Thakoor, *Physics of Thin Films: Advances in Research and Development*, 1982.

325 C. F. Baes and R. S. Mesmer, *Ber. Bunsenges. Phys. Chem.*, 1977, **81**(2), 245–246.

326 B. Houng, C. Lou Huang and S. Y. Tsai, *J. Cryst. Growth*, 2007, **307**(2), 328–333.

327 S. Takase, C. Kubo, R. Aono and Y. Shimizu, *J. Solgel Sci. Technol.*, 2016, **79**, 564–572.

328 R. W. Schwartz and M. Narayanan, *Solution Processing of Inorganic Materials*, 2008.

329 J. L. M. Rupp, B. Scherrer, N. Schäuble and L. J. Gauckler, *Adv. Funct. Mater.*, 2010, **20**, 2807–2814.

330 J. L. M. Rupp, B. Scherrer and L. J. Gauckler, *Phys. Chem. Chem. Phys.*, 2010, **12**, 11114–11124.

331 D. Perednis and L. J. Gauckler, *J. Electroceram.*, 2005, **14**, 103–111.

332 X. M. Wu, X. H. Li, S. W. Wang, Z. Wang, Y. H. Zhang, M. F. Xu and Z. Q. He, *Thin Solid Films*, 2003, **425**(1–2), 103–107.

333 R. W. Schwartz and M. Narayanan, *Solution Processing of Inorganic Materials*, 2008.

334 Z. D. Hood, Y. Zhu, L. J. Miara, W. S. Chang, P. Simons and J. L. M. Rupp, *Energy Environ. Sci.*, 2022, **15**, 2927–2936.

335 Y. Zhu, Z. Hood, J. Rupp and L. J. Miara, Solution-processed solid-state electrolyte and method of manufacture thereof, *US Pat.*, 11251460, 2022, https://patents.google.com/patent/US11251460B2/en.

336 G. Štefanić, S. Musić, S. Popović and K. Furić, *Croat. Chem. Acta*, 1996, **69**, 223–239.

337 A. E. Gobichon, J. P. Auffrédic and D. Louër, *Solid State Ionics*, 1996, **93**(1–2), 51–64.

338 J. D. D. Nicholas and L. C. C. De Jonghe, *Solid State Ionics*, 2007, **178**, 1187–1194.

339 J. Schnell, T. Günther, T. Knoche, C. Vieider, L. Köhler, A. Just, M. Keller, S. Passerini and G. Reinhart, *J. Power Sources*, 2018, **382**, 160–175.

340 R. H. Brugge, A. K. O. Hekselman, A. Cavallaro, F. M. Pesci, R. J. Chater, J. A. Kilner and A. Aguadero, *Chem. Mater.*, 2018, **30**, 3704–3713.

341 A. Sharafi, S. H. Yu, M. Naguib, M. Lee, C. Ma, H. M. Meyer, J. Nanda, M. F. Chi, D. J. Siegel and J. Sakamoto, *J. Mater. Chem. A*, 2017, **5**, 13475–13487.

342 I. Garbayo, M. Struzik, W. J. Bowman, R. Pfenninger, E. Stilp and J. L. M. M. Rupp, *Adv. Energy Mater.*, 2018, 1702265.

343 J. Sastre, M. H. Futscher, L. Pompizi, A. Aribia, A. Priebe, J. Overbeck, M. Stiefel, A. N. Tiwari and Y. E. Romanyuk, *Commun. Mater.*, 2021, **2**, 76.

344 E. G. Herbert, W. E. Tenhaeff, N. J. Dudney and G. M. Pharr, *Thin Solid Films*, 2011, **520**, 413–418.

345 S. Kalnaus, A. S. Westover, M. Kornbluth, E. Herbert and N. J. Dudney, *J. Mater. Res.*, 2021, **36**, 787–796.

This journal is © The Royal Society of Chemistry 2025

Chem. Soc. Rev., 2025, **54**, 8925–9007 | 8999

346 R. Mahbub, K. Huang, Z. Jensen, Z. D. Hood, J. L. M. Rupp and E. A. Olivetti, *Electrochem. Comm.*, 2020, **121**, 106860.

347 M. Zarabian, M. Bartolini, P. Pereira-Almao and V. Thangadurai, *J. Electrochem. Soc.*, 2017, **164**, A1133.

348 E. J. van den Ham, N. Peys, C. De Dobbelaere, J. D'Haen, F. Mattelaer, C. Detavernier, P. H. L. Notten, A. Hardy and M. K. Van Bael, *J. Solgel Sci. Technol.*, 2015, **73**, 536–543.

349 K. P. Abhilash, P. Sivaraj, P. C. Selvin, B. Nalini and K. Somasundaram, *Ceram. Int.*, 2015, **41**(10), 13823–13829.

350 C. Ma, K. Chen, C. Liang, C. W. Nan, R. Ishikawa, K. More and M. Chi, *Energy Environ. Sci.*, 2014, **7**, 1638–1642.

351 J. F. Wu and X. Guo, *Phys. Chem. Chem. Phys.*, 2017, **19**, 5880–5887.

352 B. S. Yilbas, A. Al-Sharafi and H. Ali, *Self-cleaning of surfaces and water droplet mobility*, Elsevier, 2019.

353 A. J. Hurd and C. Jeffrey Brinker, *MRS Proc.*, 1990, **180**, 575.

354 M. Faustini, B. Louis, P. A. Albouy, M. Kuemmel and D. Grosso, *J. Phys. Chem. C*, 2010, **114**(1–2), 7637–7645.

355 K. Kitaoka, H. Kozuka, T. Hashimoto and T. Yoko, *J. Mater. Sci.*, 1997, **32**, 2063–2070.

356 C. Xu, J. Huang, X. Tan, T. Yu, Z. Cui and L. Zhao, *J. Dispersion Sci. Technol.*, **31**(12), 1732–1739.

357 N. J. Arfsten, A. Eberle, J. Otto and A. Reich, *J. Sol-Gel Sci. Technol.*, 1997, 1099–1104.

358 J. A. Tallmadge, *AIChE J.*, 1971, **17**(1), 243–246.

359 J. Puetz, F. N. Chalvet and M. A. Aegerter, *Thin Solid Films*, 2003, **442**(1–2), 53–59.

360 D. Perednis and L. J. Gauckler, *J. Electroceram.*, 2005, **14**, 103–111.

361 Z. D. Hood, Y. Zhu, L. J. Miara, W. S. Chang, P. Simons and J. L. Rupp, To-be-submitted.

362 Z. D. Hood, Y. Zhu, L. J. Miara, W. S. Chang, P. Simons and J. L. M. Rupp, *Energy Environ. Sci.*, 2022, **15**, 2927–2936.

363 M. Brubaker, P. D. Mumbauer and R. Grant, *Integr. Ferroelectr.*, 2001, **36**(1–4), 305–312.

364 D. Popovici, H. Nagai, S. Fujishima and J. Akedo, *J. Am. Ceram. Soc.*, 2011, **94**, 3847–3850.

365 R. Inada, K. Ichi Ishida, M. Tojo, T. Okada, T. Tojo and Y. Sakurai, *Ceram. Int.*, 2015, **41**(9), 11136–11142.

366 G. Hodes, *Phys. Chem. Chem. Phys.*, 2007, 2181–2196.

367 G. Hodes, *Chemical Solution Deposition Of Semiconductor Films*, 2002.

368 G. Hodes, *Phys. Chem. Chem. Phys.*, 2007, **9**, 2181–2196.

369 T. P. Niesen and M. R. De Guire, *Solid State Ionics*, 2002, **151**(1), 61–68.

370 B. Derby, *J. Eur. Ceram. Soc.*, 2011, **31**(14), 2543–2550.

371 B. Derby, *Annu. Rev. Mater. Res.*, 2010, **10**, 395–414.

372 B. Derby, *J. Eur. Ceram. Soc.*, 2011, **31**(14), 2543–2550.

373 K. Sun, T. S. Wei, B. Y. Ahn, J. Y. Seo, S. J. Dillon and J. A. Lewis, *Adv. Mater.*, 2013, **25**, 4539–4543.

374 F. Zhang, M. Wei, V. V. Viswanathan, B. Swart, Y. Shao, G. Wu and C. Zhou, *Nano energy*, 2017, **40**, 418–431.

375 D. A. Neumayer, P. R. Duncombe, R. B. Laibowitz and A. Grill, *Integr. Ferroelectr.*, 1997, **18**, 297–309.

376 R. W. Schwartz, J. A. Voigt, B. A. Tuttle, D. A. Payne, T. L. Reichert and R. S. DaSalla, *J. Mater. Res.*, 1997, **12**, 444–456.

377 J. Tan and A. Tiwari, *Mater. Res. Soc. Symp. Proc.*, 2012, **1440**, 73–78.

378 X. Chen, T. Cao, M. Xue, H. Lv, B. Li and C. Zhang, *Solid State Ionics*, 2013, **314**, 92–97.

379 I. Kokal, M. Somer, P. H. L. Notten and H. T. Hintzen, *Solid State Ionics*, 2011, **185**(1), 42–46.

380 M. Vijayakumar, Y. Inaguma, W. Mashiko, M. P. Crosnier-Lopez and C. Bohnke, *Chem. Mater.*, 2004, **16**(14), 2719–2724.

381 M. Schroeder, S. Glatthaar and J. R. Binder, *Solid State Ionics*, 2011, **201**(1), 49–53.

382 G. T. K. Fey, R. F. Shiu, V. Subramanian, J. G. Chen and C. L. Chen, *J. Power Sources*, 2002, **103**(2), 265–272.

383 V. Joshi and M. L. Mecartney, *J. Mater. Res.*, 1993, 2668–2678.

384 B. Scherrer, A. Rossi, J. Martynczuk, M. D. Rossell, A. Bieberle-Hütter, J. L. M. Rupp, R. Erni and L. J. Gauckler, *J. Power Sources*, 2011, **196**(18), 7372–7382.

385 T. A. Derouin, C. D. E. Lakeman, X. H. Wu, J. S. Speck and F. F. Lange, *J. Mater. Res.*, 1997, **201**, 1391–1400.

386 J. G. Yoon and K. Kim, *Appl. Phys. Lett.*, 1996, **68**, 2523–2525.

387 T. A. Derouin, C. D. E. Lakeman, X. H. Wu, J. S. Speck and F. F. Lange, *J. Mater. Res.*, 1997, 1391–1400.

388 G. W. Scherer, *J. Non Cryst. Solids*, 1992, **147–148**, 363–373.

389 A. Atkinson and R. M. Guppy, *J. Mater. Sci.*, 1991, **26**, 3869–3873.

390 B. Scherrer, J. Martynczuk, H. Galinski, J. G. Grolig, S. Binder, A. Bieberle-Hütter, J. L. M. Rupp, M. Prestat and L. J. Gauckler, *Adv. Funct. Mater.*, 2012, **22**(16), 3509–3518.

391 Y. Zhu, W. S. Chang, L. J. Miara and J. L. M. Rupp, Lithium Solid Electrolyte and Method of Manufacture Thereof, *US Pat.*, 16860326, Pending, 2019.

392 Y. A. Jee, B. Ma, V. A. Maroni, M. Li, B. L. Fisher and U. Balachandran, *Supercond. Sci. Technol.*, 2001, **14**, 285.

393 M. Kubicek, A. Wachter-Welzl, D. Rettenwander, R. Wagner, S. Berendts, R. Uecker, G. Amthauer, H. Hutter and J. Fleig, *Chem. Mater.*, 2017, **29**(17), 7189–7196.

394 P. R. Willmott, *Prog. Surf. Sci.*, 2004, **76**, 163–217.

395 W. Y. Liu, Z. W. Fu, C. L. Li and Q. Z. Qin, *Electrochem. Solid-State Lett.*, 2004, **7**, 36–40.

396 C. L. Li, B. Zhang and Z. W. Fu, *Thin Solid Films*, 2006, **515**, 1886–1892.

397 R. Eason, *Pulsed Laser Deposition of Thin Films: applications-led growth of functional materials*, Wiley-Interscience, 2007, vol. 53.

398 K. Wasa and S. Hayakawa, *Handbook of Sputter Deposition Technology: Principles, Technology, and Applications*, 1992.

399 H. M. Christen and G. Eres, *J. Phys. Condens Matter.*, 2008, **20**, 264005.

400 J. E. Mahan, *Physical Vapor Deposition of Thin Films*, Wiley, 2000.

401 X. Yu, J. B. Bates, G. E. Jellison and F. X. Hart, *J. Electrochem. Soc.*, 1997, **144**, 524–532.

9000 | *Chem. Soc. Rev.*, 2025, **54**, 8925–9007

This journal is © The Royal Society of Chemistry 2025

402 B. Put, P. M. Vereecken, J. Meersschaut, A. Sepúlveda and A. Stesmans, *ACS Appl. Mater. Interfaces*, 2016, **8**, 7060–7069.

403 Y. Zhu, J. C. Gonzalez-rosillo, M. Balaish, Z. D. Hood, K. Joong and J. L. M. Rupp, *Nat. Rev. Mater.*, 2021, **6**, 313–331.

404 W. Xiao, J. Wang, L. Fan, J. Zhang and X. Li, *Energy Storage Mater.*, 2019, **19**, 379–400.

405 V. Siller, A. Morata, M. N. Eroles, R. Arenal, J. C. Gonzalez-Rosillo, J. M. López del Amo and A. Tarancón, *J. Mater. Chem. A*, 2021, **9**, 17760–17769.

406 Y. Sun, P. Guan, Y. Liu, H. Xu, S. Li and D. Chu, *Crit. Rev. Solid State Mater. Sci.*, 2019, **44**, 265–282.

407 Y. Zhu, J. C. Gonzalez-rosillo, M. Balaish, Z. D. Hood, K. J. Kim and J. L. M. Rupp, *Nat. Rev. Mater.*, 2021, **6**, 313–331.

408 W. Lai, C. K. Erdonmez, T. F. Marinis, C. K. Bjune, N. J. Dudney, F. Xu, R. Wartena and Y. M. Chiang, *Adv. Mater.*, 2010, **22**, E139.

409 S. Kim, M. Hirayama, W. Cho, K. Kim, T. Kobayashi, R. Kaneko, K. Suzuki and R. Kanno, *CrystEngComm*, 2014, **16**, 1044–1049.

410 I. Petrov, F. Adibi, J. E. Greene, W. D. Sproul and W. D. Münz, *J. Vac. Sci. Technol., A*, 1992, **10**, 3283–3287.

411 Y. Hamon, A. Douard, F. Sabary, C. Marcel, P. Vinatier, B. Pecquenard and A. Levasseur, *Solid State Ionics*, 2006, **177**, 257–261.

412 W. C. West, Z. D. Hood, S. P. Adhikari, C. Liang, A. Lachgar, M. Motoyama and Y. Iriyama, *J. Power Sources*, 2016, **312**, 116–122.

413 N. Kuwata, N. Iwagami, Y. Tanji, Y. Matsuda and J. Kawamura, *J. Electrochem. Soc.*, 2010, **157**, A521.

414 R. Pfenninger, M. Struzik, I. I. Garbayo, E. Stilp and J. L. M. Rupp, *Nat. Energy*, 2019, **4**, 475–483.

415 F. Aguesse, V. Roddatis, J. Roqueta, P. García, D. Pergolesi, J. Santiso and J. A. Kilner, *Solid State Ionics*, 2015, **272**, 1–8.

416 J. F. M. Oudenhoven, L. Baggetto and P. H. L. Notten, *Adv. Energy Mater.*, 2011, **1**, 10–33.

417 Cymbet, EnerChip™ CBC012 dataset, 2014.

418 N. J. Dudney and Y. Il Jang, *J. Power Sources*, 2003, **119–121**, 300–304.

419 P. Hofmann, F. Walther, M. Rohnke, J. Sann, W. G. Zeier and J. Janek, *Solid State Ionics*, 2019, **342**, 115054.

420 J. Sastre, T. Y. Lin, A. N. Filippin, A. Priebe, E. Avancini, J. Michler, A. N. Tiwari, Y. E. Romanyuk and S. Buecheler, *ACS Appl. Energy Mater.*, 2019, **2**, 8511–8524.

421 G. Tan, F. Wu, L. Li, Y. Liu and R. Chen, *J. Phys. Chem. C*, 2012, **116**, 3817–3826.

422 K. K. Bharathi, H. Tan, S. Takeuchi, L. Meshi, H. Shen, J. Shin, I. Takeuchi and L. A. Bendersky, *RSC Adv.*, 2016, **6**, 61974–61983.

423 J.-K. K. Ahn and S.-G. G. Yoon, *Electrochem. Solid-State Lett.*, 2005, **8**, A75.

424 J. K. Ahn and S. G. Yoon, *Electrochim. Acta*, 2004, **50**, 371–374.

425 T. Ohnishi, K. Mitsuishi, K. Nishio and K. Takada, *Chem. Mater.*, 2015, **27**, 1233–1241.

426 D. H. Kim, S. Imashuku, L. Wang, Y. Shao-Horn and C. A. Ross, *J. Cryst. Growth*, 2013, **372**, 9–14.

427 M. Rawlence, A. N. Filippin, A. Wäckerlin, T. Y. Lin, E. Cuervo-Reyes, A. Remhof, C. Battaglia, J. L. M. Rupp and S. Buecheler, *ACS Appl. Mater. Interfaces*, 2018, **10**, 13720–13728.

428 M. B. Dixit, B. S. Vishugopi, W. Zaman, P. Kenesei, J. S. Park, J. Almer, P. P. Mukherjee and K. B. Hatzell, *Nat. Mater.*, 2022, **21**, 1298–1305.

429 S. I. Furusawa, H. Tabuchi, T. Sugiyama, S. Tao and J. T. S. Irvine, *Solid State Ionics*, 2005, **176**, 553–558.

430 S. Ulusoy, S. Gulen, G. Aygun, L. Ozyuzer and M. Ozdemir, *Solid State Ionics*, 2018, **324**, 226–232.

431 A. S. Westover, N. J. Dudney, R. L. Sacci and S. Kalnaus, *ACS Energy Lett.*, 2019, **4**, 651–655.

432 Z. Zheng, H. Fang, Z. Liu and Y. Wang, *J. Electrochem. Soc.*, 2015, **162**, A244–A248.

433 H. Chen, H. Tao, X. Zhao and Q. Wu, *J. Non Cryst. Solids*, 2011, **357**, 3267–3271.

434 J. S. Park, L. Cheng, V. Zorba, A. Mehta, J. Cabana, G. Chen, M. M. Doeff, T. J. Richardson, J. H. Park, J. W. Son and W. S. Hong, *Thin Solid Films*, 2015, **576**, 55–60.

435 M. Rawlence, I. Garbayo, S. Buecheler and J. L. M. Rupp, *Nanoscale*, 2016, **8**, 14746–14753.

436 J. Z. Lee, Z. Wang, H. L. Xin, T. A. Wynn and Y. S. Meng, *J. Electrochem. Soc.*, 2017, **164**, A6268–A6273.

437 O. Maqueda, F. Sauvage, L. Laffont, M. L. Martínez-Sarrión, L. Mestres and E. Baudrin, *Thin Solid Films*, 2008, **516**, 1651–1655.

438 T. Ohnishi and K. Takada, *Solid State Ionics*, 2012, **228**, 80–82.

439 H. S. Lee, S. Kim, K. B. Kim and J. W. Choi, *Nano Energy*, 2018, **53**, 225–231.

440 D. Scheld, W. S. Lobe, S. Dellen, C. Ihrig, M. Häuschen, G. Hoff, L. C. Finsterbusch, M. Uhlenbruck, S. Guillon and O. Fattakhova-Rohlfing, *J. Power Sources*, 2022, **545**, 231872.

441 W. S. Scheld, S. Lobe, S. Uhlenbruck, C. Dellen, Y. J. Sohn, L. C. Hoff, F. Vondahlen, O. Guillon and D. Fattakhova-Rohlfing, *Thin Solid Films*, 2022, **749**, 139177.

442 X. Chen, J. Sastre, A. Aribia, E. Gilshtein and Y. E. Romanyuk, *ACS Appl. Energy Mater.*, 2021, **4**(6), 5408–5414.

443 E. Yarali, C. Koutsiaki, H. Faber, K. Tetzner, E. Yengel, P. Patsalas, N. Kalfagiannis, D. C. Koutsogeorgis and T. D. Anthopoulos, *Adv. Funct. Mater.*, 2020, **30**, 1–37.

444 C. S. Nimisha, G. M. Rao, N. Munichandraiah, G. Natarajan and D. C. Cameron, *Solid State Ionics*, 2011, **185**, 47–51.

445 X. Wang, Y. Li and Y. S. Meng, *Joule*, 2018, **2**, 2225–2234.

446 M. Yousaf, U. Naseer, A. Imran, Y. Li, W. Aftab, A. Mahmood, N. Mahmood, X. Zhang, P. Gao, Y. Lu, S. Guo, H. Pan and Y. Jiang, *Mater. Today*, 2022, **58**, 238–274.

447 S. Tao, M. Li, M. Lyu, L. Ran, R. Wepf, I. Gentle and R. Knibbe, *Nano Energy*, 2022, **96**, 107083.

448 O. Cojocaru-Mirédin, J. Schmieg, M. Müller, A. Weber, E. Ivers-Tiffée and D. Gerthsen, *J. Power Sources*, 2022, **539**, 231417.

This journal is © The Royal Society of Chemistry 2025

Chem. Soc. Rev., 2025, **54**, 8925–9007 | 9001

449 S. Stegmaier, R. Schierholz, I. Povstugar, J. Barthel, S. P. Rittmeyer, S. Yu, S. Wengert, S. Rostami, H. Kungl, K. Reuter, R. A. Eichel and C. Scheurer, *Adv. Energy Mater.*, 2021, **11**(26), 2100707.

450 J. Tan and A. Tiwari, *ECS Solid State Lett.*, 2012, **1**, Q57–Q60.

451 D. J. Kalita, S. H. Lee, K. S. Lee, D. H. Ko and Y. S. Yoon, *Solid State Ionics*, 2012, **229**, 14–19.

452 B. Sun, J. Pang, Q. Cheng, S. Zhang, Y. Li, C. Zhang, D. Sun, B. Ibarlucea, Y. Li, D. Chen, H. Fan, Q. Han, M. Chao, H. Liu, J. Wang, G. Cuniberti, L. Han and W. Zhou, *Adv. Mater. Technol.*, 2021, **6**(7), 2000744.

453 H. Katsui and T. Goto, *Thin Solid Films*, 2015, **584**, 130–134.

454 C. Loho, R. Djenadic, M. Bruns, O. Clemens and H. Hahn, *J. Electrochem. Soc.*, 2017, **164**, A6131–A6139.

455 C. Loho, R. Djenadic, P. Mundt, O. Clemens and H. Hahn, *Solid State Ionics*, 2017, **313**, 32–44.

456 L. Meda and E. E. Maxie, *Thin Solid Films*, 2012, **520**, 1799–1803.

457 T. Aaltonen, M. Alnes, O. Nilsen, L. Costelle and H. Fjellvåg, *J. Mater. Chem.*, 2010, **20**, 2877–2881.

458 A. C. Kozen, A. J. Pearse, C. F. Lin, M. Noked and G. W. Rubloff, *Chem. Mater.*, 2015, **27**, 5324–5331.

459 T. M. Barnes, J. Leaf, C. Fry and C. A. Wolden, *J. Cryst. Growth*, 2005, **274**, 412–417.

460 E. Kazyak, K. H. Chen, K. N. Wood, A. L. Davis, T. Thompson, A. R. Bielinski, A. J. Sanchez, X. Wang, C. Wang, J. Sakamoto and N. P. Dasgupta, *Chem. Mater.*, 2017, **29**, 3785–3792.

461 Y. Zhao, K. Zheng and X. Sun, *Joule*, 2018, **2**, 2583–2604.

462 D. Lin, Y. Liu and Y. Cui, *Nat. Nanotechnol.*, 2017, **12**, 194–206.

463 J. Dai, C. Yang, C. Wang, G. Pastel and L. Hu, *Adv. Mater.*, 2018, **30**(48), 1802068.

464 E. Østreng, P. Vajeeston, O. Nilsen and H. Fjellvåg, *RSC Adv.*, 2012, **2**, 6315–6322.

465 B. Put, M. J. Mees, N. Hornsveld, A. Sepulveda, P. M. Vereecken, W. M. M. Kessels and M. Creatore, *ECS Trans.*, 2017, **75**, 61–69.

466 K. Kang, S. Xie, L. Huang, Y. Han, P. Y. Huang, K. F. Mak, C. J. Kim, D. Muller and J. Park, *Nature*, 2015, **520**, 656–660.

467 G. Jin, C. S. Lee, X. Liao, J. Kim, Z. Wang, O. F. N. Okello, B. Park, J. Park, C. Han, H. Heo, J. Kim, S. H. Oh, S. Y. Choi, H. Park and M. H. Jo, *Sci. Adv.*, 2019, **5**, 1–7.

468 H. Yang, Y. Wang, X. Zou, R. Bai, Z. Wu, S. Han, T. Chen, S. Hu, H. Zhu, L. Chen, D. W. Zhang, J. C. Lee, X. Lu, P. Zhou, Q. Sun, E. T. Yu, D. Akinwande and L. Ji, *Research*, 2021, **2021**, 1–9.

469 M. Nisula, Y. Shindo, H. Koga and M. Karppinen, *Chem. Mater.*, 2015, **27**, 6987–6993.

470 M.-Y. Li, Y.-Y. Chang, H.-C. Wu, C.-S. Huang, J.-C. Chen, J.-L. Lue and S.-M. Chang, *J. Electrochem. Soc.*, 2007, **154**, H967.

471 A. Sekiguchi, *J. Vac. Soc. Jpn.*, 2016, **59**, 171–183.

472 C. Loho, R. Djenadic, M. Bruns, O. Clemens and H. Hahn, *J. Electrochem. Soc.*, 2017, **164**, A6131–A6139.

473 V. Miikkulainen, M. Leskelä, M. Ritala and R. L. Puurunen, *J. Appl. Phys.*, 2013, **113**, 021301.

474 E. Østreng, P. Vajeeston, O. Nilsen and H. Fjellvåg, *RSC Adv.*, 2012, **2**, 6315–6322.

475 J. Liu, M. N. Banis, X. Li, A. Lushington, M. Cai, R. Li, T. K. Sham and X. Sun, *J. Phys. Chem. C*, 2013, **117**, 20260–20267.

476 T. Aaltonen, O. Nilsen, A. Magrasó and H. Fjellvåg, *Chem. Mater.*, 2011, **23**, 4669–4675.

477 J. Hämäläinen, J. Holopainen, F. Munnik, T. Hatanpää, M. Heikkilä, M. Ritala and M. Leskelä, *J. Electrochem. Soc.*, 2012, **159**, A259–A263.

478 B. Wang, J. Liu, Q. Sun, R. Li, T. K. Sham and X. Sun, *Nanotechnology*, 2014, **25**, 504007.

479 J. Hämäläinen, F. Munnik, T. Hatanpää, J. Holopainen, M. Ritala and M. Leskelä, *J. Vac. Sci. Technol., A*, 2012, **30**, 01A106.

480 S. M. George, *Chem. Rev.*, 2010, **110**, 111.

481 J. H. Woo, J. E. Trevey, A. S. Cavanagh, Y. S. Choi, S. C. Kim, S. M. George, K. H. Oh and S.-H. Lee, *J. Electrochem. Soc.*, 2012, **159**, A1120–A1124.

482 Y. Liu, Q. Sun, Y. Zhao, B. Wang, P. Kaghazchi, K. R. Adair, R. Li, C. Zhang, J. Liu, L. Y. Kuo, Y. Hu, T. K. Sham, L. Zhang, R. Yang, S. Lu, X. Song and X. Sun, *ACS Appl. Mater. Interfaces*, 2018, **10**, 31240–31248.

483 Y. Zhao, K. Zheng and X. Sun, *Joule*, 2018, **2**, 2583–2604.

484 J. F. Wu and X. Guo, *Phys. Chem. Chem. Phys.*, 2017, **19**, 5880–5887.

485 R. Li, K. Liao, W. Zhou, X. Li, D. Meng, R. Cai and Z. Shao, *J. Membr. Sci.*, 2019, **582**, 194–202.

486 P. J. Kumar, K. Nishimura, M. Senna, A. Düvel, P. Heitjans, T. Kawaguchi, N. Sakamoto, N. Wakiya and H. Suzuki, *RSC Adv.*, 2016, **6**, 62656–62667.

487 J. van den Broek, S. Afyon and J. L. M. Rupp, *Adv. Energy Mater.*, 2016, **6**, 1–11.

488 A. Paulus, S. Kammler, S. Heuer, M. C. Paulus, P. Jakes, J. Granwehr and R.-A. Eichel, *J. Electrochem. Soc.*, 2019, **166**, A5403–A5409.

489 S. Zhang, H. Zhao, J. Guo, Z. Du, J. Wang and K. Świerczek, *Solid State Ionics*, 2019, **336**, 39–46.

490 M. Ling, X. Zhu, Y. Jiang and J. Zhu, *Ionics*, 2016, **22**, 2151–2156.

491 P. Jiang, G. Du, J. Cao, X. Zhang, C. Zou, Y. Liu and X. Lu, *Energy Technol.*, 2023, **11**(3), 2201288.

492 L. Ni, Z. Wu and C. Zhang, *Materials*, 2021, **14**, 6–13.

493 S. Ohta, T. Kobayashi and T. Asaoka, *J. Power Sources*, 2011, **196**, 3342–3345.

494 H. Aono, N. Imanaka and G. Ya Adachi, *Acc. Chem. Res.*, 1994, **27**, 265–270.

495 H. Aono, E. Sugimoto, Y. Sadaaka, N. Imanaka and G. Y. Adachi, *J. Electrochem. Soc.*, 1989, **136**, 590.

496 C. Li, Y. Liu, J. He and K. S. Brinkman, *J. Alloys Compd.*, 2017, **695**, 3744–3752.

497 L. Dhivya, K. Karthik, S. Ramakumar and R. Murugan, *RSC Adv.*, 2015, **5**, 96042–96051.

498 L. Baraket and A. Ghorbel, *Stud. Surf. Sci. Catal.*, 1998, **118**, 657–667.

9002 | *Chem. Soc. Rev.*, 2025, **54**, 8925–9007

This journal is © The Royal Society of Chemistry 2025

499 N. Ugemuge, Y. R. Parauha and S. J. Dhoble, *Energy Mater.*, 2021, 445–480.

500 Y. X. Gao, X. P. Wang, W. G. Wang and Q. F. Fang, *Solid State Ionics*, 2010, **181**, 33–36.

501 Y. Li, T. Yang, W. Wu, Z. Cao, W. He, Y. Gao, J. Liu and G. Li, *Ionics*, 2018, **24**, 3305–3315.

502 F. Aguesse, J. M. López Del Amo, V. Roddatis, A. Aguadero and J. A. Kilner, *Adv. Mater. Interfaces*, 2014, **1**, 1–9.

503 R. W. Schwartz, T. Schneller and R. Waser, *C. R. Chim.*, 2004, **7**, 433–461.

504 M. Saccoccio, J. Yu, Z. Lu, S. C. T. Kwok, J. Wang, K. K. Yeung, M. M. F. Yuen and F. Ciucci, *J. Power Sources*, 2017, **365**, 43–52.

505 V. Siller, A. Morata, M. N. Eroles, R. Arenal, J. C. Gonzalez-Rosillo, J. M. López del Amo and A. Tarancón, *J. Mater. Chem. A*, 2021, **9**, 17760–17769.

506 T. Aaltonen, M. Alnes, O. Nilsen, L. Costelle and H. Fjellvåg, *J. Mater. Chem.*, 2010, **20**, 2877–2881.

507 K. B. Dermenci and S. Turan, *Int. J. Energy Res.*, 2019, **43**, 141–149.

508 C. Ma, E. Rangasamy, C. Liang, J. Sakamoto, K. L. More, M. Chi, M. Cheng, E. Rangasamy, C. Liang, J. Sakamoto, K. L. More, M. Chi, C. Ma, E. Rangasamy, C. Liang, J. Sakamoto, K. L. More and M. Chi, *Angew. Chem.*, 2015, **127**, 131–135.

509 X. Liu, Y. Chen, Z. D. Hood, C. Ma, S. Yu, A. Sharafi, H. Wang, K. An, J. Sakamoto, D. J. Siegel, Y. Cheng, N. H. Jalarvo and M. Chi, *Energy Environ. Sci.*, 2019, **12**, 945–951.

510 J. Sakamoto, E. Rangasamy, H. Kim, Y. Kim and J. Wolfenstine, *Nanotechnology*, 2013, **24**, 424005.

511 Z. F. Yow, Y. L. Oh, W. Gu, R. P. Rao and S. Adams, *Solid State Ionics*, 2016, **292**, 122–129.

512 A. La Monaca, A. Paolella, A. Guerfi, F. Rosei and K. Zaghib, *Electrochem. Commun.*, 2019, **104**, 106483.

513 J. Boltersdorf, N. King and P. A. Maggard, *CrystEngComm*, 2015, **17**, 2225–2241.

514 L. Hu, T. Yoko, H. Kozuka and S. Sakka, *Thin Solid Films*, 1992, **219**, 18–23.

515 C. Deviannapoorani, S. Ramakumar, N. Janani and R. Murugan, *Solid State Ionics*, 2015, **283**, 123–130.

516 S. Kumazaki, Y. Iriyama, K. H. Kim, R. Murugan, K. Tanabe, K. Yamamoto, T. Hirayama and Z. Ogumi, *Electrochem. Commun.*, 2011, **13**, 509–512.

517 K. B. Dermenci and S. Turan, *Ceram. Int.*, 2018, **44**, 11852–11857.

518 J. L. Allen, J. Wolfenstine, E. Rangasamy and J. Sakamoto, *J. Power Sources*, 2012, **206**, 315–319.

519 S. Ramakumar, L. Satyanarayana, S. V. Manorama and R. Murugan, *Phys. Chem. Chem. Phys.*, 2013, **15**, 11327–11338.

520 L. Nbo, L. La and S. Nbo, *Solid State Ionics*, 1998, **110**, 206–210.

521 G. G. Amatucci, A. Safari, F. K. Shokoohi and B. J. Wilkens, *Solid State Ionics*, 1993, **60**, 357–365.

522 D. H. Kothari and D. K. Kanchan, *Phys. B*, 2016, **501**, 90–94.

523 A. Dumon, M. Huang, Y. Shen and C.-W. Nan, *Solid State Ionics*, 2013, **243**, 36–41.

524 V. Thangadurai and W. Weppner, *J. Am. Ceram. Soc.*, 2005, **88**, 411–418.

525 S. Song, B. Yan, F. Zheng, H. M. Duong and L. Lu, *Solid State Ionics*, 2014, **268**, 135–139.

526 C. Bernuy-Lopez, W. Manalastas, J. M. Lopez Del Amo, A. Aguadero, F. Aguesse and J. A. Kilner, *Chem. Mater.*, 2014, **26**, 3610–3617.

527 R. Wagner, D. Rettenwander, G. J. Redhammer, G. Tippelt, G. Sabathi, M. E. Musso, B. Stanje, M. Wilkening, E. Suard and G. Amthauer, *Inorg. Chem.*, 2016, **55**, 12211–12219.

528 H. El-Shinawi, G. W. Paterson, D. A. MacLaren, E. J. Cussen and S. A. Corr, *J. Mater. Chem. A*, 2017, **5**, 319–329.

529 F. M. Pesci, R. H. Brugge, A. K. O. Hekselman, A. Cavallaro, R. J. Chater and A. Aguadero, *J. Mater. Chem. A*, 2018, **6**, 19817–19827.

530 S. Kim, J.-S. Kim, L. Miara, Y. Wang, S.-K. Jung, S. Y. Park, Z. Song, H. Kim, M. Badding, J. Chang, V. Roev, G. Yoon, R. Kim, J.-H. Kim, K. Yoon, D. Im and K. Kang, *Nat. Commun.*, 2022, **13**, 1883.

531 G. Larraz, A. Orera and M. L. Sanjuán, *J. Mater. Chem. A*, 2013, **1**, 11419–11428.

532 Y. Li, J.-T. Han, S. C. Vogel and C.-A. Wang, *Solid State Ionics*, 2015, **269**, 57–61.

533 W. Xia, B. Xu, H. Duan, X. Tang, Y. Guo, H. Kang, H. Li and H. Liu, *J. Am. Ceram. Soc.*, 2017, **100**, 2832–2839.

534 F. Aguesse, J. M. López Del Amo, V. Roddatis, A. Aguadero and J. A. Kilner, *Adv. Mater. Interfaces*, 2014, **1**, 1–9.

535 J. F. Nonemacher, C. Hüter, H. Zheng, J. Malzbender, M. Krüger, R. Spatschek and M. Finsterbusch, *Solid State Ionics*, 2018, **321**, 126–134.

536 M. Kubicek, A. Wachter-Welzl, D. Rettenwander, R. Wagner, S. Berendts, R. Uecker, G. Amthauer, H. Hutter and J. Fleig, *Chem. Mater.*, 2017, **19**(17), 7189–7196.

537 H. Yamada, T. Ito, R. Hongahally Basappa, R. Bekarevich and K. Mitsuishi, *J. Power Sources*, 2017, **368**, 97–106.

538 J. E. Ni, E. D. Case, J. S. Sakamoto, E. Rangasamy and J. B. Wolfenstine, *J. Mater. Sci.*, 2012, **47**, 7978–7985.

539 T. Okumura, T. Nakatsutsumi, T. Ina, Y. Orikasa, H. Arai, T. Fukutsuka, Y. Iriyama, T. Uruga, H. Tanida, Y. Uchimoto and Z. Ogumi, *J. Mater. Chem.*, 2011, **21**, 10051–10060.

540 Y. S. Jung, D. W. Lee and D. Y. Jeon, *Appl. Surf. Sci.*, 2004, **221**, 136–142.

541 N. Kumar, T. M. Wilkinson, C. E. Packard and M. Kumar, *J. Appl. Phys.*, 2016, **119**, 225303.

542 L. Wang, H. Li, M. Courty, X. Huang and E. Baudrin, *J. Power Sources*, 2013, **232**, 165–172.

543 S. Y. Lee, S. K. Rha, W. J. Lee, D. W. Kim, J. S. Hwang and C. O. Park, *Jpn. J. Appl. Phys., Part 1*, 1997, **36**, 5249–5252.

544 P. Albertus, *ACS Energy Lett.*, 2021, **6**, 1399–1404.

545 E. J. Cheng, K. Hong, N. J. Taylor, H. Choe, J. Wolfenstine and J. Sakamoto, *J. Eur. Ceram. Soc.*, 2009, **37**, 3213–3217.

546 K. Wang, Y. Wu, K. Liu and H. Wu, *Chem. Res. Chin. Univ.*, 2020, **36**, 351–359.

This journal is © The Royal Society of Chemistry 2025

Chem. Soc. Rev., 2025, **54**, 8925–9007 | 9003

547 G. Vardar, W. J. Bowman, Q. Lu, J. Wang, R. J. Chater, A. Aguadero, R. Seibert, J. Terry, A. Hunt, I. Waluyo, D. D. Fong, A. Jarry, E. J. Crumlin, S. L. Hellstrom, Y. M. Chiang and B. Yildiz, *Chem. Mater.*, 2018, **30**, 6259–6276.

548 N. Zhang, X. Long, Z. Wang, P. Yu, F. Han, J. Fu, G. Ren, Y. Wu, S. Zheng, W. Huang, C. Wang, H. Li and X. Liu, *ACS Appl. Energy Mater.*, 2018, **1**, 5968–5976.

549 C. L. Tsai, Q. Ma, C. Dellen, S. Lobe, F. Vondahlen, A. Windmüller, D. Grüner, H. Zheng, S. Uhlenbruck, M. Finsterbusch, F. Tietz, D. Fattakhova-Rohlfing, H. P. Buchkremer and O. Guillon, *Sustain. Energy Fuels*, 2019, **3**, 280–291.

550 A. A. Delluva, A. A. Delluva, J. Dudoff, J. Dudoff, G. Teeter, A. Holewinski, A. Holewinski and A. Holewinski, *ACS Appl. Mater. Interfaces*, 2020, **12**, 24992–24999.

551 C. D. Fincher, C. E. Athanasiou, C. Gilgenbach, M. Wang, B. W. Sheldon, C. Carter and Y. Chiang, *Joule*, 2022, **6**, 2794–2809.

552 S. Ohta, J. Seki, Y. Yagi, Y. Kihira, T. Tani and T. Asaoka, *J. Power Sources*, 2014, **265**, 40–44.

553 C. Roitzheim, Y. J. Sohn, L. Y. Kuo, G. Häuschen, M. Mann, D. Sebold, M. Finsterbusch, P. Kaghazchi, O. Guillon and D. Fattakhova-Rohlfing, *ACS Appl. Energy Mater.*, 2022, **5**, 6913–6926.

554 S. Ohta, Y. Kihira and T. Asaoka, *J. Mater. Chem. A*, 2021, **9**, 3353–3359.

555 J. Lee, T. Lee, K. Char, K. J. Kim and J. W. Choi, *Acc. Chem. Res.*, 2021, **54**, 3390–3402.

556 D. H. S. Tan, Y. S. Meng and J. Jang, *Joule*, 2022, **6**, 1755–1769.

557 R. S. Negi, P. Minnmann, R. Pan, S. Ahmed, M. J. Herzog, K. Volz, R. Takata, F. Schmidt, J. Janek and M. T. Elm, *Chem. Mater.*, 2021, **33**, 6713–6723.

558 F. Hao, F. Han, Y. Liang, C. Wang and Y. Yao, *MRS Bull.*, 2018, **43**, 746–751.

559 A. M. Nolan, Y. Zhu, X. He, Q. Bai and Y. Mo, *Joule*, 2018, **2**, 2016–2046.

560 T. Liu, Y. Ren, Y. Shen, S. X. Zhao, Y. Lin and C. W. Nan, *J. Power Sources*, 2016, **324**, 349–357.

561 F. Strauss, T. Bartsch, L. de Biasi, A.-Y. Kim, J. Janek, P. Hartmann and T. Brezesinski, *ACS Energy Lett.*, 2018, **3**, 992–996.

562 X. Han, W. Zhou, M. Chen, L. Luo, L. Gu, Q. Zhang, J. Chen, B. Liu, S. Chen and W. Zhang, *Nano Res.*, 2022, **15**, 6156–6167.

563 T. Lan, C.-L. Tsai, F. Tietz, X.-K. Wei, M. Heggen, R. E. Dunin-Borkowski, R. Wang, Y. Xiao, Q. Ma and O. Guillon, *Nano Energy*, 2019, **65**, 104040.

564 K. Wang, Z. Gu, Z. Xi, L. Hu and C. Ma, *Nat. Commun.*, 2023, **14**, 6–15.

565 D. Wang, B. Gwalani, D. Wierzbicki, V. Singh, L. Jhang, T. Rojas, R. Kou, M. Liao, L. Ye, H. Jiang, S. Shan, A. Silver, A. T. Ngo, Y. Du, X. Li and D. Wang, *Nat. Mater.*, 2025, **24**, 243–251.

566 L. Cui, S. Zhang, J. Ju, T. Liu, Y. Zheng, J. Xu, Y. Wang, J. Li, J. Zhao, J. Ma, J. Wang, G. Xu, T. S. Chan, Y. C. Huang, S. C. Haw, J. M. Chen, Z. Hu and G. Cui, *Nat. Energy*, 2024, **9**, 1084–1094.

567 Y. Ren, T. Liu, Y. Shen, Y. Lin and C. W. Nan, *J. Mater.*, 2016, **2**, 256–264.

568 S. Panahian Jand and P. Kaghazchi, *MRS Commun.*, 2018, **8**, 591–596.

569 Y. Zhu, X. He and Y. Mo, *ACS Appl. Mater. Interfaces*, 2015, **7**, 23685–23693.

570 L. Cheng, E. J. Crumlin, W. Chen, R. Qiao, H. Hou, S. Franz Lux, V. Zorba, R. Russo, R. Kostecki, Z. Liu, K. Persson, W. Yang, J. Cabana, T. Richardson, G. Chen and M. Doeff, *Phys. Chem. Chem. Phys.*, 2014, **16**, 18294–18300.

571 T. Liu, Y. Ren, Y. Shen, S. X. Zhao, Y. Lin and C. W. Nan, *J. Power Sources*, 2016, **324**, 349–357.

572 Y. Kato, S. Hori, T. Saito, K. Suzuki, M. Hirayama, A. Mitsui, M. Yonemura, H. Iba and R. Kanno, *Nat. Energy*, 2016, **1**, 16030.

573 M. Balaish, J. C. Gonzalez-Rosillo, K. J. Kim, Y. Zhu, Z. D. Hood and J. L. M. Rupp, *Nat. Energy*, 2021, **6**, 227–239.

574 E. Rangasamy, J. Wolfenstine and J. Sakamoto, *Solid State Ionics*, 2012, **206**, 28–32.

575 M. Mann, C. Roitzheim, O. Guillon, D. Fattakhova-rohl and M. Finsterbusch, *J. Mater. Chem. A*, 2023, **11**, 5670–5680.

576 G. Delaizir, V. Viallet, A. Aboulaich, R. Bouchet, L. Tortet, V. Seznec, M. Morcrette, J. M. Tarascon, P. Rozier and M. Dollé, *Adv. Funct. Mater.*, 2012, **22**, 2140–2147.

577 M. Ihrig, M. Finsterbusch, C. Tsai, A. M. Laptev, C. Tu, M. Bram, Y. Jung, R. Ye, S. Sevinc, S. Lin, D. Fattakhova-rohlfing and O. Guillon, *J. Power Sources*, 2021, **482**, 228905.

578 F. Han, J. Yue, C. Chen, N. Zhao, X. Fan, Z. Ma, T. Gao, F. Wang, X. Guo and C. Wang, *Joule*, 2018, **2**, 497–508.

579 Y. Kim, D. Kim, R. Bliem, L. Vardar, I. Waluyo, A. Hunt, J. T. Wright, J. P. Katsoudas and B. Yildiz, *Chem. Mater.*, 2020, **32**, 9531–9541.

580 Y. Kim, I. Waluyo, A. Hunt and B. Yildiz, *Adv. Energy Mater.*, 2022, **12**(13), 2102741.

581 E. Yi, H. Shen, S. Heywood, J. Alvarado, D. Y. Parkinson, G. Chen, S. W. Sofie, M. M. Doeff, S. W. So and M. M. Doe, *ACS Appl. Energy Mater.*, 2020, **3**, 170–175.

582 G. V. Alexander, C. Shi, J. O'Neill and E. D. Wachsman, *Nat. Mater.*, 2023, **22**, 1136–1143.

583 Y. Ren, T. Liu, Y. Shen, Y. Lin and C. W. Nan, *Ionics*, 2017, **23**, 2521–2527.

584 T. Lan, C.-L. Tsai, F. Tietz, X.-K. Wei, M. Heggen, R. E. Dunin-Borkowski, R. Wang, Y. Xiao, Q. Ma and O. Guillon, *Nano Energy*, 2019, **65**, 104040.

585 K. J. Kim and J. L. M. Rupp, *Energy Environ. Sci.*, 2020, **13**, 4930–4945.

586 G. T. Hitz, D. W. McOwen, L. Zhang, Z. Ma, Z. Fu, Y. Wen, Y. Gong, J. Dai, T. R. Hamann, L. Hu and E. D. Wachsman, *Mater. Today*, 2019, **22**, 50–57.

587 C. L. Tsai, Q. Ma, C. Dellen, S. Lobe, F. Vondahlen, A. Windmüller, D. Grüner, H. Zheng, S. Uhlenbruck, M. Finsterbusch, F. Tietz, D. Fattakhova-Rohlfing,

9004 | *Chem. Soc. Rev.*, 2025, **54**, 8925–9007

This journal is © The Royal Society of Chemistry 2025

H. P. Buchkremer and O. Guillon, *Sustainable Energy Fuels*, 2019, **3**, 280–291.

588 M. Rosen, M. Finsterbusch, O. Guillon and D. Fattakhova-Rohlfing, *J. Mater. Chem. A*, 2022, **10**, 2320–2326.

589 Y. Ren, T. Liu, Y. Shen, Y. Lin and C. W. Nan, *J. Mater.*, 2016, **2**, 256–264.

590 M. Ihrig, L. Y. Kuo, S. Lobe, A. M. Laptev, C. A. Lin, C. H. Tu, R. Ye, P. Kaghazchi, L. Cressa, S. Eswara and S. K. Lin, *ACS Appl. Mater. Interfaces*, 2023, **15**, 4101–4112.

591 J. Li and R. Wang, *Ceram. Int.*, 2021, **47**, 13280–13290.

592 K. Park, B. C. Yu, J. W. Jung, Y. Li, W. Zhou, H. Gao, S. Son and J. B. Goodenough, *Chem. Mater.*, 2016, **28**, 8051–8059.

593 K. H. Kim, Y. Iriyama, K. Yamamoto, S. Kumazaki, T. Asaka, K. Tanabe, C. A. J. Fisher, T. Hirayama, R. Murugan and Z. Ogumi, *J. Power Sources*, 2011, **196**, 764–767.

594 G. Vardar, W. J. Bowman, Q. Lu, J. Wang, R. J. Chater, A. Aguadero, R. Seibert, J. Terry, A. Hunt, I. Waluyo, D. D. Fong, A. Jarry, E. J. Crumlin, S. L. Hellstrom, Y. M. Chiang and B. Yildiz, *Chem. Mater.*, 2018, **30**, 6259–6276.

595 Y. Lu, C. Z. Zhao, H. Yuan, J. K. Hu, J. Q. Huang and Q. Zhang, *Matter*, 2022, **5**, 876–898.

596 E. J. Cheng, R. Oyama, T. Abe and K. Kanamura, *J. Eur. Ceram. Soc.*, 2023, **43**, 2033–2038.

597 E. J. Cheng, Y. Kushida, T. Abe and K. Kanamura, *ACS Appl. Mater. Interfaces*, 2022, **14**, 40881–40889.

598 T. Nazarenus, Y. Sun, J. Exner, J. Kita and R. Moos, *Energy Technol.*, 2021, **9**, 2100211.

599 S. H. Lee, G. L. Messing and M. Awano, *J. Am. Ceram. Soc.*, 2008, **91**, 421–427.

600 H. G. Park, H. Moon, S. C. Park, J. J. Lee, D. Yoon, S. H. Hyun and D. H. Kim, *J. Power Sources*, 2010, **195**, 2463–2469.

601 X. V. Nguyen, C. T. Chang, G. Bin Jung, S. H. Chan, W. C. W. Huang, K. J. Hsiao, W. T. Lee, S. W. Chang and I. C. Kao, *Energies*, 2016.

602 S. H. Lee, G. L. Messing and D. J. Green, *Key Eng. Mater.*, 2004, **264–268**, 321–328.

603 S. A. A. Mansour, *Mater. Chem. Phys.*, 1994, **36**, 317–323.

604 B. Garcia and N. Baffler, *J. Power Sources*, 1995, **54**, 373–377.

605 M. Steinhardt, J. V. Barreras, H. Ruan, B. Wu, G. J. Offer and A. Jossen, *J. Power Sources*, 2022, **522**, 230829.

606 M. S. Whittingham, *Chem. Rev.*, 2004, **104**, 4271–4302.

607 K. Brandt, *Solid State Ionics*, 1994, **69**, 173–183.

608 C. Ma, Y. Cheng, K. Yin, J. Luo, A. Sharafi, J. Sakamoto, J. Li, K. L. More, N. J. Dudney and M. Chi, *Nano Lett.*, 2016, **16**, 7030–7036.

609 Z. D. Hood, X. Chen, R. L. Sacci, X. Liu, G. M. Veith, Y. Mo, J. Niu, N. J. Dudney and M. Chi, *Nano Lett.*, 2021, **21**, 151–157.

610 Y. Zhu, X. He and Y. Mo, *J. Mater. Chem. A*, 2016, **4**, 3253–3266.

611 N. Jagjit and others, *Handbook of solid state batteries*, World Scientific, 2015, vol. 6.

612 B. N. Choi, J. Y. Seo, B. Kim, Y. S. Kim and C. H. Chung, *Appl. Surf. Sci.*, 2020, **506**, 144884.

613 A. Pei, G. Zheng, F. Shi, Y. Li and Y. Cui, *Nano Lett.*, 2017, **17**, 1132–1139.

614 Y. Lu, Z. Tu and L. A. Archer, *Nat. Mater.*, 2014, **13**, 961–969.

615 X. Liang, F. Tan, F. Wei and J. Du, *IOP Conf. Ser.:Mater. Sci. Eng.*, 2019, **218**, 012138.

616 A. Levasseur, M. Menetrier, R. Dormoy and G. Meunier, *Mater. Sci. Eng., B*, 1989, **3**, 5–12.

617 B. J. Neudecker, N. J. Dudney and J. B. Bates, *J. Electrochem. Soc.*, 2000, **147**, 517.

618 W. F. Beach, C. Lee, D. R. Bassett, T. M. Austin and R. Olson, *Encyclopedia of Polymer Science and Engineering*, Wiley, New York, 1989, vol. 17, pp. 990–1025.

619 X. Han, Y. Gong, K. Fu, X. He, G. T. Hitz, J. Dai, A. Pearse, B. Liu, H. Wang, G. Rubloff, Y. Mo, V. Thangadurai, E. D. Wachsman and L. Hu, *Nat. Mater.*, 2017, **16**, 572–579.

620 C. Yang, L. Zhang, B. Liu, S. Xu, T. Hamann, D. McOwen, J. Dai, W. Luo, Y. Gong, E. D. Wachsman and L. Hu, *Proc. Natl. Acad. Sci. U. S. A.*, 2018, **115**, 3770–3775.

621 A. Sharafi, E. Kazyak, A. L. Davis, S. Yu, T. Thompson, D. J. Siegel, N. P. Dasgupta and J. Sakamoto, *Chem. Mater.*, 2017, **29**, 7961–7968.

622 X. Liu, R. Garcia-Mendez, A. R. Lupini, Y. Cheng, Z. D. Hood, F. Han, A. Sharafi, J. C. Idrobo, N. J. Dudney, C. Wang, C. Ma, J. Sakamoto and M. Chi, *Nat. Mater.*, 2020, **20**, 1485–1490.

623 J. Kriegler, H. Ballmes, S. Dib, A. G. Demir, L. Hille, Y. Liang, L. Wach, S. Weinmann, J. Keilhofer, K. J. Kim, J. L. M. Rupp and M. F. Zaeh, *Adv. Funct. Mater.*, 2024, **34**, 1–16.

624 N. J. Taylor, S. Stangeland-Molo, C. G. Haslam, A. Sharafi, T. Thompson, M. Wang, R. Garcia-Mendez and J. Sakamoto, *J. Power Sources*, 2018, **396**, 314–318.

625 S. Xu, D. W. McOwen, C. Wang, L. Zhang, W. Luo, C. Chen, Y. Li, Y. Gong, J. Dai, Y. Kuang, C. Yang, T. R. Hamann, E. D. Wachsman and L. Hu, *Nano Lett.*, 2018, **18**, 3926–3933.

626 C. Yang, H. Xie, W. Ping, K. Fu, B. Liu, J. Rao, J. Dai, C. Wang, G. Pastel and L. Hu, *Adv. Mater.*, 2019, **31**(3), 1804815.

627 Z. Zhu, L. L. Lu, Y. Yin, J. Shao, B. Shen and H. Bin Yao, *ACS Appl. Mater. Interfaces*, 2019, **11**, 16578–16585.

628 Y. G. Lee, S. Fujiki, C. Jung, N. Suzuki, N. Yashiro, R. Omoda, D. S. Ko, T. Shiratsuchi, T. Sugimoto, S. Ryu, J. H. Ku, T. Watanabe, Y. Park, Y. Aihara, D. Im and I. T. Han, *Nat. Energy*, 2020, **5**, 299–308.

629 K. J. Kim, J. J. Hinricher and J. L. M. Rupp, *Nat. Energy*, 2020, **5**, 278–279.

630 K. So Yeon and J. Li, *Energy Mater. Adv.*, 2021, **2021**, 1519569.

631 J. F. M. M. Oudenhoven, Loïc Baggetto and P. H. L. L. Notten, *Adv. Energy Mater.*, 2011, **1**, 10–33.

632 L. Liu, Q. Weng, X. Lu, X. Sun, L. Zhang and O. G. Schmidt, *Small*, 2017, **13**, 1–12.

This journal is © The Royal Society of Chemistry 2025

Chem. Soc. Rev., 2025, **54**, 8925–9007 | **9005**

633 J. B. Bates, N. J. Dudney, G. R. Gruzalski, R. A. Zuhr, A. Choudhury, C. F. Luck and J. D. Robertson, *Solid State Ionics*, 1992, **53–56**, 647–654.

634 J. B. Bates, N. J. Dudney, G. R. Gruzalski, R. A. Zuhr, A. Choudhury, C. F. Luck and J. D. Robertson, *J. Power Sources*, 1993, **43**, 103–110.

635 N. J. Dudney, *Mater. Sci. Eng., B*, 2005, **116**, 245–249.

636 N. J. Dudney, *Interface*, 2008, 44–48.

637 J. Sastre, M. H. Futscher, L. Pompizi, A. Aribia, A. Priebe, J. Overbeck, M. Stiefel, A. N. Tiwari and Y. E. Romanyuk, *Commun. Mater.*, 2021, **2**, 76.

638 A. V. Morozov, H. Paik, A. O. Boev, D. A. Aksyonov, S. A. Lipovskikh, K. J. Stevenson, J. L. M. Rupp and A. M. Abakumov, *ACS Appl. Mater. Interfaces*, 2022, **14**(35), 39907–39916.

639 J. Song, X. Yang, S. S. Zeng, M. Z. Cai, L. T. Zhang, Q. F. Dong, M. Sen Zheng, S. T. Wu and Q. H. Wu, *J. Micromech. Microeng.*, 2009, **19**, 045004.

640 J. F. Whitacre, W. C. West and B. V. Ratnakumar, *J. Electrochem. Soc.*, 2003, **150**, A1676.

641 W. C. West, J. F. Whitacre, V. White and B. V. Ratnakumar, *J. Micromech. Microeng.*, 2002, **12**, 58–62.

642 J. Lin, Y. Wu, R. Bi and H. Guo, *Sens. Actuators, A*, 2017, **253**, 218–222.

643 S. D. Jones and J. R. Akridge, *J. Power Sources*, 1993, **434**, 505–513.

644 E. M. F. Vieira, J. F. Ribeiro, R. Sousa, J. H. Correia and L. M. Goncalves, *J. Micromech. Microeng.*, 2016, **26**, 084002.

645 S. W. Song, K. C. Lee and H. Y. Park, *J. Power Sources*, 2016, **328**, 311–317.

646 J. G. Kim, B. Son, S. Mukherjee, N. Schuppert, A. Bates, O. Kwon, M. J. Choi, H. Y. Chung and S. Park, *J. Power Sources*, 2015, **282**, 299–322.

647 S. Larfaillou, D. Guy-Bouyssou, F. Le Cras and S. Franger, *J. Power Sources*, 2016, **319**, 139–146.

648 L. Le Van-Jodin, A. Claudel, C. Secouard, F. Sabary, J. P. Barnes and S. Martin, *Electrochim. Acta*, 2018, **259**, 742–751.

649 J. B. Bates, N. J. Dudney, B. Neudecker, A. Ueda and C. D. Evans, *Solid State Ionics*, 2000, **135**, 33–45.

650 S. Takai, M. Kamata, S. Fujine, K. Yoneda, K. Kanda and T. Esaka, *Solid State Ionics*, 1999, **123**, 165–172.

651 C. H. Chen, J. T. Vaughey, A. N. Jansen, D. W. Dees, A. J. Kahaian, T. Goacher and M. M. Thackeray, *J. Electrochem. Soc.*, 2001, **148**, A102–A104.

652 A. A. Hubaud, D. J. Schroeder, B. J. Ingram, J. S. Okasinski and J. T. Vaughey, *J. Alloys Compd.*, 2015, **644**, 804–807.

653 J. Schoonman and E. M. Kelder, *J. Power Sources*, 1997, **68**, 65–68.

654 C. Gong, D. Ruzmetov, A. Pearse, D. Ma, J. N. Munday, G. Rubloff, A. A. Talin and M. S. Leite, *ACS Appl. Mater. Interfaces*, 2015, **7**, 26007–26011.

655 M. S. Leite, D. Ruzmetov, Z. Li, L. A. Bendersky, N. C. Bartelt, A. Kolmakov and A. A. Talin, *J. Mater. Chem. A*, 2014, **2**, 20552–20559.

656 N. Kuwata, J. Kawamura, K. Toribami, T. Hattori and N. Sata, *Electrochem. Commun.*, 2004, **6**, 417–421.

657 C. L. Li and Z. W. Fu, *Electrochim. Acta*, 2008, **53**, 6434–6443.

658 C. L. Li and Z. W. Fu, *Electrochim. Acta*, 2008, **53**, 4293–4301.

659 J. Lin, Y. Wu, R. Bi and H. Guo, *Sens Actuators A Phys*, 2017, **253**, 218–222.

660 A. A. Talin, D. Ruzmetov, A. Kolmakov, K. McKelvey, N. Ware, F. El Gabaly, B. Dunn and H. S. White, *ACS Appl. Mater. Interfaces*, 2016, **8**, 32385–32391.

661 H. Ohtsuka and Y. Sakurai, *Solid State Ionics*, 2001, **144**, 59–64.

662 M. Koo, K.-I. Park, S. H. Lee, M. Suh, D. Y. Jeon, J. W. Choi, K. Kang and K. J. Lee, *Nano Lett.*, 2012, **12**, 4810–4816.

663 W. Y. Liu, Z. W. Fu and Q. Z. Qin, *Thin Solid Films*, 2007, **515**, 4045–4048.

664 B. Wang, J. B. Bates, F. X. Hart, B. C. Sales, R. A. Zuhr and J. D. Robertson, *J. Electrochem. Soc.*, 1996, **143**, 3203.

665 F. Le Cras, B. Pecquenard, V. Dubois, V. P. Phan and D. Guy-Bouyssou, *Adv. Energy Mater.*, 2015, **5**, 1–10.

666 A. Pearse, T. Schmitt, E. Sahadeo, D. M. Stewart, A. Kozen, K. Gerasopoulos, A. A. Talin, S. B. Lee, G. W. Rubloff and K. E. Gregorczyk, *ACS Nano*, 2018, **12**, 4286–4294.

667 G. Meunier, R. Dormoy and A. Levasseur, *Mater. Sci. Eng., B*, 1989, **3**, 19–23.

668 N. J. Dudney, *3 SPEC.ISS.*, Elsevier Ltd, 2005, vol. 116, pp. 245–249.

669 Q. Qi-Zong, L. Wen-Yuan and F. Zheng-Wen, *Thin Solid Films*, 2007, **515**, 4045–4048.

670 F. Huang, Z. W. Fu, Y. Q. Chu, W. Y. Liu and Q. Z. Qin, *Electrochem. Solid-State Lett.*, 2004, 7, 0–5.

671 E. J. Jeon, Y. W. Shin, S. C. Nam, W. Il Cho and Y. S. Yoon, *J. Electrochem. Soc.*, 2001, **148**, A318.

672 J. I. Yamaki, H. Ohtsuka and T. Shodai, *Solid State Ionics*, 1996, **86–88**, 1279–1284.

673 H. Ohtsuka and Y. Sakurai, *Solid State Ionics*, 2001, **144**, 59–64.

674 W. C. West and J. F. Whitacre, *J. Electrochem. Soc.*, 2005, **152**, A966.

675 Y. Matsuda, N. Kuwata and J. Kawamura, *Solid State Ionics*, 2018, **320**, 38–44.

676 G. Vardar, W. J. Bowman, Q. Lu, J. Wang, R. J. Chater, A. Aguadero, R. Seibert, J. Terry, A. Hunt, I. Waluyo, D. D. Fong, A. Jarry, E. J. Crumlin, S. L. Hellstrom, Y. M. Chiang and B. Yildiz, *Chem. Mater.*, 2018, **30**, 6259–6276.

677 N. Zhao, W. Khokhar, Z. Bi, C. Shi, X. Guo, L. Z. Fan and C. W. Nan, *Joule*, 2019, **3**, 1190–1199.

678 J. Sastre, X. Chen, A. Aribia, A. N. Tiwari and Y. E. Romanyuk, *ACS Appl. Mater. Interfaces*, 2020, **12**, 36196–36207.

679 X. Yan, Z. Li, H. Ying, F. Nie, L. Xue, Z. Wen and W. Q. Han, *Ionics*, 2018, **24**, 1545–1551.

680 P. C. Rath, W. Hsu, C. Chen, C. Huang, W. Wu, S. Okada, Q. Dong, C. Yang, T. Lee and J. Chang, *Int. J. Energy Res.*, 2022, **46**, 17693–17705.

9006 | *Chem. Soc. Rev.*, 2025, **54**, 8925–9007

This journal is © The Royal Society of Chemistry 2025

681 A. V. Morozov, H. Paik, A. O. Boev, D. A. Aksyonov, S. A. Lipovskikh, K. J. Stevenson, J. L. M. Rupp and A. M. Abakumov, *ACS Appl. Mater. Interfaces*, 2022, **14**(35), 39907–39916.

682 J. Song, X. Yang, S. S. Zeng, M. Z. Cai, L. T. Zhang, Q. F. Dong, M. Sen Zheng, S. T. Wu and Q. H. Wu, *J. Micromech. Microeng.*, 2009, **19**, 045004.

683 S. Nanda, A. Gupta and A. Manthiram, *Adv. Energy Mater.*, 2021, **11**, 2000804.

684 R. Murugan, V. Thangadurai and W. Weppner, *Angew. Chem., Int. Ed.*, 2007, **46**, 7778–7781.

685 H. Kozuka, S. Takenaka, H. Tokita, T. Hirano, Y. Higashi and T. Hamatani, *J. Solgel Sci. Technol.*, 2003, **26**, 681–686.

686 N. A. Kyeremateng and R. Hahn, *ACS Energy Lett.*, 2018, **3**, 1172–1175.

687 S. Moitzheim, B. Put and P. M. Vereecken, *Adv. Mater. Interfaces*, 2019, **6**, 1–17.

688 K. Sun, T. S. Wei, B. Y. Ahn, J. Y. Seo, S. J. Dillon and J. A. Lewis, *Adv. Mater.*, 2013, **25**(33), 4539–4543.

689 P. H. L. Notten, F. Roozeboom, R. A. H. Niessen and L. Baggetto, *Adv. Mater.*, 2007, **19**, 4564–4567.

690 R. Sheil and J. P. Chang, *J. Vac. Sci. Technol., A*, 2020, **38**, 032411.

691 L. Liu, Q. Weng, X. Lu, X. Sun, L. Zhang and O. G. Schmidt, *Small*, 2017, **13**, 1–12.

692 D. Ruzmetov, V. P. Oleshko, P. M. Haney, H. J. Lezec, K. Karki, K. H. Baloch, A. K. Agrawal, A. V. Davydov, S. Krylyuk, Y. Liu, J. Huang, M. Tanase, J. Cumings and A. A. Talin, *Nano Lett.*, 2012, **12**, 505–511.

693 M. Létiche, E. Eustache, J. Freixas, A. Demortière, V. De Andrade, L. Morgenroth, P. Tilmant, F. Vaurette, D. Troadec, P. Roussel, T. Brousse and C. Lethien, *Adv. Energy Mater.*, 2017, **7**, 1–12.

694 J. Oudenhoven, T. Van Dongen, R. Niessen, M. De Croon and P. Notten, *ECS Trans.*, 2009, **25**, 653–658.

695 P. H. L. Notten, F. Roozeboom, R. A. H. Niessen and L. Baggetto, *Adv. Mater.*, 2007, **19**, 4564–4567.

696 T. Karabacak and T.-M. Lu, *J. Appl. Phys.*, 2005, **97**, 124504.

697 D. W. McOwen, S. Xu, Y. Gong, Y. Wen, G. L. Godbey, J. E. Gritton, T. R. Hamann, J. Dai, G. T. Hitz, L. Hu and E. D. Wachsman, *Adv. Mater.*, 2018, **30**, 1–7.

698 The Energy Institute, Statistical Review of World Energy (2023), Smil (2017), 2023.

699 E. US Energy Information Administration, Monthly Energy Review, 2022, 1–278.

700 European Comission, The European Green Deal, **https://commission.europa.eu/strategy-and-policy/priorities-2019-2024/european-green-deal_en**, (accessed 26 January 2024).

701 M. J. Wang, J. Sakamoto, M. J. Wang, R. Choudhury and J. Sakamoto, *Joule*, 2019, **3**, 2165–2178.

702 Y. Liu, R. Zhang, J. Wang and Y. Wang, *iScience*, 2021, **24**, 102332.

703 P. A. Nelson, S. Ahmed, K. G. Gallagher and D. W. Dees, *Modeling the Performance and Cost of Lithium-Ion Batteries for Electric-Drive Vehicles*, United States, 3rd edn, 2019.

704 Y. Lu, C. Z. Zhao, H. Yuan, J. K. Hu, J. Q. Huang and Q. Zhang, *Matter*, 2022, **5**, 876–898.

This journal is © The Royal Society of Chemistry 2025

Chem. Soc. Rev., 2025, **54**, 8925–9007 | **9007**